Observational Study of O-rich Evolved Stars in the Galaxy

Jun-ichi Nakashima

12 February, 2002

Contents

List of publications

1. Imai, H., Deguchi, S., Fujii, T., Glass, I. S., Ita, Y., Izumiura, H., Kameya, O., Miyazaki, A., Nakada, Y., Nakashima, J., "Detections of SiO Masers from the Large-Amplitude Variables in the Galactic Nuclear Disk", submitted to PASJ

2. Deguchi, S., Fujii, T., Nakashima J., Wood, P. R., "Near-Infrared Observations of the IRAS/SiO Sources in the Galactic Bulge: a Large Scale Distribution", submitted to PASJ

3. Nakashima, J., Deguchi, S., "SiO Maser Survey toward the Inner Galactic Disk: $40° < l < 70°$ and $|b| < 10°$ ", submitted to PASJ

4. Deguchi, S., Fujii, T., Miyoshi, M., Nakashima, J., "Observations of SiO Maser Sources within a Few Parsec from the Glactic Center", to appear in PASJ

5. Ita, Y., Deguchi, S., Fujii, T., Kameya, O., Miyoshi, M., Nakada, Y., Nakashima, J., Parthasarathy, M., "SiO maser survey of AGB stars in the North Galactic Cap", 2001, A&Ap376, 112

6. Nakashima, J., Deguchi, S., Fujii, T., Izumiura, H., Kameya, O., Nakada, Y., "SiO Maser Survey of the Galactic Disk IRAS Sources. IV. $25° < l < 40°$, $|b| < 3°$, the Inner Galactic Disk", submitted to ApJS

7. Deguchi, S., Nakashima, J., Wood, P. R., "Near-Infrared Observations of IRAS Sources with SiO Masers at the Inner Galactic Bulge", 2001, PASJ 53, 293

8. Deguchi, S., Nakashima, J., Balasubramanyam, R., "SiO Maser Survey of the Southern IRAS Sources", 2000, PASJ 53, 305

9. Nakashima, J., Deguchi, S., "Detections of SiO and H_2O Masers in the Bipolar Nebula IRAS 19312+1950", 2000, PASJ 52, L43

10. Deguchi, S., Fujii, T., Izumiura, H., Kameya, O., Nakada, Y., Nakashima, J., "SiO Maser Survey of the Galactic Disk IRAS Sources. III. $-10° < l < 10°$ and $|b| < 3°$, a Central Part of the Galaxy", 2000, ApJS130, 351

11. Nakashima, J., Jiang, B. W., Deguchi, S., Sadakane, K., Nakada, Y., "Period Measurement of the Selected AGB Stars in the Outer Galactic Disk", 2000, PASJ 52, 275

12. Deguchi, S., Fujii, T., Izumiura, H., Kameya, O., Nakada, Y., Nakashima, J., Ootsubo, T., Ukita, N., "SiO Maser Survey of the Galactic Disk IRAS Sources. II. $|l| < 3°$ and $|b| < 3°$, the Galactic Center Area", 2000, ApJS128, 571

Chapter 1

Introduction

1.1 SiO masers

The SiO maser was accidentally discovered by Snyder and Buhl (1974) when they detected a group of new unidentified lines near 86 GHz in the Orion molecular cloud. Soon after this discovery, Kaifu et al. (1975) detected the same line emission in Miras and OH/IR stars. The narrow line width and the compactness of the emission region suggested that this was a new maser, which Snyder and Buhl promptly identified as the $J = 2 - 1$ transition of the first vibrationally excited state ($v = 1$) of SiO. The almost immediate detection of two more rotational transitions, $J = 1 - 0$ and $3 - 2$, in the same vibration state by Davis et al. (1974) and Thaddeus et al. (1974) confirmed this bold proposal. Subsequently, maser emission has been detected in rotational transitions in both $v = 2$ (Buhl et al. 1974) and $v = 3$ (Scalise and Lepine 1978). The rotational quantum numbers were also extended to higher values: $J = 4 - 3$ masers were discovered by Schwartz et al. (1982); $J = 5 - 4$ by Clemens and Lane (1983); $J = 6 - 5$ by Jewell et al. (1987). SiO was the first molecule to present such a rich spectrum of maser lines. The ground vibration state, $v = 0$, occasionally displays maser features as well. However, the nature of this emission is clearly different and has not yet been studied as thoroughly as that of the high vibration states.

Although the original discovery was made toward the Orion molecular cloud, all most all-subsequent detections were reported in late-type stars (mass losing stars), where SiO masers are common. Secure precedents of SiO masers from molecular clouds are only three (Hasegawa et al. 1985; Fuente et al. 1989; Morita et al. 1992). Today, about a thousand of SiO maser emitters have been known in the sky (e.g., Izumiura et al. 1999; Deguchi et al. 2000a; Deguchi et al. 2000b). SiO masers have been detected in a very wide range of late-type stars with all types variability and very different mass-loss rates.

High-resolution interferometry (Colomer et al. 1992) found that the observed spots of SiO maser emission are rather compact, typically $\sim$ 0.1 - 5 AU depending on stellar luminosity classes. The VLA mapping of SiO maser emitters reveal well-defined rings of maser emission at $\sim$ 2 - 4 stellar radii (Diamond et al. 1994). SiO maser spots are thus locating at $\sim 10^{13}$ - 10^{14} cm from stellar center, the innermost amid the detected masers (OH, H_2O, and SiO masers) from the central star. A polarization map of R Cas (MacIntosh et al. 1989) indicates that the SiO maser emission of different spots originates in separate cells, each one characterized by distinct radial velocity, linear polarization and polarization position angle.

SiO masers could be fascinating tools to investigate the kinematics and evolution of AGB stars (and more evolved stars). In addition, the pumping mechanism of SiO maser involves unsolved problems. Therefore, systematic search of SiO masers toward unsurveyed regions, and toward new kinds of targets, would contribute the researching areas of these researching fields. SiO maser emitters are also very important target in the VERA project, which is a next generation VLBI network with differential VLBI technique promoted by NAOJ. In this thesis, we discuss the evolution of AGB stars (especially in the late-AGB phase) on the basis of a systematic data of SiO maser surveys toward the inner galactic disk region. In particular, a systematic SiO maser survey toward cool IRAS sources, which are candidates for proto-planetary nebulae, is first attempt. Figure 1-1 shows a distribution of all of the observed sources in this thesis in the galactic coordinates.

1.2 Study of Mass Losing Stars using SiO masers

1.2.1 Kinematics of AGB stars

OH/SiO masers from late-type stars have proven to be a powerful tool for investigating stellar motions. With OH/SiO masers, we can unveil the stellar motion even in optically obscured regions of the Galaxy (e.g., Lindqvist et al. 1992). Large surveys have been made for OH 1612MHz sources in the Galactic disk (te Lintel-Hekkert et al. 1991; Chengalur et al. 1993; Blommaert et al. 1994; Sevenster et al. 1997; Sevenster et al. 2001), and for SiO source in the Galactic bulge (Izumiura et al. 1994; Izumiura et al. 1995a; Izumiura et al. 1995b; Jiang et al. 1995), in the Galactic disk (Izumiura et al. 1999; Deguchi et al. 2000a; Deguchi et al. 2000b), and in the anti-center direction (Jiang et al.

1996). These maser observations potentially can cover all the area in the Galaxy, while optical spectroscopic methods can glimpse stars in the narrow optical windows (Zhao et al. 1994). It is well established that the middle velocity of the OH 1612MHz double peaks gives the stellar velocity at which they are emitted from the approaching and resending parts of the circumstellar shell. The radial velocity of SiO maser emission from a late-type star usually falls in the middle of the OH 1612 MHz double peaks, giving the radial velocity of the central star to within a few km s^{-1} accuracy (Jewell et al. 1991; Jiang et al. 1995).

The kinematical studies of the Galaxy trough the motion of OH/SiO maser sources have a big advantage against to those through the motion of gas component; it is availability of distances to objects. We have multiple ways to determine the distance to the OH/SiO maser sources. First one is the way using bolometric corrections (van der Veen and Breukers 1989). Most of the energy from late-type mass losing star is radiated at infrared wavelength regions, and these measurements are available in IRAS point source catalog. Therefore, we can estimate the distances to the object on the assumption of a certain luminosity as an original luminosity of the late-type star, which is about 8000 $L_{\odot}$. Second, we can determine the distances with period-luminosity relation of Mira-type variables (e.g., Hughes and Wood 1990; Feast et al. 1989; Reid et al. 1988). Most of the OH/SiO maser emitters are Mira-type variables (Nakashima et al. 2000). Therefore, if we measure the periods of pulsation, we can know the original luminosity of the objects, and can determine the distance to the stars. Third way, it will be available in near future, is the way using annual parallax measured by the differential VLBI technique. The National Astronomical Observatory Japan promotes the VERA (VLBI Exploration of Radio Astronomy) project. VEAR is a new VLBI system dedicated to differential VLBI to measure the position and proper motion of the Galactic masers with 10 micro-arc-seconds level accuracy. With VERA, we can directly determine the distance to OH/SiO masers with the triangulation.

The motion of SiO maser emitters in the inner galactic ($40° < l < 70°$, $|b| < 10°$) disk in the Galaxy is one of the main themes of this thesis. This region was a region of left unsurveyed systematically in SiO masers at Nobeyama. This region is fascinating region from kinematical points of views. We can study the influence of spiral arms on the kinematics and spatial distribution of SiO maser sources in this region. In recent SiO maser surveys toward the disk region, it is suggested that SiO maser source tend to concentrate into the spiral arm (Jiang et al. 1996; Nakashima et al. 2000). In the inner Galactic disk, the tangential points of Sagittarius-Carina and Scutum-Crux arms is located at the distance of 5 kpc from the sun (e.g., Taylor and Cordes 1993); these are quite appropriate to make a precise investigation of SiO maser sources at this distance because of the sensitivity of the Nobeyama 45-m telescope. On the other hand, a local gradient of the rotation curve of the Galaxy through the motion of SiO maser emitters is also an interesting viewpoint in this region. In the outer disk of the Galaxy, the rotational velocity has been obtained on the basis of the data of SiO maser survey (Jiang et al. 1996). In the present work, therefore, we reanalysis the inclination of the rotational velocity of SiO sources combining the present and previous data of SiO maser survey. In addition, deep OH (1612 MHz) maser surveys for the IRAS sources have been made for the inner galactic disk with Arecibo 300-m telescope (e.g., Lewis et al. 1990). Therefore, we can make a minutely comparison of the present results with the OH data.

1.2.2 SiO Masers as a Probe of Very Young PPNe

Proto-planetary nebulae (PPNe) are defined as objects that rare in transition between the asymptotic giant branch (AGB) and planetary nebula phases of stellar evolution. Stars of the AGB lose mass at a high rate ($10^{-7} - 10^{-4}$ $M_{\odot} yr^{-1}$) in the form of a stellar wind. Such mass loss eventually depletes the electron-degenerate carbon-oxygen core. This leads to an increase of the effective temperature of the star and the termination of mass loss. As the small amount of remaining hydrogen above the core continues to be consumed by hydrogen shell burning, the effective temperature of the star will gradually increase. When the stellar temperature reaches approximately 30000K, the amount of stellar photons with energies above the Lyman limit (13.6 eV) will be large enough to photoionize the surrounding material. The emergence of strong recombination lines of hydrogen (e.g., H_{α}) and helium and collisionally excited lines of metals (e.g., the [OIII] line at 5007 Å) signifies the beginning of the planetary nebula phase. The evolutional phase between the end of AGB mass loss and the beginning of photoionization is referred to as the PPN phase.

In particular, we focus on the PPNe with SiO masers in this thesis, because those objects have been regarded as very young PPNe, which are important to unveil the evolution from late-AG to PNe phases. SiO, H_2O, and OH masers have been found to be associated with stars on the AGB stars, as well as post-AGB stars (or PPNe). The masers are located in the circumstellar envelopes, with the SiO masers closest to the star and the OH masers furthest away. All three types of masers are usually found around stars presently losing mass, e.g. Mira-type variables and OH/IR stars. However, when the mass loss stops the SiO masers disappear first, H_2O masers disappear second, whereas the OH masers remain active also during the PPNe and early planetary nebula phase (Lewis 1989). It means that PPNe with SiO masers exist at the very early stage of the evolution of PPNe phase just after the mass loss ceasing.

Since PPN are expected to have IRAS colors between those of late AGB stars and young PN, candidates for PPN can be identified by searching the IRAS point source catalog for objects with the appropriate colors (Volk and Kwok 1989; van der Veen et al. 1989). Generally speaking, we expect the color temperature of PPN to be in the range 150 - 250K. Approximately 1000 PNe were detected in the IRAS survey. According to the evolutionary models of Schönberner (1983), the fraction of time spent in the PPN phase in relation to the entire PN lifetime is $\sim$ 10%. If this is the case, we expect $\sim$100 PPNe in the IRAS PSC. Samples of SiO maser surveys in this thesis include plenty of candidates for PPNe. We take aim at new detections of SiO masers from PPNe. Before this work, the number of the secure precedent of PPNe with SiO masers was only one, OH 231.8+4.2 (Rotten Egg Nebula, Morris et al. 1987; Jewell et al. 1991).

First precedents of PPN with SiO masers, OH 231.8 + 4.2, exhibit lot of peculiar and unparallel characteristics: the existence of rich molecules, complex dynamics of envelope, extreme low temperature as an SiO maser emitter, and so on. New detections of this kind of objects would assist our understanding of these questions, and evolution in the early PPNe phase.

1.2.3 Pumping Mechanism of SiO Masers

The pumping mechanism of SiO masers is still controversial topic. Major two ideas of the pumping mechanism of SiO masers are collisional and IR radiative pumping mechanisms. IR radiative pumping of SiO masers was earlier studied by Kwan and Scoville (1974) and Deguchi and Iguchi (1976). After these proposals of radiative pumping, Elitzur (1980) proposed a collisional pumping mechanism. Both of the mechanisms can lead to the required population inversion in the presence of a large velocity gradient, and also can explain the coincidence of SiO maser velocity with stellar radial velocity.

In recent observations with VLBI techniques, the 7mm maser emission regions are found to be distributed in a number of spots forming a ring-like structure at about 2-3 stellar radii: see observations of TX Cam, U Her, W Hya and VX Sgr by Diamond et al. (1994), Miyoshi et al. (1994), and Greenhill et al. (1995). This ring like-structure arises naturally in the framework of the radiative pumping mechanism of SiO masers (e.g. Bujarrabal 1994), which requires a shell-like matter distribution. VLBA observations (Kemball and Diamond 1997) have also shown that most SiO spots are linearly polarized in the tangential direction, i.e. perpendicularly to the direction to the ring center, in a particularly well-defined pattern. In fact, tangential polarization was predicted from IR radiative pumping models more than the years before any VLBA observations were available (Bujarrabal and Nguyen-Q-Rieu 1981; Western and Watson 1983).

On the contrary, the ring structure may also be possible in collisional models, which are practically not geometry dependent (e.g. Doel et al. 1995). From observations with the KNIFE VLBI array, Miyoshi et al. (1994) reported that the emission of these two lines systematically arises from positionally coincident spots at least as seen with their 7 mas beam. Miyoshi et al. claimed that this result is a conclusive proof in favor of collisional pumping schemes, since radiative mechanisms, always more selective, tend to require different physical conditions to pump the $v = 1$ and $v = 2$ masers. In addition, the radiative pumping model, in which SiO maser emission is assumed to arise in the circumstellar envelope, presents two major shortcomings. First, this mechanism requires large SiO column densities in the envelope, thereby leading to mass losses, which appear to be too high. Second, the detection of SiO maser emission from the vibrational states $v = 2$, 3 suggests high pumping energies which are probably present only in the stellar atmosphere or in the very inner part of the envelope.

One of the clues to unveil the pumping mechanism of SiO masers are intensity ratios of the $J = 1 - 0$, $v = 2$ to $v = 1$ lines. The intensity ratio of the SiO $J = 1 - 0$, $v = 1$ to the $J = 1 - 0$, $v = 2$ lines of AGB stars has been observed as being nearly equal to unity (Schwartz et al. 1979; Spencer et al. 1981; Nakada et al. 1993). However, there are many exceptional cases. For instance, the intensity ratio of IRC-10414 is less than about 0.1 (Imai et al. 1999). Nyman and Olofsson (1986)'s sample is about $C_{12} = 0.2$.

The standard theory of SiO masers (e.g., Langer and Watson 1984; Bujarrabal et al. 1996) tried to explain the unity of the line ratios by the line overlap of the SiO vibration-rotation transition with the H_2O line, but this problem is still controversial. In the mechanisms of making the unity of the line ratios, we might find a clue to clarify the pumping mechanism. To clarify this problem, we observe the IRAS sources with very cool dust, which are candidates for protoplanetary nebulae, in this thesis. In the SiO maser surveys made in past, IRAS sources with the temperature, just around 300K, have been observed. On the contrary, in this work, the temperature range, as a selection criterion of the sample, extend to largely lower side reach to 150 K. The cool IRAS sources, which have very different physical condition in comparison with the sample in the previous SiO maser survey, might show a useful suggestion to unveil the pumping mechanism of SiO masers.

1.3 Outline of the Thesis

In chapters 2 to 4, results of SiO maser survey toward IRAS sources in the galactic disk region are reported. In Chapter 2 and 3, the results of SiO maser survey toward candidates for normal AGB stars are given. In these chapters, the kinematics of AGB stars with SiO

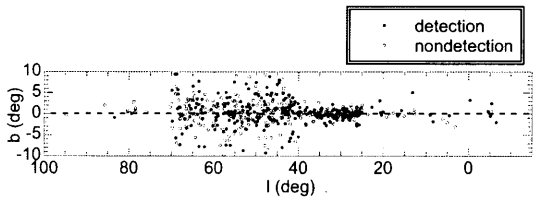

Figure 1.1: Position of all of the observed sources in this thesis in the galactic coordinates. Filled and open marks indicate the SiO detection and nondetection, respectively.

masers are discussed, and the data are minutely compared with those of OH maser survey. In Chapter 4, the results of the SiO maser survey toward cool IRAS sources, which are candidate for late-AGB stars and proto-planetary nebulae, are given. In this chapter, we discuss maser radiation from candidates for PPNe and the pumping mechanism of SiO masers. In chapter 5 and 6, detail about additional observation of a newly detected PPNe with SiO maser, IRAS 19312+1950, which was found in the survey reported in chapter 4, are discussed. The discovery of SiO masers toward IRAS 19312+1950 are reported in chapter 5. In chapter 6, results of a molecular line mapping, continuum line mapping, and near-infrared imaging observations toward IRAS 19312+1950 are reported. In chapter 7, main results of this thesis are summarized. In addition, a tentative summary of the multilane survey toward IRAS 19312+1950 are given in Appendix section.

References

[Blommaert et al.(1994)] Blommaert, J. A. D., Van Langevelde, H. J., and Michiels, W. F. P. 1994, A&Ap, 287, 479

[Buhl et al.(1974)] Buhl, D., Snyder, L. E., Lovas, F. J., and Johnson, D. R. 1974, ApJL, 192, L97

[Bujarrabal(1994)] Bujarrabal, V. 1994, A&Ap, 285, 953

[Bujarrabal and Nguyen-Q-Rieu(1981)] Bujarrabal, V., and Nguyen-Q-Rieu 1981, A&Ap, 102, 65

[Chengalur et al.(1993)] Chengalur, J. N., Lewis, B. M., Eder, J., and Terzian, Y. 1993, ApJS, 89, 189

[Clemens and Lane(1983)] Clemens, D. P., and Lane, A. P. 1983, ApJL, 266, L117

[Clomer et al.(1992)] Clomer, F., Graham, D., Krichbaum, T., Ronnang, B., de Vicente, P., Witzel, A., Barcia, A., Baudry, A., Booth, R. S., Gomez-Gonzalez, J., Alcolea, J., and Daigne, G. 1992, A&Ap, 254, L17

[Desmurs et al.(2000)] Desmurs, J. F., Bujarrabal, V., Colomer, F., and Alcolea, J. 2000, A&Ap, 360, 189

[Diamond et al.(1994)] Diamond, P. J., Kemball, A. J., Junor, W., Zensus, A., Benson, J., and Dhawan, V. 1994, ApJL, 431, L61

[Davis et al.(1974)] Davis, J. H., Blair, G. N., van Till, H. and Thaddeus, P. 1974, ApJL, 190, L117

[Deguchi et al.(2000a)] Deguchi, S., Fujii, T., Izumiura, H., Kameya, O., Nakada, Y., Nakashima, J., Ootsubo, T., and Ukita, N. 2000a, ApJS, 128 (in press, Paper II)

[Deguchi et al.(2000b)] Deguchi, S., Fujii, T., Izumiura, H., and Nakashima, J. 2000b, 130 (in press, Paper III)

[Deguchi and Iguchi(1976)] Deguchi, S., and Iguchi, T. 1976, PASJ, 28, 307

[Doel et al.(1995)] Doel, R. C., Gray, M. D., Humphreys, E. M. L., Braithwaite, M. F., and Field, D. 1995, A&Ap, 302, 797

[Elitzur(1980)] Elitzur, M. 1980, ApJ, 240, 553

[Feast et al.(1989)] Feast, M. W., Glass, I. S., Whitelock, P. A., and Catchpole, R. M. 1989, MNRAS, 241, 375

[Fuente et al.(1989)] Fuente, A., Martín-Pintado, J., Alcolea, J., and Barcia, A. 1989, A&Ap, 223, 321

[Greenhill et al.(1995)] Greenhill, L. J., Colomer, F., Moran, J. M., et al. 1995, ApJ, 449, 365

[Hasegawa et al.(1985)] Hasegawa, T., Morita, K. -I., Okumura, S., Kaifu, N., Suzuki, H., Ohishi, M., Hayashi, M., and Ukita, N. 1985, in Masers, Molecules and Mass Outflows in Star Forming Rgion, ed Haschick, A. D. (Haystack Observatory)

[Hughes and Wood(1990)] Hughes, S. M. G., and Wood, P. R. 1990, AJ, 99, 784

[Izumiura et al.(1999)] Izumiura, H., Deguchi, S., Fujii, T., Kameya, O., Matsumoto, S., Nakada, Y., Ootsubo, T., and Ukita, N. 1999, ApJS, 125, 257 (Paper I)

[Izumiura et al.(1994)] Izumiura, H., Deguchi, S., Hashimoto, O., Nakada, Y., Onaka, T., Ono, T., Ukita, N., and Yamamura, I. 1994, ApJ, 437, 419

[Izumiura et al.(1995a)] Izumiura, H., Catchpole, R., Deguchi, S., Hashimoto, O., Nakada, Y., Onaka, T., Ono, T., Sekiguchi, K., Ukita, N., and Yamamura, I. 1995, ApJS, 98, 271

[Izumiura et al.(1995b)] Izumiura, H., Deguchi, S., Hashimoto, O., Nakada, Y., Onaka, T., Ukita, N. and Yamamura, I. 1995, ApJ, 453, 837

[Jewell et al.(1987)] Jewell, P. R., Dickinson, D. F., Snyder, L. E., and Clemens, D. P. 1987, ApJ, 323, 749

[Jewell et al.(1991)] Jewell, P. R., Snyder, L. E., Walmsley, C. M., Wilson, T. L., and Gensheimer, P. D. 1991, A&Ap, 242, 211

[Jiang et al.(1995)] Jiang, B. W., Deguchi, S., Izumiura, H., Nakada, Y., and Yamamura, I. 1995, PASJ, 47, 815

[Jiang et al.(1996)] Jiang, B. W., Deguchi, S., Yamamura, I., Nakada, Y., Cho, S. H., and Yamagata, T. 1996, ApJS, 106, 463

[Kaifu et al.(1975)] Kaifu, N., Buhl, D., and Snyder, L. 1975, ApJ, 195, 359

[Kemball and Diamond(1997)] Kemball, A. J., and Diamond, P. J. 1997, ApJ, 481, L111

[Kwan and Scoville(1974)] Kwan, J. Y., and Scoville, N. 1974, ApJ, 194, L97

[Langer and Watson(1984)] Langer, S. H., and Watson, W. D. 1984, ApJ, 284, 751

[Lewis(1989)] Lewis, B. M. 1989, ApJ, 338, 234

[Lindqvist et al.(1992)] Lindqvist, M., Habing, H. J., and Winnberg, A. 1992, A&Ap, 259, 118

[Miyoshi et al.(1994)] Miyoshi, M., Morimoto, M., Kawaguchi, N., Ukita, N., Inoue, M., Miyazawa, K., Tsuboi, M., Miyaji, T. et al. 1992, Nature, 371, 395

[Morita et al.(1992)] Morita, K. I., Hasegawa, T., Ukita, N., Okumura, S. K., and Ishiguro, M. 1992, PASJ, 44, 373

[Morris et al.(1987)] Morris, M., Guilloteau, S., Lucas, R., and Omont, A. 1987, ApJ, 321, 888

[Nakada et al.(1993)] Nakada, Y., Onaka, T., Yamamura, I., Deguchi, S., Ukita, N., and Izumiura, H. 1993, PASJ, 45, 179

[Nakashima et al.(2000)] Nakashima, J., Jiang, B. W., Deguchi, S., Sadakane, K., and Nakada, Y. 2000, PASJ, 52, 275

[Nakashima and Deguchi(2000)] Nakashima, J., and Deguchi, S. 2000, PASJ, 52, L43

[Nyman et al.(1986)] Nyman, L. -Å., and Olofsson, H. 1986, A&Ap, 158, 67

[Reid et al.(1988)] Reid, N., Glass, I. S., and Catchpole, R. M. 1988, MNRAS, 232, 53

[Renzini and Fusi Pessi(1988)] Renzini, A., and Fusi Pessi, F. 1988, ARA&A, 26, 199

[Scalise and Lepine(1978)] Scalise, E., and Lepine, R. D. 1978, A&Ap, 65, L7

[Schwartz et al.(1979)] Schwartz, P. R., Waak, J. A., and Bologna, J. M. 1979, AJ, 84, 1349

[Schwartz et al.(1982)] Schwartz, P. R., Zuckerman, B., and Bologna, J. M. 1982, ApJL, 256, L55

[Sevenster et al.(1997)] Sevenster, M. N., Chapman, J. M., Habing, H. J., Killeen, N. E. B., and Lindqvist, M. 1997, A&ApS, 124, 509

[Sevenster et al.(2001)] Sevenster, M. N., van Langevelde, H. J., Moody, R. A., Chapman, J. M., Habing, H. J., and Kileen, N. E. B. 2001, A&Ap, 366, 481

[Snyder and Buhl(1974)] Snyder, L. E., and Buhl, D. 1974, ApJL, 189, L31

[Spencer et al.(1981)] Spencer, J. H., Winnberg, A., Olnon, F. M., Schwartz, P. R., Matthews, H. E., and Downes, D. 1981, AJ, 86, 392

[Taylor and Cordes(1993)] Taylor, J. H., and Cordes, J. M. 1993, ApJ, 411, 674

[te Lintel Hekkert et al.(1991)] te Lintel Hekkert, P., Caswell, J. L., Habing, H. J., Haynes, R. F., and Norris, R. P. 1991, A&ApS, 90, 327

[Thaddeus et al.(1974)] Thaddeus, P., Mather, J., Davis, J. H., and Blair, G. N. 1974, ApJL, 192, L33

[van der Veen and Breukers(1989)] van der Veen, W. E. C. J., and Breukers, R. J. L. H. 1989, A&Ap, 213, 133

[van der Veen et al.(1989)] van der Veen, W. E. C. J., Habing, H. J., and Geballe, T. R. 1989, A&Ap, 226, 108

[Volk and Kwok(1989)] Volk, K., and Kwok, S. 1989, ApJ, 342,345

[Western and Watson(1983)] Western. L. R., and Watson, W. D. 1983, ApJ, 275, 195

[Zhao et al. 1994] Chao, H., Spergel, D. N., and Rich, R. M. 1994, AJ, 108, 2154

Chapter 2

SiO Maser Survey of the Galactic Disk IRAS Sources. $25° \leq l \leq 40°$ and $|b| \leq 3°$, the Inner Galactic Disk

Abstract

A result of the SiO maser survey is presented for color-selected IRAS sources in the area, $25° < l < 40°$ and $|b| < 3°$, in the SiO $J = 1 - 0$, $v = 1$ and 2 transitions ($\sim$ 43 GHz). We have detected 64 out of 133 observed sources in SiO masers. Distances to these sources range approximately from 2 to 11 kpc, which were estimated from IRAS 12 and 25 μm flux densities. Radial velocities of objects spread between -70 and 180 km s^{-1}, which is consistent with the rotation curve of the Galaxy obtained before. The radial velocity dispersion of the detected SiO sources was found about $\sim$ 49 km s^{-1} for the stars in $25° < l < 32.5°$, and it was $\sim$30 km s^{-1}in $32.5° < l < 40°$, indicating a steep increase of the velocity dispersion toward the center of the Galaxy. The velocity–longitude diagram of the SiO sources shows a weak concentration of the sources near the Scutum tangent where the line of sight crosses the Scutum-Crux arm tangentially. A relatively large vacant part of SiO sources was found near the area, $l \sim 31° - 34°$ at V_{lsr} = 10–40 km s^{-1}, which coincides with a CO vacant area. We did not find any clear SiO features associated with the CO dense areas such as the W44 complex.

2.1 Introduction

In order to investigate the dynamics of stars in the inner galactic disk, we have surveyed the color-selected IRAS point sources in SiO maser lines at ~43 GHz. These IRAS sources are dust enshrouded evolved stars at the Asymptotic Giant Branch (AGB) phase (Habing 1996). In three succeeding papers (Izumiura et al. 1999; Deguchi et al. 2000ab; hereafter called Papers I, II and III), we presented the results of the survey; Paper I presented on the sources toward the tip of the bulge bar, ($15° < l < 25°$), while Paper II and III on the sources in the inner and outer galactic bulge ($|l| < 3°$ and $-10° < l < 25°$ [except $|l| < 3°$]), respectively. All these surveys are limited to the strip in the galactic disk, $|b| < 3°$ (for the other area, see Izumiura et al. 1995; Jiang et al. 1996).

In this paper, we describe the result of the SiO maser survey in the disk area, $25° < l < 40°$ and $|b| < 3°$. It is known that the surface density in the $l - b$ map of the color-selected IRAS sources is clearly enhanced toward the bulge (Habing 1996). The spatial density of these objects (the O-rich AGB stars) decreases with the distance from the galactic center (Weinberg 1992). It is naturally expected that the nature of the SiO-emitting IRAS sources in the galactic disk is more or less different from those in the bulge; star formation is still active in the spiral arms, but not in the bulge. Most of the sources in the present survey area, $25° < l < 40°$, are considered to be a disk population. Therefore, this SiO survey provides a good comparison sample to the bulge samples given in Paper II and III, and to the sample of Paper I that is a mixture of the bulge and disk populations.

Because the lines of sight in the present survey area cross several spiral arms (Taylor and Cordes 1993), the influence of arms, if present, may reveal in the SiO radial-velocity data. Previous works (e.g., Jiang et al. 1996) suggested a concentration of AGB stars into spiral arms. The present survey area is quite suitable to confirm this phenomena owing to the larger number of SiO detections.

Radio line observations provide accurate radial velocities of stars, while infrared continuum observations provide distances to the sources, both fundamentally important for the galactic kinematics. Though the distances that we estimate from IRAS flux densities and colors involve an error of about ±30 % or more (see Paper I; Deguchi et al. 1998), they are expect to be improved in near future using near-infrared photometric data.

2.2 Observation

Simultaneous observations in the SiO $J = 1 - 0, v = 1$ and 2 transitions at 43.122 and 42.821 GHz, respectively, were made with the 45-m radio telescope at Nobeyama in the periods from January 1997 to June 1999 (see Table 1 in Paper II). For the sake of completeness, a few additional observations were made in May 2000 for several faint sources which were missed in the periods given for the long-term project in 1997–1999. The details of the observations were already summarized in Paper I and II, so that they are not repeated here.

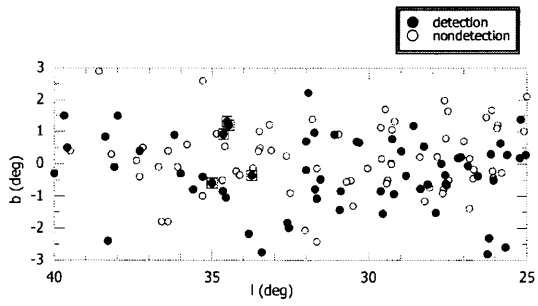

Figure 2.1: Position of the observed sources in the galactic coordinates. Circles and triangles indicate sources observed at IRAS and MSX position, respectively. Filled and open marks indicate the SiO detection and nondetection, respectively.

The source selection has been made from the IRAS Point Source Catalog (IRAS PSC) in terms of the IRAS 12 μm flux density ($F_{12} > 2$ Jy), the color ($0 < C_{12} = \log(F_{25}/F_{12}) < 0.1$), and the measurement quality index ($Q_{12} = Q_{25} = 3$), where F_{12} and F_{25} are IRAS 12 and 25 μm flux densities of a source, Q_{12} and Q_{25} are flux-measurement quality indices at 12 and 25 μm, respectively. These selection criteria extract dust - enshrouded objects with $T_{dust} \simeq 300$ K from the IRAS PSC; effectiveness of the criteria has been approved by Papers I, II, and III.

Observational results are summarized in Table 2.1 for 64 SiO detections and in Table 2.2 for 69 non-detections. IRAS positions at the epoch of 1950 were used for observations. Detections of SiO maser lines were judged by criteria described in Paper I with additional eye inspections. Sky positions of the observed sources are plotted in Figure 2.1. The sources are strongly concentrated in the lower galactic latitude ($|b| < 2°$), suggesting the scale height of the sources of about 300 pc (at the distance of 8 kpc). The spectra of the detected sources were shown in Figures 2.2a – 2.2h.

To check the dependence of the detection rate on IRAS flux, we have made a histogram of F_{12} (Figure 2.3). The IRAS data used were shown in Table 2.3. The average detection rate is 48 %, which is similar to the previous results in papers I (56 %), II (49 %), and III (62 %). The regions observed in the previous Papers I, II, and III were the inner disk and the bulge. The SiO maser lines were already searched for in most of bright sources with $F_{12} > 12$ Jy at least once (previous searches summarized in Table 2.4). However, all of these bright sources were re-observed in this survey for the sake of completeness. Papers I, II, and III found that the detection rate is roughly constant in the

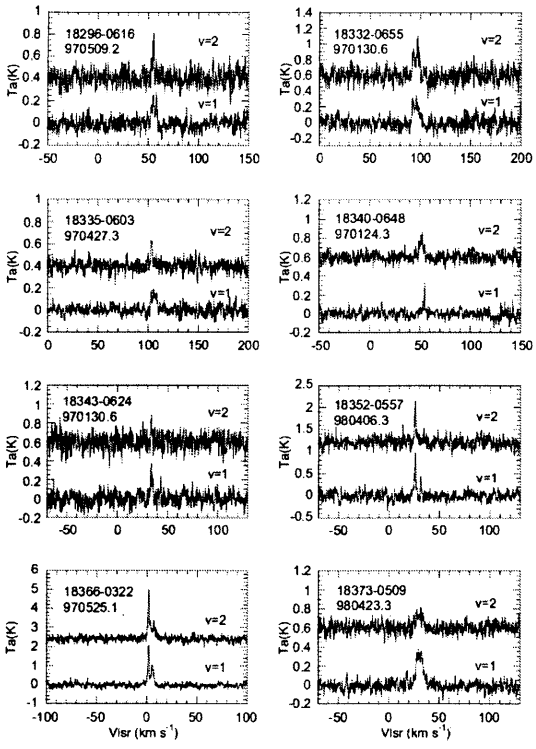

Figure 2.2a: Spectra of the SiO J = 1–0, v =1 and 2 lines for 63 detected sources. The SiO spectra of IRAS 18465−0717 were already shown in Deguchi et al. (1999), so that not shown here.

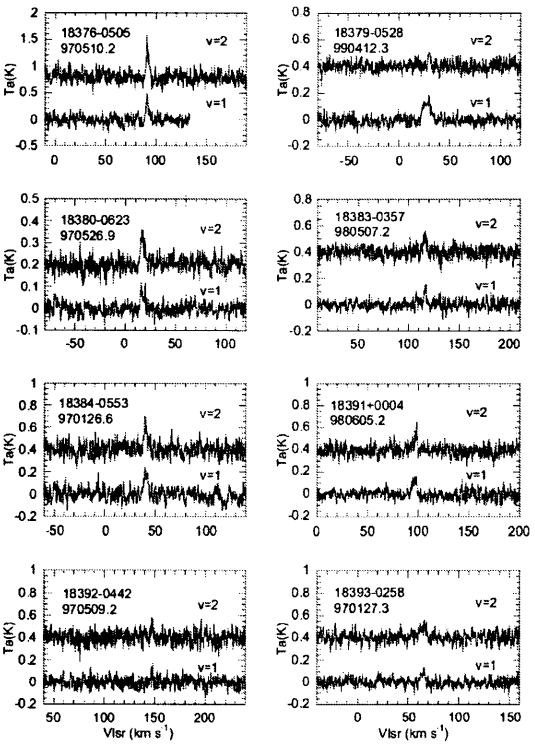

Figure 2.2b: Continued

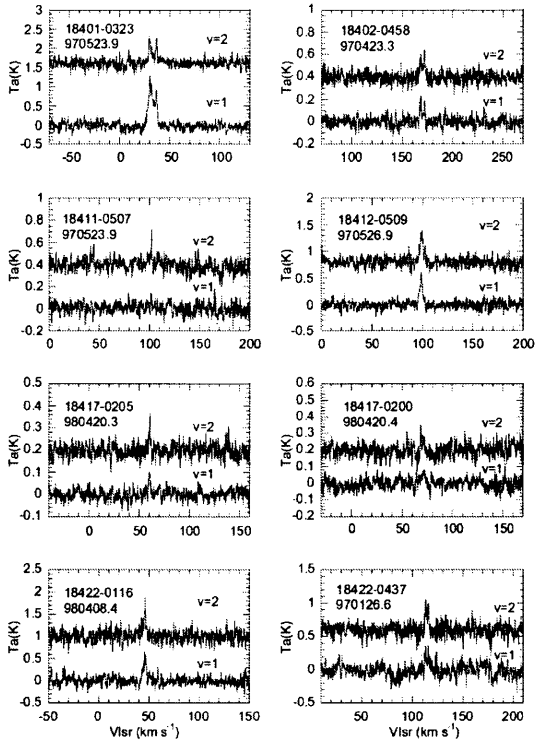

Figure 2.2c: Continued

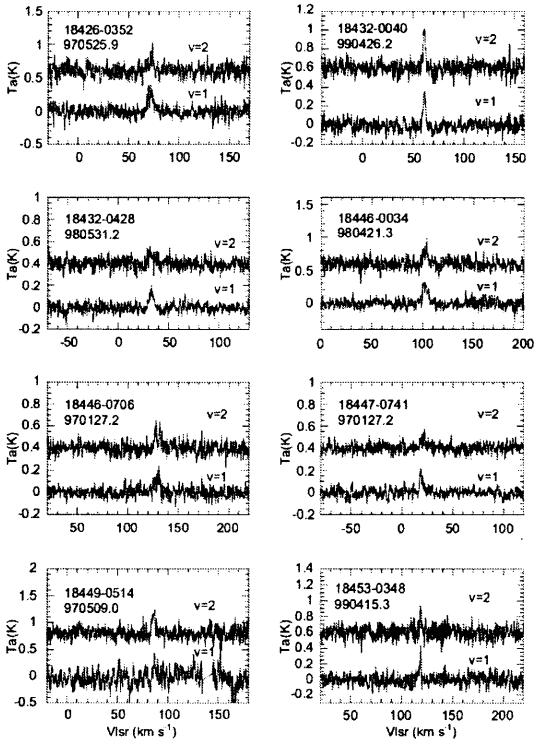

Figure 2.2d: Continued

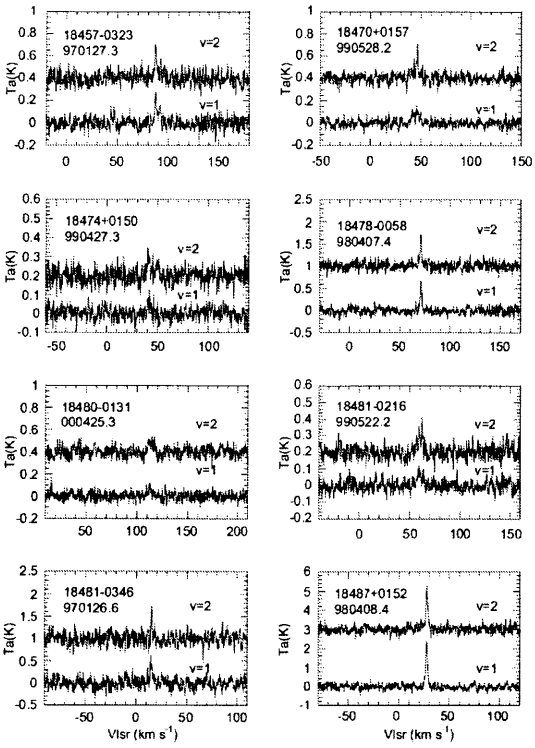

Figure 2.2e: Continued

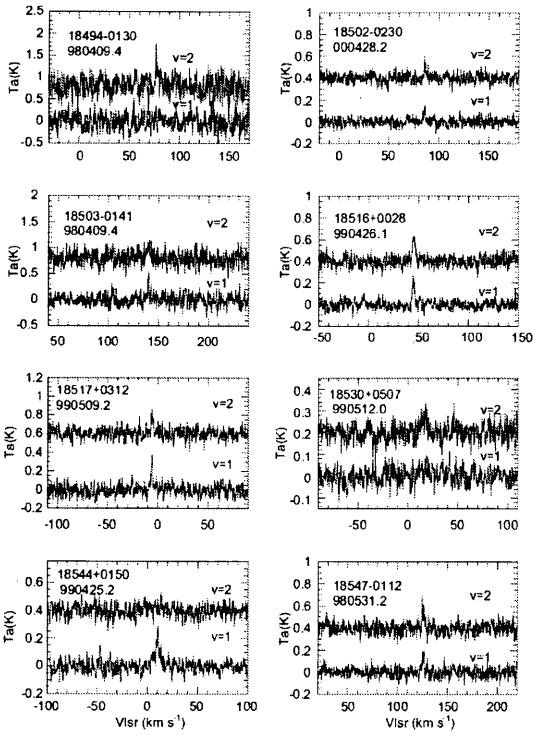

Figure 2.2f: Continued

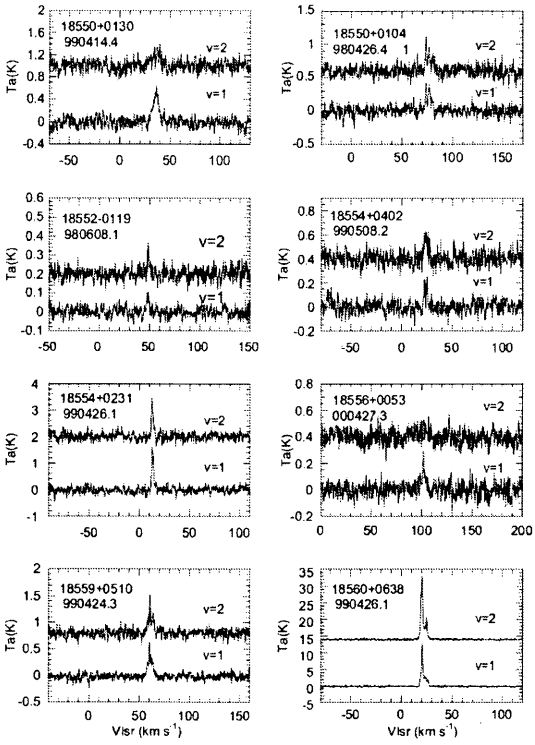

Figure 2.2g: Continued

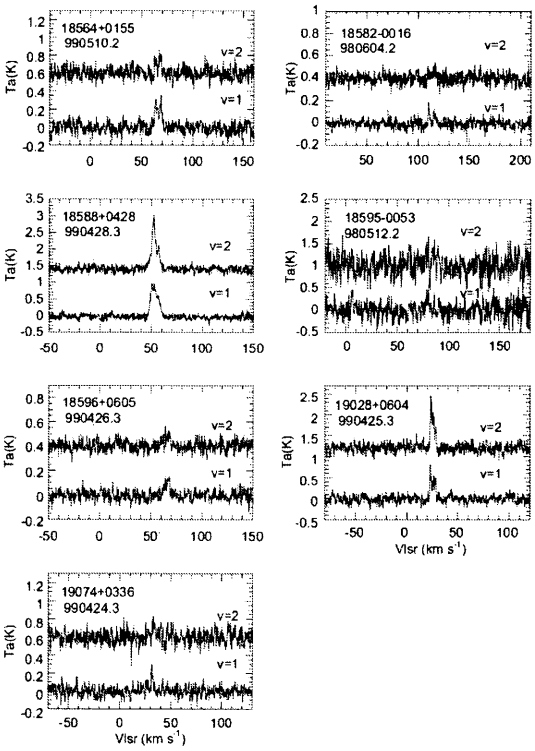

Figure 2.2h: Continued

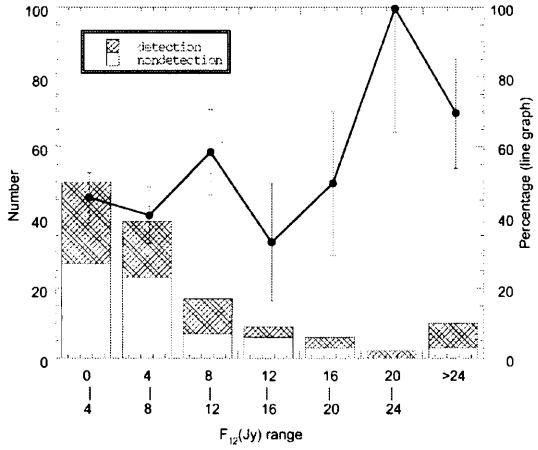

Figure 2.3: Histogram of the 12 μm flux density (bar graph) and detection rate as a function of the IRAS 12 μm flux density (line graph).

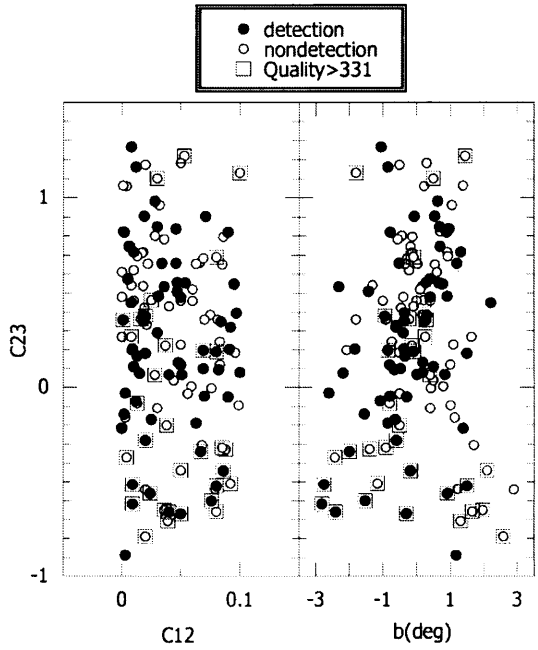

Figure 2.4: Two color ($C_{23} - C_{12}$; left panel) and color-latitude ($C_{23} - b$; right panel) diagrams for the observed sources.

range $F_{12} = 4 - 16$ Jy and it slightly drops at the faint ($F_{12} < 4$ Jy) and bright ends ($F_{12} > 16$ Jy). However, this tendency is not seen in Figure 2.3. This may be attributed to a statistical error due to small number; the increase of the detection rate at the bright end in Figure 2.3 is probably due to this effect.

The increase of the detection rate at the faint end in Figure 2.3 seems worth to note. This may suggests some difference in nature between the faint bulge and disk sources. However, we have to note observational biases on the detection rate of the faint sources. In order to detect the weak SiO signal for a weak source with F_{12} <4 Jy, we needed a long integration time, typically more than one hour. The observations were often repeated in the following days for a weak signal ($S/N = 2 - 3$), as far as the observation time allowed. For a source in the sky area of $l > 25°$, the elevation of the source was enough high to repeat the observations. In contrast, the source below $l < 15°$ were observed at the low elevation in general from Nobeyama and we could not afford to repeat observations. Therefore, it is plausible that the detection probability does not drop much for the faint IRAS sources in the present survey.

Figure 2.4 shows the two-color ($C_{12} - C_{23}$) and the color–latitude ($b - C_{23}$) diagrams. The IRAS 60 μm flux density (F_{60}), or the color $C_{23} = \log(F_{60}/F_{25})$, has often been used to extract late-tape stars from the IRAS PSC [e.g. van der Veen & Habing (1990)]. However, as described in Papers I, II, and III, the high SiO detection rate at high $C_{23}(> 0)$ indicates that these IRAS 60 micron fluxes are heavily contaminated by emission from cold dust in the galactic plane. Therefore, we have not adopted F_{60} or C_{23} to select the sample in this SiO maser surveys. In fact, the average C_{23} is lower by about 0.5 in Figure 2.4 than the average of the corresponding Figures in the paper I, II, and III. This fact suggests that the background dust emission contribute less to the IRAS 60 μm intensity at this longitude than those at the lower galactic longitude. However, we still found a number of sources above $C_{23} > 1$, especially at the lower galactic latitude ($|b| < 1°$), suggesting that the flux density, F_{60}, or the color, C_{23}, for these sources is influenced by interstellar dust.

2.3 Discussion

We have detected 64 out of 133 observed sources in either SiO J =1–0, v =1 or 2 transitions. The detection rate was 48 %, which is similar to the previous results in Papers I, II and III. It has been suggested frequently that the content of C-rich AGB star in the IRAS sample tends to increase with the galactocentoric distance, and the SiO detection rate decreases with the galactic longitude (Jiang et al. 1999). However, we could not confirm this effect at least in this sample compared with the result in Papers, I, II and III.

2.3.1 Velocity versus distance

Figure 2.5 plots V_{lsr} versus luminosity distance for 64 SiO detected sources. The luminosity distances were calculated under the assumption of a constant luminosity (8000 $L_{\odot}$) with an 12 μm bolometric correction by van der Veen and Breukers (1989) (see the detail in Paper I). Because the sampled sources are within a narrow range in the galactic longitude, it is expected that the systematic motion due to the galactic rotation appears similarly to the distance till 5 kpc (see the broken and solid curves in Figure 2.5). Beyond 5 kpc, the expected curves separate in radial velocity at the differ-

ent distances. Figure 2.5 indicates, however, that the deviation of radial velocities of stars from the expected curve seems larger in the short distance group than the deviation for stars in the large distance group. In fact, the radial velocity dispersion, a root mean square of residues subtracted by the galactic rotation at each l and D_L, is 46.9 km s^{-1} in $D_L < 5$ kpc, 36.9 km s^{-1} in $5 < D_L < 10$ kpc, and 44.3 km s^{-1} in $10 < D_L < 15$ kpc. Here, we assumed the approximately flat rotation curve, which was given in the caption of figure 2.5 of Paper I. The decrease of the dispersion for the middle distance group , $5 < D_L < 10$ kpc, can clearly be seen in figure 2.5; this group of stars is considered to be located near the Scutum arm tangent. However, a statistical test (F-test; William et al. 1986) does not necessarily give enough high confidence level for any pairs of groups having different velocity dispersions.

To check the distance effect on the velocity dispersion further, we separated the sources into two sets by longitude, i.e., sources below and above $l = 32.5°$. The dispersions for these sets are 48.9 km s^{-1} and 29.6 km s^{-1}, respectively (also see figure 2.5; the sources for the two groups are indicated in filled and unfilled circles). A statistical test (F-test) gives a probability of less than 1 % for the null hypothesis for two sets being statistically compatible, assuring that velocity dispersion of the set of sources above $l = 32.5°$ is definitely larger than the dispersion of the set below $l = 32.5°$.

The analyses made here somewhat depend on the assumption of rotation curve (the flat rotation curve) and the accuracy of the luminosity distances obtained. We should note that the velocity dispersion of the IRAS / SiO sources near solar neighborhood is ~35 km s^{-1} (Deguchi et al. 2001). The dispersion obtained for the outer-source set ($32.5° < l < 40°$) is comparable with the dispersion near the solar neighborhood. If the distance estimation involves considerably larger errors, the velocity dispersion would increase with the amount of distance errors. In fact, the low dispersion, 29.6 km s^{-1}, of the $32.5° < l < 40°$ source set implies that the errors in the present distance estimation do not influence much on the velocity dispersion. The origin of the large velocity dispersion for the inner source set ($25° < l < 32.5°$) is not clear at present. It is possible that the motions of the IRAS / SiO sources are influenced by the bar structure of the galaxy and deviate much from the average galactic rotation (Weinberg 1994). In fact, based on the distance estimations including near-infrared photometric data, Deguchi et al. (1998) found that the stars with large deviation of motion from the galactic rotation are located at distances around ~5.5 kpc for the IRAS / SiO stars in $15° < l < 25°$.

Here, we dare not pursue this problem further without accurate distance estimations, but remain to state that the velocity dispersion of IRAS / SiO maser sources decreases with the galactocentric distance. If periods of light variation for these sources are known, we can use the period-luminosity relation of the mira variable and can obtain better distances (e.g. Nakashima et al. 2000).

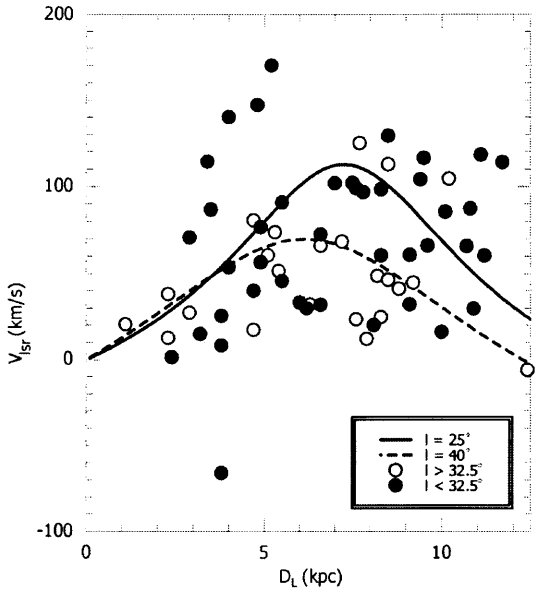

Figure 2.5: Observed radial velocity versus luminosity distance. The broken and solid curves are radial velocities expected at l =25°, and 40°, respectively, calculated from the approximately flat galactic rotation curve used in Izumiura et al. (1999).

2.3.2 Longitude–velocity diagram

Figure 2.6 shows the $l - V_{lsr}$ diagram for SiO detected sources overlaid on the CO $J = 1 - 0$ line map (taken from Dame et al. 1987). The notable CO features are "Aquila Rift" (spreading between $l = 25° - 40°$ at $V_{lsr} = 0 - 10$ km s^{-1}), the W44 complex (around $l = 33° - 36°$ at $V_{lsr} = 30 - 50$ km s^{-1}), and a large CO-vacant area ($l = 31 - 34$ at $V_{lsr} = 10 - 60$ km s^{-1}) (see Figure 2.6 in Dame et al. 1987 for naming). The "molecular ring" feature, which has been seen in the area $l = -25 - 25°$, is not recognizable well in Figure 2.6, but the edge of the ring is still there in the region of $l = 25 - 27°$ at $V_{lsr} = 80 - 100$ km s^{-1}. More details of the individual features and relations to the spiral arms are found in Dame et al. (1987, 2000).

The radial velocities of SiO detected sources spread between 0 and 150 km s^{-1} in Figure 2.6. The SiO source distribution on the $l-v$ map does not seem completely random, and it exhibits a correlation with the CO emission features in some degree. For example, the concentration of 5 sources at $l \sim 35°$ and $V_{lsr} \sim 40$ km s^{-1} seems just at the position of the CO W44-complex feature. The large SiO vacant area at $l \sim 31 - 34°$ and $V_{lsr} \sim 10 - 40$ km s^{-1} is seen in figure 2.6, where the CO-vacant area mentioned above is present. Maybe, we can list up such cases with the weaker correlations further; e.g., the SiO source concentration at $l \sim 26.5°$ and $V_{lsr} \sim 0 - 30$ km s^{-1}, or the densely populated

area of SiO sources at $l = 30 - 33°$ and $V_{lsr} = 50 - 80$ km s^{-1}. However, the correlation to the CO features does not seems so evident for the last two cases.

The features in the $l - v$ map should be, in principle, interpreted in term of the galactic dynamic, more specifically here, in term of the spiral structure. According to the previous studies of galactic spiral arms based on free electron distribution (Taylor and Cordes 1993), the lines of sight cross two arms between $l = 25° - 40°$ (see Figure 2.7); so called Scutum-Crux and Sagittarius-Carina arms (designated as 2 and 3, respectively, in Figure 1 of Taylor and Cordes 1993). The Scutum-Crux arm is present at the inner part of the Galaxy compared with Sagittarius arm and it crosses tangentially to the line of sight at the longitude $l = 30°$. The tangential point of this arm corresponds to the area in Figure 2.6 near $l \sim 30°$ and $V_{lsr} \sim 90$ km s^{-1}. Thus the relatively high density area of SiO sources at the upper right part of Figure 2.6 can well be understood by this crossing of the lines of sight with the tangential point of the Scutum-Crux arm.

The above conjecture implicitly assumes that the IRAS / SiO sources in the disk are relatively young population and are associated with the spiral arms in some degree. Also it assumes that the local velocity dispersion of the sources at the given point in the Galaxy is not very large compared with the velocity of galactic rotation (say, less than $\sim$ 30 km s^{-1}). These assumptions are valid for M giants and supergiants which are involved in the sample. The content of massive stars in the sample, however, is not known at present. These issues are already discussed in section 3.3 in Paper I, and not repeated here.

The origin of the CO vacant area at ($l = 31 - 34°$ at $V_{lsr} = 10 - 60$ km s^{-1}) is not clear. The CO (and HI too) gas in the Sagittarius-Carina arm is apparently deficient at this position, so that the lines of sight do not encounter any giant clouds until to the Scutum arm. The vacancy of SiO sources in the same directions suggests that the IRAS / SiO sources are also not present much there.

A striking coincidence of position in SiO concentration onto the W44 complex in Figure 2.6 is somewhat curious. The distance to this CO cloud is estimated to be 3 kpc (Sato 1986), suggesting that it is on the Sagittarius arm. Only two (18516+0028, and 18550+0130) of five SiO stars in that concentration are located within 1° from the W44 supernova remnant (G34.0−0.5) on the $l - b$ plane, and the other three (18470+0157, 18474+0150, and 18487+0152) are slightly far (by more than 1°). Moreover, the distances to these SiO sources spreads from 2 to 9 kpc, suggesting that the coincidence occurred just by chance. However, it is not impossible that the apparent concentration of SiO maser sources in the $l - v$ diagram is yielded by the overlap of several high density area in spur tracks out of spiral arms along the line of sight as tangential points.

Figure 2.7 shows the positions of the observed sources projected onto the galactic plane, overlaid on the spiral model of the Galaxy (Taylor and Cordes 1993). We can recognize a moderate concentration into the Scutum arm at 5 – 7 kpc from the Sun in the direction $l = 30°$. On the other hand, we can not see any strong concentration onto the Sagittarius-Carina arm. In the area far from the Sun over 10 kpc, the estimated luminosity distances involve large errors. The concentration into Sagittarius-Carina arm at the far side is difficult to be confirmed.

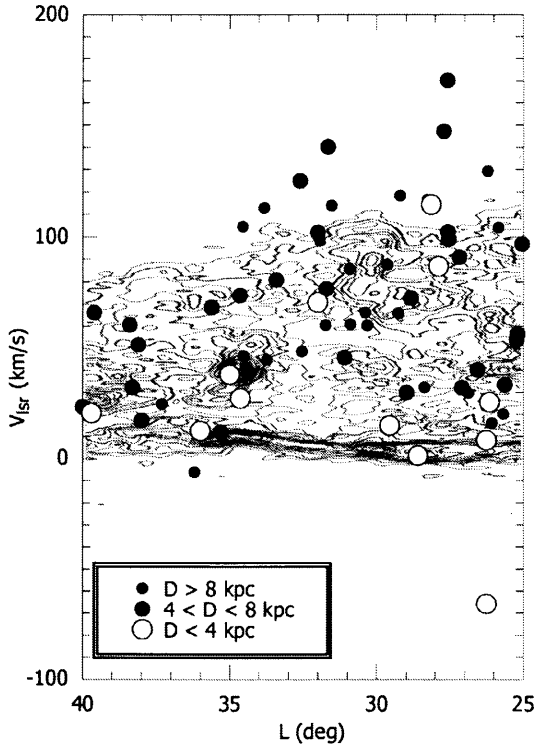

Figure 2.6: The longitude-velocity diagram of the SiO detected sources overlaid on the CO $v - l$ map (taken from Dame et al. 1987, integrated in the range between $b = \pm 3°$).

2.3.3 The other molecular line observations and individual objects

A cross check of the present SiO maser sample with the OH 1612 MHz data finds 8 sources with both OH and SiO detections, 1 with OH but no SiO detections, 1 with SiO but no OH detections, 6 with no OH and no SiO detections. The observations by molecular lines are summarized in Table 2.5. A source, 18465−0717, is an apparent double SiO maser source, exhibiting the two SiO peaks widely separated in radial velocity, where two stars were seen by chance in the same telescope beam (Deguchi et al. 1999). Some individually interesting objects in the present sample are noted:

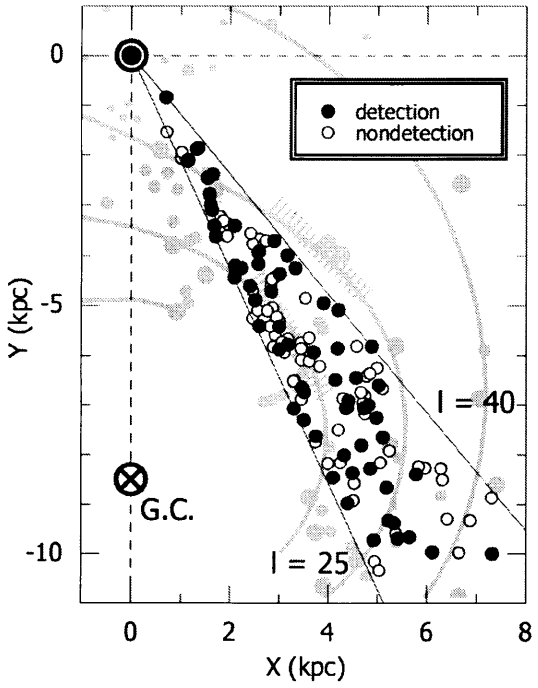

Figure 2.7: Positions of the observed sources projected onto the galactic plane, overlaid on the spiral model of the Galaxy (Taylor and Cordes 1993). The Sun is at the origin, and the galactic center is at $(X, Y) = (0, -8.5)$.

18267-0606

This star (=V431 Sct) has been suggested as a candidate of the Herbig Ae/Be star (Finkenzeller and Mundt 1984). However, it is doubtful because no nebulosity is associated with this star (Skinner et al. 1993). Wolf and Stahl (1985) and Humphreys and Ney (1974) discussed similarities of this star to the B1 I star, HD 169454, concluding that this star is a B1 hypergiant at a distance 15.5 kpc. No SiO maser emission was found in the present paper.

18554+0231

The 22 GHz H_2O maser, OH 1612 MHz maser, and CO thermal lines (the J =1–0 and 2–1 transitions) have been detected from this source (Le Squeren et al. 1992; Eder et al. 1988; Engels and Lewis 1996; Josselin et al. 1998). The radial velocity of the SiO maser line, 12.1 km s^{-1}, in the present paper is consistent with the OH maser velocity, 5 or 15 km s^{-1}, which was a single peak detection (Le Squeren et al. 1992; Eder et al. 1988). Lewis (1989) suggested this source as a candidate of protoplanetary nebulae, based on IRAS colors and nondetection of water or SiO masers. SiO masers were found in the present paper. We find no evidence for the protoplanetary nature of this source.

18560+0638

This source (= AFGL 2290, OH 39.7+1.5, or V1366 Aql) is a typical, bright O-rich Mira with F_{12} = 273 Jy, accompanying the 9.7 μm silicate band absorption. The 1612 MHz OH maser emission has been detected (Le Squeren et al. 1992; Bowers 1978; Te Lintel Hekkert et al. 1989). The distance to this source was determined with a OH double-peak phase-lag method (D = 0.98 kpc; van Langevelde et al. 1990). Van der Veen and Rugers (1989) derived the bolometric flux of this star from infrared photometry between 1 μm and 12 μm and the IRAS fluxes. The derived luminosity, L = 7200 $L_\odot$ (at the distance of 1 kpc), is close to the luminosity, 8000 $L_\odot$, adopted in the present paper. Non-spherical structure of the circumstellar envelope was suggested from speckle masking interferometry (Gauger et al. 1999). SiO masers have been detected in the present paper.

18588+0428

Strong SiO maser emission was detected at V_{lsr}=51.6 km s^{-1} in the present paper. We do not find any previous OH 1612 MHz observation for this source in literature. Lewis (1994) proposed this source as a candidate of "fossil" symbiotic novae, based on the 9.7 μm silicate absorption in the IRAS low resolution spectra without OH 1612 MHz maser emission. However, the presence of SiO maser emission excludes this possibility.

2.4 Conclusion

We have observed 133 color-selected IRAS sources in the galactic disk area, $25° < l < 40°$ and $|b| < 3°$, in the SiO $J = 1 - 0, v = 1$ and 2 transitions; 64 are detected. Distances to these sources are deduced from the IRAS 12 and 25 μm flux densities and range from 2 *kpc* to 11 *kpc*. The local radial velocity dispersion, i.e., rms of the radial velocities subtracted by the galactic rotation, was found to increase rapidly with decreasing the galactocentric distance. The distribution of SiO masers in the $V_{lsr} - l$ diagram is found to correlate weakly with the CO distribution.

TABLE 2.1
List of Detections

IRAS name	$J=1-0$ V_{lsr}	$J=1-0$ T_a	$v=1$ S	rms	$J=1-0$ V_{lsr}	$J=1-0$ T_a	$v=2$ S	rms	obs. date
	(km s^{-1})	(K)	(K km s^{-1})	(K)	(km s^{-1})	(K)	(K km s^{-1})	(K)	(yymmdd.d)
18296−0616	57.8	0.273	0.795	0.056	55.4	0.411	0.831	0.062	970509.2
18332−0655	96.1	0.352	1.401	0.073	97.5	0.494	1.631	0.090	970130.6
18335−0603	105.3	0.209	0.879	0.039	102.8	0.229	0.623	0.046	970427.3
18340−0648	54.9	0.324	0.410	0.040	52.4	0.258	0.945	0.046	970124.3
18343−0624	33.4	0.364	0.747	0.068	33.4	0.304	0.587	0.084	970130.6
18352−0557	25.7	0.958	1.574	0.102	25.6	0.958	2.263	0.108	980406.3
18366−0322	1.4	2.059	6.778	0.141	1.4	2.607	7.873	0.126	970525.1
18373−0509	32.4	0.394	2.591	0.060	31.7	0.215	1.061	0.052	980423.3
18376−0505	91.1	0.482	1.072	0.089	90.8	0.775	1.249	0.097	970510.2
18379−0528	29.6	0.182	1.127	0.036	29.9	0.111	0.316	0.035	990412.3
18380−0623	15.8	0.124	0.353	0.026	16.5	0.169	0.633	0.030	970526.9
18383−0357	117.1	0.205	0.513	0.035	115.7	0.165	0.545	0.045	980507.2
18384−0553	40.2	0.243	0.845	0.053	40.3	0.350	1.038	0.055	970126.6
18391+0004	98.2	0.164	0.54	0.036	98.5	0.254	0.679	0.045	980605.2
18392−0442	147.1	0.201	0.197	0.049	147.2	0.199	0.344	0.057	970509.2
18393−0258	65.5	0.153	0.373	0.039	66.1	0.175	0.894	0.044	970127.3
18401−0323	30.3	1.266	7.515	0.143	29.7	0.711	3.840	0.097	970523.9
18402−0458	168.4	0.227	0.644	0.044	171.7	0.241	0.698	0.041	970423.3
18411−0507	101.6	0.141	0.135	0.053	102.5	0.320	0.562	0.048	970523.9
18412−0509	98.8	0.618	1.674	0.081	99.2	0.595	2.030	0.079	970526.9
18417−0205	60.1	0.101	0.247	0.024	60.7	0.178	0.119	0.027	980420.3
18417−0200	64.0	0.104	0.226	0.033	68.3	0.188	0.018	0.037	980420.4
18422−0116	45.5	0.715	2.064	0.106	46.0	0.880	2.595	0.125	980408.4
18422−0437	115.6	0.357	0.459	0.106	113.0	0.470	0.918	0.098	970126.6
18426−0352	71.7	0.415	1.786	0.082	73.5	0.443	1.012	0.083	970525.9
18432−0040	61.1	0.385	0.629	0.053	59.9	0.447	0.917	0.058	990426.2
18432−0428	32.8	0.198	0.676	0.041	31.6	0.176	0.507	0.048	980531.2
18446−0034	100.3	0.331	1.556	0.065	103.5	0.377	0.906	0.069	980421.3
18446−0706	130.6	0.245	0.982	0.044	127.8	0.254	0.780	0.052	970127.2
18447−0741	18.4	0.236	0.837	0.040	22.0	0.172	0.605	0.038	970127.2
18449−0514	86.7	0.468	0.587	0.140	86.9	0.486	1.483	0.090	970509.0
18453−0348	118.4	0.424	0.628	0.069	118.1	0.333	0.735	0.077	990415.3
18457−0323	87.5	0.278	1.018	0.046	87.5	0.310	1.055	0.055	970127.3
18465−0717[1]	8.3	0.605	3.080	0.053	8.2	0.548	2.370	0.051	970524.9
	-65.8	0.485	1.010	0.053	-65.9	0.618	1.920	0.051	970524.9
18470+0157	46.0	0.158	0.797	0.032	46.8	0.313	1.047	0.037	990528.2
18474+0150	42.0	0.133	0.246	0.029	40.3	0.155	0.384	0.041	990427.3
18478−0058	70.6	0.658	1.340	0.084	70.7	0.758	2.215	0.086	980407.4
18480−0131	113.2	0.135	0.374	0.036	114.5	0.141	0.318	0.043	000425.3
18481−0216	59.6	0.120	0.449	0.032	62.1	0.208	0.645	0.034	990522.2
18481−0346	14.8	0.626	1.661	0.111	15.1	0.781	0.988	0.130	970126.6
18487+0152	27.3	2.458	4.724	0.183	27.3	2.293	6.564	0.175	980408.4
18494−0130	76.8	0.342	0.305	0.177	76.7	0.970	2.072	0.180	980409.4
18502−0230	85.7	0.163	0.380	0.033	85.5	0.194	0.237	0.038	000428.2
18503−0141	139.7	0.527	0.962	0.107	140.4	0.356	1.254	0.126	980409.4
18516+0028	44.6	0.257	0.583	0.041	45.1	0.244	0.955	0.045	990426.1
18517+0312	-6.1	0.417	0.814	0.058	-5.9	0.259	0.581	0.055	990509.2
18530+0507	17.0	0.115	0.342	0.035	17.8	0.133	0.445	0.037	990512.0
18544+0150	10.2	0.287	1.171	0.044	14.0	0.127	0.388	0.044	990425.2
18547−0112	125.2	0.195	0.512	0.046	124.5	0.288	0.494	0.051	980531.2
18550+0130	36.3	0.638	3.430	0.098	39.8	0.435	2.452	0.089	990414.4
18550+0104	73.8	0.415	1.853	0.067	73.9	0.513	1.957	0.072	980426.4
18552−0119	48.5	0.103	0.242	0.025	48.7	0.163	0.393	0.030	980608.1
18554+0402	25.4	0.246	0.592	0.050	24.1	0.260	0.875	0.054	990508.2
18554+0231	12.6	1.635	3.428	0.145	12.7	1.492	2.796	0.130	990426.1
18556+0053	101.9	0.285	0.780	0.047	107.0	0.152	0.953	0.052	000427.3
18559+0510	60.5	0.640	2.140	0.070	60.6	0.714	2.379	0.068	990424.3
18560+0638	20.6	12.649	33.483	0.672	20.6	18.787	63.496	0.172	990426.1
18564+0155	69.2	0.352	1.711	0.062	67.5	0.273	0.702	0.057	990510.2
18582−0016	110.2	0.214	0.267	0.039	115.3	0.144	0.317	0.047	980604.2
18588+0428	50.9	0.989	7.226	0.122	52.4	1.611	8.995	0.080	990428.3
18595−0053	80.9	0.573	0.991	0.165	80.5	0.850	2.544	0.208	980512.2
18596+0605	68.2	0.161	0.632	0.039	64.0	0.166	0.618	0.041	990426.3
19028+0604	23.3	0.849	2.525	0.095	23.8	1.285	4.106	0.096	990425.3
19074+0336	31.4	0.301	0.871	0.057	33.0	0.226	0.606	0.071	990424.3

[1] 18465−0717 is an apparent double source reported by Deguchi et al. (1999).

TABLE 2.2
List of nondetections

IRAS name	rms (J =1–0 v =1)	rms (J =1–0 v =2)	obs. date
	(K)	(K)	(yymmdd.d)
18267−0606	0.081	0.074	990525.0
18303−0519	0.066	0.062	990525.1
18307−0632	0.124	0.114	970124.6
18314−0517	0.049	0.041	980423.3
18316−0542	0.036	0.032	970510.2
18320−0352	0.065	0.058	970514.1
18320−0544	0.031	0.029	970526.2
18330−0408	0.043	0.038	980510.2
18353−0500	0.051	0.046	990524.2
18361−0427	0.059	0.048	970422.4
18364−0220	0.057	0.049	970127.6
18367−0630	0.066	0.058	980426.3
18369−0525	0.052	0.047	980511.2
18370−0614	0.085	0.075	980406.3
18372−0247	0.072	0.064	970509.1
18377−0620	0.044	0.034	980530.2
18379−0541	0.033	0.031	970523.9
18383−0250	0.026	0.022	980531.2
18386−0428	0.050	0.044	990412.3
18387−0228	0.048	0.043	970523.0
18390−0547	0.094	0.083	970523.2
18397−0400	0.066	0.059	970509.2
18406−0508	0.067	0.062	970514.2
18418−0025	0.029	0.026	980421.3
18419−0507	0.042	0.042	970514.1
18420−0123	0.032	0.025	980408.3
18420−0316	0.034	0.027	980422.3
18421−0257	0.074	0.061	980406.4
18421−0318	0.093	0.075	980406.4
18424−0509	0.043	0.037	980425.3
18425−0607	0.082	0.070	980513.2
18425−0442	0.050	0.045	970522.9
18440−0241	0.161	0.135	980409.3
18441+0311	0.055	0.051	990414.3
18441−0325	0.103	0.089	970422.4
18443−0446	0.083	0.067	970427.3
18445−0326	0.082	0.071	990523.2
18449+0042	0.078	0.067	980407.3
18463+0053	0.048	0.040	990528.2
18463−0223	0.061	0.048	980513.2
18467−0217	0.036	0.041	000424.3
18470−0115	0.074	0.062	980422.4
18474−0013	0.055	0.046	980425.3
18476+0017	0.078	0.069	980407.4
18481+0038	0.043	0.036	990426.3
18485+0038	0.104	0.085	980526.2
18487+0617	0.049	0.046	990414.3
18490−0249	0.079	0.063	980530.2
18491+0205	0.044	0.043	990522.2
18500+0139	0.050	0.040	000521.0
18507+0033	0.051	0.045	000522.0
18512−0051	0.048	0.044	980421.4
18520+0058	0.106	0.100	980424.3
18521+0247	0.035	0.033	990509.2
18522+0049	0.049	0.045	990523.2
18537+0314	0.041	0.031	990424.2
18538+0114	0.116	0.064	980426.3
18545−0148	0.056	0.046	990426.2
18550+0242	0.050	0.046	990414.4
18550+0358	0.033	0.031	990513.2
18551−0218	0.075	0.071	990523.2
18562+0315	0.035	0.031	990508.3
18567+0358	0.038	0.033	990510.3
18567+0134	0.032	0.026	990511.2
18576+0442	0.035	0.030	990512.2
18581+0339	0.042	0.035	990512.2
18597+0556	0.054	0.044	990526.2
19015+0212	0.042	0.036	990513.3
19018+0222	0.038	0.047	990514.2

TABLE 2.3
Continued

IRAS name	l °	b °	F_{12} Jy	C_{12}	C_{23}	D_L (kpc)	V_{lsr} (km s^{-1})
18267−0606	25.01	2.10	100.60	0.050	-0.439	1.7	—
18296−0616	25.20	1.38	9.30	0.000	-0.216	4.9	56.6
18303−0519	26.12	1.67	59.80	0.080	-0.658	2.3	—
18307−0632	25.10	1.01	9.64	0.099	-0.094	5.8	—
18314−0517	26.29	1.45	6.69	0.053	1.217	6.5	—
18316−0542	25.93	1.21	2.31	0.066	0.660	11.3	—
18320−0352	27.60	1.98	56.97	0.036	-0.651	2.2	—
18320−0544	25.95	1.10	2.10	0.050	0.227	11.5	—
18330−0408	27.49	1.64	2.69	0.000	0.268	9.2	—
18332−0655	25.04	0.28	4.46	0.047	0.556	7.8	96.8
18335−0603	25.84	0.63	2.87	0.028	0.981	9.4	104.1
18340−0648	25.23	0.18	17.11	0.048	0.133	4.0	53.7
18343−0624	25.63	0.28	6.30	0.001	0.358	6.0	33.4
18352−0557	26.14	0.30	16.79	0.018	0.383	3.8	25.6
18353−0500	26.99	0.70	4.30	0.001	0.823	7.3	—
18361−0427	27.56	0.79	7.23	0.059	0.006	6.3	—
18364−0220	29.48	1.70	7.84	0.068	-0.305	6.1	—
18366−0322	28.58	1.18	39.55	0.003	-0.889	2.4	1.4
18367−0630	25.80	-0.28	4.02	0.069	0.683	8.6	—
18369−0525	26.81	0.16	2.43	0.018	0.537	10.0	—
18370−0614	26.09	-0.23	10.72	0.016	0.362	4.8	—
18372−0247	29.18	1.32	19.06	0.039	-0.709	3.7	—
18373−0509	27.08	0.21	7.06	0.084	0.350	6.6	32.0
18376−0505	27.17	0.18	10.64	0.100	0.080	5.5	90.9
18377−0620	26.07	-0.44	3.08	0.028	0.800	9.1	—
18379−0528	26.86	-0.07	2.50	0.071	0.902	10.9	29.8
18379−0541	26.68	-0.18	3.89	0.007	0.743	7.7	—
18380−0623	26.06	-0.52	2.74	0.046	0.657	10.0	16.1
18383−0357	28.25	0.54	2.73	0.019	0.903	9.5	116.4
18383−0250	29.26	1.06	2.15	0.032	0.960	11.0	—
18384−0553	26.55	-0.38	10.47	0.009	0.205	4.7	40.2
18386−0428	27.83	0.22	2.45	0.004	1.059	9.7	—
18387−0228	29.62	1.13	6.90	0.003	-0.160	5.8	—
18390−0547	26.70	-0.46	7.47	0.019	0.422	5.7	—
18391+0004	31.93	2.22	3.42	0.008	0.449	8.3	98.4
18392−0442	27.70	0.00	12.02	0.051	0.068	4.8	147.1
18393−0258	29.25	0.77	2.77	0.095	0.548	10.7	65.8
18397−0400	28.38	0.21	7.54	0.025	0.463	5.8	—
18401−0323	28.97	0.39	6.11	0.005	0.574	6.2	30.0
18402−0458	27.58	-0.35	8.87	0.013	0.166	5.2	170.1
18406−0508	27.47	-0.51	7.65	0.056	-0.033	6.1	—
18411−0507	27.56	-0.62	5.57	0.092	0.320	7.5	102.1
18412−0509	27.53	-0.66	5.40	0.082	0.094	7.6	99.0
18417−0205	30.31	0.66	2.25	0.054	0.554	11.2	60.4
18417−0200	30.38	0.69	2.79	0.030	0.848	9.6	66.1
18418−0025	31.80	1.39	2.49	0.001	1.062	9.6	—
18419−0507	27.64	-0.80	8.47	0.013	-0.084	5.3	—
18420−0123	30.96	0.92	5.40	0.018	0.715	6.7	—
18420−0316	29.29	0.02	3.89	0.063	0.654	8.6	—
18421−0257	29.59	0.16	6.13	0.075	0.386	7.0	—
18421−0318	29.28	-0.01	5.52	0.010	0.461	6.5	—
18422−0116	31.09	0.91	8.69	0.031	0.484	5.5	45.8
18422−0437	28.13	-0.64	21.74	0.025	-0.170	3.4	114.3
18424−0509	27.66	-0.92	6.84	0.081	0.360	6.7	—
18425−0607	26.82	-1.39	5.90	0.088	-0.327	7.3	—
18425−0442	28.08	-0.74	7.43	0.083	0.243	6.5	—
18426−0352	28.82	-0.37	5.55	0.018	0.353	6.6	72.6
18432−0040	31.73	0.97	3.93	0.046	0.837	8.3	60.5
18432−0428	28.36	-0.78	2.74	0.002	0.819	9.1	32.2
18440−0241	30.04	-0.14	15.91	0.017	0.711	3.9	—
18441+0311	35.30	2.60	12.49	0.020	-0.790	4.5	—
18441−0325	29.40	-0.51	18.45	0.038	-0.201	3.8	—
18443−0446	28.23	-1.16	18.81	0.092	-0.509	4.1	—
18445−0326	29.43	-0.61	6.82	0.021	0.332	6.0	—
18446−0034	32.00	0.70	4.76	0.006	0.745	7.0	101.9
18446−0706	26.20	-2.31	3.60	0.036	0.534	8.5	129.2
18447−0741	25.68	-2.60	3.50	0.003	-0.030	8.1	20.2
18449−0514	27.88	-1.52	25.10	0.076	-0.601	3.5	86.8
18449+0042	33.17	1.22	15.06	0.079	-0.537	4.5	—
18453−0348	29.20	-0.94	2.01	0.020	0.378	11.1	118.3
18457−0323	29.62	-0.85	2.04	0.012	1.159	10.8	87.5
18463+0053	33.49	1.01	3.39	0.083	0.121	9.5	—
18463−0223	30.57	-0.52	6.34	0.096	0.185	7.1	—
18465−0717	26.25	-2.81	16.37	0.009	-0.618	3.8	8.3, -65.9[1]
18467−0217	30.71	-0.56	2.54	0.036	0.782	16.71	—
18470−0115	31.65	-0.14	9.06	0.037	0.221	5.4	—
18470+0157	34.52	1.32	3.24	0.010	0.716	8.5	46.4
18474+0150	34.46	1.20	3.34	0.034	0.656	8.8	41.2
18474−0013	32.62	0.25	5.15	0.008	0.268	6.7	—
18476+0017	33.11	0.42	13.90	0.076	-0.004	4.7	—
18478−0058	32.00	-0.19	36.96	0.086	-0.441	2.9	70.7
18480−0131	31.53	-0.48	2.20	0.069	0.100	11.7	113.9
18481+0038	33.47	0.49	3.68	0.044	0.037	8.6	—
18481−0216	30.89	-0.85	3.55	0.069	0.197	9.1	60.8

TABLE 2.3
Continued

IRAS name	l °	b °	F_{12} Jy	C_{12}	C_{23}	D_L (kpc)	V_{lsr} (km s^{-1})
18481−0346	29.55	-1.55	22.43	0.002	-0.142	3.2	15.0
18485+0038	33.52	0.39	8.94	0.028	0.066	5.3	—
18487+0152	34.64	0.92	29.66	0.024	-0.561	2.9	27.3
18487+0617	38.60	2.90	3.87	0.020	-0.540	8.0	—
18490−0249	30.50	-1.31	5.12	0.008	0.541	6.8	—
18491+0205	34.86	0.93	3.52	0.013	0.694	8.3	—
18494−0130	31.71	-0.79	12.58	0.070	-0.046	4.9	76.8
18500+0139	34.59	0.54	2.46	0.085	0.650	11.3	—
18502−0230	30.92	-1.43	2.71	0.047	0.509	10.1	85.6
18503−0141	31.65	-1.08	14.65	0.012	-0.072	4.0	140.1
18507+0033	33.69	-0.13	2.18	0.086	0.795	12.0	—
18512−0051	32.50	-0.91	11.12	0.085	-0.318	5.3	—
18516+0028	33.73	-0.36	3.78	0.097	0.395	9.2	44.8
18517+0312	36.20	0.90	2.09	0.090	0.820	12.4	-6.0
18520+0058	34.22	-0.23	12.92	0.010	0.620	4.3	—
18521+0247	35.80	0.60	2.22	0.000	0.610	10.2	—
18522+0049	34.11	-0.35	3.51	0.022	0.654	8.4	—
18530+0507	38.00	1.50	11.33	0.020	0.180	4.7	17.4
18537+0314	36.40	0.40	12.26	0.030	-0.110	4.6	—
18538+0114	34.67	-0.51	3.68	0.020	1.171	8.2	—
18544+0150	35.30	-0.40	4.12	0.030	0.290	7.9	12.1
18545−0148	32.03	-2.07	3.54	0.008	0.198	8.1	—
18547−0112	32.59	-1.83	5.27	0.091	0.203	7.7	124.9
18550+0242	36.10	-0.10	8.65	0.080	0.690	6.0	—
18550+0130	35.00	-0.60	47.15	0.020	-0.280	2.3	38.1
18550+0104	34.65	-0.85	10.24	0.063	-0.189	5.3	73.8
18550+0358	37.20	0.50	2.42	0.030	1.100	10.4	—
18551−0218	31.65	-2.42	4.30	0.004	-0.371	7.3	—
18552−0119	32.54	-1.99	4.39	0.067	-0.339	8.2	48.6
18554+0402	37.30	0.40	4.10	0.050	0.480	8.3	24.8
18554+0231	36.00	-0.30	51.86	0.050	-0.670	2.3	12.6
18556+0053	34.55	-1.05	2.26	0.008	1.265	10.2	104.5
18559+0510	38.39	0.84	10.44	0.040	0.068	5.1	60.6
18560+0638	39.70	1.50	273.50	0.080	-0.520	1.1	20.6
18562+0315	36.70	-0.10	4.21	0.040	0.430	8.0	—
18564+0155	35.60	-0.80	5.45	0.050	0.120	7.2	68.4
18567+0358	37.40	0.10	4.09	0.060	0.520	8.4	—
18567+0134	35.30	-1.00	2.73	0.050	0.460	10.1	—
18576+0442	38.20	0.30	5.17	0.050	1.180	7.4	—
18581+0339	37.30	-0.40	3.58	0.000	0.480	8.0	—
18582−0016	33.82	-2.18	3.37	0.015	0.075	8.5	112.8
18588+0428	38.10	-0.10	10.77	0.080	0.190	5.4	51.6
18595−0053	33.41	-2.75	10.58	0.009	-0.514	4.7	80.7
18596+0605	39.60	0.50	5.55	0.010	0.110	6.6	66.1
18597+0556	39.50	0.40	2.20	0.060	0.460	11.5	—
19015+0212	36.40	-1.80	2.44	0.100	1.130	11.6	—
19018+0222	36.60	-1.80	2.66	0.070	0.360	10.6	—
19028+0604	40.00	-0.30	5.52	0.090	-0.050	7.6	23.5
19074+0336	38.30	-2.40	6.80	0.040	-0.660	6.3	32.2

TABLE 2.4
data of molecule lines in past works.

IRAS name	SiO	line	ref.	OH	ref.	H_2O	ref.	CO & HCN	line	ref.
18267−0606	N	v=2, J=1−0	Dic78	N	LeS92	N	Pal93			
18303−0519	N	v=2, J=1−0	Nym98	N	LeS92	Y(15.4)	Han98			
	N	v=1, J=2−1	Nym98							
18314−0517						N	Pal91			
18320−0352				N	LeS92			Y(CO,64)	1−0	Lou93
				N	TeL91			Y(CO,64)	2−1	Lou93
18364−0220				N	TeL91					
18376−0505				Y(92.5)	Bow78					
				Y(92.5)	TeL89					
18425−0607				Y(55.9)	TeL91					
18441+0311				Y(27.8)	Ede88	N	Eng96			
18449−0514	N	v=1, J=1−0	Gom90	Y(85.0)	Bow78	N	Gom90			
				Y(85.0)	Joh77	N	Ben96			
				Y(85.2)	TeL89					
18465−0717	Y(8.3, −65.8)	v=1, J=1−0	Deg99	Y(−66.4)	LeS92					
	Y(8.2, −65.9)	v=2, J=1−0	Deg99							
18487+0152	N	v=1, J=1−0	Gom90	Y(28.5)	Bow78	N	Eng96			
				Y(28.5)	TeL89	Y(39.6)	Gom90			
						Y(60.0)	Bra94			
18487+0617						Y(170.0)	Eng96			
18494−0130	N	v=1, J=1−0	Nym86	Y(79.5)	Bow78	N	Nym86			
	N	v=1, J=1−0	Nym93	Y(78.8)	Joh77	Y(69.9)	Eng86			
	N	v=1, J=2−1	Nym93	Y(78.8)	TeL89	N	Oln80			
	Y(78.2)	v=1, J=1−0	Jew85	Y(79.0)	Win75					
18530+0507						N	Eng96			
18550+0130	N	v=2, J=1−0	Nym98	N	TeL91			Y(CO,37.8)	1−0	Jos98
	Y(32)	v=1, J=2−1	Nym98					Y(CO,39.7)	2−1	Jos98
18552−0119				Y(49.3)	TeL91					
18554+0231				Y(5.1)	LeS92	Y(5.2)	Eng96	Y(CO,8.5)	1−0	Jos98
				Y(15.4)	Ede88			Y(CO,8.7)	2−1	Jos98
18560+0638	Y(22)	v=1, J=2−1	Nym86	Y(20.0)	LeS92	Y(30.5)	Eng96	Y(CO, 0)	1−0	Lou93
	N	v=1, J=2−1	Nym98	Y(20.0)	Bow78	Y(20.6)	Eng86	Y(CO,21)	2−1	Lou93
	Y(22)	v=1, J=1−0	Nym86	Y(20.0)	TeL89			N(HCN)	1−0	Luc88
	Y(22)	v=2, J=1−0	Nym86							
	Y(20)	v=1, J=1−0	Nym98							
	Y(20)	v=2, J=1−0	Nym98							
	Y(17.1)	v=1, J=1−0	Jew84							
	Y(22.8)	v=1, J=1−0	Nym93							
	Y(22.0)	v=2, J=1−0	Nym93							
	Y(23.2)	v=1, J=2−1	Nym93							
19074+0336						N	Engels 1996			

Note. — Ben96, Benson and Little-Marenin 1996; Bow78, Bowers 1978;
Bra94, Brand et al. 1994; Deg99, Deguchi et al. 1999; Dic78, Dickinson et al. 1978;
Ede88, Eder et al. 1988; Eng86, Engels et al. 1986; Eng96, Engels and Lewis 1996;
Gom90, Gomez et al. 1990; Han98, Han et al. 1998; Jew84, Jewell et al. 1984;
Jew85, Jewell et al. 1985; Joh77, Johansson et al. 1977; Jos98, Josselin et al. 1998;
LeS92, Le Squeren et al. 1992; Lou93, Loup et al. 1993; Luc88, Lucas et al. 1988;
Nym86, Nyman et al. 1986; Nym93, Nyman et al. 1993; Nym98, Nyman et al. 1998;
Oln80, Olnon et al. 1980; Pal91, Palla at al. 1991; Pal93, Palla and Prusti 1993;
Tel89, Te Lintel Hekkert et al. 1989; TeL91, Te Lintel Hekkert et al. 1991;
Win75, Winnberg 1975
Note. — "Y" and "N" indicate the detection and nondetection.
V_{lsr} of the line is shown in the parenthes.

References

[Benson & Little-Marenin 1996] Benson, P, J. & Little-Marenin, I. R. 1996, ApJS, 106, 579

[Bowers 1978] Bowers, P. F. 1978, A&Ap, 64, 307

[Brand et al. 1994] Brand, J., Cesaroni R., Caselli, P., Catarzi, M., Codella, C., Comoretto, G., Curioni, G. P., Curioni, P., Di Franco, S., Felli, M., Giovanardi, C., Olmi, L., Palagi, P., Palla, F., Panella, D., Pareschi, G., Rossi, R., Speroni, N. & Tofani, G. 1994, A&ApS, 103, 541

[Dame et al. 1987] Dame, T. M., Ungerechts, H., Cohen, R. S., & Thaddeus, P. 1987, ApJ, 322, 706

[Dame et al. 2000] Dame, T. M., Hartmann, D. Thaddeus, P. 2000, ApJ(in press, aspro−ph/0009217)

[Deguchi et al. 2000a] Deguchi, S., Fujii, T., Izumiura, H., Kameya, O., Nakada, Y., Nakashima, J., Ootsubo, T. & Ukita, N. 2000a, ApJS, 128 (in press, Paper II)

[Deguchi et al. 2000b] Deguchi, S., Fujii, T., Izumiura, H. & Nakashima, J. 2000b, 130 (in press, Paper III)

[Deguchi et al. 1999] Deguchi, S., Fujii, T., Izumiura, H., Matsumoto, S., Nakada, Y., Wood, P. R., & Yamamura, I. 1999, PASJ, 51, 355

[Deguchi et al. 1998] Deguchi, S., Matsumoto, S. & Wood, P. R., 1998, PASJ, 50, 597

[Deguchi et al. 2001] Deguchi, S., Nakashima, J., & Balsabramaniam, R., 2001, PASJ, submitted

[Dickinson et al. 1978] Dickinson, D, F., Snyder, L. E., Brown, L. W. & Buhl, D. 1978, AJ, 83, 36

[Eder et al. 1988] Eder, J., Lewis, B. M. & Terzian, Y. 1988, ApJS, 66, 183

[Engels and Lewis 1996] Engels, D. & Lewis, B. M. 1996, A&ApS, 116, 117

[Engels et al. 1986] Engels, D., Schmid-Burgk, J. & Wlmsley C. M. 1986, A&Ap, 167, 129

[Finkenzeller and Mundt 1984] Finkenzeller, U. & Mundt, R. 1984, A&ApS, 55, 109

[Gauger et al. 1999] Gauger, A., Balega, Y. Y., Irrgang, P., Osterbart, R. & Weigelt, G. 1999, A&Ap, 346, 505

[Gómez et al. 1990] Gómez, Y., Moran, J. M. & Rodriguez, L. F. 1990, Mexican Astron. Astrof., 20, 55

[Han et al. 1998] Han, F., Mao, R. Q., Lu, J., Wu, Y. F., Sun J., Wang, J. S., Pei, C. C., Fan, Y., Tang, G. S. &, Ji, H. 1998, A&ApS, 127, 181

[Habing 1996] Habing, H. J. 1996, A&AR, 7, 97

[Humphreys and Ney 1974] Humphreys, R. M. & Ney, E. P. 1974, ApJ, 187, L75

[Izumiura et al. 1999] Izumiura, H., Deguchi, S., Fujii, T., Kameya, O., Matsumoto, S., Nakada, Y., Ootsubo, T., Ukita, N. 1999, ApJS, 125, 257 (Paper I)

[Izumiura et al. 1995] Izumiura, H., Deguchi, S., Hashimoto, O., Nakada, Y., Onaka, T., Ukita, N & Yamamura, I. 1995, ApJ, 453, 837

[Jewell et al. 1984] Jewell, P. R., Batrla, W., Walmsley, C. M. & Wilson, T. L. 1984, A&Ap, 130, L1

[Jewell et al. 1985] Jewell, P. R., Walmsley, C. M., Wilson, T. L. & Snyder, L. E. 1985, ApJ, 298, L55

[Jiang et al. 1996] Jiang, B. W., Deguchi, S., Yamamura, I., Nakada, Y., Cho, S. H. & Yamagata, T. 1996, ApJS, 106, 463

[Jiang et al. 1999] Jiang, B. W., Deguchi, S. & Ramesh, B. 1999, PASJ, 51, 95

[Johansson et al. 1985] Johannson, L. E. B., Andersson C., Goss, W. M. & Winnberg, A. 1977, A&ApS, 28, 199

[Josselin et al. 1998] Josselin, E., Loup, C., Omont, A., Barnbaum, C., Nyman, N. -Å. & Sevre, F. 1998, A&ApS, 129, 45

[Le Squeren et al. 1998] Le Squeren, A. M., Sivagnanam, P., Dennefeld, M. & David, P. 1992, A&Ap, 25, 133

[Lewis 1989] Lewis, B. M. 1989, ApJ, 338, 234

[Lewis 1994] Lewis, B. M. 1994, A&Ap, 288, 5

[Loup et al. 1993] Loup, C., Forveille, T., Omont, A. & Paul, J. F. 1993, A&ApS, 99, 291

[Lucas et al. 1988] Lucas, R., Guilloteau, S. & Omont, A. 1988, A&Ap, 194, 230

[Nakashima et al. 2000] Nakashima, J., Jiang, B. W., Deguchi, S., Sadakane, K. & Nakada, Y. 2000, PASJ, 52, 275

[Nyman et al. 1993] Nyman, L. -Å., Hall, P. J. & Le Bertre, T. 1993, A&Ap, 280, 551

[Nyman et al. 1998] Nyman, L. -Å., Hall, P. J. & Olofsson, H. 1998, A&ApS, 127, 185

[Nyman et al. 1986] Nyman, L. -Å., Johansson, L. E. B. & Booth, R. S. 1986, A&Ap, 160, 352

[Olnon et al. 1980] Olnon, F. M., Winnberg H. E., Matthews, H. E. & Schultz, G. V. 1980, A&ApS, 42, 119

[Palla et al. 1991] Palla, F., Brand, J., Cesaroni, R., Comoretto, G. & Felli, M. 1991, A&Ap, 246, 249

[Palla and Prusti 1993] Palla, F. & Prusti, T. 1993, A&Ap, 272, 249

[Sato 1986] Sato, F. 1986, AJ, 91, 378

[Skinner et al. 1993] Skinner, S. L., Brown, A. & Stewart, R. T. 1993, ApJS, 87, 217

[Taylor and Cordes 1993] Taylor, J. H. & Cordes, J. M. 1993, ApJ, 411, 674

[te Lintel Hekkert et al. 1991] te Lintel Hekkert, P., Caswell, J. L., Habing, H. J., Haynes, R. F. & Norris, R. P. 1991, A&ApS, 90, 327

[te Lintel Hekkert et al. 1989] te Lintel Hekkert, P., Versteege-Hensel, H. A., Habing, H. J. & Wiertz, M. 1989, A&ApS, 78, 399

[van der Veen & Bruekers 1989] van der Veen, W. E. C. J., & Bruekers, R.J.L.H. 1989, A&Ap, 212, 133

[van der Veen & Habing 1990] van der Veen, W. E. C. J., & Habing, H. J., 1990, A&Ap, 239, 193

[van der Veen & Rugers 1989] van der Veen, W. E. C. J., Rugers, M. 1989, A&Ap, 226, 183

[van Langevelde et al. 1990] van Langevelde, H. J., van der Heiden, R., van Schoonefeld, C. 1990, A&Ap, 239, 193

[Weinberg 1992] Weinberg, M.D. 1992, ApJ, 384, 81

[Weinberg 1994] Weinberg, M.D. 1994, ApJ, 420, 597

[William et al. 1986] William, H. P., Brian, P. F., Saul, A. T., William, T. V. 1986, Numerical Recipes The Art of Scientific Computing (Cambridge Univ. Press., Cambridge), p.466

[Winnberg et al. 1975] Winngerg, A., Nguyen-Q-Rieu, Johansson, L. E. B. & Goss, W. M. 1975, A&Ap, 38, 145

[Wolf & Stahl 1985] Wolf, B. & Stahl, O. 1985, A&Ap, 148, 412

Chapter 3

SiO Maser Survey toward the Inner Galactic Disk: $40^\circ \leq l \leq 70^\circ$ and $|b| \leq 10^\circ$

Abstract

We present the results of an SiO maser survey for color-selected IRAS sources in the area, $40^\circ < l < 70^\circ$ and $|b| < 10^\circ$, in the SiO $J = 1 - 0$, $v = 1$ and 2 transitions ($\sim$ 43 GHz). We have detected 134 out of 272 observed sources in SiO masers; 127 are new detections. A systematic difference in detection rates between SiO and OH maser searches was found. Especially in the color ranges with $\log(F_{25}/F_{12})$ smaller than -0.1, the detection rate of the SiO masers is significantly larger than that of OH masers. We found a weak kinematic influence of the galactic arm on the distribution of SiO maser sources. A decreasing tendency of the velocity dispersion of SiO maser sources with the galactocentric distance was found. Using the present and previous data of SiO maser surveys, we found that the local velocity gradient of the rotational velocity of the Galaxy is consistent with the values obtained from the other kind of disk population stars within a statistical uncertainty. The Oort's constants, A and B, computed from a gradient of the rotation curve for the present data, are consistent with the IAU standard values. In addition, in order to check the reliability of IRAS positions, we observed the MSX positions for 5 MSX counterparts which are located more than $20''$ away (but within $60''$) from IRAS positions. We detected all of these 5 sources in SiO masers.

3.1 Introduction

In order to investigate the kinematic properties of disk AGB stars, we have made an SiO maser survey of IRAS sources at 43 GHz towards the inner galactic disk, $40° < l < 70°$, $|b| < 10°$. The color selected IRAS sources are good probes for the structure and dynamics of the Galaxy (e.g. Habing 1987). These are AGB stars which very often exhibit SiO maser emission (Nakada et al. 1993; Izumiura et al. 1994; Izumiura et al. 1995). The precise radial velocities can be known (uncertainty less than 1 km s^{-1}) through the observations of SiO masers. Extensive SiO maser surveys have been made for the inner and outer bulge (Izumiura et al. 1999; Deguchi et al. 2000a; Deguchi et al. 2000b) and the outer disk (Jiang et al. 1996). The inner area of the Galactic disk was a region left unsurveyed systematically in SiO masers at Nobeyama.

Three main issues are to be studied in the present SiO maser survey for the inner galactic disk:

- First, deep OH (1612 MHz) maser surveys for the IRAS sources have been made for the inner disk region with the Arecibo 300-m telescope (e.g. Lewis et al. 1990). Therefore, we can make a minutely comparison of the present results with the OH data.
- Second, we would like to study the influence of spiral arms on the kinematics and spatial distribution of SiO maser sources. In recent SiO maser surveys toward the disk region, it is suggested that SiO maser sources tend to concentrate into the spiral arm (Jiang et al. 1996; Nakashima et al. 2000). In the present survey region, the tangential point of Sagittarius-Carina arm is located at the distance of 5 kpc from the Sun; it is quite appropriate to make a precise investigation of SiO maser sources at this distance because of the sensitivity of the Nobeyama 45-m telescope.
- The last issue is a local gradient of the rotation curve of the Galaxy. In the outer disk, the rotational velocity has been obtained on the data of SiO maser surveys (Jiang et al. 1996; Nakashima et al. 2000). In the present work, therefore, we reanalysis the inclination of the rotational velocity of SiO sources combining the present and previous data of SiO maser survey.

In section 3.2, the observational details, results of observations, and statistical characteristics of the data are described, and then a reliability of the IRAS positions is discussed. In section 3.3, a statistical comparison with OH maser survey and kinematical analysis of the present data are made. In the final section, results of this work is summarized.

3.2 Observations and Results

3.2.1 SiO Maser Survey toward IRAS Sources

Simultaneous observations in the SiO $J = 1 - 0$, $v = 1$ and 2 transitions at 43.122 and 42.821 GHz, respectively, were made with the 45-m radio telescope at Nobeyama in the periods from 2000 April to 2001 March. A cooled SIS receiver (S40) with a bandwidth of about 0.5 GHz was used, and the system temperature (including atmospheric noise) was about 200 – 300 K (SSB). The aperture efficiency of the telescope was about 0.61 at 43 GHz. The conversion factor from the antenna temperature to the flux density was 2.9 Jy K^{-1}. Acousto-optical spectrometer arrays of high and low resolutions (AOS-H and AOS-W) were used (mainly, we used AOS-H). Each spectrometer of a high resolution has a 40 MHz bandwidth and 2048 frequency channels, with an effective spectral resolution of 0.29 km s^{-1}. The radial-velocity coverage was ± 350 km s^{-1} for each transition. All of the observations were made by position switching mode using a 5′ off position in azimuth. The pointing of the telescope was checked every 2 or 3 hours with the nearby SiO maser sources, V1111 Oph and χ Cyg. The pointing accuracy was usually found to be better than 10″.

We have chosen a sample of sources in the Galactic plane area, $40° < l < 70°$ and $|b| < 10°$, from the IRAS Point Source Catalog (Version 2, 1988, here after PSC). The distribution of the sources in the galactic coordinates are shown in Figure 3.1. The source selection has been made in terms of the IRAS 12 μm flux density, the color, and the measurement quality flags:

1. $F_{12} > 3$ Jy
2. $-0.2 < C_{12} \equiv \log(F_{25}/F_{12}) < 0.2$
3. $C_{23} \equiv \log(F_{60}/F_{25}) < -0.5$
4. $Q_{12} = Q_{25} = 3$

where F_{12}, F_{25} and F_{60} are the IRAS 12, 25 and 60 μm flux densities, Q_{12} and Q_{25} are the measurement quality flags for 12 and 25 μm, respectively, and "3" means the highest quality. These selection criteria effectively extract dust-enshrouded objects with $T_{dust} \simeq 240-450$ K from the IRAS PSC. The color range taken in the present paper, $-0.2 < C_{12} < 0.2$, is slightly wider than the range taken in previous SiO maser surveys ($0.0 < C_{12} < 0.1$; Izumiura et al. 1999; Deguchi et al. 2000a; Deguchi et al. 2000b; Nakashima et al. 2001). The effectiveness of this color criterion for the SiO search has been well approved in the previous outer bulge study (e.g. Izumiura et al. 1995). In the present work, we took larger range to cover objects with different thickness of dust shell. Finally, 340 sources were selected from IRAS PSC by above criteria, and 272 have been observed. Almost all of the sample (more than 99%) above $F_{12} = 8$ Jy has been surveyed. In the

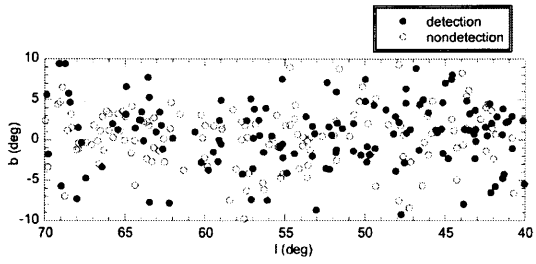

Figure 3.1: Distribution of the observed sources in the galactic coordinates. Filled and open circles indicate the SiO detection and nondetection, respectively.

case of faint sources with $F_{12} < 8$ Jy, the completeness of the survey is somewhat low.

The raw data were processed by flagging out bad scans, making rms-weighted integrations, and removing the slope in the baseline. Detections of the SiO maser lines were judged by the following criteria: for a narrow spike-type emission, the peak antenna temperature must be greater than 5 σ level of the rms noise, with line widths greater than 6 channels (corresponds to 1.0 km s^{-1} in velocity). For a broad emission, the effective signal-to-noise ratio (S/N) over the line width must be larger than 10; the effective S/N is calculated from the half-power line width (the integrated intensity divided half of the peak intensity) and the average rms noise. Furthermore, we inspected each spectrum by eye and discarded some marginal detections that satisfy the above criteria. They were observed under bad weather.

Finally, we have detected 134 out of 272 observed sources in either SiO $J = 1 - 0$, $v = 1$ or 2 transitions; 127 of 134 detected sources were new detections in SiO. The observational results are summarized in Table 3.1 for SiO-detected sources and in Table 3.2 for nondetections. The spectra of the detections are shown in Figure 3.2. The velocity, V_{lsr}, shown in Table 3.1 is the radial velocity at the intensity peak. The intensity-weighted radial velocity normally coincides with the velocity at the peak within a few km s^{-1}. The detection rate was 49%. The detection rates in the ranges of $40° \leq l < 50°$, $50° \leq l < 60°$, $60° \leq l < 70°$ are 61%, 47%, and 38%, respectively. The variation of the detection rate with galactic longitude can also be seen in Figure 3.1.

3.2.2 Position Confirmation Using MSX Catalog

The uncertainties of the source positions in the IRAS PSC are known to be about 10″ (Beichman et al. 1988; Jiang et al. 1997), and are accurate enough for most of the sources in comparison with the telescope half-power beam width of 40″ at the 43 GHz. However, bright near-infrared counterparts at a position separated from the IRAS position by more than 20″ have occasionally

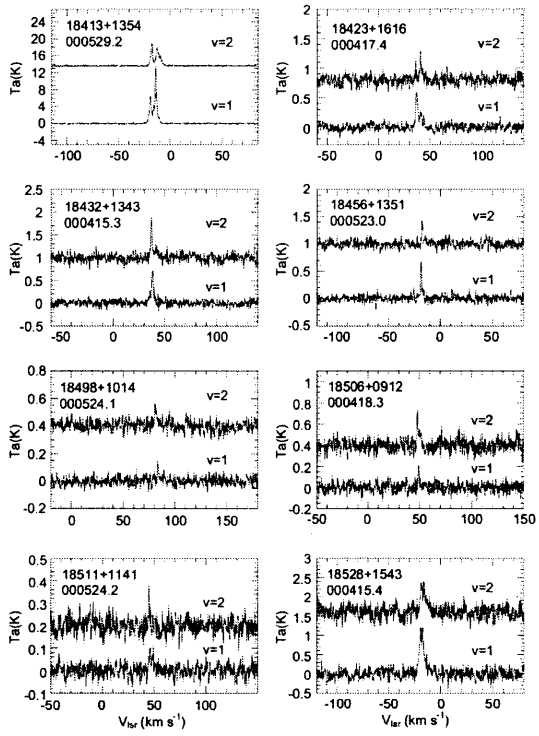

Figure 3.2a: Spectra of the SiO $J = 1 - 0$, $v = 1$ and 2 lines for 134 detected sources.

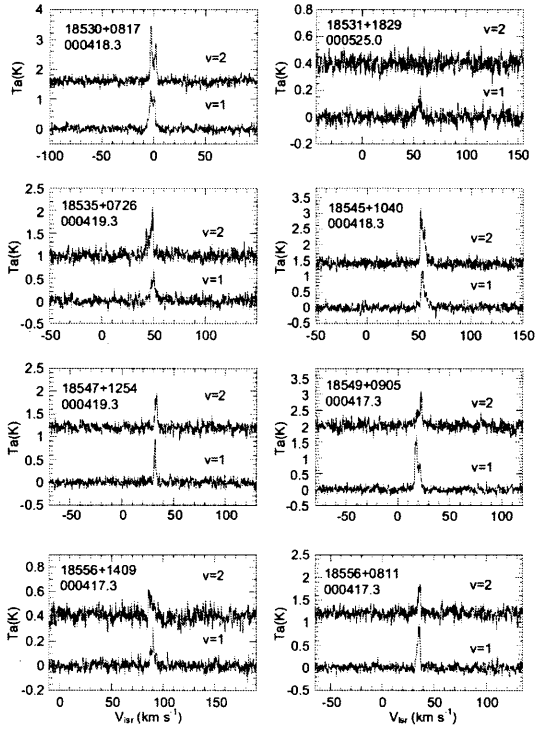

Figure 3.2b: Continued

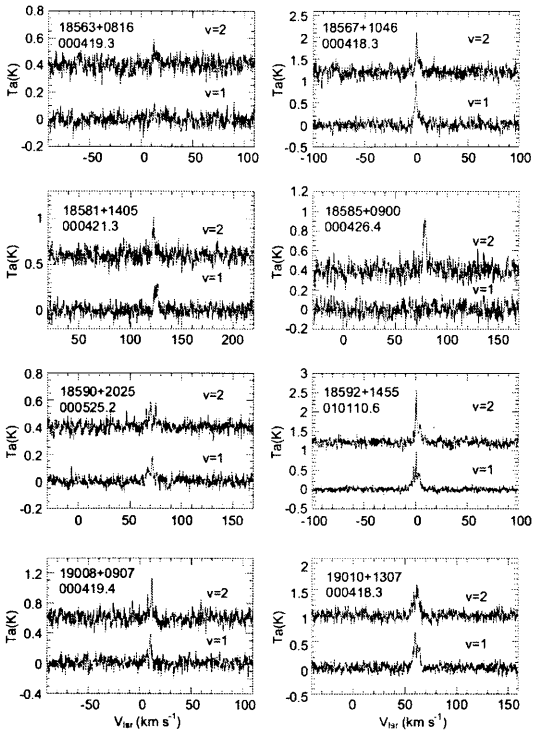

Figure 3.2c: Continued

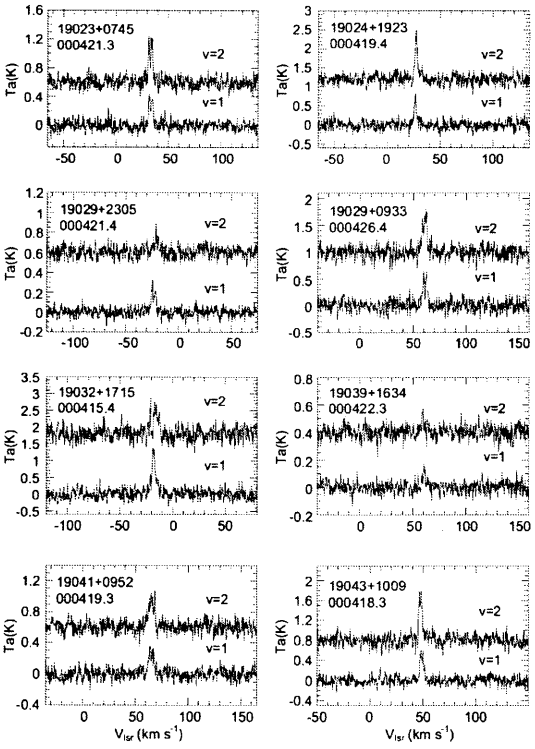

Figure 3.2d: Continued

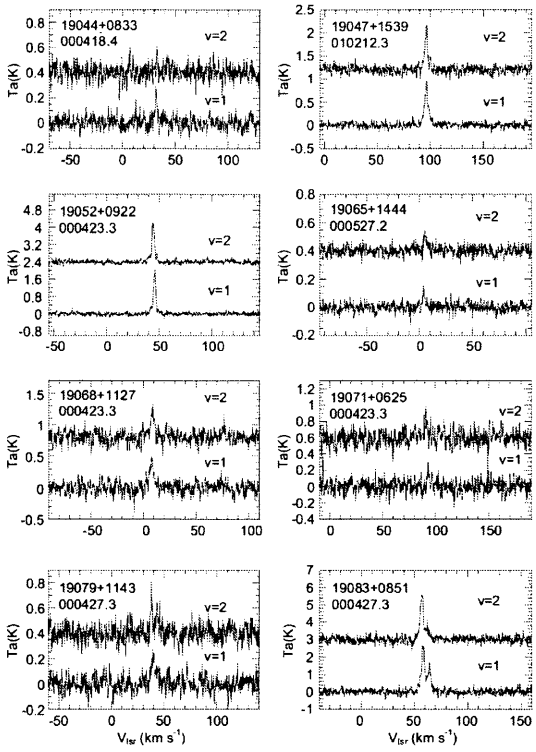

Figure 3.2e: Continued

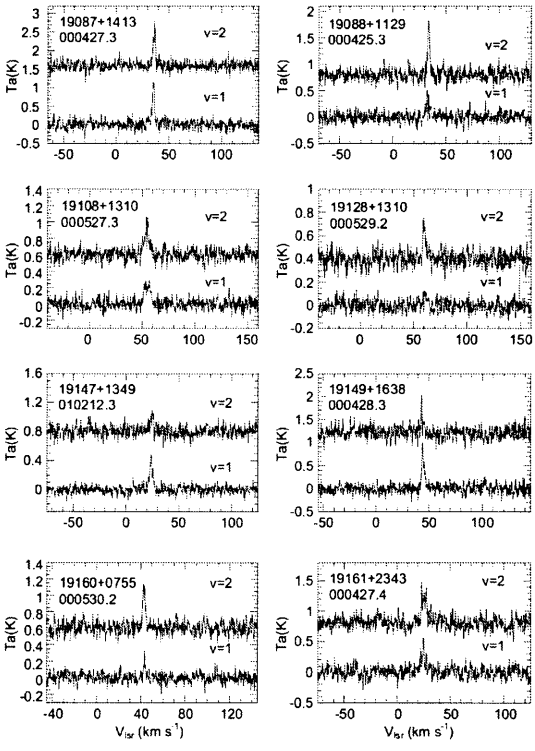

Figure 3.2f: Continued

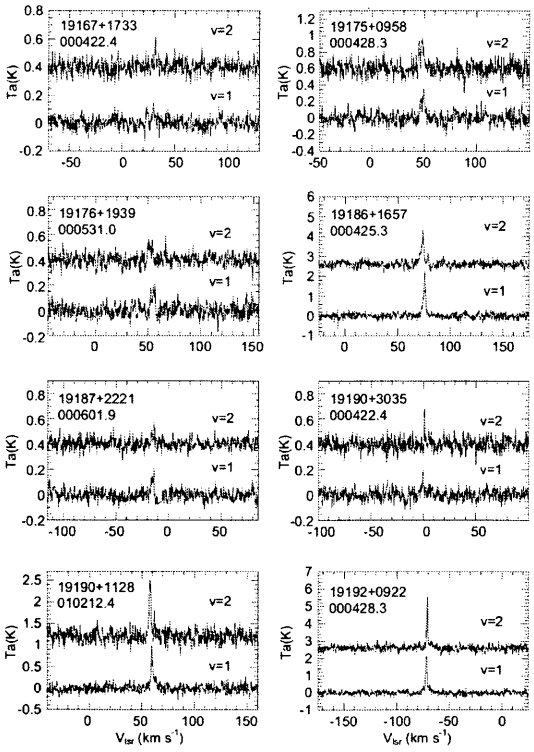

Figure 3.2g: Continued

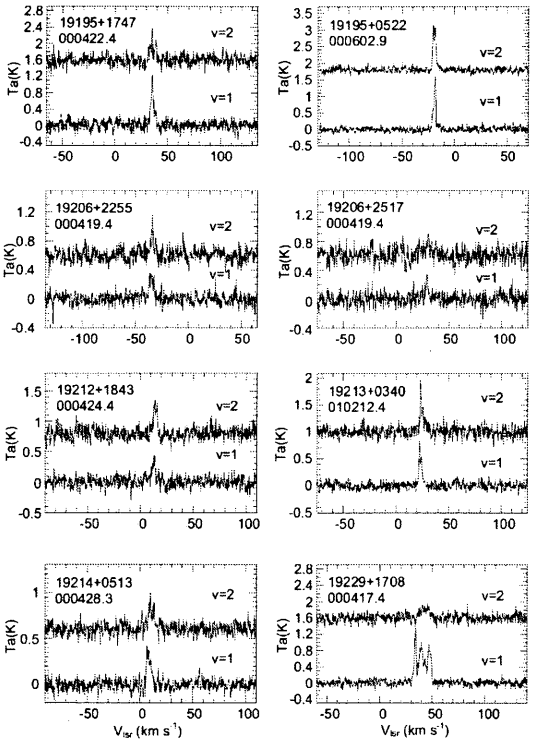

Figure 3.2h: Continued

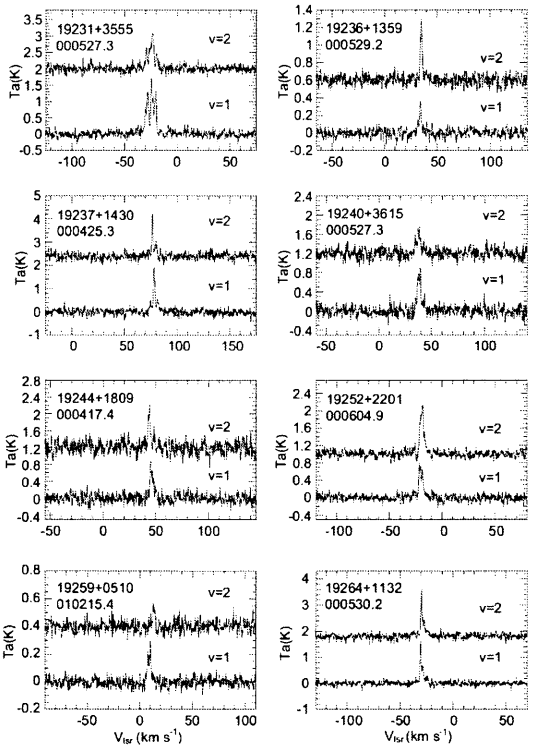

Figure 3.2i: Continued

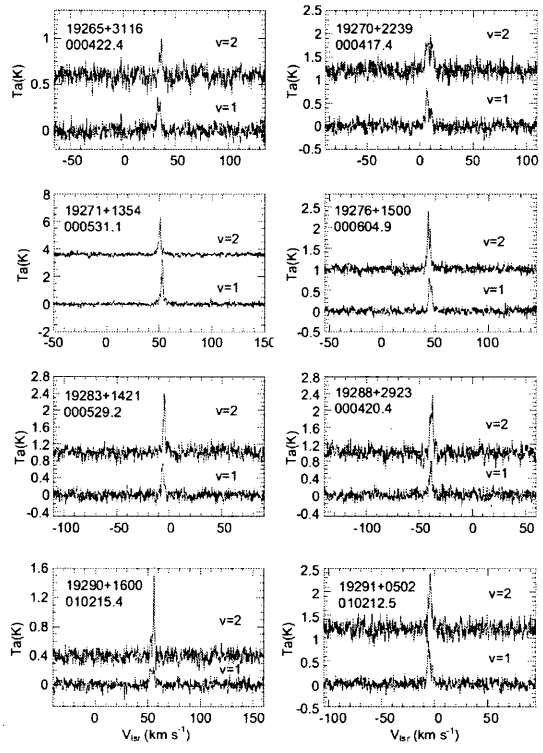

Figure 3.2j: Continued

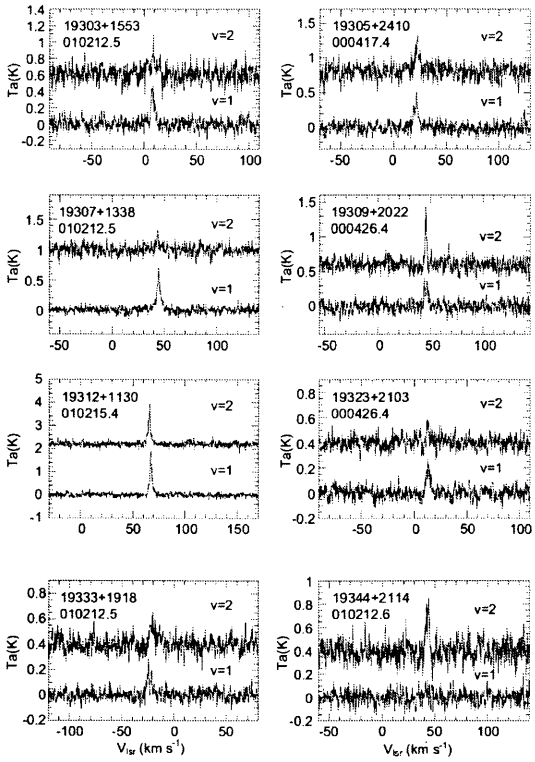

Figure 3.2k: Continued

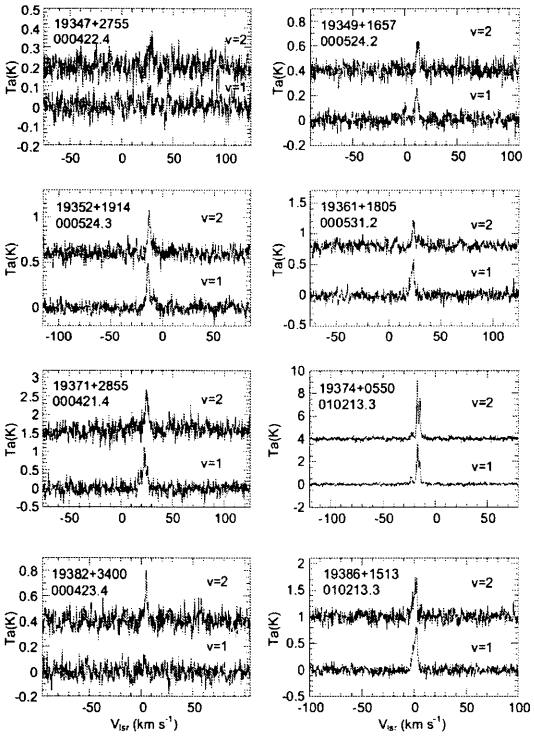

Figure 3.2l: Continued

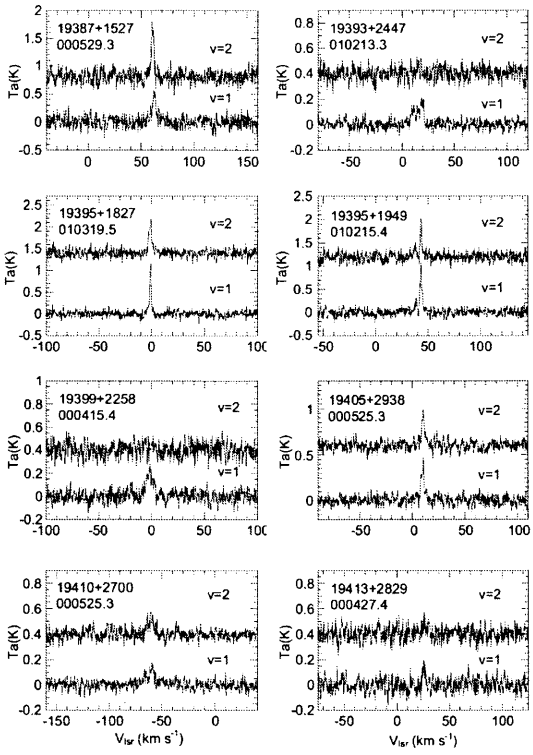

Figure 3.2m: Continued

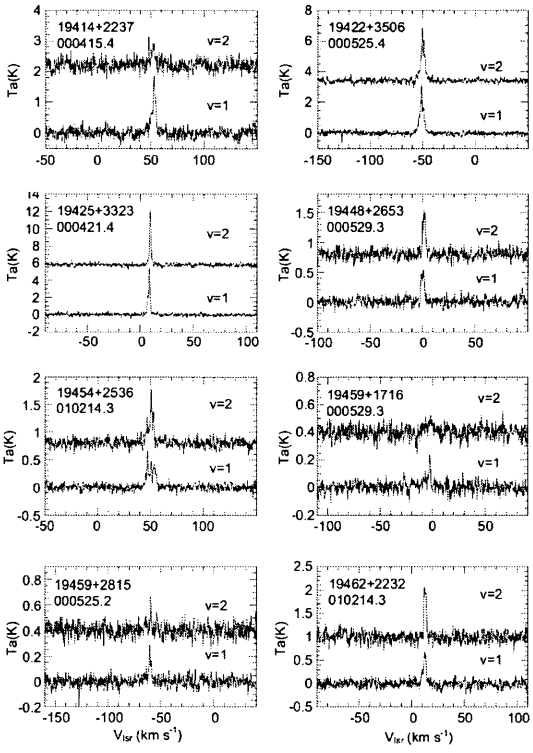

Figure 3.2n: Continued

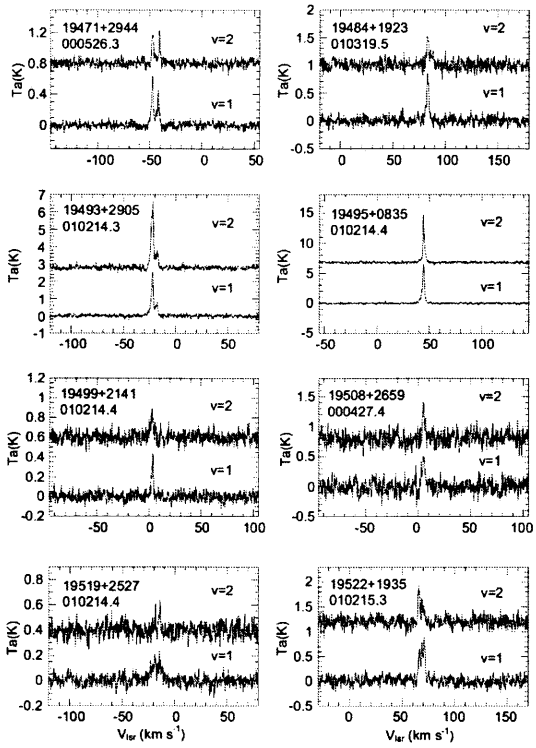

Figure 3.2o: Continued

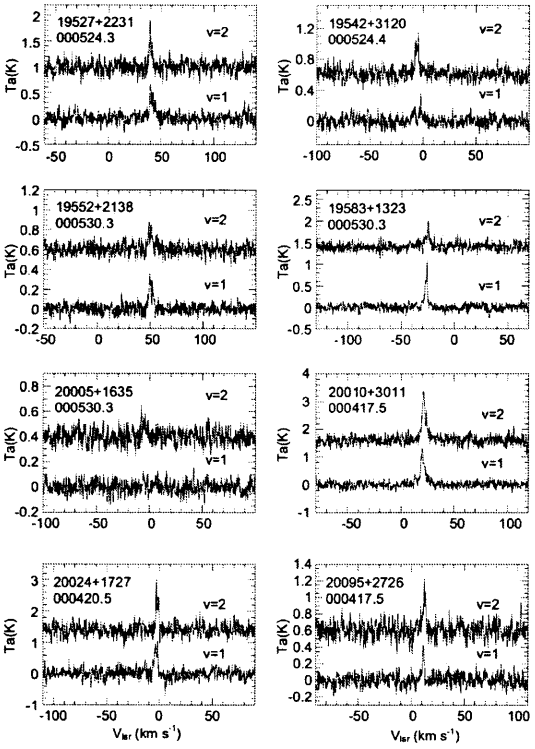

Figure 3.2p: Continued

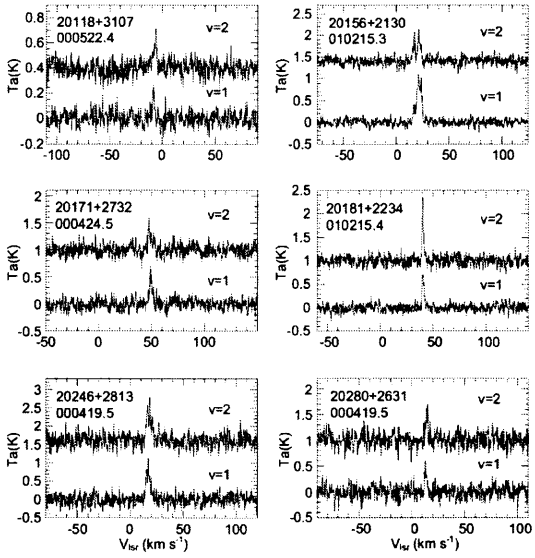

Figure 3.2q: Continued

been found in the work on the near infrared photometry of SiO maser sources at the inner galactic bulge (Deguchi et al. 2001). It seems that the main reasons of the position uncertainty of IRAS PSC are large beam of an infrared detector of IRAS and a congestion of sources. Sources in the present surveyed region are not so crowded in comparison with the inner bulge region studied by Deguchi et al. (2001). Therefore the IRAS positions would be relatively reliable than the inner bulge cases. To check the reliability of source positions of the present sample, we compared the IRAS positions for SiO nondetections with the MSX positions (MSX: Midcourse Space Experiment; Price et al. 1997). Because a typical uncertainty of astrometric positions in the MSX catalog is a few arc seconds, it is sufficient to pinpoint any candidate of the mid-infrared point source. We found from MSX catalog that 5 IRAS sources with SiO nondetection separate from MSX positions more than $20''$ (but within $60''$). In Table 3.3, separations between IRAS position and MSX position, C-band (centered at 12.13 μm) and E-band (centered at 21.34 μm) intensities in the MSX catalog, and IRAS 12 and 25 μm flux densities are given. The MSX flux densities are approximately proportional to the IRAS flux, though there are differences which may be due to pulsation of the AGB star. For above 5 sources, we searched SiO masers at the MSX positions; SiO masers are detected for all of the 5 sources. The results of this additional observation is summarized in Table 3.4, and spectra of SiO masers are shown in Figure 3.3. In the previous SiO maser surveys, IRAS positions have been used as observing positions. In order to keep consistency with the previous SiO maser surveys, above 5 detections at MSX positions are excluded in the discussion in following sections. The number of sources with large position uncertainty more than $20''$ is only 5 in 138 nondetections, which would be negligible in

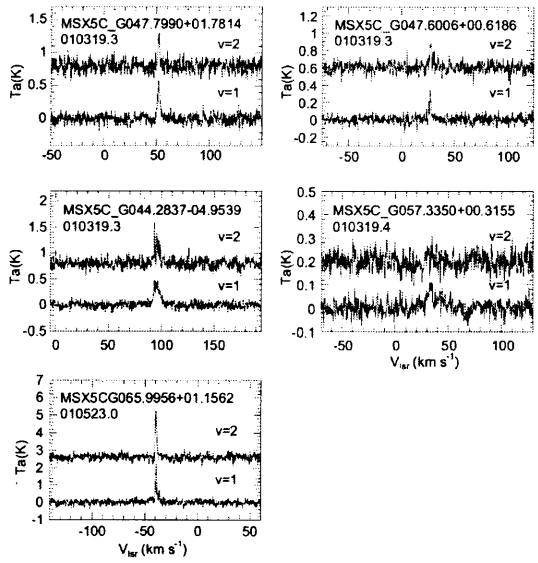

Figure 3.3: Spectra of the SiO $J = 1 - 0$, $v = 1$ and 2 lines for MSX sources as counterparts of IRAS PSC with large position uncertainty.

statistics.

3.2.3 Statistical Characteristics

In the present work, we extended the survey latitude up to $|b| = 10°$ ($|b| < 3°$ in previous works, c.f. Izumiura et al. 1999; Deguchi et al. 2000a; Deguchi et al. 2000b). Therefore, we checked the variation of the detection rate with the galactic latitude. Detection rates were 47% in the range, $|b| < 3°$, and 52% in the range, $3° < |b| < 10°$; these values coincide within a statistical uncertainty.

The detection rate, 49%, in the present survey suggests a decreasing tendency of the detection rate with galactic longitude. This tendency is consistent with the results in previous SiO maser surveys toward the inner galactic area (Izumiura et al. 1999; Deguchi et al. 2000a; Deguchi et al. 2000b; Nakashima et al. 2001; Jiang et al. 1996). However, we have to be cautious on this result, because of the difference of the color selection criteria between samples. In the previous SiO maser surveys towards the inner bulge (Izumiura et al. 1999; Deguchi et al. 2000a; Deguchi et al. 2000b), the color range, $0.0 < C_{12} < 0.1$, has been used as source selection criteria. In every 10°-step subsamples from $l = 40°$ in the longitude, the detection rates in the color range, $0.0 < C_{12} < 0.1$, are 44%, 40%, and 31%, respectively; the average detection rate is 42%. In fact, detection rates in previous surveys were 56% for the bulge bar ($15° < l < 25°$, $|b| < 3°$; Izumiura et al. 1999), 49% for the inner galactic bulge ($|l| < 3°$, $|b| < 3°$; Deguchi et al. 2000a), 62% for the outer galactic bulge ($-10° < l < 25°$, $|b| < 3°$; Deguchi et al. 2000b), and 48% for the inner galactic disk ($25° < l < 40°$, $|b| < 3°$; Nakashima et al. 2001). The present detection rate is less than the values obtained in the inner Galaxy surveys. This clearly confirms the decreasing tendency of the detection rate with galactic longitude. The detection rate in the outer galactic disk ($90° \leq l < 230°$, $|b| < 10°$), which is limited in the sample with the color, $0.0 < C_{12} < 0.1$, was 0% (14 sources were observed.). The detection rate obtained in the present work is between two detection rates of outer and inner disk surveys, supporting the monotonous decrease of the detection rate with the galactic longitude.

3.2.4 IRAS Characteristics of the sample

Figure 3.4 shows a histogram of IRAS 12 μm flux densities and the variation of the detection rate with the IRAS 12 μm flux density in the present sample. The detection rate shows a slightly increasing tendency with the 12 μm flux density. In ranges of $20 < F_{12} < 24$ Jy and $F_{12} < 4$ Jy, detection rates tend to be slightly higher and lower, respectively, than those of other ranges. In $20 < F_{12} < 24$ Jy, the number of the sample is extremely few, so that the rise may be a statistical fluctuation. Instead, in $F_{12} < 4$ Jy, because the number of the sample in this range is more than 25, it can not be regarded as a statistical fluctuation. In fact, this kind of the decline of the detection rate has been seen in previous SiO maser surveys (e.g. Deguchi et al. 2000b; Izumiura et al. 1999). The intensity of SiO maser lines tends to increase with the IRAS 12 μm flux density. For instance, in the case of NRO 45m telescope, the expected antenna temperature of the SiO maser line from the IRAS PSC source with $F_{12} = 4$ Jy is approximately 0.2 K. Because of the time variation, the intensity of maser line varies by a factor of about 10. Therefore, the antenna temperature of the SiO maser line from IRAS PSC sources with $F_{12} = 4$ Jy is expected between 0.02 and 0.2 K. Whereas, the rms level of the present survey data was 0.05 K on average. In the present work, we used the 5 σ level as a border of detection. The 5 σ level corresponds to 0.25 K in the antenna temperature; it is comparable with expected maximum intensity of the sources with $F_{12} = 3 - 4$ Jy. Hence, it is possible that nearly a half of the potential SiO detections in the range, $3 < F_{12} < 4$ Jy, are missed at this noise level. In fact, the detection rate in the range, $3 < F_{12} < 4$ Jy, is 26.9% in the present sample, which is reasonable at this noise level.

Figure 3.5 shows the two–color (left) and C_{23}–b (right) for the present sample. The SiO detection rates are 68%, 52%, 50% and 30% in C_{23} ranges, $0.9 > C_{23} \geq 0.8$, $0.8 > C_{23} \geq 0.7$, $0.7 > C_{23} \geq 0.6$, $0.6 > C_{23} \geq 0.5$, respectively.

In general, carbon stars in the two-color diagram distribute at the upper part of O-rich stars (van der Veen and Habing 1990). The present sample involves three carbon stars (IRAS 19029+0808, IRAS 19238+1159, IRAS 19304+2529, Jura and Kleinmann 1990; Volk

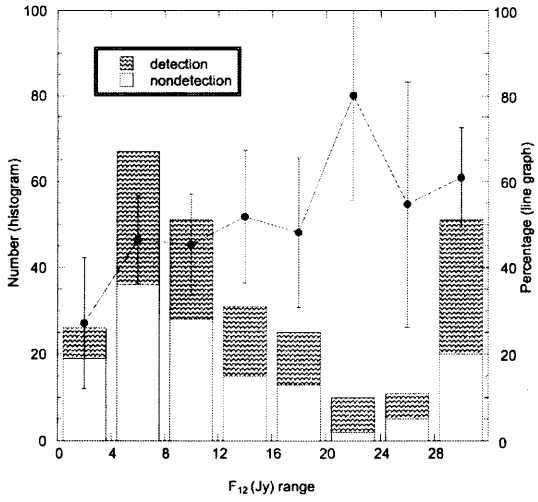

Figure 3.4: Histogram of the 12 μm flux density (bar graph) and detection rate as a function of the IRAS 12 μm flux density (line graph).

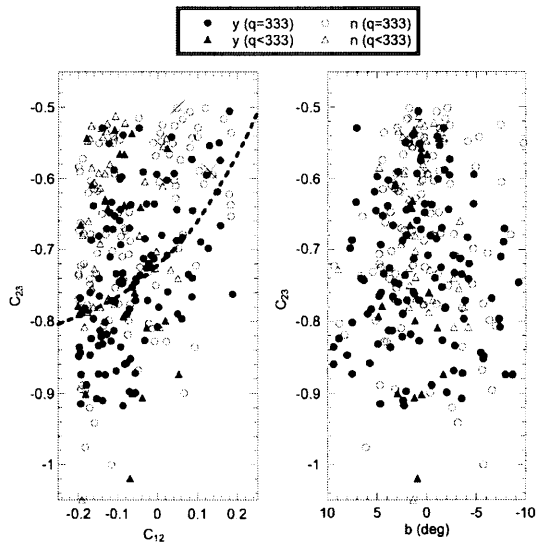

Figure 3.5: Two color ($C_{23} - C_{12}$; left panel) and color-latitude ($C_{23} - b$; right panel) diagram for the observed sources. The dotted line indicates an evolutionary track of the O-rich AGB star (van der Veen and Habing 1988).

et al. 1992), as indicated in the left panel with large crosses. Three carbon stars distribute at the most upper part in the left panel. This fact supports that the rate of carbon stars in the sample tends to increase with the color C_{23}.

In the case of the previous SiO maser surveys towards inner disk/bulge regions, $C_{23} - b$ diagram showed an arch-like structure at the bottom (the peak of the arch is at $b = 0°$), indicating a strong reddening in the Galactic plane (e.g. Figure 4 of Deguchi et al. 2000b). Whereas, such a structure is not seen in the $b - C_{23}$ diagram in the present sample. This suggests that the contamination by the interstellar dust in the C_{23} color is not strong in the present sample. The IRAS 60 μm flux densities for the present sample reflect the characteristics of mass losing AGB stars correctly.

3.2.5 Comparison with OH data

Figure 3.6 shows a histogram of the color, C_{12}, for observed sources. The number of sources surveyed in both SiO and OH masers is 240 (in 272 sources), and the number of sources, which are detected in both of SiO and OH masers, are 75. Mainly, OH maser surveys have been made with Arecibo 300-m telescope (about 95% of OH observations in Table 3.3 have been made at Arecibo.). Owing to the large aperture of Arecibo 300-m telescope, the OH maser survey was made deeper than the present SiO maser survey. Shaded portions show the numbers of SiO and OH detections. Solid and dotted lines (line graph) show the detection rates of the present SiO maser survey and OH maser survey.

The main characteristic in Figure 3.6 is a difference of the two line graphs. The detection rate of the SiO maser is roughly constant through all of the color ranges. On the other hand, the detection rate of the OH maser tends to increase with the color. This difference of the detection rates between OH and SiO masers implies that evolved AGB stars with thick circumstellar envelope tend to exhibit OH masers more than SiO masers, but AGB stars with thin circumstellar envelope tend to exhibit SiO masers more than OH masers. However, large ($\geq$ 80 %) OH detection rate may be due to poor statistics at $C_{12} > 0.1$.

According to the above results, it seems that we observed slightly different population distribution of AGB stars in SiO maser survey comparing with the case of OH maser surveys.

3.3 Discussion

3.3.1 Luminosity distance

The distance is calculated from the bolometric flux of the sources which is computed from IRAS 12 μm flux density F_{12}, and a bolometric correction for O-rich stars (van der Veen and Breukers 1989). In the present paper, we assume that the luminosity of the AGB star is 8000 $L_{\odot}$. The details can be found in our previous papers (e.g. Nakashima et al. 2000). The obtained distances are shown in Table 3.3. The distance calculated by this method involves an uncertainty of about 20 – 30%, which is mainly due to the light variation of AGB stars (in fact, many of the color-selected AGB star candidates are mira variables. See Nakashima et al. 2000). If we know the pulsation period of the star, the distance can be obtained with higher accuracy using the period–luminosity relation of Miras (e.g., Nakashima et al. 2000).

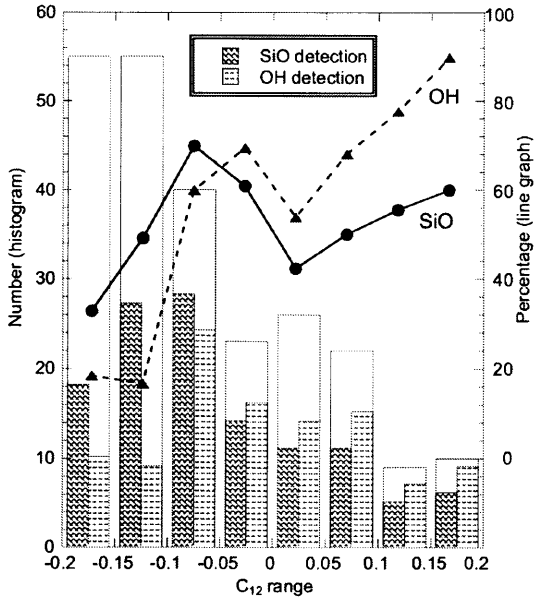

Figure 3.6: Histogram of the color index, C_{12} (bar graph), and detection rate as a function of the C_{12} for SiO maser search (solid line) and OH maser searches (dotted line). Shaded portions in columns indicate the number of detections of SiO and OH masers.

3.3.2 Kinematical Characteristics of the Sample

Figure 3.7 shows V_{lsr} versus luminosity distance (D_L) for 134 SiO detected sources. Sources above and below $l = 50°$ are classified by open and filled circles, respectively. Solid and broken curves are radial velocities expected from the circular motion and the flat rotation curve on the directions $l = 40°$ and $70°$ (see caption of Figure 3.7 in detail of the flat rotation curve.). These two curves gradually separate each other with the distance. Therefore, if the motion of SiO maser sources follows the galactic rotation (circular motion and flat rotation curve), open circles ($l < 50°$) in Figure 3.7 should distribute in relatively higher velocity range than open circles ($l > 50°$). Actually, we can see the difference of the two distribution of open and filled circles in Figure 3.7.

Figure 3.8 shows the $l - V_{lsr}$ diagram for SiO detected sources overlaid on the CO $J = 1 - 0$ line map (taken from Dame et al. 1987). The presence of the upper edge of the data distribution suggests that the present survey reaches enough to the tangential point. The V_{lsr} distribution of SiO maser sources is relatively wider than the extent of the CO map. This difference of V_{lsr} distribution would originate mainly in the difference of the velocity dispersions between CO clouds and SiO maser sources.

The moderate concentration of sources can be seen in the area, $l \simeq 40° - 53°$ and $V_{lsr} \simeq 30$ km s^{-1} — 60 km s^{-1}. Taylor and Cordes (1993) pointed out on the study of the distribution of free electrons that the tan-

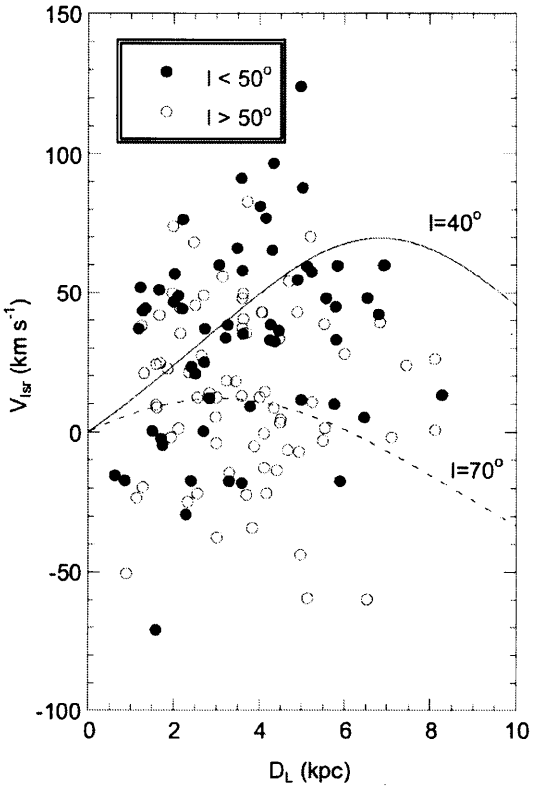

Figure 3.6: The observed radial velocity versus the luminosity distance. The solid and dotted curves are radial velocities expected at $l = 40°$ and $70°$, respectively, from the Galactic rotation curve $V_{rot} = 220\mathrm{km\,s^{-1}} R(8.5+R_a)/[8.5(R+R_a)]\{1+1.1/[1+3(R-R_a)^2]\}$, where R is the distance from the Galactic center in kpc and R_a is an adjustable parameter that creates a peak of the rotation curve near R_a, and is adopted 0.3 kpc.

gential point of the Sagittarius-Carina arm exists at the distance 4 $\sim$ 8 kpc from the Sun on the direction l = 45°. Therefore, it is possible that this weak concentration of sources originates from the Sagittarius-Carina arm (though it is not so clear.). A similar week concentration of the sources possibly due to the Scutum-Crux arm has been also reported in Nakashima et al. (2001). We can see a source deficient-region (roughly surrounded by a dotted ellipse in Figure 3.8). In order to confirm this deficiency, we applied the Kolmogorov-Smirnov (K-S) test (Chakravarti et al. 1967) for three subsets of the SiO detections divided by the galactic longitude: group A (40° $< l <$ 45°), group B (45° $< l <$ 55°), and group C (50° $< l <$ 55°). The source deficient region mentioned above is mainly included in group B. The cumulative probability distributions for three groups are shown in Figure 3.9. The maximum difference of cumulative probability (D value) between group A and B, group B and C, group C and A are 0.21, 0.24, and 0.13, respectively. The values of D_α, which is the boundary to judge at the 99% confidence level whether a difference of two distributions is reliable, are 0.15, 0.13, and 0.15 for pairs of groups A and B, groups B and C, groups C and A, respectively. According to D and D_α values, the difference in the distribution along the perpendicular axis in Figure 3.9 is significant with more than 99% confidence level between groups A and B, groups B and C, but it is not between groups A and C. In addition, maximum different points in the cumulative probability diagram between the groups A and B, and between groups B and C correspond to just at the source deficient region. Based on these results, we conclude the source deficient region surely exists on the l-v diagram.

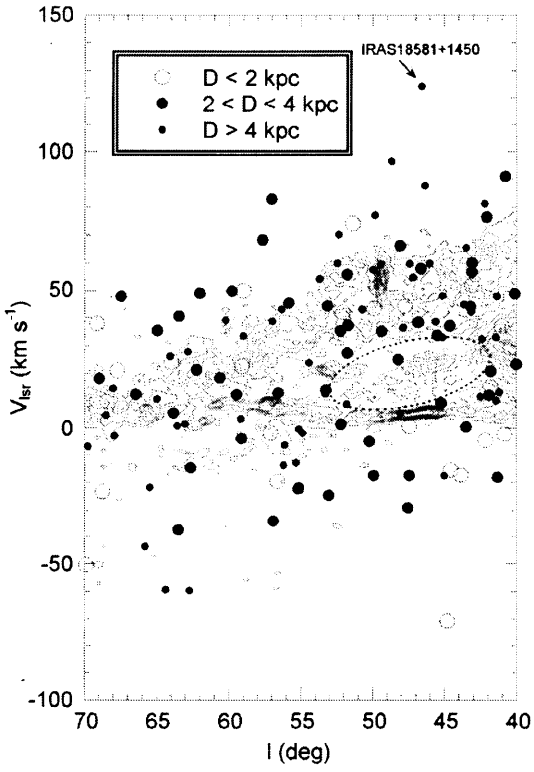

Figure 3.6: The longitude-velocity diagram of the SiO detected sources overlaid on the CO $v - l$ map, integrated in the range between b = ±3°.25 (taken from Dame et al. 1987) The region surrounded by a dotted ellipse indicate a source vacant area (see text).

3.3.3 Variation of Velocity Dispersion

We divided the detected sources into three groups by galactocentric distance: I($R <$ 6.5 kpc, 25 sources), II(6.5 $\leq R <$ 7.5 kpc, 64 sources), and III($R \geq$ 7.5 kpc, 44 sources). Then velocity dispersion (root mean square of residues extracted by the circular and solar motions from V_{lsr}) are calculated for three groups. Here, we assumed that the circular orbit and flat rotation curve for the galactic rotation (see the caption of Figure 3.7 in detail), and that the galactocentric distance of the Sun is 8.5 kpc. The calculated velocity dispersions are 35.2 km s^{-1}, 32.2 km s^{-1}, and 30.6 km s^{-1} for the groups I, II, and III, respectively. It seems that the velocity dispersion tends to decrease with the galactocentric distance. In order to confirm this tendency from the statistical view point, F-test has been made. The confidence level of the difference in dispersion between the nearest group I($R <$ 6) and the furthest group III($R \geq$ 7) is 79%. According to the results from the F-test, the increasing tendency of the velocity dispersion with the galactic radius can not be denied, though the confidence level is low.

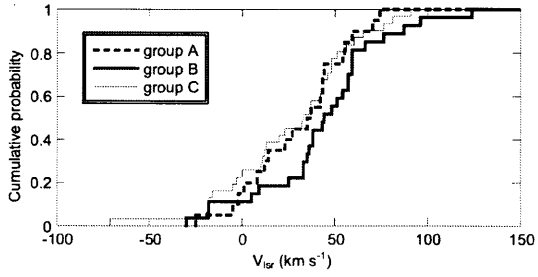

Figure 3.6: Cumulative probability plot of the V_{lsr} distribution of the present sample. The cumulative probability is shown for three groups (see text).

3.3.4 Influence of Arms on SiO maser source distribution

In the previous section 3.2, we found that the weak concentration of SiO sources in the $l - V_{lsr}$ diagram possibly due to the spiral arm, but it was not so clear. Figure 3.10 shows the positions of the sources projected onto the galactic plane; it is overlaid on the spiral model of the Galaxy (Taylor and Cordes 1993). In order to check the selection bias of observed sources, some of IRAS sources ($F_{12} > 3$ Jy) for which observations were not made are also plotted with a small dot. In addition, faint sources with $F_{12} = 1 - 3$ Jy, which have the same colors as those in the present sample, are plotted as small crosses. The distribution of the color selected IRAS PSC sources (AGB star) seems quite homogeneous.

On the other hand, it seems that the distribution of the SiO detected sources shown with filled is somewhat inhomogeneous. We performed the K-S test against to the SiO maser sources among three longitude ranges, $40° < l < 50°$, $50° < l < 60°$, and $60° < l < 70°$. Probability distributions of the sources with distance are different with 99% confidence levels for all combinations of these three subsets. It is possible that this inhomogeneity of SiO maser sources are caused by the spiral arm. In fact, it is confirmed that the sources in the $l - V_{lsr}$ diagram mentioned in section 3.3 moderately concentrate into the tangential point of the Sagittarius-Carina arm. It has been suggested that mass-loss rate depends on the initial mass of the star (van der Veen and Habing 1988). If AGB stars near the spiral arm have large initial mass and large mass-loss rate and they still stay near the arm, the detection rate of SiO masers would increase near the spiral arm. AGB stars with large initial mass formed in the arm would evolve quickly, and are difficult to leave from the arm due to the arm gravitational potential. AGB stars with SiO maser may tend to cling to the arm.

However, we already mentioned in the previous section about the decrease of the SiO detection rate with the galactocentric distance. Therefore, it is possible alternatively that this inhomogeneity of the SiO maser source distribution originate partly from the decrease of the detection rate with the galactocentric distance. To clarify the arm influence, we need to survey in SiO masers for the other area, which includes the tangential point of the other spiral arms.

3.3.5 Rotation Curve

Figure 3.11 is a plot of rotational velocity of the SiO sources against the galactocentoric distance. The rotational velocity is calculated from radial velocities by extracting the rotational velocity 220 km s^{-1} of the local standard of rest, assuming that the radial velocity is a projection of circular rotational velocity along the line of sight. The solid line shows a running mean of V_{lsr} in every 1 kpc width with 0.5 kpc steps from 5.5 kpc to 11 kpc. The dotted line shows a best fit line to the data. In the calculation, we added the data in Jiang et al. (1996) in the outer disk; the selection criteria of the sample and the method to obtain distances in Jiang et al. (1996) are the same as those used in the present work. The least square gives the best fit,

$$V_{rot} = 202.2(\pm 14.24)\,\mathrm{km\ s^{-1}} - 4.8(\pm 1.7)\,\mathrm{km\ s^{-1}kpc^{-1}} \times (R - R_0)\,\mathrm{kpc}, \quad (3.1)$$

where R_0 is assumed to be 8.5 kpc. The obtained inclination is consistent with the values obtained for the other disk population stars (-2.1 ± 2.4 km s^{-1} kpc^{-1} for OB stars, -5.7 ± 3.2 km s^{-1} kpc^{-1} for Cepheid, e.g. Frink et al. 1996) within a statistical uncertainty. Oort's constants estimated from this inclination are $A = 15.4 \pm 0.9$ km s^{-1} kpc^{-1}, $B = -10.5 \pm 0.9$ km s^{-1} kpc^{-1}. These values are close to the IAU standard values ($A = 15$ km s^{-1} kpc^{-1}, $B = -10$ km s^{-1} kpc^{-1}; Kerr and Lynden-Bell 1986). According to the present results, the bulk motion of the SiO maser sources at the solar neighborhood would be the same with the other disk population stars.

In the recent works on the kinematics of SiO maser sources in the outer disk, the obtained inclinations of the rotation curve, which were limited in $R = 8.5 - 11.5$ kpc, were -21.7 ± 5.7 km s^{-1} kpc^{-1} (Jiang et al. 1996), and -15.4 ± 7.7 km s^{-1} kpc^{-1} (Nakashima et al. 2000) respectively. These values are slightly steeper than the present results, indicating that the rotational velocity of the Galaxy tends to decrease in the outer region further than the Sun, and this result is consistent with the observations of the other kind of disk population stars (Frink et al. 1996).

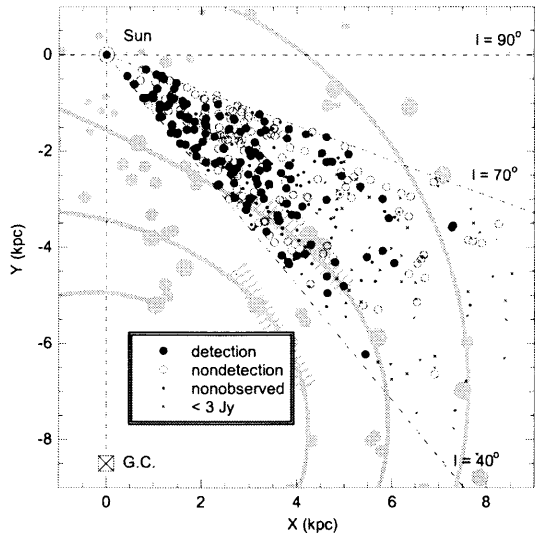

Figure 3.6: Positions of the observed sources projected onto the galactic plane, overlaid on the spiral model of the Galaxy (Taylor and Cordes 1993). The position of the Sun and the Galactic center are at the origin and $(X, Y) = (0, -8.5)$, respectively.

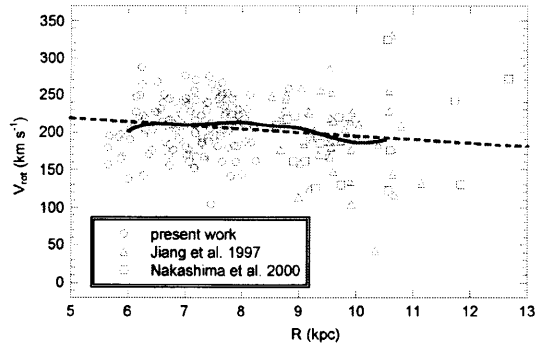

Figure 3.6: Rotation curve of SiO maser sources. Solid line indicates a running mean of data.

3.4 Individual Sources

IRAS 18413+1354 (V837 Her)

The SiO maser from this source is extreme strong (12 K in the $J = 1-0$, $v = 1$ transition). This source is included in the catalog of nearby dusty AGB stars within 1 kpc (Jura and Kleinmann 1989). This source is also very bright at 12 μm (225 Jy) with IRAS LRS (IRAS Low Resolution Spectrum) class of 29. OH and H_2O masers have been detected (Slootmaker et al. 1985; Comoretto et al. 1990); ^{12}CO (1–0) was detected (Margulis et al. 1990); CS (1–0) and NH_3 (1, 1) searches were negative (Anglade et al. 1996).

IRAS 18530+0817 (EIC 719)

The IRAS LRS of this source exhibits unusual spectrum (LRS class 04; 04 means strange band shape). It has strong silicate emission peaking near 9 μm (Olnon and Raimond 1989), which is either self-absorption at 10 μm or the silicate feature affected by the other molecular bands. SiO masers have been detected in the present work. OH search was negative (Lewis et al. 1990). This object has the strongest stellar photospheric H_2O absorption yet observed at near-infrared (Walker et al. 1997).

IRAS 18581+1405

Observed radial velocity, V_{lsr} = 124.4 km s^{-1} of this source is somewhat high as a disk population star (highest in Figure 3.7). Main-line of OH maser (1665 MHz) has been detected at V_{lsr} = 114.4 km s^{-1} (Lewis 1997), which is consistent with the SiO radial velocity. H_2O maser search was negative (Engels and Lewis 1996).

IRAS 18585+0900

IRAS LRS class of this source is 41 (indicating a carbon star). However, this is due to absorption at the 10 μm silicate feature. In fact, SiO maser emission (only the $J = 1-0$, $v = 2$ transition) was detected in the present work. Double peaks OH maser (1612 MHz) gave an expansion velocity of 61 km s^{-1} (Eder et al. 1988), whereas the expansion velocity in the CO observation was 20 km s^{-1} (Loup et al. 1993). H_2O maser was negative (Engels and Lewis 1996).

IRAS 19192+0922 (AFGL 2374)

Based on the radio observations of ^{12}CO ($J = 1-0$ and $J = 2-1$ transitions; Heske et al. 1990), the mass loss rates of this source was estimated as 9.0×10^{-6} $M_\odot$. The distance to this source, 1.13 kpc, has been obtained by the OH phase lag measurement (van Langevelde et al. 1990). The distance (1.6 kpc) used in the present work is consistent with this value. IRAS LRS class is 31. Meixner et al. (1999) selected this source as a proto-planetary nebula candidate. We detected SiO masers in this star, so that this source is still at the AGB phase.

IRAS 19229+1708

The profile of SiO masers of this source is somewhat unusual, exhibiting a relatively wide line width and multiple peaks in the $J = 1-0$, $v = 1$ line which is stronger than that of $v = 2$. H_2O maser has been detected (Engels and Lewis 1996).

IRAS 19371+2855 (NSV 12260)

This star was classified as an S-type star, based on the presence of the (0,0) sub-bands of the optical region of LaO (Stephenson 1990), but reclassified by Evans and Little-Marenin (1999) as a late M-type star. SiO masers detection in the present work and a strong silicate emission (Evans and Little-Marenin 1999) are consistent with non-S-type. The thermal lines of CO ($1-0$ and $2-1$) are also detected at $V_{lsr} \simeq 20$ km s^{-1} (Groenewegen and Jong 1998), which is consistent with V_{lsr} = 24.3 km s^{-1} in the present work. OH and H_2O have been detected (Chengalur et al. 1993; Engels and Lewis 1996).

IRAS 19558+3333

This is a suspected symbiotic star. Radio continuum emission from this source implies a hot, ionizing companion (Seaquist and Ivison 1994). A search for the 3.1 μm absorption feature, a characteristics of carbon stars, was negative (Groenewegen et al. 1994). SiO (present work) and OH (Le Squeren et al. 1992) maser searches were negative.

IRAS 20056+1834 (QY Sge)

The optical counter part of this source is a G0 supergiant with a visual magnitude of 12.5, indicating a post AGB star. The spectrum has very strong, broad Na D emission lines (Menzias and Whitelock 1988). SiO

maser search was negative in the present work. Aperture spectropolarimetry in optical region and a near-infrared imaging polarimetry have been done for this object (Trammell et al. 1994; Gledhill et al. 2001).

3.5 Conclusion

We have observed 272 color-selected IRAS sources in the galactic disk area, $40° < l < 75°$ and $|b| < 10°$, in the SiO $J = 1 - 0$, $v = 1$ and 2 transitions, and detected 134 in SiO masers; 127 were new detections in SiO masers. The main results of this work are:

1. A systematic difference in detection rates between SiO and OH maser searches was found. In the ranges below $C_{12} = -0.1$, SiO detection rate is higher than OH detection rate.

2. The weak concentrations of SiO sources in the $l - V_{lsr}$ diagram and in the face-on view diagram, were probably attributed to the spiral arm (Sagittarius-Carina arm). The sources moderately concentrate into the tangential point of the Sagittarius-Carina arm in the spatial distribution.

3. The velocity dispersion of SiO sources tends to decrease with the galactocentric distance.

4. Data in the present and previous SiO maser surveys give the local inclination of the rotation curve which is consistent with the values obtained previously in observations of the other kind of disk population stars.

TABLE 3.1
List of Detections

IRAS name	$J=1-0$ V_{lsr}	$J=1-0$ T_a	$v=1$ S	rms	$J=1-0$ V_{lsr}	$J=1-0$ T_a	$v=2$ S	rms	obs. date
	(km s^{-1})	(K)	(K km s^{-1})	(K)	(km s^{-1})	(K)	(K km s^{-1})	(K)	(yymmdd.d)
18413+1354	−12.9	13.364	47.770	0.084	−17.9	5.335	31.542	0.099	000529.2
18423+1616	35.9	0.595	2.216	0.052	40.8	0.495	1.368	0.071	000417.4
18432+1343	37.1	0.712	2.323	0.058	37.2	0.878	2.116	0.080	000415.3
18456+1351	−17.3	0.730	1.428	0.054	−17.7	0.516	0.895	0.064	000523.0
18498+1014	81.5	0.149	0.395	0.029	80.8	0.185	0.524	0.034	000524.1
18506+0912	47.8	0.225	0.250	0.043	48.1	0.334	0.541	0.052	000418.3
18511+1141	45.0	0.101	0.361	0.027	44.8	0.180	0.028	0.033	000524.2
18528+1543	−18.3	1.293	6.896	0.122	−16.6	0.835	4.528	0.157	000415.4
18530+0817	−2.1	1.382	6.700	0.095	−2.6	1.851	7.040	0.105	000418.3
18531+1829	55.2	0.229	0.670	0.039	—	—	—	0.044	000525.0
18535+0726	49.0	0.757	2.839	0.081	48.9	1.080	3.930	0.100	000419.3
18545+1040	52.1	1.155	5.043	0.090	51.7	1.775	7.484	0.105	000418.3
18547+1254	32.7	0.943	1.902	0.066	33.2	0.760	1.982	0.087	000419.3
18549+0905	19.4	1.701	7.022	0.081	22.3	1.087	4.366	0.126	000417.3
18556+0811	37.4	0.970	2.808	0.067	36.7	0.688	2.145	0.098	000417.3
18556+1409	88.4	0.328	0.835	0.032	87.1	0.217	0.924	0.050	000417.3
18563+0816	13.8	0.121	0.296	0.040	12.7	0.199	0.554	0.048	000419.3
18567+1046	0.5	0.995	3.493	0.088	0.1	0.917	2.394	0.106	000418.3
18581+1405	125.9	0.297	0.934	0.053	122.5	0.431	1.082	0.067	000421.3
18585+0900	—	—	—	0.061	78.4	0.526	2.066	0.067	000426.4
18590+2025	70.4	0.183	0.822	0.027	69.8	0.188	0.866	0.033	000525.2
18592+1455	0.5	1.003	3.771	0.051	0.3	1.373	4.315	0.086	010110.6
19008+0907	11.4	0.414	1.083	0.062	11.5	0.534	1.033	0.074	000419.4
19010+1307	58.6	0.675	2.919	0.065	61.1	0.616	2.735	0.076	000418.3
19023+0745	31.3	0.441	1.814	0.058	34.8	0.740	2.740	0.072	000421.3
19024+1923	27.7	0.816	2.073	0.105	27.0	1.384	4.090	0.118	000419.4
19029+2305	−23.4	0.363	1.152	0.042	−21.3	0.282	0.888	0.053	000421.4
19029+0933	58.6	0.664	2.271	0.095	61.3	0.794	3.732	0.104	000426.4
19032+1715	−17.9	1.363	5.624	0.139	−16.9	1.003	2.911	0.182	000415.4
19039+1634	59.1	0.170	0.489	0.036	59.7	0.198	0.366	0.044	000422.3
19041+0952	62.4	0.396	1.798	0.061	68.4	0.463	2.399	0.070	000419.3
19043+1009	46.9	0.636	2.510	0.077	46.4	1.072	4.237	0.095	000418.3
19044+0833	32.4	0.287	0.797	0.047	32.4	0.205	0.336	0.058	000418.4
19047+1539	96.5	1.012	4.072	0.049	96.7	1.026	3.070	0.071	010212.3
19052+0922	44.7	2.077	6.356	0.066	43.7	1.803	5.908	0.077	000423.3
19065+1444	5.1	0.156	0.438	0.029	5.3	0.144	0.521	0.032	000527.2
19068+1127	9.3	0.491	2.123	0.089	9.1	0.570	1.883	0.093	000423.3
19071+0625	91.4	0.311	0.507	0.078	91.0	0.391	0.924	0.090	000423.3
19079+1143	39.6	0.284	1.252	0.057	37.6	0.403	1.356	0.063	000427.3
19083+0851	56.7	2.647	16.574	0.148	56.8	2.772	12.360	0.169	000427.3
19087+1413	36.4	1.225	3.591	0.108	36.4	1.192	2.513	0.113	000427.3
19088+1129	33.6	0.512	0.930	0.084	33.8	1.052	1.736	0.106	000425.3
19108+1310	55.6	0.307	1.757	0.057	53.9	0.481	1.954	0.064	000527.3
19128+1310	59.7	0.133	0.306	0.048	59.6	0.417	1.089	0.060	000529.2
19147+1349	25.1	0.509	1.573	0.049	24.9	0.285	1.049	0.072	010212.3
19149+1638	42.9	0.981	2.585	0.093	43.0	0.875	1.654	0.116	000428.3
19160+0755	42.2	0.320	0.581	0.055	42.2	0.539	1.626	0.068	000530.2
19161+2343	26.3	0.576	2.018	0.084	23.1	0.696	3.366	0.092	000427.4
19167+1733	42.9	0.103	0.297	0.038	31.6	0.222	0.367	0.046	000422.4
19175+0958	47.9	0.360	1.163	0.063	48.2	0.363	1.434	0.074	000428.3
19176+1939	54.6	0.204	0.361	0.049	53.8	0.185	0.513	0.044	000531.0
19186+1657	74.1	2.274	5.648	0.126	73.8	1.718	4.985	0.144	000425.3
19187+2221	−13.1	0.203	0.042	0.037	−14.0	0.177	0.386	0.041	000601.9
19190+3035	0.7	0.190	0.355	0.039	0.8	0.276	0.400	0.045	000422.4
19190+1128	58.2	1.003	2.708	0.083	57.6	1.315	3.478	0.128	010212.4
19192+0922	−70.9	2.232	5.462	0.120	−70.9	2.947	5.636	0.147	000428.3
19195+1747	35.1	1.227	3.685	0.107	35.5	0.755	2.557	0.118	000422.4
19195+0522	−17.6	1.614	4.095	0.067	−18.7	1.338	4.484	0.070	000602.9
19206+2255	−34.3	0.360	1.664	0.068	−33.9	0.560	1.308	0.082	000419.4
19206+2517	30.1	0.341	1.174	0.080	37.1	0.362	1.373	0.095	000419.4
19212+1843	14.0	0.470	1.263	0.076	13.9	0.601	1.404	0.093	000424.4
19213+0340	23.4	0.828	2.320	0.064	23.3	0.965	2.580	0.088	010212.4
19214+0513	9.7	0.430	1.713	0.052	10.3	0.390	1.953	0.063	000428.3
19229+1708	38.8	0.989	8.360	0.065	45.1	0.360	2.255	0.090	000417.4
19231+3555	−23.5	1.694	10.855	0.087	−23.3	1.112	6.367	0.096	000527.3
19236+1359	35.3	0.386	1.054	0.043	35.0	0.688	1.816	0.051	000529.2
19237+1430	76.8	1.991	4.812	0.117	76.8	1.834	4.449	0.132	000425.3
19240+3615	38.7	0.900	3.379	0.086	37.3	0.574	2.380	0.094	000527.3
19244+1809	44.4	0.888	2.888	0.096	44.4	1.107	3.280	0.132	000417.4
19252+2201	−21.0	0.783	3.479	0.067	−18.2	1.121	4.828	0.065	000604.9
19259+0510	11.2	0.311	0.801	0.030	13.0	0.163	0.186	0.038	010215.4
19264+1132	−29.2	1.625	4.514	0.074	−29.5	1.892	5.362	0.098	000530.2
19265+3116	34.3	0.377	1.649	0.055	36.8	0.445	0.635	0.069	000422.4
19270+2239	7.5	0.827	3.137	0.099	10.1	0.791	4.393	0.125	000417.4
19271+1354	51.0	3.350	8.386	0.106	50.9	2.832	7.158	0.107	000531.1
19276+1500	42.9	0.817	2.808	0.056	43.2	1.445	4.067	0.066	000604.9
19283+1421	−5.1	0.752	2.104	0.083	−4.8	1.451	3.453	0.106	000529.2
19288+2923	−37.7	0.810	2.253	0.088	−37.4	1.382	3.369	0.111	000420.4
19290+1600	55.8	0.262	1.260	0.050	55.8	1.177	1.997	0.067	010215.4
19291+0502	−5.0	0.942	3.309	0.085	−4.2	1.206	3.555	0.130	010212.5
19303+1553	8.2	0.461	1.868	0.061	9.2	0.485	1.767	0.086	010212.5
19305+2410	22.7	0.546	1.714	0.068	22.6	0.518	2.086	0.094	000417.4

TABLE 3.1
Continued

IRAS name	$J=1-0$ V_{lsr}	$J=1-0$ T_a	$v=1$ S	rms	$J=1-0$ V_{lsr}	$J=1-0$ T_a	$v=2$ S	rms	obs. date
	(km s^{-1})	(K)	(K km s^{-1})	(K)	(km s^{-1})	(K)	(K km s^{-1})	(K)	(yymmdd.d)
19307+1338	43.5	0.741	2.908	0.048	43.5	0.342	0.857	0.074	010212.5
19309+2022	45.6	0.397	1.260	0.076	45.3	0.898	1.132	0.081	000426.4
19312+1130	65.9	1.905	5.394	0.075	66.3	1.776	4.771	0.094	010215.4
19323+2103	14.0	0.263	0.805	0.041	11.8	0.183	0.479	0.046	000426.4
19333+1918	−23.5	0.300	0.914	0.038	−20.3	0.282	0.686	0.058	010212.5
19344+2114	—	—	—	0.053	44.3	0.476	0.997	0.080	010212.6
19347+2755	26.4	0.113	0.218	0.041	29.5	0.185	0.325	0.046	000422.4
19349+1657	12.5	0.264	1.014	0.040	12.5	0.282	0.840	0.048	000524.2
19352+1914	−12.8	0.500	2.070	0.050	−12.6	0.490	1.866	0.061	000524.3
19361+1805	24.5	0.590	2.108	0.059	23.1	0.422	1.492	0.057	000531.2
19371+2855	23.6	1.220	4.974	0.130	25.0	1.150	3.611	0.174	000421.4
19374+0550	−17.0	3.696	12.452	0.085	−17.5	5.195	15.051	0.126	010213.3
19382+3400	4.7	0.176	0.266	0.051	4.5	0.418	0.812	0.056	000423.4
19386+1513	1.8	0.818	3.485	0.061	0.7	0.743	2.824	0.086	010213.3
19387+1527	59.8	0.370	0.694	0.088	59.9	0.713	0.795	0.103	000529.3
19393+2447	18.8	0.220	1.649	0.031	18.0	0.148	0.240	0.050	010213.3
19395+1827	−0.5	1.160	2.030	0.063	−0.4	0.829	2.583	0.081	010319.5
19395+1949	43.2	1.060	2.939	0.069	42.8	0.843	2.310	0.089	010215.4
19399+2258	−0.3	0.283	1.715	0.049	—	—	—	0.062	000415.4
19405+2938	11.2	0.463	1.584	0.049	10.2	0.386	1.310	0.049	000525.3
19410+2700	−58.8	0.196	1.201	0.033	−60.8	0.184	0.835	0.034	000525.3
19413+2829	26.7	0.240	0.405	0.050	25.7	0.169	0.578	0.052	000427.4
19414+2237	51.8	1.861	6.950	0.132	47.8	0.929	3.883	0.159	000415.4
19422+3506	−50.4	3.115	11.364	0.118	−50.4	3.471	13.080	0.112	000525.4
19425+3323	9.8	5.458	11.280	0.138	9.6	6.255	10.192	0.156	000421.4
19448+2653	1.7	0.529	1.925	0.061	1.1	0.726	2.626	0.074	000529.3
19454+2536	47.4	0.647	3.446	0.051	50.8	1.020	3.593	0.070	010214.3
19459+1716	−1.9	0.236	0.745	0.035	−2.1	0.130	0.653	0.042	000529.3
19459+2815	−59.4	0.293	0.867	0.036	−59.6	0.290	0.677	0.047	000525.2
19462+2232	12.4	0.672	2.243	0.075	12.3	1.102	2.877	0.099	010214.3
19471+2944	−46.5	0.648	2.299	0.036	−40.9	0.454	1.850	0.039	000526.3
19484+1923	85.0	0.851	2.373	0.063	82.8	0.558	2.157	0.079	010319.5
19493+2905	−21.9	2.580	8.931	0.070	−21.8	3.911	13.190	0.093	010214.3
19495+0835	44.5	6.438	16.734	0.098	44.3	7.977	16.065	0.125	010214.4
19499+2141	3.6	0.449	0.973	0.040	2.9	0.292	0.919	0.053	010214.4
19508+2659	6.1	0.555	1.632	0.097	4.7	0.598	1.720	0.102	000427.4
19519+2527	−14.6	0.243	1.527	0.038	−14.4	0.231	0.339	0.052	010214.4
19522+1935	70.6	0.944	4.796	0.080	65.7	0.715	2.265	0.095	010215.3
19527+2231	39.0	0.675	2.791	0.092	39.5	0.899	1.727	0.111	000524.3
19542+3120	−1.4	0.356	0.965	0.062	−4.7	0.545	2.201	0.076	000524.4
19552+2138	48.6	0.365	1.135	0.046	51.0	0.312	1.196	0.055	000530.3
19583+1323	−24.9	1.072	2.745	0.068	−24.7	0.643	2.266	0.084	000530.3
20005+1635	−5.0	0.135	0.143	0.048	−7.7	0.251	0.475	0.060	000530.3
20010+3011	21.2	1.325	6.778	0.100	21.0	1.891	7.774	0.142	000417.5
20024+1727	−0.6	1.074	2.555	0.148	−3.3	1.626	3.099	0.178	000420.5
20095+2726	12.3	0.430	0.884	0.068	12.4	0.636	1.866	0.095	000417.5
20118+3107	−7.5	0.267	0.430	0.050	−6.4	0.321	0.928	0.058	000522.4
20156+2130	21.2	1.094	5.741	0.066	21.5	0.729	3.590	0.087	010215.3
20171+2732	48.0	0.710	1.814	0.090	48.1	0.616	1.497	0.098	000424.5
20181+2234	40.8	0.739	1.844	0.078	40.4	1.368	2.607	0.091	010215.4
20246+2813	18.1	1.211	4.178	0.145	18.2	1.214	5.260	0.172	000419.5
20280+2631	14.0	0.637	1.069	0.116	15.0	0.699	1.499	0.127	000419.5

TABLE 3.2
List of nondetections

IRAS name	rms (J =1–0 v =1)	rms (J =1–0 v =2)	obs. date
	(K)	(K)	(yymmdd.d)
18392+1328	0.074	0.052	000415.3
18425+1727	0.057	0.041	000415.3
18462+1208	0.069	0.045	000417.3
18490+1158	0.044	0.030	000417.3
18501+1019	0.091	0.069	000415.4
18512+2029	0.091	0.069	000415.4
18520+1014	0.067	0.050	000417.3
18526+0945	0.060	0.053	000418.3
18554+1333	0.050	0.055	000525.2
18563+2319	0.060	0.062	000526.0
18568+1814	0.056	0.049	000426.3
18578+0951	0.062	0.053	000418.3
18588+1400	0.074	0.065	000419.4
19005+0843	0.072	0.057	000419.3
19007+1652	0.050	0.053	000527.0
19012+1128	0.065	0.052	000418.3
19025+0702	0.075	0.062	000421.3
19026+1300	0.041	0.037	000426.3
19029+0808	0.074	0.050	010212.3
19035+1010	0.068	0.057	000418.3
19039+1733	0.047	0.046	000527.2
19041+1734	0.062	0.054	000422.4
19061+1041	0.057	0.048	000425.3
19099+1145	0.048	0.043	000427.3
19102+1356	0.063	0.063	000527.2
19106+1708	0.060	0.061	000527.2
19112+1439	0.086	0.060	000529.2
19114+0920	0.075	0.066	000424.4
19114+0743	0.060	0.050	000425.3
19131+1551	0.068	0.054	000428.3
19135+0931	0.062	0.057	000420.3
19136+2055	0.080	0.084	000421.4
19140+0652	0.062	0.053	000424.4
19140+1313	0.048	0.052	000530.1
19148+1138	0.080	0.064	000419.4
19159+1744	0.075	0.059	000428.3
19201+1040	0.048	0.051	000530.2
19202+2009	0.070	0.050	000417.4
19206+2121	0.068	0.051	000417.4
19211+1606	0.071	0.049	010212.4
19227+1700	0.070	0.046	010212.4
19236+2003	0.075	0.065	000424.4
19236+2404	0.099	0.079	000421.4
19238+1159	0.059	0.051	000425.4
19244+2015	0.077	0.053	000417.4
19246+1736	0.051	0.057	000529.2
19253+1114	0.043	0.035	000529.2
19263+1810	0.086	0.065	010207.6
19267+0345	0.074	0.050	010212.4
19267+1354	0.050	0.054	000530.2
19268+1904	0.070	0.048	010212.4
19274+1835	0.070	0.047	010212.4
19276+0739	0.084	0.069	000606.9
19276+2158	0.068	0.048	010212.4
19282+2253	0.085	0.061	000603.1
19283+2753	0.061	0.055	000527.3
19285+1808	0.081	0.065	000425.4
19296+2227	0.070	0.049	010212.5
19304+2529	0.073	0.062	000423.4
19315+1807	0.071	0.048	010212.5
19320+2013	0.077	0.049	010212.5
19325+1725	0.067	0.063	000427.4
19325+2346	0.077	0.048	010212.5
19329+2641	0.152	0.121	000420.4
19338+1522	0.050	0.037	010319.4
19339+2408	0.064	0.054	000424.4
19342+2331	0.061	0.049	010319.5
19343+0912	0.078	0.055	010212.6
19344+1921	0.062	0.068	000531.1
19348+2136	0.068	0.044	010213.3
19349+2438	0.070	0.067	000426.4
19351+1922	0.052	0.055	000524.3
19352+2000	0.053	0.060	000524.3
19355+2949	0.069	0.059	000426.4
19360+3442	0.091	0.074	000419.4
19366+2147	0.083	0.058	010212.6
19382+2753	0.083	0.078	000419.4
19394+2959	0.098	0.069	000529.3
19396+1637	0.066	0.043	010213.3
19403+1141	0.050	0.041	010215.4
19410+2800	0.061	0.059	000525.3
19411+2400	0.068	0.044	010213.3
19412+2619	0.051	0.055	000530.2

TABLE 3.2
Continued

IRAS name	rms (J =1–0 v =1)	rms (J =1–0 v =2)	obs. date
	(K)	(K)	(yymmdd.d)
19414+3004	0.063	0.061	000525.3
19415+2832	0.071	0.066	000525.4
19415+2814	0.051	0.045	000527.3
19417+3053	0.095	0.077	000421.4
19417+2930	0.047	0.042	000527.3
19423+1653	0.049	0.063	000530.2
19427+2741	0.082	0.074	000527.4
19427+3034	0.063	0.072	000525.4
19438+0933	0.089	0.078	000428.3
19439+3357	0.052	0.044	000424.4
19450+1556	0.062	0.040	010213.4
19451+3045	0.075	0.066	000426.4
19454+3356	0.071	0.075	000525.4
19457+0832	0.081	0.066	000428.3
19466+1726	0.084	0.062	000417.4
19470+2603	0.041	0.054	010214.3
19485+3235	0.107	0.088	000421.4
19488+1719	0.083	0.063	000529.3
19495+2854	0.062	0.052	000526.3
19500+2239	0.060	0.052	000526.3
19507+3039	0.048	0.040	000428.4
19508+2014	0.063	0.068	000529.3
19509+2930	0.078	0.057	000417.5
19510+1917	0.058	0.066	000529.3
19520+2729	0.056	0.042	010215.3
19524+2957	0.081	0.074	000427.4
19526+2600	0.056	0.046	000428.4
19533+2530	0.053	0.058	000524.3
19534+1757	0.061	0.069	000524.3
19534+2802	0.065	0.060	000526.3
19535+2157	0.039	0.031	000530.2
19537+2850	0.075	0.064	000526.4
19552+3142	0.101	0.085	000421.5
19558+3333	0.109	0.097	000421.5
19563+1725	0.071	0.078	000531.3
19573+3143	0.127	0.102	000415.4
19577+2430	0.137	0.163	000531.3
19579+2926	0.078	0.067	000526.4
19584+2652	0.055	0.042	010215.3
19587+2257	0.091	0.064	000417.5
19588+2541	0.030	0.036	000428.4
19591+1817	0.077	0.058	010214.4
19594+2512	0.053	0.058	000530.3
20004+2955	0.083	0.079	000419.5
20005+2931	0.089	0.084	000426.5
20014+2830	0.074	0.060	000428.5
20015+3019	0.081	0.068	000420.4
20046+2954	0.086	0.097	000428.5
20053+2958	0.088	0.078	000420.4
20056+1834	0.052	0.057	000530.3
20084+2750	0.081	0.069	000526.4
20117+1634	0.055	0.044	010215.3
20127+2430	0.051	0.039	010214.4
20180+3015	0.061	0.062	000524.4
20287+2719	0.088	0.080	000427.5

TABLE 3.3
MSX counterparts of IRAS Sources with large separation.

IRAS name	F_{12}^{iras} Jy	F_{25}^{iras} Jy	MSX name	F_{12}^{msx} Jy	F_{21}^{msx} Jy	sep. (")
19102+1356	5.78	5.71	MSX5C_G047.7990+01.7814	7.501	4.900	37
19140+1313	14.27	13.25	MSX5C_G047.6006+00.6186	27.033	21.611	38
19276+0736	6.36	4.03	MSX5C_G044.2837−04.9539	7.250	5.599	29
19348+2136	50.25	33.37	MSX5C_G057.3350+00.3155	49.489	37.488	25
19509+2930	13.92	13.84	MSX5C_G065.9956+01.1562	26.909	29.816	34

TABLE 3.4
List of Detections

IRAS name	$J=1-0$ V_{lsr}	$J=1-0$ T_a	$v=1$ S	rms	$J=1-0$ V_{lsr}	$J=1-0$ T_a	$v=2$ S	rms	obs. date
	(km s^{-1})	(K)	(K km s^{-1})	(K)	(km s^{-1})	(K)	(K km s^{-1})	(K)	(yymmdd.d)
19102+1356	52.1	0.580	1.403	0.063	52.6	0.521	0.994	0.082	010319.3
19140+0652	27.3	0.366	0.886	0.041	28.3	0.287	0.844	0.052	010319.3
19276+0739	94.9	0.499	3.040	0.055	93.2	0.801	2.391	0.078	010319.3
19348+2136	34.3	0.134	0.831	0.026	34.8	0.123	0.265	0.035	010319.4
19509+2930	−40.0	2.194	5.043	0.132	−39.5	2.765	5.141	0.165	010523.0

TABLE 3.5
IRAS data

IRAS name	l (°)	b (°)	F_{12} Jy	C_{12}	C_{23}	D_L (kpc)	V_{lsr} (km s^{-1})	OH	H_2O	SiO
18392+1328	43.95	8.28	8.968	−0.08	−0.82	4.1	—			
18413+1354	44.56	8.02	225.100	−0.17	−0.85	0.6	−15.4	y[26]	y[5]	y[7]
18423+1616	46.82	8.85	8.255	−0.17	−0.82	3.3	38.4	n[21]		
18425+1727	47.91	9.32	24.970	−0.19	−0.72	1.8	—	n[21]		
18432+1343	44.60	7.51	15.230	−0.13	−0.80	2.7	37.1	n[21]		
18456+1351	44.99	7.05	3.056	−0.14	−0.53	5.9	−17.5	n[21]		
18462+1208	43.52	6.15	8.551	−0.18	−0.98	3.1	—	n[4]		
18490+1158	43.67	5.46	9.061	−0.02	−0.73	4.8	—	y[17]	n[8]	
18498+1014	42.21	4.50	4.449	−0.20	−0.78	4.0	81.2	n[21]		
18501+1019	42.32	4.47	11.230	0.06	−0.57	5.1	—	y[17]	n[8]	
18506+0912	41.38	3.86	8.056	0.02	−0.60	5.6	48.0	y[6]	n[8]	
18511+1141	43.65	4.87	4.288	−0.09	−0.79	5.8	44.9	y[6]	n[8]	
18512+2029	51.60	8.79	36.110	−0.02	−0.80	2.4	—	y[17]	y[8]	
18520+1014	42.45	4.02	9.728	−0.01	−0.83	4.7	—	y[6]	y[3]	
18526+0945	42.10	3.67	5.808	−0.07	−0.65	5.3	—			
18528+1543	47.45	6.35	13.260	−0.09	−0.74	3.3	−17.5			
18530+0817	40.82	2.92	43.750	−0.11	−0.77	1.7	−2.4	n[21]		
18531+1829	49.97	7.51	3.658	−0.15	−0.87	5.2	57.5	n[4]		
18535+0726	40.13	2.42	62.980	0.05	−0.79	2.1	48.9	y[17]	y[3]	n[12]
18545+1040	43.12	3.68	48.200	−0.20	−0.84	1.2	51.9	n[21]		
18547+1254	45.14	4.65	7.993	−0.09	−0.69	4.2	33.0			
18549+0905	41.76	2.86	22.920	−0.09	−0.75	2.5	20.8	y[6]	y[3]	
18554+1333	45.79	4.80	4.667	−0.07	−0.71	5.9	—	y[6]	n[8]	
18556+0811	41.04	2.29	103.500	−0.09	−0.92	1.2	37.1	y[6]	y[3]	
18556+1409	46.36	5.01	5.722	−0.09	−0.60	5.0	87.8	y[6]	n[8]	
18563+0816	41.18	2.18	5.345	0.15	−0.55	8.3	13.3	y[6]	n[8]	
18563+2319	54.69	8.97	3.471	−0.16	−0.73	5.2	—	n[21]		
18567+1046	43.47	3.24	18.670	−0.10	−0.75	2.7	0.3	y[4]	n[8]	
18568+1814	50.15	6.61	7.676	−0.20	−0.74	3.1	—	n[21]		
18578+0951	42.78	2.58	16.900	−0.08	−0.67	3.0	—			
18581+1405	46.58	4.45	5.181	−0.11	−0.65	5.0	124.2	y[29]	n[8]	
18585+0900	42.09	2.05	56.840	0.05	−0.64	2.2	76.4	y[6]	n[8]	
18588+1400	46.58	4.28	18.380	0.02	−0.83	3.7	—	y[6]	n[8]	
18590+2025	52.35	7.13	4.458	−0.12	−0.63	5.2	70.1	n[4]		
18592+1455	47.45	4.60	37.650	−0.17	−0.76	1.5	0.4		y[8]	
19005+0843	42.06	1.46	17.380	0.08	−0.56	4.2	—	n[4]		
19007+1652	49.34	5.16	4.301	−0.07	−0.80	6.1	—	y[6]	y[8]	
19008+0907	42.47	1.58	7.610	−0.04	−0.64	5.0	11.5	y[4]	y[8]	
19010+1307	46.03	3.39	7.741	0.16	−0.67	6.9	59.9	y[6]	y[8]	
19012+1128	44.59	2.58	6.920	−0.14	−0.69	3.9	—	y[4]	y[8]	
19023+0745	41.42	0.64	11.080	0.16	−0.57	5.8	33.1	y[6]	n[8]	
19024+1923	51.78	5.96	21.670	−0.08	−0.79	2.6	27.3	y[6]	n[8]	
19025+0702	40.80	0.24	20.400	0.09	−0.54	4.0	—	n[4]		
19026+1300	46.11	2.99	3.557	0.10	−0.53	9.6	—	y[4]	n[8]	
19029+2305	55.16	7.53	6.406	−0.17	−0.69	3.7	−22.4	n[4]		
19029+0808	41.83	0.67	80.550	−0.11	−0.54	1.3	—	n[4]		
19029+0933	43.09	1.32	18.180	−0.06	−0.54	3.1	60.0	y[6]	n[8]	
19032+1715	49.96	4.81	17.190	−0.15	−0.77	2.4	−17.4	n[4]		
19035+1010	43.69	1.48	7.560	0.01	−0.55	5.6	—	y[4]	n[8]	
19039+1733	50.30	4.80	3.919	−0.17	−0.59	4.7	—	n[4]		
19039+1634	49.44	4.35	5.180	−0.10	−0.73	5.1	59.4	n[4]		
19041+0952	43.50	1.21	13.490	0.02	−0.80	4.3	65.4	y[6]	n[8]	
19041+1734	50.35	4.76	6.301	−0.19	−0.72	3.5	—	y[4]	y[8]	
19043+1009	43.78	1.30	54.770	−0.01	−0.71	2.0	46.7	y[17]	y[3]	
19044+0833	42.36	0.54	13.140	0.02	−0.56	4.4	32.4	n[4]		
19047+1539	48.69	3.76	10.590	−0.03	−0.73	4.3	96.6			
19052+0922	43.19	0.74	24.780	−0.12	−0.55	2.2	44.2	y[4]	y[8]	
19061+1041	44.46	1.16	9.484	0.05	−0.63	5.4	—	y[6]	y[3]	
19065+1444	48.09	2.94	4.073	−0.06	−0.90	6.5	5.2			
19068+1127	45.22	1.36	18.150	0.03	−0.76	3.8	9.2	y[6]	y[8]	
19071+0625	40.79	−1.06	15.520	−0.03	−0.81	3.6	91.2			
19079+1143	45.58	1.24	10.410	−0.04	−0.91	4.3	38.6	y[6]	n[8]	
19083+0851	43.08	−0.19	41.600	−0.06	−0.76	2.0	56.8	n[17]	y[8]	
19087+1413	47.88	2.22	9.513	−0.04	−0.74	4.5	36.4	n[4]		
19088+1129	45.47	0.94	15.650	−0.07	−1.02	3.2	33.7	y[6]	y[3]	
19099+1145	45.84	0.83	6.900	−0.11	−0.51	4.3	—	n[21]		
19102+1356	47.79	1.79	5.784	−0.01	−0.73	6.1	—			
19106+1708	50.68	3.18	4.080	−0.16	−0.61	4.8	—	n[21]		
19108+1310	47.18	1.29	5.331	−0.11	−0.53	4.9	54.7	n[21]		
19112+1439	48.55	1.91	4.444	−0.05	−0.52	6.4	—			
19114+0920	43.87	−0.63	9.900	0.00	−0.57	4.8	—	n[21]		
19114+0743	42.43	−1.39	10.610	−0.19	−0.68	2.7	—	n[4]		
19128+1310	47.41	0.87	11.280	0.18	−0.51	5.8	59.7	y[6]	n[8]	
19131+1551	49.81	2.06	25.820	0.06	−0.52	3.4	—	n[4]		
19135+0931	44.27	−0.99	233.700	−0.07	−0.78	0.8	—	n[4]		
19136+2055	54.35	4.32	6.242	0.18	−0.54	7.8	—			
19140+0652	41.98	−2.36	8.376	0.12	−0.61	6.4	—	y[6]	n[8]	
19140+1313	47.59	0.63	14.270	−0.03	−0.60	3.7	—			
19147+1349	48.21	0.77	23.070	−0.06	−0.77	2.7	25.0	y[4,17]	n[8]	

TABLE 3.5
Continued.

IRAS name	l (°)	b (°)	F_{12} Jy	C_{12}	C_{23}	D_L (kpc)	V_{lsr} (km s^{-1})	OH	H_2O	SiO
19148+1138	46.30	−0.29	11.210	0.03	−0.73	4.8	—	n[4]		
19149+1638	50.71	2.05	14.480	0.01	−0.68	4.1	43.0	y[4]	n[8]	
19159+1744	51.80	2.36	3.452	0.01	−0.61	8.3	—	n[21]		
19160+0755	43.14	−2.30	7.451	0.12	−0.60	6.8	42.2	y[6]	y[3]	
19161+2343	57.12	5.12	112.200	0.09	−0.65	1.7	24.7	y[26]	y[3]	
19167+1733	51.72	2.09	12.460	−0.07	−0.90	3.6	37.2	y[6]	n[8]	
19175+0958	45.13	−1.65	6.559	0.05	−0.87	6.5	48.1	y[6]	y[8]	
19176+1939	53.68	2.91	8.604	−0.04	−0.59	4.7	54.2	y[27]	n[8]	
19186+1657	51.41	1.42	36.280	−0.09	−0.54	2.0	74.0		n[8]	
19187+2221	56.18	3.95	4.808	−0.16	−0.64	4.4	−13.6		n[8]	
19190+3035	63.55	7.72	5.337	0.13	−0.70	8.1	0.7	y[6]	n[8]	
19190+1128	46.63	−1.28	27.130	0.13	−0.55	3.6	57.9	y[17,6]	n[8]	
19192+0922	44.80	−2.31	127.200	0.09	−0.57	1.6	−70.9	y[4]		y[23]
19195+1747	52.24	1.63	24.240	−0.13	−0.82	2.2	35.3	y[4]	n[8]	
19195+0522	41.31	−4.27	16.160	−0.02	−0.72	3.6	−18.1	y[17]	n[8]	
19201+1040	46.05	−1.88	6.708	0.17	−0.52	7.5	—	y[4]	n[8]	
19202+2009	54.41	2.60	13.620	−0.01	−0.81	4.0	—	n[17]		
19206+2255	56.90	3.83	7.208	−0.14	−0.81	3.8	−34.1	n[21]	y[8]	
19206+2121	55.51	3.08	10.350	−0.11	−0.75	3.5	—	y[4]		
19206+2517	58.98	4.93	5.332	−0.14	−0.83	4.5	33.6	y[6]	n[8]	
19211+1606	50.95	0.49	27.180	−0.11	−0.59	2.2	—	n[4]		
19212+1843	53.27	1.70	9.550	−0.19	−0.67	2.8	14.0	n[21]		
19213+0340	40.02	−5.46	13.160	−0.19	−0.84	2.4	23.4	n[21]		
19214+0513	41.40	−4.77	6.905	0.00	−0.59	5.8	10.0	y[6]	y[8]	
19227+1700	51.93	0.58	52.020	0.18	−0.62	2.7	—	n[17]	y[19]	
19229+1708	52.07	0.59	46.080	−0.11	−0.67	1.7	42.0		y[8]	
19231+3555	68.74	9.39	111.900	−0.09	−0.84	1.1	−23.4		n[8]	
19236+2003	54.70	1.85	15.240	−0.09	−0.55	3.1	—	n[4]		
19236+2404	58.24	3.77	7.788	−0.17	−0.74	3.4	—	n[21]		
19236+1359	49.37	−1.06	19.910	0.03	−0.54	3.6	35.2	n[4]		
19237+1430	49.85	−0.83	18.490	0.09	−0.74	4.2	76.8	y[6]	n[8]	
19238+1159	47.64	−2.07	53.030	0.05	−0.50	2.3	—	n[21]		
19240+3615	69.12	9.39	97.390	−0.08	−0.86	1.2	38.0			
19244+1809	53.13	0.78	25.890	−0.12	−0.83	2.2	44.4	n[4]		
19244+2015	54.96	1.78	10.240	0.04	−0.55	5.1	—	n[4]		
19246+1736	52.67	0.47	16.840	0.04	−0.60	4.0	—	n[4]		
19252+2201	56.61	2.47	65.210	−0.14	−0.82	1.3	−19.6	n[21]		
19253+1114	47.16	−2.74	3.936	0.01	−0.81	7.8	—	y[6]	n[8]	
19259+0510	41.87	−5.76	8.931	−0.20	−0.85	2.8	12.1	n[25]	y[8]	
19263+1810	53.36	0.39	17.410	−0.12	−0.58	2.6	—	n[4]		
19264+1132	47.55	−2.83	19.040	−0.15	−0.83	2.3	−29.4	n[4]		
19265+3116	64.91	6.60	7.326	−0.15	−0.74	3.7	35.5	n[11]	y[8]	
19267+0345	40.72	−6.60	44.730	−0.18	−0.90	1.4	—	n[21]		
19267+1354	49.66	−1.75	3.072	−0.17	−0.54	5.3	—	n[4]		
19268+1904	54.21	0.71	13.840	−0.13	−0.52	2.9	—	n[4]		
19270+2239	57.36	2.39	41.260	−0.14	−0.91	1.6	8.8	n[21]		
19271+1354	49.72	−1.85	29.820	−0.18	−0.78	1.7	51.0	y[4]	y[8]	
19274+1835	53.85	0.36	34.450	−0.11	−0.78	1.9	—	n[21]	y[20]	
19276+1500	50.73	−1.41	8.732	−0.02	−0.73	4.9	43.1		y[8]	
19276+0739	44.28	−4.95	6.360	−0.20	−0.58	3.4	—		n[8]	
19276+2158	56.84	1.94	11.230	−0.11	−0.55	3.4	—	n[4]		
19282+2253	57.70	2.28	19.340	−0.08	−0.67	2.8	—	n[4]		
19283+1421	50.25	−1.88	15.200	0.00	−0.78	3.9	−5.0	y[18]		
19283+2753	62.11	4.65	4.028	−0.02	−0.73	7.2	—	n[21]		
19285+1808	53.59	−0.10	41.830	−0.15	−0.59	1.5	—			
19288+2923	63.48	5.28	40.430	0.15	−0.62	3.0	−37.6	y[6]	y[3]	y[23]
19290+1600	51.78	−1.23	8.339	−0.18	−0.54	3.1	55.8	y[4]	n[8]	
19291+0502	42.14	−6.53	23.770	−0.20	−0.77	1.7	−4.59	y[4]	y[8]	
19296+2227	57.48	1.78	31.730	0.12	−0.50	3.3	—	n[21]	y[22]	
19303+1553	51.82	−1.56	10.540	−0.03	−0.83	4.3	8.72	y[6,27]	y[8,3]	
19304+2529	60.23	3.09	37.090	0.13	−0.59	3.1	—	n[21]		
19305+2410	59.08	2.43	22.120	−0.19	−0.79	1.9	22.6	y[4]	y[8]	
19307+1338	49.89	−2.73	83.070	−0.10	−0.87	1.3	43.5	n[21]	y[20]	
19309+2022	55.81	0.50	13.130	−0.18	−0.90	2.5	45.5	n[4]		
19312+1130	48.09	−3.87	9.948	−0.12	−0.77	3.5	66.1	y[4,27,25]	y[8]	
19315+1807	53.91	−0.72	16.720	−0.08	−0.52	3.0	—	n[4]		
19320+2013	55.80	0.20	14.040	−0.04	−0.72	3.7	—	n[4]		
19323+2103	56.56	0.56	10.540	−0.10	−0.57	3.6	12.9	n[4]		
19325+1725	53.42	−1.26	13.750	0.10	−0.59	4.9	—			
19325+2346	58.96	1.83	44.050	−0.13	−0.63	1.6	—	n[21]	y[20]	
19329+2641	61.55	3.19	55.900	−0.19	−0.89	1.2	—	n[21]		
19333+1918	55.15	−0.51	24.590	−0.07	−0.64	2.6	−21.9	y[4,17]	y[8]	
19338+1522	51.78	−2.56	8.718	−0.17	−0.92	3.2	—	n[30]		
19339+2408	59.43	1.74	5.242	−0.06	−0.75	5.7	—	n[21]		
19342+2331	58.93	1.37	7.350	−0.19	−1.05	3.2	—	n[4]		
19343+0912	46.44	−5.67	10.200	−0.10	−0.78	3.6	—	y[27]	n[8]	
19344+1921	55.32	−0.71	10.350	−0.17	−0.60	2.9	—	n[4]		
19344+2114	56.96	0.21	7.179	−0.01	−0.64	5.5	38.7			

TABLE 3.5
Continued.

IRAS name	l (°)	b (°)	F_{12} Jy	C_{12}	C_{23}	D_L (kpc)	V_{lsr} (km s^{-1})	OH	H_2O	SiO
19347+2755	62.81	3.44	8.859	0.09	−0.77	6.0	27.9	y[6]	n[8]	
19348+2136	57.33	0.32	50.250	−0.18	−0.78	1.3	—	n[21]		
19349+2438	59.98	1.79	5.158	−0.16	−0.78	4.3	—	n[21]		
19349+1657	53.29	−2.01	10.570	−0.06	−0.90	4.0	12.5			
19351+1922	55.41	−0.85	14.950	−0.09	−0.68	3.1	—	n[4]		
19352+1914	55.31	−0.94	11.750	−0.03	−0.69	4.1	−12.7	y[4]	y[8]	
19352+2000	55.98	−0.57	12.650	−0.13	−0.68	3.0	—	n[4]		
19355+2949	64.57	4.20	5.264	−0.19	−0.66	3.8	—	n[21]		
19360+3442	68.91	6.50	7.043	0.18	−0.65	7.4	—	y[6]	n[8]	
19361+1805	54.42	−1.68	3.237	−0.05	−0.53	7.4	23.8	n[4]		
19366+2147	57.69	0.04	14.120	−0.18	−0.55	2.4	—	n[4]		
19371+2855	63.95	3.48	50.390	−0.11	−0.81	1.6	24.3	y[4]	y[8]	
19374+0550	43.85	−7.95	155.200	−0.13	−0.87	0.9	−17.2	n[21]	y[31]	n[13]
19382+2753	63.17	2.75	10.220	−0.17	−0.62	2.9	—	n[4]		
19382+3400	68.51	5.76	7.517	−0.08	−0.86	4.5	4.6	y[21]		
19386+1513	52.22	−3.63	38.160	−0.06	−0.87	2.1	1.24	y[6]	y[8,12,3,28,10]	y[12]
19387+1527	52.44	−3.54	6.479	0.08	−0.73	6.9	59.8	y[6]	y[8]	n[12]
19393+2447	60.61	0.99	12.940	−0.10	−0.66	3.2	18.4	n[4,11,25]		
19394+2959	65.14	3.56	6.008	0.05	−0.61	6.8	—	n[21]		
19395+1827	55.13	−2.20	8.346	−0.09	−0.64	4.1	−0.5	n[29]	n[8]	
19395+1949	56.32	−1.52	9.834	−0.07	−0.67	4.0	43.0	y[21]	n[8]	
19396+1637	53.57	−3.15	119.100	−0.16	−0.94	0.9	—	n[21,24]	n[24]	n[1]
19399+2258	59.10	−0.02	16.980	−0.08	−0.57	3.0	−4.0	n[4]		
19403+1141	49.34	−5.73	8.903	−0.12	−1.00	3.7	—	n[21]		
19405+2938	64.94	3.18	3.195	−0.17	−0.61	5.2	10.7	n[4]		
19410+2700	62.72	1.77	3.571	−0.08	−0.64	6.5	−59.8	n[4]		
19410+2800	63.59	2.27	5.082	−0.20	−0.59	3.8	—	n[4]		
19411+2400	60.13	0.25	15.440	−0.17	−0.53	2.4	—	n[4,11]		
19412+2619	62.15	1.39	6.760	0.10	−0.72	7.0	—			
19413+2829	64.04	2.45	4.257	0.05	−0.69	8.1	26.2	y[21]	n[8]	
19414+2237	58.97	−0.50	21.210	−0.18	−0.89	2.0	49.8	y[6]	n[8]	
19414+3004	65.43	3.23	3.134	−0.14	−0.61	5.8	—	n[4]		
19415+2832	64.09	2.45	3.172	−0.14	−0.54	5.8	—	n[4]		
19415+2814	63.84	2.30	3.753	−0.13	−0.59	5.5	—	n[21]		
19417+3053	66.15	3.58	25.430	−0.11	−0.70	2.2	—	n[4]		
19417+2930	64.96	2.89	3.011	−0.13	−0.53	6.1	—	n[4]		
19422+3506	69.89	5.59	202.900	−0.07	−0.78	0.9	−50.4	y[21]	y[8]	
19423+1653	54.12	−3.57	11.500	−0.19	−0.78	2.6	—	n[4]		
19425+3323	68.42	4.67	30.640	−0.19	−0.91	1.6	9.7	y[4]	y[8]	
19427+2741	63.49	1.79	4.146	−0.19	−0.68	4.3	—	n[21]		
19427+3034	66.00	3.24	14.060	−0.20	−0.77	2.3	—	n[4]		
19438+0933	47.91	−7.53	19.330	0.00	−0.60	3.4	—			
19439+3357	69.05	4.72	8.829	−0.19	−0.89	2.9	—	n[21]		
19448+2653	63.04	0.98	8.794	0.04	−0.59	5.5	1.4	y[21]	n[8]	
19450+1556	53.62	−4.61	21.190	−0.17	−0.75	2.0	—	n[4]		
19451+3045	66.42	2.88	11.880	−0.15	−0.62	2.9	—	n[4]		
19454+2536	62.00	0.21	16.480	−0.12	−0.65	2.7	49.1	y[4]	y[8]	
19454+3356	69.19	4.44	3.251	−0.16	−0.62	5.4	—	n[4]		
19457+0832	47.24	−8.45	16.180	0.06	−0.68	4.2	—			
19459+1716	54.88	−4.11	5.755	0.06	−0.68	7.1	−2.0	y[6]	n[8]	
19459+2815	64.35	1.46	4.299	−0.13	−0.63	5.1	−59.5	n[21]		
19462+2232	59.46	−1.51	18.870	−0.06	−0.75	3.0	12.3	y[11,17,6]	y[8,3]	
19466+1726	55.11	−4.18	3.926	−0.18	−0.81	4.6	—	n[21]		
19470+2603	62.58	0.13	10.930	−0.19	−0.57	2.7	—	n[4]		
19471+2944	65.77	1.99	8.046	−0.03	−0.77	5.0	−43.7	y[21]	y[8]	
19484+1923	57.00	−3.55	7.062	−0.15	−0.91	3.7	82.8	n[21]		
19485+3235	68.37	3.20	29.960	−0.15	−0.73	1.8	—	n[4]		
19488+1719	55.27	−4.70	4.200	0.05	−0.70	8.2	—	y[6]	n[8]	
19493+2905	65.44	1.25	22.340	0.19	−0.76	4.2	−21.8	y[17,6,27]	y[8,12,9,28]	y[12,15,14]
19495+2854	65.31	1.13	3.066	−0.08	−0.74	7.0	—	n[21]		
19495+0835	47.75	−9.24	80.020	−0.09	−0.75	1.3	44.4	y[6]	y[8,3]	
19499+2141	59.17	−2.68	10.390	−0.02	−0.71	4.5	3.3	y[11,17,6]	y[8,3]	
19500+2239	60.01	−2.20	6.476	0.00	−0.75	5.9	—	y[6]	n[8]	
19507+3039	66.95	1.80	3.095	0.02	−0.54	9.0	—	n[21]		
19508+2014	58.03	−3.60	5.141	0.09	−0.84	7.9	—	y[6]	n[8]	
19508+2659	63.83	−0.12	28.120	0.02	−0.71	3.0	5.4	y[17]	y[3]	
19509+2930	65.99	1.16	13.920	0.00	−0.70	4.1	—			
19510+1917	57.24	−4.14	3.851	0.01	−0.55	7.9	—	n[4]		
19519+2527	62.63	−1.13	13.220	−0.09	−0.60	3.3	−14.5	y[11]	y[20]	
19520+2729	64.38	−0.10	17.970	0.18	−0.64	4.6	—	y[6]	y[2]	
19522+1935	57.65	−4.22	29.300	−0.05	−0.74	2.5	68.2	y[6]	y[8,3]	
19524+2957	66.54	1.11	15.030	−0.12	−0.77	2.8	—	n[4]		
19526+2600	63.19	−0.98	4.248	0.08	−0.51	8.5	—	n[21]		
19527+2231	60.22	−2.80	3.075	−0.09	−0.73	6.8	39.3	y[6]	n[8]	
19533+2530	62.84	−1.37	7.376	0.01	−0.54	5.7	—	n[21]		
19534+1757	56.38	−5.30	5.293	0.10	−0.54	7.9	—			
19534+2802	65.02	−0.06	8.530	0.14	−0.59	6.5	—	y[6]	n[8]	n[12]
19535+2157	59.83	−3.25	3.323	−0.17	−0.75	5.1	—	y[4]	y[8]	

TABLE 3.5
Continued.

IRAS name	l (°)	b (°)	F_{12} Jy	C_{12}	C_{23}	D_L (kpc)	V_{lsr} (km s^{-1})	OH	H_2O	SiO
19537+2850	65.74	0.30	15.240	−0.07	−0.69	3.2	—	n[4]		
19542+3120	67.92	1.51	3.748	−0.13	−0.64	5.5	−3.1	n[21]		
19552+3142	68.34	1.52	35.030	−0.20	−0.67	1.4	—	n[4]		
19552+2138	59.77	−3.75	7.158	−0.16	−0.80	3.6	49.8	n[21]		
19558+3333	69.98	2.38	42.940	0.03	−0.57	2.5	—	n[17]		
19563+1725	56.29	−6.16	6.415	−0.15	−0.71	3.9	—	n[21]		
19573+3143	68.59	1.16	19.100	−0.05	−0.68	3.1	—	n[4]		
19577+2430	62.51	−2.74	7.445	−0.17	−0.68	3.4	—	n[4]		
19579+2926	66.71	−0.16	5.602	−0.18	−0.79	3.8	—	y[4]	y[8]	
19583+1323	53.05	−8.67	14.200	−0.19	−0.87	2.3	−24.8	n[4]		
19584+2652	64.60	−1.62	14.270	−0.01	−0.55	3.9	—	n[4,11,17]	n[19]	
19587+2257	61.32	−3.76	3.234	−0.14	−0.78	5.7	—	n[4]		
19588+2541	63.64	−2.32	3.469	0.04	−0.53	8.8	—	y[4]	n[8]	
19591+1817	57.38	−6.29	40.260	−0.12	−0.80	1.7	—	n[4,25]		
19594+2512	63.30	−2.69	3.756	0.05	−0.74	8.6	—	n[4]		
20004+2955	67.43	−0.36	31.720	0.07	−0.90	3.1	—			
20005+2931	67.09	−0.60	10.730	−0.13	−0.77	3.2	—	n[4]		n[16]
20005+1635	56.10	−7.47	5.534	−0.12	−0.71	4.7	−6.4	n[4]		
20010+3011	67.72	−0.34	58.180	−0.15	−0.68	1.3	21.1	n[4]		
20014+2830	66.33	−1.31	24.070	−0.15	−0.53	2.0	—	n[4]		
20015+3019	67.90	−0.37	162.200	−0.14	−0.65	0.8	—	y[4]	y[8]	
20024+1727	57.08	−7.39	60.990	0.00	−0.81	1.9	−1.9	y[6]	y[8]	
20046+2954	67.90	−1.15	11.470	−0.20	−0.73	2.5	—	n[4]		
20053+2958	68.03	−1.23	11.500	−0.10	−0.65	3.4	—	n[4]		n[16]
20056+1834	58.44	−7.46	17.520	0.01	−0.52	3.7	—	n[17]		
20084+2750	66.62	−2.98	9.734	−0.09	−0.71	3.8	—			y[16]
20095+2726	66.42	−3.38	28.830	−0.04	−0.71	2.6	12.4	y[17]	n[8]	
20117+1634	57.53	−9.75	10.600	−0.15	−0.55	3.1	—	n[21]		
20118+3107	69.77	−1.77	5.258	−0.11	−0.59	4.9	−6.9	n[21]		
20127+2430	64.36	−5.62	17.400	−0.05	−0.87	3.2	—	y[4,11,6]	n[8]	
20156+2130	62.21	−7.82	20.360	−0.13	−0.67	2.4	21.4	n[11,25]	n[8]	
20171+2732	67.44	−4.73	15.370	−0.03	−0.64	3.6	48.0	y[17]	y[3]	
20180+3015	69.80	−3.36	4.125	−0.17	−0.66	4.6	—	n[4]		
20181+2234	63.44	−7.72	25.620	0.11	−0.69	3.6	40.6	y[17,6]	y[28]	n[12]
20246+2813	68.97	−5.71	13.560	−0.07	−0.85	3.4	18.1	y[6]	y[3]	y[16]
20280+2631	68.00	−7.30	17.000	0.06	−0.80	4.1	14.5	y[17]	y[8]	
20287+2719	68.74	−6.97	7.199	−0.14	−0.81	3.8	—	n[21]		

References. – 1. Allen et al. (1989); 2. Benson and Little-Marenin (1996); Cesaroni et al. (1988);
4. Chengalur et al. (1993); 5. Comoretto et al. (1990); 6. Eder et al. (1988);
7. Engels and Heske (1989); 8. Engels and Lewis (1996); 9. Engels et al. (1986);
10. Engels et al. (1988); Galt et al. (1989); 12. Gomez et al. (1990);
13. Hall et al. (1990); Jewell et al. (1991); 15. Jewell et al. (1985);
16. Jiang et al. (1999); 17. Le Squeren et al. (1992); 18. Lewis (1994);
19. Lewis and Engels (1993); 20. Lewis and Engels (1995); 21. Lewis et al. (1990);
22. Marvel and Boboltz (1999); 23. Nyman et al. (1998); 24. Seaquist et al. (1995);
25. Sivagnanam et al. (1990); Slootmaker et al. (1985); 27. te Lintel Hekkert et al. (1991);
28. te Lintel Hekkert et al. (1989); 29. Lewis (1997); 30. Lewis (1987);
31. Takaba et al. (2000)

References

[Allen et al.(1989)] Allen, D. A., Hall, P. J., Norris, R. P., Troup, E. R., Wark, R. M., and Wright, A. E. 1989, MNRAS, 236, 363

[Anglada et al.(1996)] Anglada, G., Estalella, R., Pastor, J., Rodríguez, L. F., and Haschick, A. D. 1996, ApJ, 463, 205

[Beichman et al.(1988)] Beichman, C. A., Neugebauer, G., Habing, H. J., Clegg, P. E., Chester, T. J. 1988, IRAS Catalogs and Atlases, I. Explanatory Supplement, NASA RP-1190 (US Goverment Printing Office, Washinton) pVII-22

[Benson and Little-Marenin(1996)] Benson, P. J., and Little-Marenin, I. R. 1996, ApJS, 106, 579

[Boboltz and Marvel(2000)] Boboltz, D. A. and Marvel, K. B. 2000, ApJL, 545, 149

[Cesaroni et al.(1988)] Cesaroni, R., Palagi, F., Felli, M., Catarzi, M., Comoretto, G., di Franco, S., Giovanardi, C., and Palla, F. 1988, A&ApS, 76, 445

[Chakravarti et al(1967)] Chakravarti, I. M., Laha, R. G., and Roy, J. 1967, Handbook of methods of applied statistics (Wiley, New York), p.392

[Chengalur et al.(1993)] Chengalur, J. N., Lewis, B. M., Eder, J., and Terzian, Y. 1993, ApJS, 89, 189

[Comoretto et al.(1990)] Comoretto, G., Plagi, f., Cesaroni, R., Felli, M., Bettarini, A., Catarzi, M., Curioni, G. P., Curioni, P., di Franco, S., Giovanardi, C., Massi, M., Palla, F., Panella, D., Rossi, E., Speroni, N., and Tofani, G. 1990, A&ApS, 84, 179

[Dame et al.(1987)] Dame, T. M., Ungerechts, H., Cohen, R. S., de Geus, E. J., Grenier, I. A., May, J., Murphy, D. C., Nyman, L. -å. and Thaddeus, P. 1987, ApJ, 322, 706

[Deguchi et al.(2000a)] Deguchi, S., Fujii, T., Izumiura, H., Kameya, O., Nakada, Y., and Nakashima, J. 2000a, ApJS, 130, 351

[Deguchi et al.(2000b)] Deguchi, S., Fujii, T., Izumiura, H., Kameya, O., Nakada, Y., Nakashima, J., Ootsubo, T., and Ukita, N. 2000b, ApJS, 128, 571

[Deguchi et al.(2001)] Deguchi, S., Fujii, T., Matsumoto, S., Nakashima, J., and Wood, P. R. 2001, PASJ, in printing

[Eder et al.(1988)] Eder, J., Lewis, B. M., and Terzian, Y. 1988, ApJS, 66, 183

[Engels and Heske(1989)] Engels, D., and Heske, A. 1989, A&ApS, 81, 323

[Engels and Lewis(1996)] Engels, D., and Lewis, B. M. 1996, A&ApS, 116, 117

[Engels et al.(1986)] Engels, D., Schmid-Burgk, J., and Walmsley, C. M. 1986, A&Ap, 167, 129

[Engels et al.(1988)] Engels, D., Schmid-Burgk, J., and Walmsley, C. M. 1988, A&Ap, 191, 283

[Evans and Little-Marenin(1999)] Evans, T. L., and Little-Marenin, I. R. 1999, MNRAS, 304, 421

[Frink et al.(1996)] Frink, S., Fuchs, B., Roeser, S., and Wielen, R. 1996, A&Ap, 314, 430

[Galt et al.(1989)] Galt, J. A., Kwok, S., and Frankow, J. 1989, AJ, 98, 2182

[Gledhill et al.(2001)] Gledhill, T. M., Chrysostomou, A., Hough, J. H., and Yates, J. A. 2001, MNRAS, 322, 321

[Gomez et al.(1990)] Gomez, Y., Moran, J. M., and Rodriguez, L. F. 1990, Rev. Mex. Astron. Astrofis., 20, 55

[Groenewegen et al.(1994)] Groenewegen, M. A. T., de Jong, T., and Geballe, T. R. 1994, A&Ap, 287, 163

[Groenewegen and Jong(1998)] Groenewegen, M. W. T., and de Jong, T. 1998, A&Ap, 337, 797

[Habing(1987)] Habing, H. J. 1987, in The Galaxy, ed. G. Gilmore & B. Caswell (Dordrecht: Reidel), 173

[Hall et al.(1990)] Hall, P. J., Wright, A. E., Troup, E. R., Wark, R. M., and Allen, D. A. 1990, MNRAS, 247, 549

[Heske et al.(1990)] Heske, A., Forveille, T., Omont, A., van der Veen, W. E. C J., and Habing, H. J. 1990, A&Ap, 239, 173

[Ivezić and Elitzur(1995)] Ivezić, Z., and Elitzur, M. 1995, ApJ, 445, 415

[Izumiura et al.(1999)] Izumiura, H., Deguchi, S., Fujii, T., Kameya, O., Matsumoto, S., Nakada, Y., Ootsubo, T., and Ukita, N. 1999, ApJS, 125, 257

[Izumiura et al.(1994)] Izumiura, H., Deguchi, S., Hashimoto, O., Nakada, Y., Onaka, T., Ono, T., Ukita, N., and Yamamura, I. 1994, ApJ, 437, 419

[Izumiura et al.(1995)] Izumiura, H., Deguchi, S., Hashimoto, O., Nakada, Y., Onaka, T., Ono, T., Ukita, N., and Yamamure, I. 1995, ApJ, 453, 837

[Jewell et al.(1991)] Jewell, P. R., Snyder, L. E., Walmsley, C. M., Wilson, T. L., and Gensheimer, P. D. 1991, A&Ap, 242, 211

[Jewell et al.(1985)] Jewell, P. R., Walmsley, C. M., Wilson, T. L., and Snyder, L. E. 1985, ApJL, 298, 55

[Jiang et al.(1997)] Jiang, B. W., Deguchi, S., Hu, J. Y., Yamamura, I., Nishihara, E., Matsumoto, S., and Nakada, Y. 1997, AJ, 113, 1315

[Jiang et al.(1999)] Jiang, B. W., Deguchi, S., Ramesh, R. 1999, PASJ, 51, 95

[Jiang et al.(1996)] Jiang, B. W., Deguchi, S., Yamamura, I., Nakada, Y., Cho, S. H., and Yamagata, T. 1996, ApJS, 106, 463

[Jura and Kleinmann(1989)] Jura, M., and Kleinmann, S. G. 1989, ApJ, 341, 359

[Jura and Kleinmann(1990)] Jura, M., and Kleinmann, S. G. 1990, ApJ, 364, 663

[Kerr and Lynden-Bell(1986)] Kerr, F. J., and Lynden-Bell, D. 1986, MNRAS, 221, 1023

[Le Squeren et al.(1992)] Le Squeren, A. M., Sivagnanam, P., Dennefeld, M., and David, P. 1992, A&Ap, 254, 133

[Lewis(1994)] Lewis, B. M. 1994, ApJS, 93, 549

[Lewis(1997)] Lewis, B. M. 1997, ApJS, 109, 489

[Lewis(1987)] Lewis, B. M., Eder, J., and Terzian, Y. 1987, AJ, 94, 1025

[Lewis and Engels(1993)] Lewis, B. M., and Engels, D. 1993, MNRAS, 265, 161

[Lewis and Engels(1995)] Lewis, B. M., and Engels, D. 1995, MNRAS, 274, 439

[Lewis et al.(1990)] Lewis, B. M., Eder, J., and Terzian, Y. 1990, ApJ, 362, 634

[Loup et al.(1993)] Loup, C., Forveille, Omont, A., and Paul, J. F. 1993, A&ApS, 99, 291

[Margulis et al.(1990)] Margulis, M., van Blerkom, D. J., Snell, R. L., and Kleinmann, S. G. 1990, ApJ, 361, 637

[Marvel and Boboltz(1999)] Marvel, K. B., and Boboltz, D. A., AJ, 1999, AJ, 118, 1791

[Menzies and Whitelock(1988)] Menzies, J. W., and Whitelock, P. A. 1988, MNRAS, 233, 697

[Meixner et al.(1999)] Meixner, M., Uete, T., Dayal, A., Hora, H. L, Fazio, G., Hrivnak, B. J., Skinner, C. J., and Hoffmann, W. F. 1999, ApJ, 122, 221

[Nakada et al.(1993)] Nakada, Y., Onaka, T., Yamamura, I., Deguchi, S., Ukita, N., and Izumiura, H. 1993, PASJ, 45, 179

[Nakashima and Deguchi(2000)] Nakashima, J., and Deguchi, S. 2000, PASJ, 52, L43

[Nakashima et al.(2001)] Nakashima, J., Deguchi, S., Fujii, T., Izumiura, H., Kameya, O., and Nakada, Y. 2001, ApJ,(submitted to ApJ)

[Nakashima et al.(2000)] Nakashima, J., Jiang, B. W., Deguchi, S., Sadakane, K., and Nakada, Y. 2000, PASJ, 52, 275

[Nyman et al.(1998)] Nyman, L. -Å., Hall, P. J., and Olofsson, H. 1998, A&ApS, 127, 185

[Olnon and Raimond(1986)] Olnon, F. M., Rainmond, E., and the IRAS Science Team, 1986, A&ApS, 65, 607

[Price et al.(1997)] Price, S. D., Egan, M. P., Shipman, R. F., Tedesco, E. F., Cohen, M., Walker, R. G., and Moshir, M. 1997, BAAS, 29, 1294

[Seaquist and Ivison(1994)] Seaquist, E. R., and Ivison, R. J. 1994, MNRAS, 269, 512

[Seaquist et al.(1995)] Seaquist, E. R., Ivison, R. J., and Hall, P. J., 1995, MNRAS, 276, 867

[Sevenster et al.(1997)] Sevenster, M. N., Chapman, J. M., Habing, H. J., Killeen, N. E. B., and Lindqvist, M. 1997, A&ApS, 122,79

[Sivagnanam et al.(1990)] Sivagnanam, P., Braz, M. A., Le Squeren, A. M., and Tranminh, F. 1990, A&Ap, 233, 112

[Slootmaker et al.(1985)] Slootmaker, A., Herman, J., and Habing, H. J. 1985, A&ApS, 59, 465

[Stephenson(1990)] Stephenson, C. B. 1990, AJ, 100, 569

[Takabe et al.(2000)] Takabe, H., Iwata, T., Miyaji, T., and Deguchi, S. 2000, PASJ, 53, 517

[Taylor and Cordes(1993)] Taylor, J. H., Cordes, J. M. 1993, ApJ, 411, 674

[te Lintel Hekkert et al.(1991)] te Lintel Hekkert, P., Caswell, J. L., Habing, H. J., Haynes, R. S., Haynes, R. F., and Norris, R. P. 1991, A&ApS, 90, 327

[te Lintel Hekkert et al.(1989)] te Lintel Hekkert, P., Versteege-Hansel, H. A., Habing, H. J., and Wiertz, M. 1989, A&ApS, 78, 399

[Trammell et al.(1994)] Trammell, S. R., Dinerstein, H. L., and Goodrich, R. W. 1994 AJ, 108, 984

[van der Veen and Breukers(1989)] van der Veen, W. E. C. J., Breukers, R. J. L. H. 1989, A&Ap, 212, 133

[van der Veen and Habing(1988)] van der Veen, W. E. C. J., and Habing, H. J. 1988, A&Ap, 194, 125

[van der Veen and Habing(1990)] van der Veen, W. E. C. J., and Habing, H. J. 1990, A&Ap, 231, 404

[van Langevelde et al.(1990)] van Langevelde, H. J., van der Heiden, R., and van Schooneveld, C. 1990, A&Ap, 239, 193

[Volk and Cohen(1989)] Volk, K., and Cohen, M. 1989, AJ, 98, 931

[Volk et al.(1992)] Volk, K., Kwok, S., and Langill, P. P. 1992, ApJ, 391, 285

[Walker et al.(1997)] Walker, H. J., Tsikoudi, V., Clayton, C. A., Geballe, T., Wooden, D. H., and Butner, H. M. 1997, A&Ap, 323, 442

Chapter 4

SiO Maser Survey of Cold IRAS Sources: A Search for Proto-Planetary Nebulae

Abstract

We present the results of observations of cold IRAS sources in the Galactic disk area, $-10° < l < 120°$ and $|b| < 5°$, in the SiO $J = 1$–0, $v = 1$ and 2 maser lines. SiO masers were detected in 51 out of 143 observed sources; 45 are new detections in SiO. The selected IRAS sources were cold objects with dust temperatures between 150 and 260 K. The Asymptotic Giant Branch (AGB) stars and protoplanetary objects are involved in this color range. In addition, young stellar objects in star forming regions, however, contaminate this sample; approximately 20% of the selected objects are considered to be young stellar objects (or dusty HII regions). Detections of SiO masers confirmed that a considerable percentage of the selected objects are AGB or post-AGB stars. Among these new detections, three were well known candidate proto-planetary nebulae: IRAS 18450−0148 (W43A), 18498−0017, and 19312+1950. We also found that the intensity ratios of the SiO $J = 1$–0, $v = 2$ to the $v = 1$ line of the objects correlate with the IRAS colors. The detection rate of SiO masers tends to increase toward the Galactic center as in the cases of previous SiO maser surveys for typical AGB stars. Any strong associations of the objects to the spiral arms were not found. The radial-velocity dispersion of the present sample is comparable with the dispersion of the SiO maser sample of typical AGB stars. These facts suggest that the present sample of cool IRAS sources with SiO masers has a kinematic property very similar to that of typical AGB stars.

4.1 Introduction

The nature of cold IRAS point sources ($T_{dust} \sim 100$–280 K) spreading in the Galactic plane is not well understood (te Lintel Hekkert 1991). They are very often identified to evolved stars with a thick dusty envelope, or young stellar objects in star forming regions, and are occasionally to dusty HII regions accompanying hot stars (van der Veen and Habing 1988). Because all of these objects have thick dust envelopes, they are rarely seen at optical wavelengths. Because they exhibit very similar colors, it is difficult to distingiush the evolved stars from young stellar objects solely from IRAS color indices (e.g., van der Veen et al. 1989). In addition, because considerable percentages of the IRAS 60 μm flux densities of the Bulge AGB stars near the galactic plane were found to be contamination by dust emission from surrounding interstellar clouds (Izumiura et al. 1999; Deguchi et al. 2000a), the color index, C_{23} (a logarithmic ratio of IRAS 60 to 25 μm flux density), may not effectively be used to identify the AGB/post-AGB stars among these cold objects.

Mass-losing O-rich AGB stars very often exhibit maser emission; OH / H_2O / SiO maser lines have been used to identify evolved objects among cold IRAS sources (Likkel 1989; te Lintel Hekkert 1991a; Silva et al. 1993; Nyman et al. 1998). However, it has been found in the past SiO maser surveys that the detection rate of SiO masers are highest for objects with $C_{12} \sim 0$ ($T_{dust} = 300$K) and the rate drops quickly in $|C_{12}| > 0.2$ ($T_{dust} = 280$K, Jiang et al. 1995), where C_{12} is a logarithmic ratio of IRAS 25 to 12 μm flux density. Therefore, for objects with $C_{12} > 0.3$, a SiO masers survey has not been made rigorously at Nobeyama.

In the IRAS two-color diagram (van der Veen and Habing 1988), typical mass-losing AGB stars occupy the region, $C_{12} < 0.4$ and $C_{23} < -0.1$ (the region III of van der Veen and Habing 1988). More evolved objects with thicker/hollow dust shells fall in the region, $C_{12} > 0.4$ or $C_{23} > -0.1$ (the regions IV and VIII). The boundary between AGB and post-AGB phase (PPNe phase) is considered to lie around $C_{12} \simeq 0.5$ (van der Veen and Habing 1988). Therefore, the cold IRAS objects with SiO masers are stars with a very thick dust shell, which are certainly at very late stage of the AGB stellar evolution.

Protoplanetary nebulae are transient objects from the AGB stars to planetary nebulae. These objects often have colors beyond $C_{12} = 0.4$. Detections of SiO masers from such objects must indicate that they are at very early phase of proto-planetary nebulae, objects decreasing mass loss, developing a high-velocity flow, and creating a hollow dust shell. Such objects often appear as O-rich bipolar nebulae (Zuckerman 1978) on the near-infrared images as OH231.8+1.4 (Morris et al. 1987) or IRAS 19312+1950 (Nakashima and Deguchi 2000). However, not all of the objects with colors beyond $C_{12} \simeq 0.5$ exhibit the bipolar-type nebulosity. It is rather relatively rare to find such well-developed nebulous objects as OH231.8+1.4 in near- and middle-infrared imaging surveys (Meixner et al. 1999). Therefore, it is possible that only a small percentage of protoplanetary objects develop the bipolar nebulosity by some mechanisms; for example, by the influence of a binary counter part (e.g., Morris 1981).

An alternative idea (Suh and Jones 1997) is that these objects with high C_{23} (≥ 0) are not yet at the protoplanetary stage, but are at the period soon after a He-shell flash in a super-wind phase when a central star temporally decreases or terminates the mass loss (e.g., Vassiliadis and Wood 1993; Blöcker 1992). Because of the highly reddened colors ($C_{12} \simeq 0.5$), these objects must be at a phase nearly leaving AGB (but still O-rich). A temporal termination of mass loss creates the hollow shell which exhibits high C_{23}. Gradual recovery of mass loss after the He-shell flash restarts SiO masers, which are emitted near the central star within a few stellar radii. These objects may mimic the colors of protoplanetary nebulae, but may not show bipolar morphology.

In order to find more these miscellaneous objects and to investigate their properties and evolutions, we have surveyed cold IRAS objects near the galactic plane in SiO maser lines. We have detected 51 among 143 observed objects, indicating that a considerable percentage of these cold objects in the present sample are mass losing evolved stars. Among these, we detected SiO masers in three candidates for protoplanetary nebulae. We present the results of these observations and give discussions on the nature of these objects in this paper.

4.2 Observations

4.2.1 Source selection

The present sample was selected from the IRAS Point Source Catalog (version 2) in the area of the Galactic plane, $-10° < l < 100°$, and $|b| < 5$. The selected color ranges were $0.2 < C_{12} \equiv \log(F_{25}/F_{12}) < 0.8$, and $-1 < C_{23} \equiv \log(F_{60}/F_{25}) < 1.5$, where F_{12}, F_{25}, and F_{60} are the IRAS 12, 25, and 60 μm flux densities, respectively. These color criteria effectively extract dust-enshrouded objects with $T_{dust} \simeq 160-280$ K. The total number of observed sources was 143. Figure 4.1 shows the distribution of the observed sources in the Galactic coordinates. The IRAS 12 μm flux densities of observed sources range from about 2 Jy to over 1000 Jy, and most of the observed sources are brighter than 10 Jy at 12 μm.

Near-infrared imaging observations of IRAS / SiO sources at the inner disk (Deguchi et al. 2001a) confirmed that a considerable number of near-infrared counterparts are located at the positions with large angular separations (more than 10″) from the IRAS positions. Because of the high source density in the Galactic disk and bulge, IRAS positions may not be enough

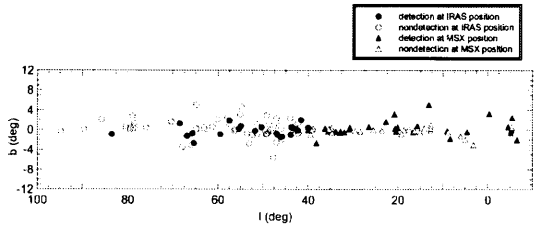

Figure 4.1: Positions of the observed sources in the galactic coordinates. Circles and triangles indicate sources observed at IRAS and MSX positions, respectively. Filled and open marks indicate the SiO detection and nondetection, respectively.

to place faint mid-infrared sources in a telescope beam. Therefore, we also used the positions in the MSX catalog (MSX: Midcourse Space Experiment; Price et al. 1997). Since the typical astrometric uncertainty of positions in the MSX catalog is a few arc seconds, it is sufficient to place mid-infrared point sources in the telescope beam of $HPBW = 40''$ for the present SiO observations. We crosschecked the source positions between IRAS and MSX catalogs, and adopted the MSX sources nearest to the IRAS positions within $40''$ as a counterpart. The adopted MSX counterparts and angular separation from IRAS positions are shown in Table 4.1. We found that only three MSX counterparts have large separations (more than $20''$) from IRAS position. Figures 4.2 shows the comparisons of flux densities between the corresponding IRAS and MSX sources, and Figure 4.3 mid-infrared colors. Because the MSX fluxes and colors correlate well with those of IRAS, most of identifications are considered to be made correctly. Because most of the sources in the present sample are Mira-type pulsating stars (cf. Nakashima et al. 2000), the sample in Figures 4.2 and 4.3 has a moderate dispersion as expected from time variations of ~ 0.5 mag at mid-infrared wavelengths (Onaka et al. 1997). In fact, because the MSX catalog became available around May 2000 when we had finished the survey of 90 sources at $l > 40°$, we used the MSX positions for the survey of 53 sources at $-10 < l < 40°$. Therefore, we listed in Table 4.1 the MSX counterparts of IRAS sources only for the sources at $-10 < l < 40°$.

4.2.2 Observations and Results

Simultaneous observations in the SiO $J = 1$–0, $v = 1$ and 2 transitions at 43.122 and 42.821 GHz, respectively, were made with the 45-m radio telescope at Nobeyama in the periods of 2000 April–May and 2001 March. In addition to the SiO lines, observations in the H_2O, $6(1,6) - 5(2,3)$ line at 22.235 GHz were made for the SiO maser emitters which were found during the present SiO observations. The beam size of the telescope was about $40''$ at 43 GHz and $72''$ at 22 GHz. In the SiO observations, a cooled SIS receiver (S40) with a bandwidth of about 0.4 GHz was used, and system

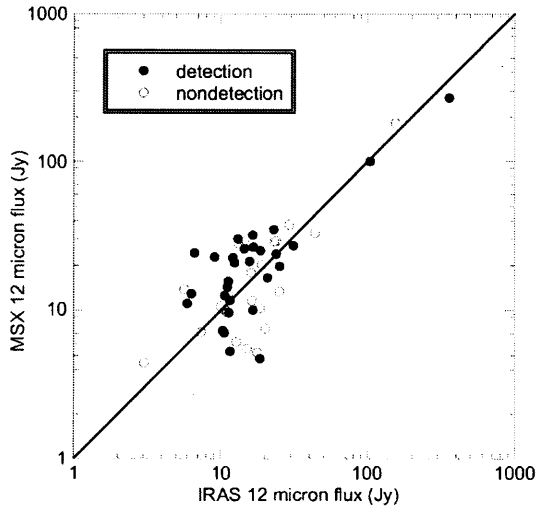

Figure 4.2: Correlation between IRAS and MSX 12 μm flux densities for the sources with $l < 40°$.

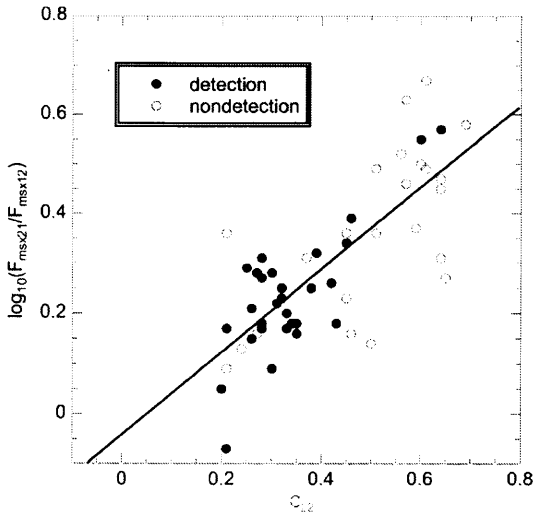

Figure 4.3: Correlation between IRAS and MSX colors for the sources with $L < 40°$. F_{msx12} and F_{msx21} and indicate MSX flux densities at 12 (C-band) and 21 (E-band) μm.

noise temperatures (including atmospheric noise and antenna ohmic loss) were about 200 – 300 K (SSB), depending on weather conditions. In the H_2O observations, a cooled HEMT receiver (H22) with a bandwidth of about 2 GHz was used, and system noise temperatures were about 170 – 300 K. The aperture efficiency of the telescope was about 0.57 at 43 GHz and 0.62 at 22 GHz. The conversion factor from the antenna temperature to the flux density was 2.9 Jy K^{-1} at 43 GHz and 3.0 Jy K^{-1} at 22 GHz. Acousto-optical spectrometer arrays of high and low resolutions (AOS-H and AOS-W) were used. In particular, the AOS-H spectrometer has a 40 MHz bandwidth and 2048 frequency channels, with an effective spectral resolution of 0.29 km s^{-1} at 43 GHz and 0.50 km s^{-1} at 22 GHz. The radial-velocity coverage was ± 350 km s^{-1} at 43 GHz and ±600 km s^{-1} at 22 GHz. All of the observations were made in position switching mode using $'$ (at 43 GHz) and $10'$ (at 22 GHz) off-source positions. The pointing of the telescope was checked every 2 or 3 hours by reference to nearby SiO maser sources, V1111 Oph and χ Cyg. Pointing accuracy was found to be better than $10''$.

Raw data were processed by flagging out bad scans, making rms-weighted integrations, and removing slopes in baselines. Detections of maser lines were judged by following criteria: for narrow spike-type emissions, the peak antenna temperature must be greater than 5 σ level of the rms noise, with line widths greater than 6 channels (corresponds to 1.0 km s^{-1} in velocity). For broad emissions, the effective signal-to-noise ratio (S/N) over the line width must be larger than 10; the effective S/N is calculated from half-power line width (the integrated intensity divided half of the peak intensity) and the average rms noise. Furthermore, we inspected each spectrum by eye and discarded some marginal detection that satisfies the above criteria. They were observed under bad weather.

Finally, we obtained 51 detections out of 143 observed sources in either SiO $J = 1$–0, $v = 1$ or 2 transitions; 45 of 51 detected sources were new detections in SiO, and 9 of 45 new were not detected before in OH nor H_2O maser lines. The detection rate of SiO masers was 36%. Results of the observations are summarized in Table 4.2 for SiO detections and in Table 4.3 for non-detections. Spectra of the detections are shown in Figure 4.4. Velocities, V_{lsr}, in Table 4.2 are radial velocities at intensity peaks. Intensity weighted radial velocities normally coincide with the velocities at the peak within a few km s^{-1}. In the H_2O maser line, we detected 3 out of 23 observed sources; only one of them (IRAS 19312+1950) was a new detection in the H_2O maser line (see Nakashima and Deguchi 2000). The H_2O maser spectra are shown in Figure 4.5, and the results are summarized in Table 4.4 for detections and Table 4.5 for non-detections. The detection rate of H_2O was 13%.

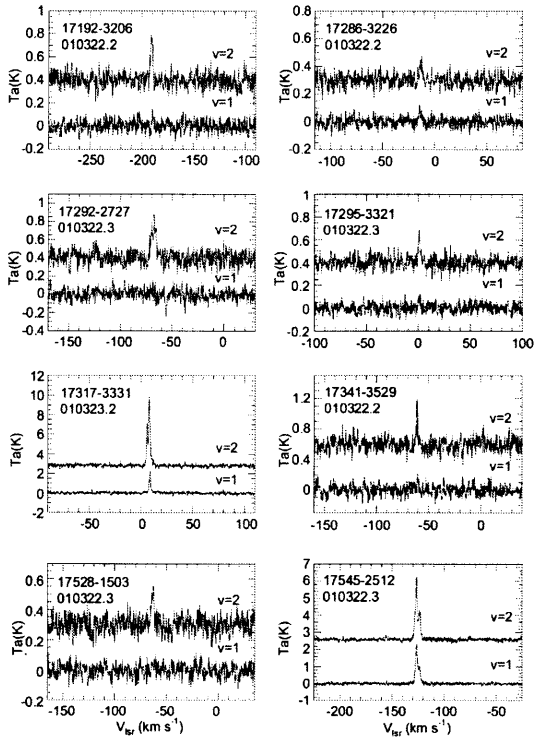

Figure 4.4a: Spectra of the SiO $J = 1$–0, $v = 1$ and 2 lines for 50 of 51 detected sources except IRAS 19312+1950 (cf. Nakashima and Deguchi 2000)

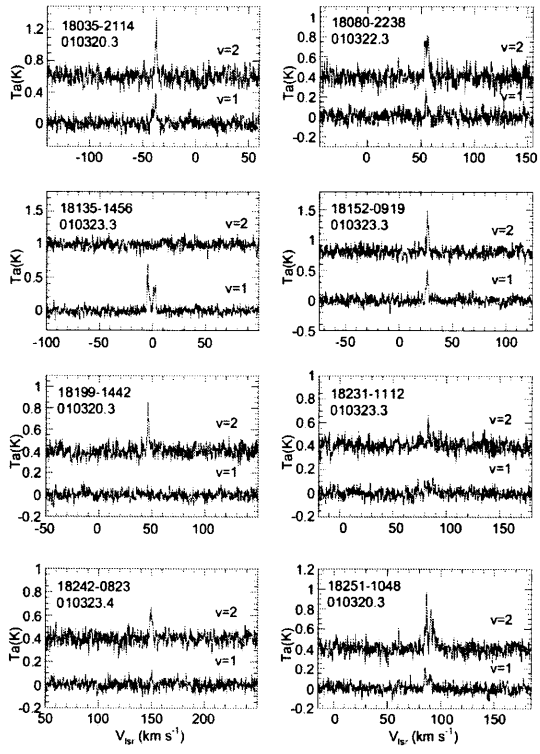

Figure 4.4b: Continued.

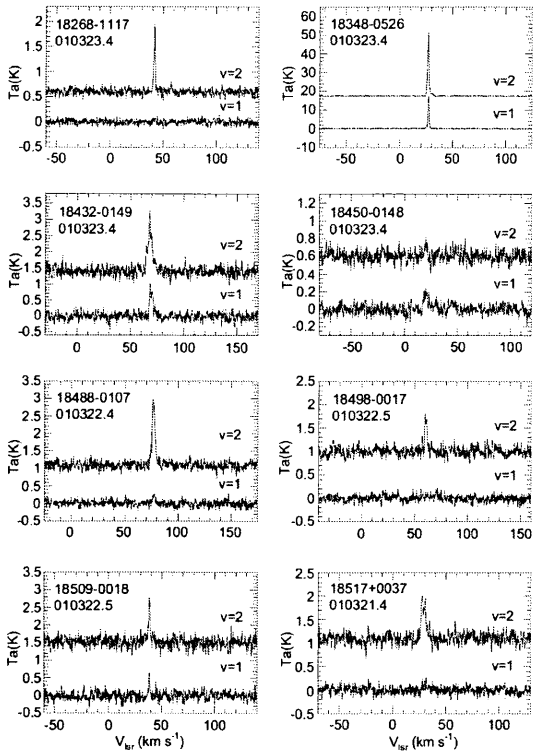

Figure 4.4c: Continued.

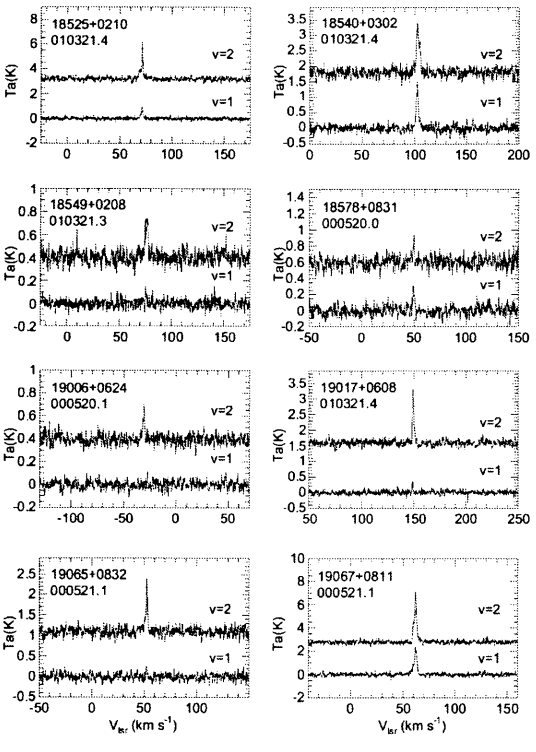

Figure 4.4d: Continued.

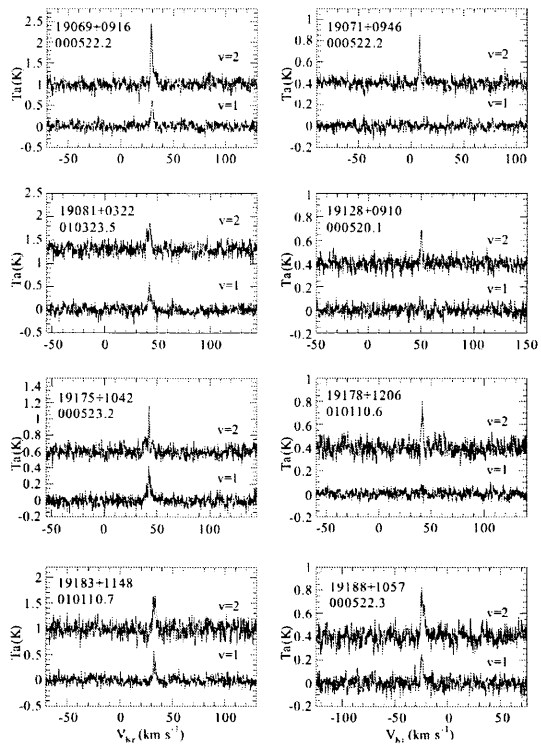

Figure 4.4e: Continued.

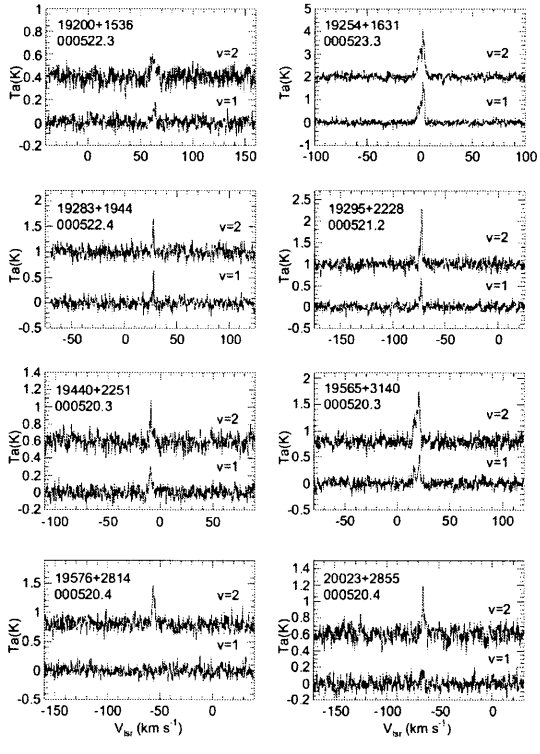

Figure 4.4f: Continued.

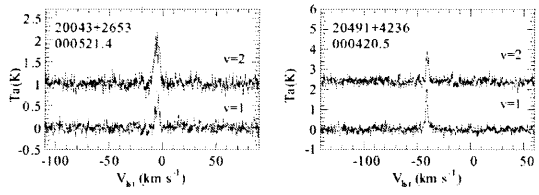

Figure 4.4g: Continued.

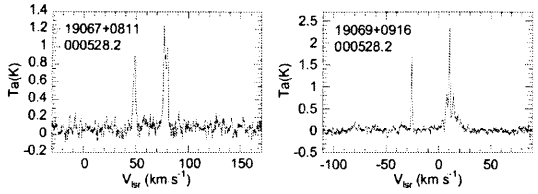

Figure 4.5: Spectra of the H_2O maser lines at 22 GHz for 2 of 3 detected sources except IRAS 19312+1950 (cf. Nakashima and Deguchi 2000).

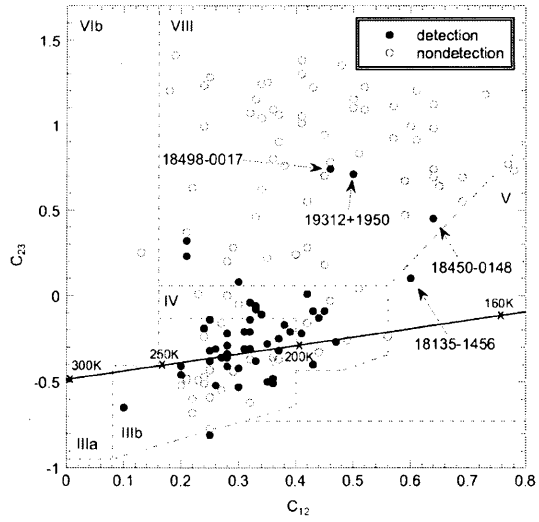

Figure 4.6: IRAS two color diagram of the present sample. Filled and open circles indicate SiO detections and non-detections, respectively. The black body curve is indicated by the solid line. Regions in the diagram indicate the classification of IRAS sources by van der Veen and Habing (1988).

4.3 Discussion

4.3.1 Color Characteristics of SiO Detections

Figure 4.6 shows a two-color diagram for the observed sources. The broken lines in Figure 4.6 indicate the boundaries of source regions suggested by van der Veen and Habing (1988). The observed sources distribute mostly in regions, IIIb, IV, and VIII, composed of variable stars with thick O-rich circumstellar shells, variable stars with very thick O-rich circumstellar shells, and the other kind of very cool objects, respectively (van der Veen and Habing 1988). It is natural that SiO detections concentrate into the regions, IIIb and IV, because most of SiO masers are emitted from AGB stars with an O-rich dust envelope. On the other hand, a few SiO detections are out of regions, IIIb and IV; The sources in region VIII show a very different color characteristics from the sources in regions IIIb and IV.

The region VIII involves late AGB and post-AGB stars, young stellar objects, and galaxies. In a two-color diagram, the young stars concentrate more in the region with $C_{12} \simeq 1.0$ (< 100 K) (Walker and Cohen 1988; Sutes and Zealey 1991). Associations of IRAS sources with known objects were studied by van der Veen and Habing (1988); only 8% of IRAS sources in region VIII are associated with early type stars, and about 35% are associated with AGB or post-AGB stars. Galaxies are also minor components in the region VIII. More than 99% of the IRAS galaxies indicate a weak 12 μm flux density less than 2 Jy (Fullmer and Lonsdale 1989). All objects in the present sample are brighter than 2 Jy in 12 μm, and approximately 80 % of the objects are brighter than 5 Jy in 12 μm. Because of the 12 μm flux densities, it is rare that galaxies contaminate the present sample.

The color index, C_{12}, of a AGB star increases with mass-loss rate. Near the end of the AGB phase, the mass loss rate often increases enormously (up to 10^{-4} $M_\odot$ y^{-1}; Blöcker 1992; Yamamura et al. 1996). When the central star turnes into a post-AGB phase, the mass loss decreases. It has been suggested that the boundary between AGB and post-AGB phase is at $C_{12} = 0.5$ in the two-color diagram (van Hoof et al. 1997). After the mass loss ceases, circumstellar gases are not supplied from the central star; SiO masers disappear first among the circumstellar masers (OH and H_2O) in the O-rich circumstellar envelope, because SiO masers are emitted within a few stellar radii of the central star. Therefore, SiO emitters with IRAS colors above $C_{12} \sim 0.5$ can be regarded as objects at a very early post-AGB stage decreasing/ceasing mass loss. We found three SiO emitters with the IRAS colors, $C_{12} \sim 0.5$, in the present sample: IRAS 18135−1456 (OH15.7+0.8), 18450−0148 (W43A), and 19312+1950. Two (IRAS 18450−0148 and 19312+1950) are the first detections in SiO. We also detected SiO in IRAS 18498−0017, a candidate proto-planetary nebula with $C_{12} = 0.46$. We checked whether or not the near-infrared counterparts have any nebulosity on the 2MASS J-, H-, and K-band images. The 2MASS archive (ver. 2) gave images of 55 of 143 observed sources. We found two extended objects with bipolar morphology: IRAS 19312+1950 and 20249+3953. The present SiO maser search for 20249+3953 was negative. Ueta et al. (2000) found that a few dozen of sources in their sample were extended in a few arcsec using the NICMOS near-infrared camera on board on the Hubble Space Telescope. Unfortunately, their sample does not overlap with the

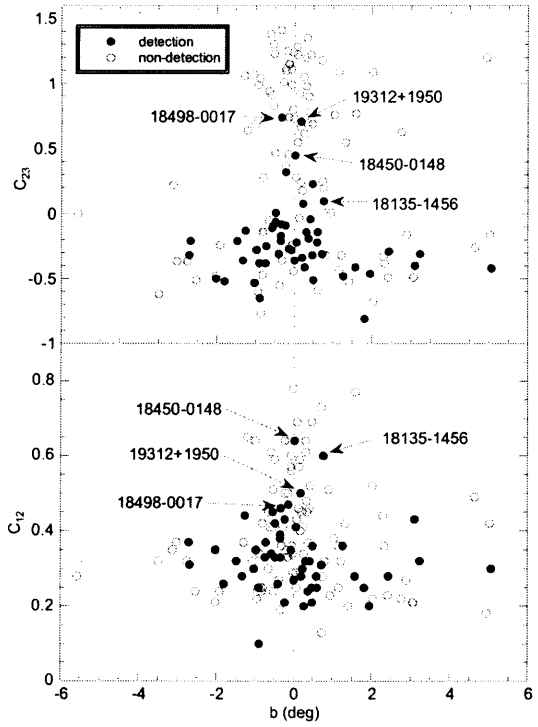

Figure 4.7: Galactic latitude vs. IRAS colors. Filled and open circles are detections and non-detections in SiO, respectively. Names of the candidates for proto-planetary nebulae are indicated in the diagram.

present sample of cool IRAS sources.

In order to check contamination by interstellar dust in the IRAS 60 μm flux densities, we made the color–latitude diagrams, plots of IRAS colors, C_{12} and C_{23}, against galactic latitudes, as shown in Figure 4.7. In both panels of Figure 4.7, strong concentrations of sources toward the galactic plane ($b = 0°$) can be seen. This is partly due to the source concentration toward the galactic plane, and partly due to contamination by young stellar objects which are bound within $|b| \leq 1°$. A characteristic in Figure 4.7 is a clear separation in distribution between SiO detections and non-detections. IRAS colors of the SiO detections do not strongly depend on the galactic latitudes except a few candidate for proto-planetary negulae. In contrast, a concentration of nondetections around $C_{23} \sim 1$ is remarkable. Some of these sources are, in fact, known objects in star forming regions. Therefore, we conclude that the concentration around $C_{23} \sim 1$ is caused by a contamination by young stellar objects. Approximately 20 % of the present sample are inferred to be young stellar objects.

The bulge SiO sources distribute quite differently in the color-latitude diagram [see figure 4 of Deguchi et al. (2000a) and Deguchi et al. (2000b)]; the color index, C_{23}, of the SiO detections increase steeply up to $\sim$ 0.5 near $|b| \sim 0°$. The SiO detections in the upper panel of figure 4.7 do not show such behavior, except candidate for proto-planetary nebulae with SiO masers (indicated by arrows in figure 4.7). Of course, the proto-planetary nebulae have intrinsic colors with higher C_{12} and C_{23} than the other SiO detections do. Therefore, we conclude that the IRAS colors, C_{23} of SiO detections in the present sample are intrinsic to the sources and that contamination by interstellar dust in the IRAS 60 μm flux densities in the present sample is small. This is probably because the IRAS sources in the present sample are relatively bright ($F_{12} \geq 10$ Jy) and nearby objects compared with the sources in the previous bulge samples (Deguchi et al. 2000a; Deguchi et al. 2000b).

4.3.2 Intensity Ratio of the $J = 1$–0, $v = 2$ to $v = 1$ Line

Figure 4.8 shows plots of intensity ratios of the $J = 1$–0, $v = 2$ to the $J = 1$–0, $v = 1$ line (integrated and peak intensities) against IRAS color indices, C_{12}. The filled circles show the data in the present observation and the unfilled circles indicate the data from the previous SiO maser survey of the inner-disk IRAS sources with $C_{12} < 0.2$ (Nakashima and Deguchi 2001). Both of the sources are located in nearly the same galactic longitude ranges. We can see that the v =2/1 line intensity ratio tends to increase with IRAS color of the objects till $C_{12} = 0.5$. Beyond $C_{12} = 0.5$, the intensity ratios dramatically decrease. The least-square best fits in Figure 4.8 give

$$\log(F_{v=2}/F_{v=1}) = 1.05\,(\pm 0.13)\,C_{12} + 0.08\,(\pm 0.03), \tag{4.1}$$

for the integrated intensity ratio and

$$\log(T_{v=2}/T_{v=1}) = 0.61\,(\pm 0.08)\,C_{12} + 0.08\,(\pm 0.02), \tag{4.2}$$

for the peak intensity ratio.

The intensity ratio of the SiO $J = 1$–0, $v = 2$ to the $J = 1$–0, $v = 1$ lines of AGB stars has been observed as being nearly equal to unity (Schwartz et al. 1979; Spencer et al. 1981; Nakada et al. 1993). However, there are many exceptional cases. For example, the intensity ratio of IRC−10414 is less than about 0.1 (Imai et al. 1999). Nyman and Olofsson (1986) suggested that the average intensity ratio of SiO masers from OH/IR stars were nearly 4. An average of IRAS colors of OH/IR sources in the Nyman and Olofsson (1986)'s sample is $C_{12} = 0.2$. Therefore, the intensity ratios observed in OH/IR stars (Nyman and Olofsson 1986) are consistent with the color correlation found in this paper.

In the present observations, both two SiO transitions, $J = 1$–0, $v = 1$ and 2, are near the band edges of the SIS receiver with the band widths of about 0.4 GHz. Therefore, the sensitivity at each frequency varies depending on the daily tuning condition of the receiver. Therefore, we checked the reliability of intensity calibration at the different frequencies using the pointing

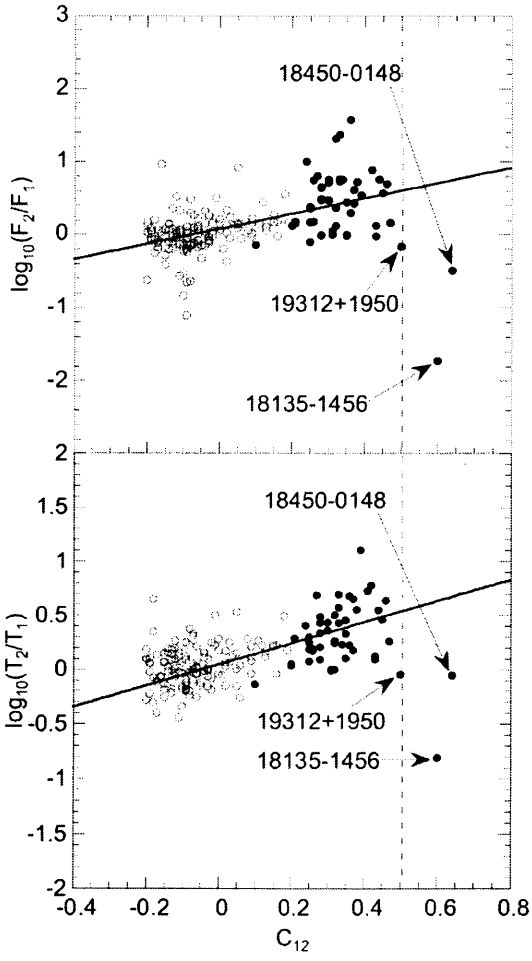

Figure 4.8: IRAS Color vs. Intensity Ratio of the J = 1–0, $v = 2$ to the J = 1–0, $v = 1$ lines. In upper panel, integrated intensities are used to calculate the intensity ratios. In lower panel, peak intensities are used.

sources and Sgr B2 every day, and confirmed that the intensity calibrations of all spectrometers are nearly equal through all the observing sessions.

It seems difficult to explain the intensity ratio of near unity of the two rotational lines in the very different vibrational states, such as v=1 (T_{ex} = 1600 K) and v=2 (T_{ex} = 3200 K). In fact, it has been observed with VLBI (Miyoshi et al. 1992) that both masers are emitted approximately at the same radii in a circumstellar envelope (Miyoshi et al. 1992). The standard theory of SiO masers (e.g., Langer and Watson 1984; Bujarrabal et al. 1996) explains this phenomenon by the line overlap of the SiO vibration-rotation transition with the H_2O line; this line overlap mechanism utilizes the overlap of the SiO ($J = 0$ $v = 1$) – ($J = 1$ $v = 2$) transition with the H_2O (ν_2=0 12_{73}) – (ν_2=1 11_{66}) transition, making the pump cycle between the SiO energy levels, J =0 v =1 $\Rightarrow$ J =1 v =2 $\rightarrow$ J =0 v =2 $\Rightarrow$ J =1 v =1 $\rightarrow$ J =0 v =1, where vibration-rotation and maser transitions are indicated by $\Rightarrow$ and $\rightarrow$, respectively. This pump cycle, if it works, produces the same numbers of maser photons in the two J = 1–0 transitions in the v =1 and 2 states. Therefore, for the normal AGB stars with $C_{12} \sim 0$, it can naturally be considered that this pump cycle is working.

In contrast, in the cold IRAS sources with SiO masers ($0.2 < C_{12} \leq 0.5$), the J = 1–0 v =2 line tends to be much stronger than the J = 1–0 v =1 line as shown in Figure 4.7. The maser intensities in the vibrational states are influenced by the spectral energy distribution of the central star at 4 and 8 μm, the wavelengths at the first overtone and fundamental vibrational transitions (Langer and Watson 1984). According to the near-infrared observations of the spectra of AGB/post-AGB stars in the wide IRAS color range systematically sampled by Fujii (2001), infrared continuum spectral profiles change continuously from single peak to double peak during a transition stage from the AGB to post-AGB phase. In particular, the spectral energy distribution from 4 to 8 μm changes during a transition from the AGB to post-AGB phase. It may explain intensity ratio changing with IRAS colors.

The other interesting cases are three SiO maser sources ever found in star forming regions: Orion IRc 2, W51 IRs 2, and Sgr B2 MD5 (Hasegawa et al. 1985; Fuente et al. 1989; Morita et al. 1992). The line intensity ratios in the latter two SiO masers in star-forming regions deviate largely from unity. The intensity of J = 1–0, $v = 1$ line from Sgr B2 is about 1.5 Jy while that of the J = 1–0, $v = 2$ line is less than 0.3 Jy (Shiki et al. 1997). In the case of W51 IRs2, the J = 1–0, $v = 2$ intensity is more than 10 times stronger than that of J = 1–0, $v = 1$. Unfortunately IRAS colors of these objects are not well known except Sgr B2 MD5 (IRAS 17441-2822). Even in this source, the colors, (C_{12}, C_{23})=(0.95, 2.28), might be suffered from serious contamination by surrounding objects. According to the mid-infrared photometry for Ori KL region with SiO masers by Gezarini et al. (1998), the mid-infrared

color of IRc2 (a logarithmic ratio of the 12 to 20 μm intensity) is about 0.2. For the case of W51 IRs2, it is more difficult to estimate the mid-infrared fluxes because this source consists of at least 7 continuum sources; four of them are ultra compact HII regions (Okamoto et al. 2001). Extrapolating the OKYM 4 flat spectrum of Figure 2 of Okamoto et al. (2001) to the longer wavelengths, we estimate the color as $C_{12} \sim 0.6$. Therefore, the increasing color sequence of these three sources is Orion IRc 2 – W51 IRS 2 – Sgr B2 MD5. The observed line intensity ratios to the mid-infrared color for these three sources are consistent with the correlation shown in Figure 4.7. The ratio increases with C_{12}, but decrease beyond $C_{12} \sim 0.6$; in fact we need to correct 0.1 for W51 for the ambiguity of the 25 μm flux). Therefore, the line intensity-color correlation found in the evolved objects seems also to be appled to the SiO maser sources in the star forming regions, and it may be useful to deduce physical conditions of these objects. If we apply above correlation of the line intensity ratio to color index to these three SiO masers, the sequence according to the color would be as Orion IRc 2, W51 IRS 2, and Sgr B2 MD5.

Figure 4.12 shows a plot of the SiO intensity ratio against the expansion velocities obtained from OH maser observations. It has been known that the OH expansion velocity increases up to ≤ 100 km s^{-1} at the protoplanetary phase (Morris and Bowers 1980). We cannot find any clear correlations between expansion velocity and intensity ratio, but most of the SiO sources tend to be concentrated near $(V_e, \log(F_2/F_1)) \simeq (34, 0.2)$ except a few proto-planetary candidates with small expansion velocities. This fact implies that the OH high-velocity flow is not well developed yet for objects with SiO masers.

4.3.3 Longitude distribution

Figure 4.9 shows a histogram of galactic longitudes for the SiO detections (shadow) and nondetections (blank). The detection rates are also shown in solid line with filled circles. For comparison, the detection rates in the previous SiO surveys for the sources with normal colors are also shown in the dotted line with filled squares (Nakashima and Deguchi 2001; Nakashima et al. 2001; Izumiura et al. 1999; Deguchi et al. 2000a; Deguchi et al. 2000b). The detection rate in this sample tends to decrease with the galactic longitude, as found in the previous SiO surveys of the IRAS sources with the color, $0.0 < C_{12} < 0.1$. We see a sudden increase of the detection rate at the range between $l = 20$ and 40°. Because we used the MSX positions instead of IRAS positions in the inner region ($l < 40°$), the deference in the survey condition can possibly be a cause of the sudden change of detection rates; the detection rate is 55% for 53 sources in $l < 40°$, and 24% for 90 sources in $l > 40°$. However, the improvement of the positions is not enough to make the overall change of detection rates above and below $l = 40°$, because the number

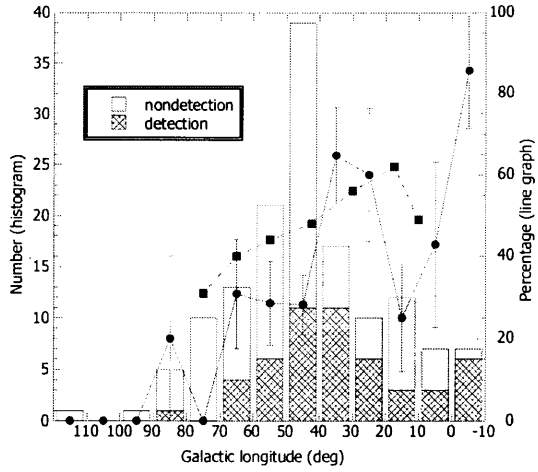

Figure 4.9: Histogram of the present sample with the galactic longitude. Shaded and white portions in the histogram indicate the number of SiO detections and non-detections. Line graph written by solid line indicate the detection rate of the present SiO observations. Line graph written by dotted line indicate the detection rate of SiO observation for blue IRAS sources with the color, $0.0 < C_{12} < 0.1$ (Nakashima and Deguchi 2001; Nakashima et al. 2001; Izumiura et al. 1999; Deguchi et al. 2000a; Deguchi et al. 2000b).

of MSX counterpart with the large separation ($> 20''$) from the IRAS position were only 3 in the present sample. The maximum of the detection rate between $l = 20$ and 40° may be caused by a statistical fluctuation due to the small numbers of the observed sources in the bin.

Figure 4.10 shows a longitude–velocity diagram for SiO detections overlaid on the CO $J = 1$–0 line map (taken from Dame et al. 2001). Filled and unfilled circles indicate the sources with the luminosity distance below and above 5 kpc. The spread of radial velocities of the SiO sources seems to be within velocity limits produced by the galactic rotation, which are indicated by the CO gas distribution [except IRAS 17454−2512 at ($l = 4.56°$ and $V_{lsr} = -126$ km s^{-1})]. In terms of the spiral arm model (Taylor and Cordes 1993), the upper edge of the SiO distribution corresponds to the tangential points of the Sagittarius-Carina arm and the Scutum-Crux arm at the distance of 4–5 kpc, and the lower edge (between $l = 30$ and 100°) corresponds to the outer arm at the distance of 8–10 kpc. We found that only one source in our sample, IRAS 17192-3206 at $l = -5.4°$, has a large negative velocity; this source is probably associated with the central nuclear disk which is rapidly rotating as seen in the overlaid CO map.

Figure 4.11 shows a distribution of observed sources projected onto the Galactic plane. The SiO sources in the present sample seem to concentrate onto tangential points of spiral arms. However, concentrations seem to be quite weak in Figure 4.11. As in the previous papers, distances are estimated from the bolometric flux

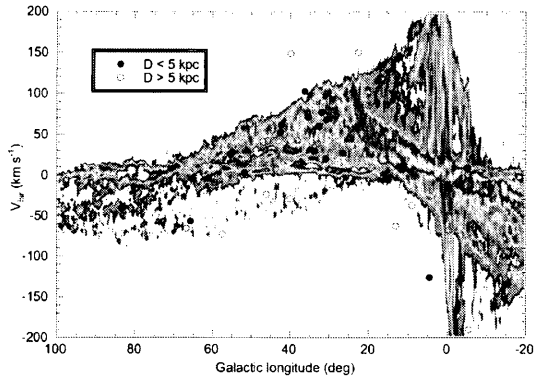

Figure 4.10: The longitude-velocity diagram of the SiO detections overlaid on the CO $v - l$ map (taken from Dame et al. 2001). Filled and open circles indicate sources at the distance above and below $D = 5$ kpc.

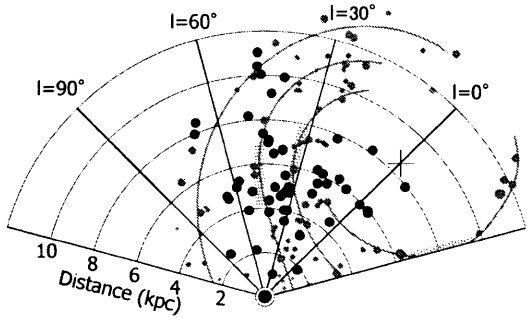

Figure 4.11: Distribution of observed sources projected onto the Galactic plane.

of sources which are computed from IRAS 12 and 25 μm flux densities and a bolometric correction for O-rich stars (van der Veen and Breukers 1989) with assuming the constant luminosity of $8 \times 10^3 L_\odot$. For post-AGB stars, the bolometric flux tends to be underestimated in the bolometric correction, because the spectral energy distributions of post-AGB stars are more or less weighted on the shorter and longer wavelengths, which is different from those of AGB stars. Because the AGB stars have a single-peak spectral energy distribution, which is peaked at a mid-infrared wavelength, the bolometric correction is relatively accurate. On the contrary, post-AGB stars have a doubly peaked SED, peaked at the mid and near-infrared wavelengths (Fujii 2001). To make more precise bolometric corrections for post-AGB stars, we need to obtain near-infrared fluxes.

We also calculated the radial velocity dispersion (root mean squares of residues subtracted by circular and solar motions from V_{lsr}) for the 22 SiO sources in $40° < l < 70°$, and obtained the dispersion 27.9 km s^{-1}. Here, a flat rotation curve (see caption of Figure 7 in Nakashima and Deguchi 2001) and the galactocentric distance of the Sun (8.5 kpc) are assumed in the calculation. This value is comparable with the dispersion, ~30–35 km s^{-1}, for the SiO sources with the bluer IRAS colors ($C_{12} < 0.2$) in several galactocentric distance ranges (Nakashima and Deguchi 2001). This value is also comparable with the dispersion of ~30 km s^{-1} for the nearby SiO maser sources in the southern hemisphere (Deguchi et al. 2001b). For the sub sample of 29 sources in $l < 40°$, we obtained slightly larger radial velocity dispersion, 35 km s^{-1}. Because of the large rotational velocity due to galactic rotation, this sub sample tends to give a larger velocity dispersion caused by the errors involved in the distance estimations.

It is possible that evolved objects with cold IRAS colors are relatively massive stars, because they have a high mass-loss rate (Olivier et al. 2001). In such case, we naturally expected that the massive stars were strongly associated with spiral arms and that the velocity dispersions of massive-star samples were smaller than those of light star samples. However, we could not find any such kinematical evidence in the present analysis, i.e., any strong association with spiral arms, or significantly small velocity dispersions. A part of the reason is probably because the distances used in this analysis are somewhat inaccurate.

The longitude dependence of the SiO detection rate is very similar between the present samples and the previously surveyed samples of normal AGB stars, though it is slightly lowered for the increase of contamination by young stellar objects to the sample. The increase of the SiO detection rates toward the galactic center is considered to be due to the metallicity gradient in the galaxy (Jiang et al. 1999).

From these facts, we conclude that the evolved objects with cold IRAS colors in the present sample have very similar kinematic properties, though they have large differences in infrared and maser line properties.

4.4 Individual Sources

Among the observed sources, known young stellar objects in star forming regions are IRAS 17271-3309 (Brofman et al. 1996), 18196−1331 (Minchin et al. 1991; Kastner et al. 1992; Geballe and Oka 1996), 18551−0146 (Watt and Mundy 1999), 19089+1542 (Thé et al. 1994; Meeus et al. 2001), 19598+3324 (Cesaroni et al. 1988), 20187+4111 (Hillenbrand et al. 1995). Notable evolved stars are as follows;

IRAS 17295-3321 (OH 354.76-0.06), IRAS 17317-3331 (V1018 Sco)

These sources have been studied as maser sources associated with the globular cluster, Liller 1. However, because of the radial velocity differences (Sevenster et al. 1997; te Lintel Hekkert et al. 1991; te Lintel Hekkert et al. 1989), Frail and Beasley (1994) concluded that these are not associated with Liller 1. SiO masers were

detected in the present paper, and radial velocities coincided with those of OH masers. A dense core of the molecular cloud is located near to IRAS 17317−3331; the ^{13}CO J = 1–0 line exhibits a complex spectrum toward this source (Vilas-Boas et al. 2000).

IRAS 18016−2743

The OH 1612 MHz maser has been detected (te Lintel Hekkert et al. 1991; David et al. 1993; Sevenster et al. 1997), but SiO maser searches have been negative in the J = 2–1 v =1 line (Nyman et al. 1998) and in the J = 1–0 v =1 and 2 lines in the present paper. This object was classified as a proto-planetary nebula by Nyman et al. (1998).

IRAS 18071−1727 (OH 12.8 +0.9)

The OH 1612 MHz maser has been detected from this object (te Lintel Hekkert et al. 1989; David et al. 1993). SiO maser searches (J = 1–0 v =1 and 2, and J = 2–1 v =1) have been negative (Nyman et al. 1998; this paper). This source was not resolved ($\leq 1''$) in mid-infrared imaging observations (Meixner et al. 1999). Nyman et al. (1998) classified this source as a proto-planetary nebula.

IRAS 18135−1456 (OH 15.7+0.8)

In this source, the SiO J = 1–0 v =2 line intensity has been extreme weak compared with that of J = 1–0 v =2 (Nyman et al. 1998; this paper). SiO, OH and H_2O masers has been detected (David et al. 1993; te Lintel Hekkert et al. 1989; Engels et al. 1986; Nyman et al. 1993). Nyman et al. (1998) classified this source as a proto-planetary nebula.

IRAS 18251−1048 (OH 20.7+0.2)

OH 1612 MHz maser has been detected (te Lintel Hekkert et al. 1989). The position of OH maser determined by VLA (Bowers and de Jong 1983) coincide with the MSX position within 2.2″. SiO masers have been detected in this paper.

IRAS 18348−0526 (OH 26.5+0.6, V437 Sct)

The observations of time variation of the OH 1612 MHz maser intensity indicated a period of 1566 days (Herman and Habing 1985). The monitoring observations of SiO maser intensity variation gave approximately the same period (Alcolea et al. 1999). Mid-infrared images reveal the compact nature of the circumstellar shell ($< 0.5''$) (Justtanont et al. 1996).

The low- and high-velocity OH emissions from this source are spatially displaced by about ??″ (Diamond et al. 1985; Masheder et al. 1974), indicating a bipolar geometry. The low- and high-velocity H_2O emissions are also spatially displaced by about ??″, which is larger than the spatial separation of the OH (Diamond and Nyman 1988). This source has been classified as a proto-planetary nebula (Nyman et al. 1998). Weak SiO maser emission has been detected in this paper.

IRAS 18498−0017

IRAS colors, C_{12} and C_{23}, of this source are similar to those of IRAS 19312+1950, a proto-planetary nebula with SiO masers (Nakashima and Deguchi 2000). Weak SiO maser emission (J = 1–0 v =2) was detected in this object in this paper, suggesting that this source is also a proto-planetary nebula with SiO masers. OH and H_2O masers have been detected (te Lintel Hekkert et al. 1989; Engels et al. 1986; Cesaroni et al. 1988).

IRAS 19069+0916

Both the SiO and H_2O masers were detected in this paper. SiO emission was found at V_{lsr} =30.0 km^{-1}, though H_2O masers were detected at V_{lsr} = −25.7 and 10.7 km^{-1} in the present paper (Figure 4.5). The OH 1612 MHz double peaks were found at V_{lsr} = 10 and 54 km s^{-1} (Eder et al. 1988), giving the stellar velocity at V_{lsr} ∼32 km s^{-1}; this is consistent with the SiO radial velocity. The low-velocity component at V_{lsr} = −26 km s^{-1} of H_2O maser emission, which appears lower than the velocity expected from the OH double peaks, had not been detected in the past (Engels and Lewis 1996). It may indicate an activity of the central star at a transient stage to the post-AGB phase.

IRAS 19327+3024 (BD+30°3639)

This is a planetary nebula, and has rigorously been observed from X-ray to radio wavelengths, including optical imaging with the HST (Harrington et al. 1997). The relatively low temperature of the central star ($T \sim$ 40000K) and the small expansion time sacle of the nebula (900yr, Kawamura and Masson 1996) suggests recent emergence to the planetary-nebula phase. No maser has ever been detected.

IRAS 20249+3953

The 2MASS near-infrared image shows a large (∼ 30″) point-symmetric, spiral nebulosity around the bright near-IR counterpart. IRAS 12 μm flux density of this object is 19 Jy, which is too strong for this object to be an extra-galactic object. This is probably a proto-planetary nebula with bipolar structure. No maser has ever been detected toward this object.

4.5 Conclusion

We observed 143 cold IRAS sources in the SiO J = 1–0, v = 1 and 2 lines, and detected 51 objects; 45 of 51 are new detections. SiO masers were newly detected in three candidate protoplanetary nebulae: IRAS 18450−0148

(W43A), 18498−0017, and 19312+1950. We also detected 3 of 23 observed sources in the H_2O maser line. The results of this observations are:

1. The intensity ratio of the SiO $J = 1$–0, $v = 2$ to the $J = 1$–0, $v = 1$ line is correlated with the IRAS color for objects with $C_{12} < 0.5$. Beyond $C_{12} = 0.5$, the intensity ratio dramatically drops.

2. IRAS colors, C_{12} and C_{23}, of SiO emitters near the Galactic plane do not strongly depend on the Galactic latitude, though the colors of SiO non-detections tend to vary with the latitude. This fact indicates that young stellar objects considerably contaminates the sample, and that the IRAS colors of SiO emitters exhibit intrinsic colors of the objects themselves.

3. The SiO sources are not strongly associated with the spiral arms in the longitude–velocity diagram and on the galactic-plane map. The velocity dispersion of the SiO detections in the sub sample ($l > 40°$) is comparable with the dispersions found in previous SiO surveys for sources with different colors. These facts suggest that the evolved stars involved in the present sample are not particularly massive than the AGB stars observed before.

TABLE 4.1
IRAS data

IRAS name	l	b	F_{12}	C_{12}	C_{23}	D_L	V_{lsr}	MSX name	sep.	2MASS
	(°)	(°)	Jy			(kpc)	(km s^{-1})		($''$)	
17192−3206	354.60	2.44	11.580	0.28	−0.29	5.9	−190.3	354.5978+02.4362	3	ps
17271−3309	354.66	0.48	43.800	0.69	0.69	2.5	—	354.6629+00.4759	6	sf
17286−3226	355.44	0.60	11.350	0.28	−0.22	6.0	−13.2	355.4344+00.5970	6	ps
17292−2727	359.66	3.23	11.550	0.32	−0.31	5.9	−68.3	359.6625+03.2309	2	no
17295−3321	354.76	−0.06	11.300	0.35	−0.28	6.0	0.6	354.7620−00.0612	10	ps
17317−3331	354.88	−0.54	104.000	0.45	−0.09	1.9	8.5	354.8848−00.5381	9	ps
17341−3529	353.50	−2.02	6.348	0.35	−0.50	7.9	−60.6	353.5038−02.0207	18	ps
17528−1503	13.14	5.06	10.310	0.30	−0.42	6.3	−62.7	013.1444+05.0638	3	
17545−2512	4.56	−0.40	20.730	0.26	−0.31	4.4	−126.2	004.5628−00.3974	3	ps
18008−2419	6.06	−1.20	17.630	0.65	0.64	4.1	—	006.0569−01.1969	7	
18016−2743	3.18	−3.02	3.022	0.37	−0.37	11.4	—	003.1764−03.0243	2	
18016−2540	4.97	−2.02	13.100	0.21	−0.48	5.5	—	004.9722−02.0207	3	
18035−2114	9.03	−0.21	5.957	0.21	0.32	8.2	−37.3	009.0299−00.2175	19	
18042−2131	8.87	−0.49	11.230	0.59	0.47	5.3	—	008.8729−00.4928	10	
18071−1727	12.76	0.90	23.660	0.51	0.04	3.8	—	012.7577+00.8951	4	
18080−2238	8.33	−1.80	11.110	0.26	−0.52	6.1	55.5	008.3283-01.8028	9	ps
18092−1742	12.77	0.33	15.050	0.61	1.20	4.5	—	012.7747+00.3351	6	
18112−1801	12.73	−0.22	24.960	0.64	1.12	3.4	—	012.7263−00.2210	18	sf
18125−1631	14.18	0.22	10.060	0.45	0.18	6.1	—	014.1831+00.2209	3	
18135−1456	15.70	0.77	31.020	0.60	0.10	3.2	−4.9	015.7002+00.7711	7	
18152−0919	20.82	3.10	14.480	0.43	−0.40	5.1	26.3	020.8253+03.0969	19	
18171−1603	15.13	−0.53	20.080	0.51	0.83	4.2	—	015.1296−00.5266	1	
18184−1449	16.36	−0.21	18.420	0.50	1.10	4.4	—	016.3609−00.2073	4	
18196−1331	17.64	0.15	154.800	0.57	0.92	1.4	—	017.6369+00.1568	14	
18199−1442	16.65	−0.48	12.050	0.33	−0.06	5.8	46.0	016.6452−00.4833	1	
18223−1243	18.66	−0.06	16.200	0.60	0.99	4.4	—	018.6545−00.0582	12	
18231−1112	20.09	0.49	10.590	0.21	0.23	6.1	85.0	020.0897+00.4860	7	
18242−0823	22.71	1.58	10.660	0.28	−0.41	6.2	150.0	022.7076+01.5775	10	
18251−1048	20.67	0.24	6.668	0.30	0.08	7.8	86.1	020.6720+00.2398	3	
18262−1233	19.26	−0.82	14.350	0.24	−0.47	5.3	—	019.2580−00.8184	16	no
18268−1117	20.43	−0.34	12.370	0.39	−0.21	5.6	43.4	020.4323−00.3441	5	
18321−0820	23.66	−0.13	15.960	0.64	0.74	4.3	—	023.6582−00.1268	6	
18348−0526	26.54	0.62	359.800	0.25	−0.14	1.1	27.2	026.5439+00.6178	3	ps
18354−0638	25.55	−0.05	18.920	0.56	−0.24	4.2	—	025.5469−00.0529	2	
18418−0415	28.40	−0.38	28.970	0.27	−0.55	3.8	—	028.4037−00.3812	18	
18432−0149	30.72	0.43	25.060	0.32	−0.04	4.0	68.2	030.7152+00.4268	5	
18434−0308	29.58	−0.22	11.040	0.21	0.37	6.0	—	029.5757−00.2198	12	
18450−0148	30.94	0.04	23.730	0.64	0.45	3.5	20.1	030.9444+00.0347	8	
18488−0107	31.98	−0.48	16.450	0.42	0.01	4.8	76.9	031.9853−00.4854	10	
18498−0017	32.83	−0.32	22.850	0.46	0.74	4.0	60.1	032.8286−00.3155	5	
18509−0018	32.95	−0.57	15.650	0.34	−0.11	5.1	38.4	032.9535−00.5695	12	
18511+0146	34.82	0.35	23.050	0.45	0.70	4.0	—	034.8213+00.3516	4	
18517+0037	33.87	−0.34	16.580	0.38	−0.17	4.9	29.6	033.8735−00.3356	4	
18525+0210	35.34	0.21	18.410	0.28	−0.34	4.7	71.3	035.3461+00.2122	6	
18529+0210	35.39	0.14	5.692	0.46	−0.03	8.0	—	035.3877+00.1349	1	
18540+0302	36.29	0.28	18.570	0.20	−0.41	4.6	102.4	036.2929+00.2709	28	
18542+0114	34.71	−0.59	10.680	0.61	0.91	5.4	—	034.7132−00.5952	10	
18549+0208	35.58	−0.33	13.070	0.33	−0.08	5.6	75.2	035.5811−00.3335	17	
18578+0831	41.59	1.96	9.353	0.20	−0.46	6.5	49.5	—	—	
18587+0521	38.87	0.32	5.432	0.64	0.98	7.4	—	038.8744+00.3090	24	
19006+0624	40.02	0.38	4.082	0.24	−0.19	9.9	−28.9	—	—	
19008+0530	39.25	−0.07	12.740	0.57	1.11	5.0	—	039.2483−00.0649	28	
19011+0852	42.27	1.41	6.284	0.20	−0.52	7.9	—	—	—	
19011+1049	44.00	2.30	9.395	0.44	−0.33	6.3	—	—	—	
19017+0608	39.91	0.02	16.500	0.27	−0.36	5.0	148.7	039.9158+00.0180	8	
19025+0613	40.07	−0.12	3.044	0.33	1.15	11.5	—	—	—	
19026+0614	40.12	−0.15	3.044	0.33	0.46	11.5	—	—	—	
19045+0518	39.49	−0.99	7.395	0.64	0.69	6.3	—	039.4939−00.9927	5	
19048+0914	43.02	0.76	3.064	0.28	0.20	11.5	—	—	—	
19057+1002	43.84	0.94	3.973	0.23	0.01	10.1	—	—	—	
19065+0832	42.60	0.07	20.220	0.41	−0.22	4.4	52.2	—	—	
19067+0811	42.31	−0.13	24.630	0.47	−0.27	3.8	62.0	—	—	
19069+0916	43.28	0.32	4.798	0.32	−0.14	9.2	30.1	—	—	
19069+1335	47.12	2.33	6.851	0.36	−0.38	7.6	—	—	—	ps
19071+0946	43.76	0.51	7.943	0.36	−0.51	7.1	8.3	—	—	
19077+0839	42.83	−0.14	9.125	0.50	1.15	6.2	—	—	—	
19080+0748	42.12	−0.61	14.140	0.41	1.38	5.2	—	—	—	
19081+0322	38.19	−2.68	9.089	0.31	−0.21	6.7	42.8	038.1932−02.6822	3	
19085+0755	42.27	−0.65	4.630	0.30	−0.05	9.4	—	—	—	
19089+1542	49.21	2.89	23.440	0.27	−0.16	4.2	—	—	—	ps*
19108+0901	43.52	−0.65	3.689	0.45	0.94	10.0	—	—	—	
19112+1220	46.50	0.81	3.697	0.32	−0.32	10.5	—	—	—	no
19123+1139	46.01	0.27	9.285	0.34	0.62	6.6	—	—	—	
19128+0910	43.88	−1.02	8.410	0.30	−0.53	7.0	49.7	—	—	
19134+2131	54.87	4.64	5.058	0.49	−0.26	8.4	—	—	—	ps
19143+1427	48.72	1.15	3.031	0.36	1.09	11.5	—	—	—	
19167+1313	47.90	0.06	4.183	0.29	0.28	9.9	—	—	—	
19171+1119	46.28	−0.94	14.190	0.22	−0.60	5.3	—	—	—	
19175+1042	45.78	−1.32	7.519	0.28	−0.36	7.4	42.3	—	—	
19177+1333	48.32	−0.01	4.814	0.29	−0.44	9.2	—	—	—	
19178+1206	47.06	−0.72	3.659	0.37	−0.25	10.4	41.3	—	—	
19183+1148	46.84	−0.97	3.290	0.35	−0.28	11.0	32.7	—	—	
19188+1057	46.14	−1.47	4.020	0.32	−0.21	10.0	-24.0	—	—	
19195+1650	51.42	1.16	14.610	0.25	−0.43	5.3	—	—	—	no

TABLE 4.1
Continued.

IRAS name	l	b	F_{12}	C_{12}	C_{23}	D_L	V_{lsr}	MSX name	sep.	2MASS
	(°)	(°)	Jy			(kpc)	(km s^{-1})		($''$)	
19199+2100	55.13	3.07	19.040	0.21	−0.49	4.6	—	—	—	
19200+2101	55.14	3.05	30.900	0.21	−0.49	3.6	—	—	—	
19200+1536	50.37	0.48	6.059	0.25	−0.32	8.2	63.0	—	—	ps
19200+1035	45.96	−1.91	3.409	0.24	−0.24	10.9	—	—	—	
19205+1447	49.72	−0.02	5.760	0.34	1.24	8.4	—	—	—	no
19207+1348	48.88	−0.52	7.349	0.24	1.23	7.4	—	—	—	ps
19207+1346	48.85	−0.54	4.172	0.41	1.30	9.6	—	—	—	
19211+1432	49.57	−0.27	4.414	0.41	1.01	9.3	—	—	—	no
19223+1359	49.23	−0.79	6.401	0.25	−0.14	8.0	—	—	—	no
19226+1401	49.29	−0.82	6.401	0.25	−0.14	8.0	—	—	—	no
19228+1403	49.34	−0.86	6.401	0.25	−0.77	8.0	—	—	—	no
19244+1115	47.06	−2.54	1346.000	0.24	−0.51	0.5	—	—	—	
19254+1631	51.80	−0.22	16.570	0.43	−0.09	4.8	3.1	—	—	no
19270+1550	51.40	−0.89	6.048	0.34	1.04	8.2	—	—	—	
19281+2308	57.91	2.42	4.612	0.23	−0.49	9.3	—	—	—	ps
19283+1944	54.95	0.73	88.500	0.31	−0.31	2.1	27.8	—	—	ps
19294+1649	52.54	−0.93	6.694	0.24	0.99	7.8	—	—	—	
19295+2228	57.49	1.82	14.250	0.25	−0.81	5.3	−73.0	—	—	ps
19295+1637	52.37	−1.05	5.051	0.32	1.07	9.0	—	—	—	
19310+1745	53.54	−0.80	12.300	0.42	0.28	5.6	—	—	—	ps
19312+1950	55.37	0.19	22.470	0.50	0.71	4.0	26.1	—	—	ppn
19319+2214	57.55	1.22	3.182	0.32	−0.32	11.3	—	—	—	ps
19327+3024	64.78	5.02	89.390	0.42	−0.16	2.1	—	—	—	ps*
19332+2028	56.15	0.08	6.116	0.25	1.28	8.1	—	—	—	ps
19340+2016	56.08	−0.17	3.374	0.35	1.25	10.9	—	—	—	no
19341+2038	56.41	−0.03	5.569	0.36	0.80	8.5	—	—	—	ps
19344+2457	60.20	2.04	4.946	0.22	−0.68	9.0	—	—	—	
19352+2030	56.41	−0.31	42.890	0.36	−0.36	3.0	—	—	—	ps
19365+1023	47.75	−5.57	3.066	0.28	0.00	11.5	—	—	—	
19374+1626	53.14	−2.76	4.067	0.32	−0.37	10.0	—	—	—	
19421+2507	61.21	0.62	8.114	0.25	−0.59	7.1	—	—	—	
19440+2251	59.48	−0.90	15.700	0.25	−0.38	5.1	−9.4	—	—	no
19473+2638	63.11	0.39	6.026	0.37	0.90	8.1	—	—	—	
19479+2620	62.92	0.09	4.574	0.43	1.22	9.1	—	—	—	
19520+2759	64.81	0.18	46.850	0.40	0.24	2.9	—	—	—	ps
19565+3140	68.45	1.27	6.252	0.36	−0.48	8.0	20.5	—	—	ps
19576+2814	65.67	−0.74	17.410	0.33	−0.38	4.8	−56.8	—	—	ps
19598+3324	70.29	1.60	302.300	0.77	0.77	0.9	—	—	—	sf
20023+2855	66.79	−1.25	5.259	0.44	−0.13	8.4	−65.7	—	—	ps
20028+2903	66.96	−1.28	20.260	0.37	1.06	4.4	—	—	—	sf
20043+2653	65.32	−2.71	17.890	0.37	−0.32	4.7	−4.7	—	—	
20072+2710	65.91	−3.12	3.056	0.35	0.22	11.4	—	—	—	ps
20137+2838	67.93	−3.49	4.459	0.32	−0.62	9.5	—	—	—	
20187+4111	78.87	2.76	65.290	0.22	0.63	2.5	—	—	—	sf
20197+3722	75.84	0.41	423.700	0.46	0.78	0.9	—	—	—	ps*
20237+4003	78.48	1.33	2.202	0.42	0.55	13.2	—	—	—	ps*
20249+3953	78.48	1.04	18.830	0.38	0.76	4.6	—	—	—	ppn
20255+3932	78.26	0.74	5.300	0.13	0.25	8.2	—	—	—	ps
20288+3934	78.68	0.26	3.501	0.41	1.05	10.5	—	—	—	ps
20305+4010	79.34	0.34	2.461	0.48	1.35	12.1	—	—	—	ps
20319+3958	79.35	0.00	26.610	0.78	0.73	3.0	—	—	—	sf
20321+4112	80.35	0.72	5.227	0.73	1.18	7.1	—	—	—	ps
20331+4024	79.83	0.10	7.379	0.69	0.55	6.1	—	—	—	no
20333+4102	80.36	0.44	22.850	0.52	1.22	3.9	—	—	—	ppn?
20446+4613	85.70	2.03	3.250	0.52	1.09	10.3	—	—	—	
20491+4236	83.42	−0.89	54.810	0.10	−0.65	2.4	−40.8	—	—	
21080+4758	89.64	0.17	7.490	0.59	0.67	6.5	—	—	—	
21329+5113	94.79	−0.33	2.477	0.19	1.41	12.5	—	—	—	
23572+6702	117.97	4.94	4.307	0.18	1.20	9.4	—	—	—	

ps: red point source, ps*:bright point source with blue color,
sf: possible star forming region, no: no clear counterpart,
ppn: proto planetary nebula

TABLE 4.2
List of Detections

IRAS name	J=1–0		v=1		J=1–0		v=2		obs. date
	V_{lsr}	T_a	S	rms	V_{lsr}	T_a	S	rms	
	(km s^{-1})	(K)	(K km s^{-1})	(K)	(km s^{-1})	(K)	(K km s^{-1})	(K)	(yymmdd.d)
17192−3206*	−189.6	0.147	0.227	0.046	−191.0	0.399	1.001	0.065	010322.2
17286−3226*	−14.1	0.123	0.128	0.033	−12.3	0.199	0.384	0.044	010322.2
17292−2727*	−68.9	0.149	0.084	0.058	−67.8	0.477	1.753	0.071	010322.3
17295−3321*	0.5	0.132	0.230	0.039	0.6	0.282	0.636	0.049	010322.3
17317−3331*	9.1	2.426	5.516	0.102	7.9	7.025	20.441	0.129	010323.2
17341−3529*	−60.6	0.212	0.487	0.066	−60.7	0.607	0.464	0.083	010322.2
17528−1503*	—	(0.116)	(0.155)	0.041	−62.7	0.268	0.793	0.055	010322.3
17545−2512*	−126.1	2.299	8.126	0.056	−126.4	3.618	12.294	0.073	010322.3
18035−2114*	−37.6	0.387	0.920	0.061	−37.1	0.753	1.321	0.080	010320.3
18080−2238*	54.4	0.279	0.271	0.053	56.6	0.416	1.509	0.064	010322.3
18135−1456*	−4.6	0.735	2.395	0.052	−5.2	0.114	0.046	0.063	010323.3
18152−0919*	26.3	0.520	1.453	0.061	26.4	0.694	1.370	0.075	010322.4
18199−1442*	45.9	0.093	0.127	0.036	46.1	0.461	0.731	0.048	010320.3
18231−1112*	87.4	0.132	0.541	0.037	82.7	0.256	0.816	0.045	010323.3
18242−0823*	150.4	0.124	0.174	0.036	149.6	0.271	0.469	0.049	010323.4
18251−1048*	85.4	0.207	0.783	0.042	86.8	0.565	2.311	0.054	010320.3
18268−1117*	44.9	0.109	0.457	0.046	41.9	1.386	1.590	0.058	010323.4
18348−0526*	27.2	17.172	26.853	0.109	27.2	34.386	65.085	0.140	010323.4
18432−0149*	68.5	1.089	3.491	0.105	67.9	1.924	8.283	0.131	010323.4
18450−0148*	20.1	0.235	1.127	0.049	20.0	0.208	0.360	0.059	010323.4
18488−0107*	76.8	0.320	0.868	0.081	76.9	1.929	6.604	0.101	010322.4
18498−0017*	—	(0.189)	(0.500)	0.069	60.1	0.824	2.449	0.094	010322.5
18509−0018*	38.6	0.738	0.572	0.111	38.3	1.258	3.255	0.140	010322.5
18517+0037*	31.4	0.265	0.727	0.077	27.7	0.952	3.828	0.103	010321.4
18525+0210*	71.4	0.942	1.944	0.096	71.3	2.911	5.972	0.137	010321.4
18540+0302*	102.3	1.533	4.220	0.098	102.5	1.732	5.538	0.136	010321.4
18549+0208*	75.2	0.142	0.245	0.037	75.2	0.384	1.329	0.054	010321.3
18578+0831	49.3	0.313	0.504	0.056	49.7	0.343	0.671	0.064	000520.0
19006+0624	−27.2	0.117	0.045	0.035	−30.7	0.301	0.453	0.042	000520.1
19017+0608*	148.3	0.348	0.370	0.058	149.0	1.708	2.369	0.082	010321.4
19065+0832	52.0	0.250	0.007	0.079	52.3	1.329	3.025	0.091	000521.1
19067+0811	62.0	2.386	8.140	0.124	61.9	4.353	11.839	0.136	000521.1
19069+0916	30.0	0.608	0.895	0.082	30.1	0.611	1.185	0.099	000522.2
19071+0946	—	(0.101)	(0.028)	0.035	8.3	0.484	1.048	0.040	000522.2
19081+0322*	42.6	0.601	1.756	0.083	43.0	0.587	1.960	0.106	010323.5
19128+0910	48.9	0.131	0.124	0.040	50.4	0.300	0.694	0.045	000520.1
19175+1042	42.3	0.453	1.297	0.057	42.2	0.562	1.261	0.065	000523.2
19178+1206	—	(0.090)	(0.142)	0.032	41.3	0.405	0.580	0.058	010110.6
19183+1148	32.2	0.582	0.966	0.071	33.2	0.745	0.953	0.117	010110.7
19188+1057	−23.9	0.263	0.662	0.048	−24.0	0.485	1.532	0.057	000522.3
19200+1536	64.2	0.179	0.422	0.041	61.8	0.214	0.633	0.051	000522.3
19254+1631	3.2	1.775	7.519	0.095	3.0	2.197	9.960	0.111	000523.3
19283+1944	28.0	0.663	2.587	0.079	27.6	0.640	2.549	0.095	000522.4
19295+2228	−73.2	0.706	1.455	0.076	−72.8	1.268	3.292	0.089	000521.2
19312+1950**	25.4	0.131	0.731	0.024	26.8	0.118	0.499	0.022	000531.2
19440+2251	−9.6	0.304	0.781	0.056	−9.1	0.472	0.612	0.070	000520.3
19565+3140	20.7	0.556	1.887	0.074	20.3	0.937	3.728	0.089	000520.3
19576+2814	—	(0.181)	(0.082)	0.076	−56.8	0.684	1.915	0.089	000520.4
20023+2855	−66.2	0.191	0.285	0.064	−65.2	0.678	1.614	0.080	000520.4
20043+2653	−3.9	0.785	2.243	0.088	−5.5	1.186	5.904	0.099	000521.4
20491+4236	−40.8	2.045	6.321	0.129	−40.8	1.502	4.504	0.157	000420.5

*: Sources observed at MSX position (see text).
**: A PPN reported in the separete paper (Nakashima and Deguchi 2000).
(): The numbers in parentheses are tentative results for very week lines.

TABLE 4.3
List of nondetections

IRAS name	rms (J =1–0 v =1) (K)	rms (J =1–0 v =2) (K)	obs. date (yymmdd.d)
17271−3309*	0.078	0.065	010323.2
18008−2419*	0.072	0.059	010323.2
18016−2743*	0.062	0.050	010320.3
18016−2540*	0.070	0.056	010322.3
18042−2131*	0.059	0.044	010320.3
18071−1727*	0.068	0.053	010323.2
18092−1742*	0.068	0.055	010322.4
18112−1801*	0.067	0.053	010323.2
18125−1631*	0.064	0.053	010323.3
18171−1603*	0.060	0.048	010323.3
18184−1449*	0.059	0.046	010323.3
18196−1331*	0.060	0.046	010323.3
18223−1243*	0.058	0.046	010323.3
18262−1233*	0.065	0.051	010323.4
18321−0820*	0.063	0.046	010320.4
18354−0638*	0.076	0.056	010322.4
18418−0415*	0.076	0.060	010322.4
18434−0308*	0.080	0.063	010322.4
18511+0146*	0.084	0.061	010321.5
18529+0210*	0.077	0.056	010321.4
18542+0114*	0.062	0.046	010321.4
18587+0521*	0.089	0.072	010323.5
19008+0530*	0.070	0.050	010321.3
19011+0852	0.039	0.032	000522.1
19011+1049	0.058	0.049	000520.0
19025+0613	0.046	0.047	000524.0
19026+0614	0.046	0.034	010319.4
19045+0518*	0.085	0.063	010321.5
19048+0914	0.044	0.031	010320.2
19057+1002	0.051	0.036	010321.3
19069+1335	0.045	0.056	000522.4
19077+0839	0.049	0.043	000520.0
19080+0748	0.058	0.050	000522.2
19085+0755	0.061	0.051	000522.2
19089+1542	0.048	0.041	000521.1
19108+0901	0.059	0.044	010321.3
19112+1220	0.045	0.036	000521.2
19123+1139	0.063	0.051	000522.2
19134+2131	0.045	0.037	000520.1
19143+1427	0.052	0.037	010321.4
19167+1313	0.060	0.048	000522.3
19171+1119	0.063	0.050	000522.3
19177+1333	0.043	0.035	000521.2
19195+1650	0.052	0.062	000522.3
19199+2100	0.074	0.063	000522.3
19199+2100	0.064	0.078	000522.3
19200+2101	0.056	0.046	000523.2
19200+1035	0.062	0.037	010110.7
19205+1447	0.056	0.047	000523.2
19207+1348	0.056	0.046	000523.2
19207+1346	0.057	0.050	000523.2
19211+1432	0.059	0.048	000523.3
19223+1359	0.058	0.048	000523.3
19226+1401	0.042	0.033	000520.1
19228+1403	0.061	0.054	000523.3
19244+1115	0.115	0.097	000420.4
19270+1550	0.066	0.053	000523.3
19281+2308	0.044	0.036	000521.2
19294+1649	0.064	0.058	000523.3
19295+1637	0.068	0.055	000523.3
19310+1745	0.071	0.063	000523.3
19319+2214	0.044	0.036	000521.3
19327+3024	0.060	0.052	000521.3
19332+2028	0.043	0.036	000520.2
19340+2016	0.066	0.054	000521.3
19341+2038	0.066	0.053	000523.4
19344+2457	0.045	0.038	000520.2
19352+2030	0.079	0.064	000521.3
19365+1023	0.053	0.039	010321.4
19374+1626	0.059	0.052	000521.3
19421+2507	0.045	0.037	000520.3
19473+2638	0.068	0.062	000523.4
19479+2620	0.048	0.041	000520.3
19520+2759	0.061	0.052	000521.3
19598+3324	0.084	0.080	000527.4
20028+2903	0.130	0.106	000520.4
20072+2710	0.056	0.044	000520.3
20137+2838	0.095	0.080	000521.4
20187+4111	0.068	0.059	000420.5
20197+3722	0.082	0.071	000427.5
20237+4003	0.076	0.116	000530.3
20249+3953	0.113	0.098	000426.5
20255+3932	0.056	0.068	000530.4

TABLE 4.3
Continued.

IRAS name	rms (J =1–0 v =1)	rms (J =1–0 v =2)	obs. date
	(K)	(K)	(yymmdd.d)
20288+3934	0.054	0.064	000530.3
20305+4010	0.060	0.067	000530.4
20319+3958	0.058	0.066	000529.4
20321+4112	0.079	0.105	000530.3
20331+4024	0.072	0.080	000529.4
20333+4102	0.079	0.063	000529.4
20446+4613	0.077	0.085	000530.3
21080+4758	0.073	0.065	000527.4
21329+5113	0.062	0.110	000531.3
23572+6702	0.051	0.057	000531.4

*: Sources observed at MSX position (see text).

TABLE 4.4
H_2O detections

IRAS name	ΔV (km s^{-1})	V_c (km s^{-1})	V_p (K)	T_p (K)	Flux (K km s^{-1})	r.m.s. (K)	obs. date (yymmdd.d)
19067+0811	27.8	62.8	76.7	1.243	8.482	0.053	000528.2
			48.9	0.897	7.239		
19069+0916	36.4	−7.5	10.7	2.328	35.166	0.049	000528.2
			−25.7	1.675	8.801		
19312+1950		17.4	17.4	2.339	7.455	0.062	000601.0

TABLE 4.5
H_2O non-detections

IRAS name	r.m.s. (K)	obs. date (yymmdd.d)
18171−1603	0.055	000528.1
18578+0831	0.080	000528.2
19006+0624	0.081	000528.2
19065+0832	0.067	000528.2
19071+0946	0.077	000528.2
19128+0910	0.081	000528.3
19175+1042	0.080	000528.3
19178+1206	0.023	010210.0
19183+1148	0.023	010210.0
19188+1057	0.096	000528.3
19200+1536	0.101	000528.3
19254+1631	0.066	000531.9
19283+1944	0.052	000601.0
19295+2228	0.073	000601.0
19309+2646	0.033	010210.0
19440+2251	0.090	000528.3
19565+3140	0.088	000528.3
19576+2814	0.087	000528.3
20023+2855	0.073	000601.0
20043+2653	0.145	000528.3

TABLE 4.6
Previously detected masers.

IRAS name	OH (1612MHz)			H_2O		SiO, $J=1-0$, $v=1,2$	
	V_{lsr} (km s^{-1})	ΔV (km s^{-1})	ref.	V_{lsr} (km s^{-1})	ref.	V_{lsr} (km s^{-1})	ref.
17192−3206						−190.3	this paper
17286−3226	−12.5	30.5	sev97, tel91			−13.2	this paper
17292−2727	−67.2	35.2	tel91, dav93			−68.3	this paper
17295−3321	0.6	30.1	sev97, tel89, tel91			0.6	this paper
17317−3331	8.6	29.2	sev97, dav93, tel89			8.5	this paper, nym93
17341−3529						−60.6	this paper
17528−1503	−67.5	29.0	tel89			−62.7	this paper
17545−2512	−123.5	45.2	sev97, dav93, tel89			−126.2	this paper
18016−2743	72.5	22.0	sev97, dav93, tel91				
18035−2114						−37.3	this paper
18042−2131	193.3	33.6	sev97				
18071−1727	25.9	16.9	dav93, tel89				
18080−2238	55.0	33.6	sev97, tel91			55.5	this paper
18092−1742	138.5	27.0	tel89				
18135−1456	−1.15	28.2	dav93, tel89	y	eng86	−4.9	this paper, nym93
18152−0919	26.7	28.2	dav93, tel89			26.3	this paper
18196−1331	31.0	18.0	tel89				
18199−1442	40.6	7.7	tel91			46.0	this paper
18231−1112						85.0	this paper
18242−0823						150.0	this paper
18251−1048	91.0	40.0	tel89			86.1	this paper
18268−1117	42.5	34.5	tel91, dav93			43.4	this paper
18348−0526	27.8	27.9	tel91, dav93, tel89	35.0	ces88	27.2	this paper, nym93
18432−0149	67.1	35.1	tel91, dav93, tel89	55.0	ces88	68.2	this paper
18434−0308	76.2	41.0	tel91				
18450−0148	34.0	14.0	tel89			20.1	this paper
18488−0107	75.8	40.9	dav93, tel89			76.9	this paper
18498−0017	60.7	30.8	tel89	48.0	eng86, ces88	60.1	this paper
18509−0018						38.4	this paper
18517+0037	28.0	34.2	tel91, dav93	28.4	eng96	29.6	this paper
18525+0210	70.0	38.6	tel91, dav93	70.7	eng96	71.3	this paper
18540+0302	102.9	37.4	tel91, tel89	85.8	eng96, ces88	102.4	this paper
18549+0208	78.6	27.4	tel91, dav93	y	eng96	75.2	this paper
18578+0831	49.3	29.0	tel91	y	eng96	49.5	this paper
19006+0624	−29.9	30.4	tel91, dav93			−28.9	this paper
19017+0608	149.6	28.5	tel91, dav93	y	eng96	148.7	this paper, jew91
19065+0832	53.1	35.4	dav93, tel89			52.2	this paper
19067+0811	59.5	32.5	dav93, tel89	y	eng96	62.0	this paper,nym93, jew91
19069+0916	31.7	43.6	ede88	26.7	eng96, ces88	30.1	this paper
19071+0946	9.1	23.2	dav93, tel89	y	eng86, eng96	8.3	this paper
19081+0322	42.2	32.0	tel91, dav93	43.0	eng96	42.8	this paper
19085+0755	77.3	38.9	tel91, dav93	78.1	eng96		
19112+1220	62.2	33.1	dav93				
19128+0910	52.4	25.3	tel91, tel89			49.7	this paper
19134+2131				−17.2	ces88		
19175+1042				y	eng96	42.3	this paper
19178+1206						41.3	this paper
19183+1148	35.5	31.8	tel91			32.7	this paper
19188+1057	−21.2	27.2	tel91			−24.0	this paper
19199+2100	56.3	26.2	tel91				
19200+2101	55.3	26.7	tel89				
19200+1536	61.0	26.2	tel91, dav93,tel89			63.0	this paper
19244+1115	76.4	61.4	tel91, tel89				
19254+1631	1.4	37.2	dav93, tel89			3.1	this paper
19283+1944	27.0	28.0	tel89			27.8	this paper
19295+2228	−74.5	25.0	tel89			−73.0	this paper
19312+1950						26.1	this paper
19319+2214	20.6	16.3	dav93	14.2	eng96		
19344+2457	16.1	22.9	tel91				
19352+2030	0.5	7.0	tel89				
19374+1626	−28.6	26.1	tel91, dav93				
19440+2251	−7.58	34.9	dav93, tel89			−9.4	this paper
19565+3140				y	eng96	20.5	this paper
19576+2814	−58.87	21.5	dav93, lik89, tel89			−56.8	this paper
19598+3324				−19	ces88		
20023+2855	−63.65	25.6	dav93, tel89			−65.7	this paper
20043+2653	−4.56	26.4	dav93, lik89			−4.7	this paper
20072+2710	n		che93				
20137+2838				−67.9	ces88, eng96		
20491+4236	−39	36.0	tel89			−40.8	this paper

References: ces88–Cesaroni et al. 1988; che93–Chengalur et al. 1993; dav93–David et al. 1993
eng86–Engels et al. 1986; eng96–Engels and Lewis 1996; jew91–Jewell et al. 1991,
nym93–Nyman et al. 1993; tel89–te Lintel Hekkert et al. 1989; tel91–te Lintel Hekkert 1991

References

[Adams et al.(1987)] Adams, F. C., Lada, C. J., and Shu, F. H. 1987, ApJ, 312, 788

[Alcolea et al.(1999)] Alcolea, J., Pardo, J. R., Bujarrabal, V., Bachiller, R., Barcia, A., Colomer, F., Gallego, J. D., Gómez-González, J., del Pino, A., Planesas, P., del Río, S., Rodoríguez-Franco, A., del Romero, A., Taffella, M., and de Vicente, P. 1999, A&ApS, 139, 461

[Becker et al.(1992)] Becker, R. H., White, R. L., and Proctor, D. D. 1992, AJ, 103, 544

[Blöcker (1992)] Blöcker, T. 1995, A&Ap, 297, 272

[Bowers and de Jong(1983)] Bowers, P. F., and de Jong, T. 1983, AJ, 88, 655

[Bronfman et al.(1996)] Bronfman, L., Nyman, L. -Å., and May, J. 1996, A&ApS, 115, 81

[Bujarrabal et al. (1996)] Bujarrabal, V., Alcolea, J., Sanchez Contrearas, C., Colmer, F. 1996, A&Ap, 314, 883

[Cesaroni et al.(1988)] Cesaroni, R., Palagi, F., Felli, M., Catarzi, M., Comoretto, G., Di Franco, S., Giovanardi, C., and Palla, F. 1988, A&ApS, 76, 445

[Chengalur et al.(1993)] Chengalur, J. N., Lewis, B. M., Eder, J., Terzian, Y. 1993, ApJS, 89, 189

[Dame et al.(2001)] Dame, T. M., Hartmann, D., and Thaddeus, P. 2001, ApJ, 547, 792

[David et al.(1993a)] David, P., Le Squeren, A. M., and Sivagnanam, P. 1993, A&Ap, 277, 453

[David et al.(1993b)] David, P., Le Squeren, A. M., Sivagnanam, P., and Braz, M. A. 1993, A&ApS, 98, 245

[Deguchi et al.(2000a)] Deguchi, S., Fujii, T., Kameya, O., Nakada, Y., and Nakashima, J. 2000a, ApJS, 130, 351

[Deguchi et al.(2000b)] Deguchi, S., Fujii, T., Kameya, O., Nakada, Y., Nakashima, J., Ootsubo, T., and Ukita, N. 2000b, ApJS, 128, 571

[Deguchi et al.(2001)] Deguchi, S., Fujii, T., Matsumoto, S., Nakashima, J., and Wood, P. R. 2001, PASJ, 53, 293

[Deguchi et al.(2001)] Deguchi, S., Nakashima, J., and Balasubramanyam, R. 2001, PASJ, 53, 305

[Diamond et al.(1985)] Diamond, P. J., Norris, R., Rowland, P., Booth, R., and Nyman, L. A. 1985, MNRAS, 212, 1

[Diamond and Nyman(1988)] Diamond, P. J., and Nyman, L. -A. 1988, in: ed Reid, M. J., and Moran, J. M., IAU Symp. 129, The Impact of VLBI on Astrophysics and Geophysics. Kluwer Acad. Pub.(Boston), p.249

[Dickinson and Turner(1991)] Dickinson, D F., and Turner, B. E. 1991, ApJS, 75, 1323

[Eder et al.(1988)] Eder, J., Lewis, B. M., and Terzian, Y. 1988, ApJS, 66, 183

[Engels and Lewis(1996)] Engels, D., and Lewis, B. M. 1996, A&ApS, 116, 117

[Engels et al.(1986)] Engels, D., Schmid-Burgk, J., and Walmsley, C. M. 1986, A&Ap, 167, 129

[Fouqué et al.(1992)] Forqué, P., Le Bertre, T., Epchtein, N., Guglielmo, F., and Kerschbaum, F. 1992, A&ApS, 93, 151

[Frail and Beasley(1994)] Frail, D. A., and Beasley, A. J. 1994, A&Ap, 290, 796

[Fuente et al.(1989)] Fuente, A., Martín-Pintado, J., Alcolea, J., and Barcia, A. 1989, A&Ap, 223, 321

[Fujii(2001)] Fujii, T. 2001, Ph.D. Thesis, Univ. of Tokyo

[Fullmer and Lonsdale(1989)] Fullmer, L., and Lonsdale, C. 1989, Cataloged Galaxies and Quasers Observed in the IRAS Survey (Pasadene: JPL)

[García-Lario et al.(1997)] García-Lario, P., Manchaco, A., Pych, W., and Pottasch, S. R. 1997, A&ApS, 126, 479

[Geballe and Oka(1996)] Geballe, T. R., and Oka, T. 1996, Nature, 384, 334

[Gezari et al.(1998)] Gezari, D. Y., Backman, D. E., and Werner, M. W. 1998, ApJ, 509, 283

[Hasegawa et al.(1985)] Hasegawa, T., Morita, K. -I., Okumura, S., Kaifu, N., Suzuki, H., Ohishi, M., Hayashi, M., and Ukita, N. 1985, in Masers, Molecules and Mass Outflows in Star Forming Rgion, ed Haschick, A. D. (Haystack Observatory)

[Harrington et al.(1997)] Harrington, J. P., Lame, N. J., White, S. M., and Borkowski, K. J. 1997, AJ, 113, 2147

[Herman and Habing(1985)] Herman, J., and Habing, H. J. 1985, A&ApS, 59, 523

[Hillenbrand et al.(1995)] Hillenbrand, L. A., Meyer, M. R., Strom, S. E., and Skrutskie, M. F. 1995, AJ, 109, 280

[Hu et al.(1994)] Hu, J. Y., te Lintel Hekkert, P., Slijkhuis, S., Baas, F., Sahai, R., and Wood, P. R. 1994, A&ApS, 103, 301

[Imai et al.(1999)] Imai, H., Deguchi, S., and Miyoshi, M. 1999, PASJ, 51, 587

[Izumiura et al.(1999)] Izumiura, H., Deguchi, S., Fujii, T., Kameya, O., Matsumoto, S., Nakada, Y., Ootsubo, T., and Ukita, N. 1999, ApJS, 125, 257

[Jewell et al.(1991)] Jewell, P. R., Snyder, L. E., Walmsley, C. M., Wilson, T. L., and Gensheimer, P. D. 1991, A&Ap, 242, 211

[Jiang et al.(1995)] Jiang, B. W., Deguchi, S., Izumiura, H., Nakada, Y., Yamamura, I., 1995, PASJ, 47, 815

[Jiang et al.(1996)] Jiang, B. W., Deguchi, S., Yamamura, I., Nakada, Y., Cho, S. H., and Yamagata, T. 1996, ApJS, 106, 463

[Jiang et al.(1999)] Jiang, B. W., Deguchi, S., and Ramesh,B. 1996, PASJ, 334, 981

[Justtanont et al.(1996)] Justtanont, K., Skinner, C. J., Tielens, A. G. G. M., Meixner, M., and Baas, F. 1996, ApJ, 456, 337

[Kastner et al.(1992)] Kastner, J. H., Weintraub, D. A., and Aspin, C. 1992, ApJ, 389, 357

[Kawamura and Masson(1996)] Kawamura, J., and Masson, C. 1996, ApJ, 461, 282

[Kwok(2000)] Kwok, S. 2000, The origin and evolution of planetary nebulae (Cambridge Univ. Press, Cambridge)

[Langer and Watson(1984)] Langer, S. H., and Watson, W. D. 1984, ApJ, 284, 751

[Lepine et al.(1995)] Lepine, J. R. D., Ortiz, R., and Epchtein, N. 1995, A&Ap, 299, 453

[Le Squeren et al.(1992)] Le Squeren, A. M., Sivagnanam, P., Dennefeld, M., and David, P. 1992, A&Ap, 254, 133

[Lewis(2001)] Lewis, B. M. 2001, private communication

[Likkel(1989)] Likkel, L. 1989, ApJ, 344, 350

[Likkel et al.(1991)] Likkel, L., Forveille, T., Omont, A., and Morris, M. 1991, A&Ap, 246, 153

[Likkel et al.(1992)] Likkel, L., Morris, M., and Maddalena, R. J. 1994, A&Ap, 256, 581

[Masheder et al.(1974)] Masheder, M., Booth, R., and Davies, R. 1974, MNRAS, 166, 561

[Meeus et al.(2001)] Meeus, G., Waters, L. B. F. M., Bouwman, J., van den Ancker, M. E., Waelkens, C., and Malfait, K. 2001, A&Ap, 365, 476

[Meixner et al.(1999)] Meixner, M., Ueta, T., Dayal, A., Hora, J. L., Fazio, G., Hrivnak, B, J., Skinner, C. J., Hoffmann, W. F., and Deutsch, L. K. 1999, ApJS, 122, 221

[Minchin et al.(1991)] Minchin, N. R., Hough, J. H., Burton, M. G., and Yamashima, T. 1991, MNRAS, 251, 522

[Miyoshi et al.(1992)] Miyoshi, M., Morimoto, M., Kawaguchi, N., Ukita, N., Inoue, M., Miyazawa, K., Tsuboi, M., Miyaji, T., et al. 1992, Nature, 371, 395

[Morita et al.(1992)] Morita, K. I., Hasegawa, T., Ukita, N., Okumura, S. K., and Ishiguro, M. 1992, PASJ, 44, 373

[Morris (1981)] Morris, M. 1981, ApJ, 249, 572

[Morris and Bowers (1980)] Morris, M., Bowers, P. F., 1980, 85, 724

[Nakada et al.(1993)] Nakada, Y., Onaka, T., Yamamura, I., Deguchi, S., Ukita, N., and Izumiura, H. 1993, PASJ, 45, 179

[Nakashima and Deguchi(2000)] Nakashima, J., and Deguchi, S. 2000, PASJ, 52, L43

[Nakashima and Deguchi(2001)] Nakashima, J., and Deguchi, S. 2001, PASJ, (submitted to PASJ)

[Nakashima et al.(2001)] Nakashima, J., Deguchi, S., Fujii, T., Izumiura, H., Kameya, O., and Nakada, Y. 2001, ApJ,(submitted to ApJ)

[Nakashima et al.(2000)] Nakashima, J., Jiang, B. W., Deguchi, S., Sadakane, K., and Nakada, Y. 2000, PASJ, 52, 275

[Nyman et al.(1993)] Nyman, L. -Å., Hall, P. J., and Le Bertre, T. 1993, A&Ap, 280, 551

[Nyman et al.(1998)] Nyman, L. -Å., Hall, P. J., and Olofsson, H. 1998, A&ApS, 127, 185

[Nyman and Olofsson(1986)] Nyman, L. -Å., and Olofsson, H. 1986, A&Ap, 158, 67

[Okamoto et al. (2001)] Okamoto,Y. K., Kataza,H., Yamashita,T., Miyata,T., Onaka,T., 2001, ApJ, 553, 254

[Olivier et al. (2001)] Olivier, E. A., Whitelock, P., Marang, F. 2001, MNRAS, 326, 490

[Onaka et al. (1997)] Onaka, T., Yamamura, I., Jong, T. D., Tanabé, T., Hashimoto, O., Izumiura, H. 1997, Ap&SS 255, 33

[Price et al.(1997)] Price, S. D., Egan, M. P., Shipman, R. F., Tedesco, E. F., Cohen, M., Walker, R. G., and Moshir, M. 1997, BAAS, 29, 1294

[Schwartz et al.(1979)] Schwartz, P. R., Waak, J. A., and Bologna, J. M. 1979, AJ, 84, 1349

[Sevenster et al.(1997)] Sevenster, M. N., Chapman, J. M., Habing, H. J., Killeen, N. E. B., and Lindqvist, M. 1997, A&ApS, 122, 79

[Silva et al.(1993)] Silva, A. M., Azcarate, I.N., Poppel, W.G. L., and Likkel, L.1993, A&Ap, 275, 510

[Spencer et al.(1981)] Spencer, J. H., Winnberg, A., Olnon, F. M., Schwartz, P. R., Matthews, H. E., and Downes, D. 1981, AJ, 86, 392

[Suh and Jones (1997)] Suh, K.-W. Jones, T. J. 1997, ApJ, 479, 918

[Suters and Zealey(1991)] Suters, M., and Zealey, W. 1991, PASAu, 9, 140

[Taylor and Cordes(1993)] Taylor, J. H., and Cordes, J. M. 1993, ApJ, 411, 674

[te Lintel Hekkert (1991)] te Lintel Hekkert, P. 1991, A&Ap, 248, 209

[te Lintel Hekkert et al.(1991)] te Lintel Hekkert, P., Caswell, J. L., Habing, H. J., Haynes, R. F., and Norris, R. P. 1991, A&ApS, 90, 327

[te Lintel Hekkert et al.(1989)] te Lintel Hekkert, P., Versteege-Hensel, H. A., Habing, H. J., and Wiertz, M. 1989, A&ApS, 78, 399

[Thé et al.(1994)] Thé, P. S., de Winter, D., and Pérez, M. R. 1994, A&ApS, 104, 315

[Ueta et al.(2000)] Ueta, T., Meixner, M., and Bobrowsky, M. 2000, ApJ, 528, 861

[van der Veen and Breukers(1989)] van der Veen, W. E. C. J., and Breukers, R. J. L. H. 1989, A&Ap, 212, 133

[van der Veen and Habing(1988)] van der Veen, W. E. C. J., and Habing, H. J. 1988, A&Ap, 194, 125

[van der Veen et al.(1989)] van der Veen, W. E. C. J., Habing, H. J., and Geballe, T. R. 1989, A&Ap, 226, 108

[van Hoof et al.(1997)] van Hoof, P. A. M., Oudmaijer, R. D., Waters, L. B. F. M. 1997, MNRAS, 289, 371

[Vassiliadis, Wood (1993)] Vassiliadis, E., Wood, P. R. 1993, ApJ, 413, 641

[Vilas-Boas et al.(2000)] Vilas-Boas, J. W. S., Myers, P. C., and Fuller, G. A. 2000, ApJ, 532, 1038

[Walker and Cohen(1988)] Walker, H. J., and Cohen, M. 1988, AJ, 95, 1081

[Watt and Mundy(1999)] Watt, S., and Mundy, L. G. 1999, ApJS, 125, 143

[Wilking et al.(1989)] Wilking, B., Lada, C. J., and Young, E. T. 1989, ApJ, 340, 823

[Yamamura et al.(1996)] Yamamura, I., Onaka, T., Kamijo, F., Deguchi, S., Ukita, N. 1996, ApJ, 465, 926

[Zuckerman (1978)] IAU sympo. 78, "Planetary nebulae" (Reidel; Dordrecht) P305

Chapter 5

Detections of SiO and H_2O Masers in the Bipolar Nebula IRAS 19312+1950

Abstract

We report on the detection of SiO and H_2O masers toward a newly found bipolar nebula, IRAS 19312+1950. This object exhibits extreme red IRAS color [$\log(F_{25}/F_{12}) = 0.5$ and $\log(F_{60}/F_{25}) = 0.7$] and a nebulosity having a size of about 30″ extended to the South–West in the 2MASS near-infrared image. Toward this object, we have detected emission from the H_2O 6(1,6)–5(2,3) transition, the SiO $J = 1 - 0, v = 1$ and 2, and $J = 2 - 1, v = 1$ transitions, and the SO 2(2)–1(1) and $H^{13}CN$ $J = 1 - 0$ transitions. The thermal lines of SO and $H^{13}CN$ are shifted by about 12 km s^{-1} in radial velocity with respect to the maser lines, indicating that thermal emission comes from the background molecular cloud. However, the SiO $J = 2 - 1, v = 2$ spectrum shows another component of SiO emission separated by 26 km s^{-1} from the main component, that might be formed in a rotating or expanding shell.

5.1 Introduction

SiO, H_2O, and OH masers have been known to be associated with late-type stars. These are stars on the Asymptotic Giant Branch (AGB) with a large mass loss rate. Occasionally, an OH 1612 MHz maser has been found in the envelopes of further evolved objects, e.g., proto-planetary and planetary nebulae (Nyman et al. 1998). The central stars of these nebulae are in the post-AGB phase or beyond (white dwarf), in which the AGB mass loss has already ceased.

These evolved objects are very often recognized based on their peculiar shape on the optical and near-infrared images (Kwok 2000), or from their spectral energy distribution(Kwok 1990). The point-symmetric morphology of proto-planetary and planetary nebulae has been well studied recently with the Hubble Space Telescope (Sahai 1999; Ueta et al. 2000). However, it is not clear whether the aspherical shape of these objects is developed throughout the AGB phase, or only in the last transient phase of mass loss to the proto-planetary nebula.

SiO masers are emitted in an envelope close to the central star, and OH masers much further away (Lewis 1989). When the mass loss ceases, the H_2O and SiO masers disappear within a few years, whereas the OH masers remain active also during the proto-planetary and early planetary nebula stages (Lewis 1989). Therefore, SiO and H_2O masers can be useful probes for the mass loss of transient objects.

During a survey of galactic disk objects with very red IRAS colors for SiO masers at Nobeyama, we found SiO masers in IRAS 19312+1950 with $F_{12} = 22.5$ Jy and the colors $C_{12} \equiv \log(F_{25}/F_{12}) = 0.50$ and $C_{23} \equiv \log(F_{60}/F_{25}) = 0.70$, one of the reddest objects with SiO masers in this survey. Here, F_{12}, F_{25}, and F_{60} are the IRAS flux densities at 12, 25, and 60 μm, respectively. A bipolar-type nebulosity is seen in the 2MASS near-infrared, J,H,K–band image of this object. Up to now, one positive detections and three questionable detections of SiO masers from proto-planetary nebula candidates have been reported (Nyman et al. 1998). This object is the second detection of SiO masers in this type of object. The observed spectra of maser and thermal lines toward IRAS 19312+1950 show slightly odd characteristics, i.e., two peaks in the SiO maser spectrum, and a shift in the radial velocity of the $H^{13}CN$ and SO lines from the maser lines. In this letter, we report on molecular line observations of this newly found interesting object.

5.2 Observations

The observations were made in 2000 May with the 45-m radio telescope at Nobeyama. The detected lines and the observed line parameters are summarized in table 5.1. The galactic coordinates of IRAS 19312+1950 are (l, b) = (55.4°, 0.20°). The IRAS position at the epoch of 1950.0 was used for the observations. The half-power beam width (HPBW) of the telescope was 72″ at 23 GHz, 38″ at 43 GHz and 18″ at 86 GHz, respectively. The pointing was checked every 2 or 3 hours with the nearby strong SiO maser sources, V1111 Oph, or, χ Cyg. A typical position error for an IRAS source is less than 10″ (Jiang et al. 1996), accurate enough if compared with the telescope HPBW of about 20″ at 43 GHz. The typical pointing accuracy of the telescope was about 5″, or under windless condition, a pointing accuracy better than 2″ was achieved. We used a cooled HEMT amplifier at 22 GHz, and SIS mixer receivers at 43 and 86 GHz. The system temperature (including atmospheric noise) was 190–400 K at 22 GHz, 160–270 K at 43 GHz, and 250–300 K at 86 GHz, depending on the weather conditions. The aperture and main-beam efficiencies were 0.64 and 0.82 at 23 GHz, 0.58 and 0.73 at 43 GHz, and 0.45 and 0.53 at 86 GHz, respectively. Acousto–optical spectrometer arrays, AOS-H and AOS-W, with 40 and 250 MHz bandwidths with 2048 frequency channels each were used as backends. A high-resolution spectrometer (AOS-H) was used for the SiO ($J = 1-0, v = 1$ and 2) and H_2O maser lines, and a spectrometer with a wide band coverage (AOS-W) was used for both SiO ($J = 2-1, v = 1$ and $J = 1-0, v = 1$ and 2) lines. The SO 2(2)–1(1) and $H^{13}CN$ $J = 1-0$ lines at 86.094 and 86.340 GHz were also observed with the same spectrometer (AOS-W) observing the SiO $J = 2-1, v = 1$ line. The effective spectral resolution was 1.74 km s^{-1} at 43 GHz and 0.87 km s^{-1} at 86 GHz in the case of AOS-W, and 0.28 km s^{-1} at 43 GHz, and 0.55 km s^{-1} at 22 GHz in the case of AOS-H. All of the observations were made in the position–switching mode using a 10′ off position in azimuth.

The observational results are summarized in table 5.1 and the spectra obtained are shown in figure 5.1. Emission from the SiO $J = 2-1, v = 1$, and $J = 1-0, v = 1$ and 2, and H_2O lines were found near $V_{\rm lsr} = 20$ km s^{-1}. However, the SO and $H^{13}CN$ lines ($V_{\rm lsr} \simeq 32$ km s^{-1}) are significantly shifted in radial velocity from the maser lines. Looking carefully at the spectrum of the SiO $J = 1-0, v = 2$ transition (the second spectrum from the bottom in figure 5.1), we recognized the presence of another component at 52.8 km s^{-1}. The corresponding component in the SiO $J = 1-0, v = 1$ spectrum was missing. In the spectrum of the SiO $J = 1-0, v = 1$ transition, a faint secondary component can be seen around $V_{\rm lsr} = 18.0$ km/s, at the left of main peak at 25.5 km s^{-1}. These differences in radial velocities in the different transitions need careful interpretation, and are discussed in the next section.

5.3 Discussion

The IRAS color of 19312+1950, $(C_{12}, C_{23}) = (0.50, 0.78)$, suggests a uniqueness of this object. In a two-color diagram (van der Veen, Habing 1988), this object falls into region VIII, which is occupied by a number of

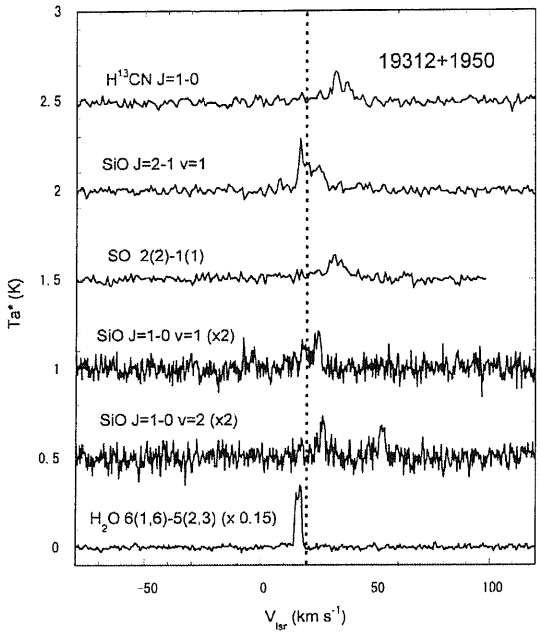

Figure 5.1: Spectra of the molecular lines detected in IRAS 19312+1950. The antenna temperatures of the bottom three spectra are scaled by factors of 2, 2, and 0.15. The vertical broken line shows a guide for the eye to mark the stellar radial velocity which, is adopted to be at about $V_{\rm lsr}$ =20 km s^{-1}. The spectrum in the SiO $J = 1 - 0v = 1$ transition was contaminated by strong spurious signals in the receiver system at $V_{\rm lsr} = -10$ — -5 km s^{-1}, so that the bad channels were removed.

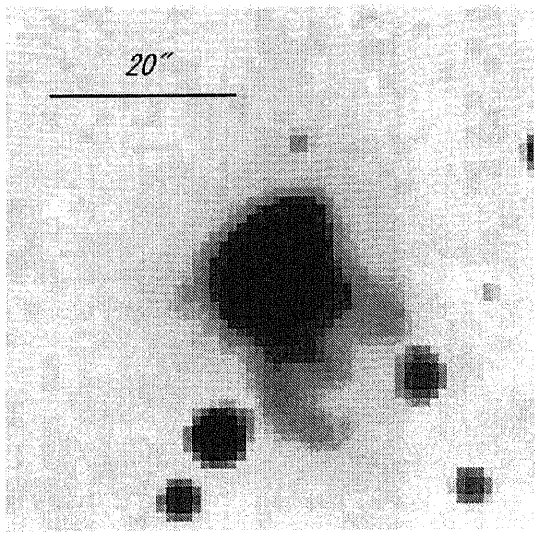

Figure 5.2: Composite near-infrared image from 2MASS data archive, composed of J, H and K-band images. The image size is $1' \times 1'$. The center of the image is the IRAS position of 19312+1950, and north is up, west is right.

very cool stars. About 30% of objects with the IRAS LRS spectra in region VIII indicate planetary nebulae. The LRS spectra of this object (Volk et al. 1991) exhibits weak silicate absorption on a red continuum. On the other hand, this object mimics the color of young stars found in star–forming regions (MacLeod et al. 1998a). Based on the IRAS colors, it is hard to classify IRAS 19312+1950 as a young planetary nebula or a young star in a star–forming region. It is not surprising that a negative result of the 6.7 GHz methanol maser search was reported toward this object (MacLeod et al. 1998b).

Figure 5.2 shows the 2MASS near-infrared image (Skrutskie et al. 2000) [1] of the region around IRAS 19312+1950. We can see a nebulosity with two horns extended towards to south west. These horns can clearly be seen on this image, though the IRAS source is point-like in the J band. From this image and the detections of SiO masers in this source, we conclude that this is a post-AGB star surrounded by a bipolar-type nebulosity (like the Rotten Egg Nebula, OH 231.8+4.2; Morris et al. 1987). There is no nearby infrared star which is bright in the 2MASS K-band image. We conclude that the extended nebulosity at the center of figure 5.2 is a part of this object.

A more observational investigation is necessary to clarify the nature of this object. For instance, the radial velocities of the maser and thermal lines toward this object are puzzling. From the velocities of the

[1] Atlas Image obtained as part of the Two Micron All Sky Survey (2MASS), a joint project of the University of Massachusetts and the Infrared Processing and Analysis Center/California Institute of Technology, funded by the National Aeronautics and Space Administration and the National Science Foundation, U.S.A.

maser lines (SiO and H_2O), we infer a stellar velocity of approximately $V_{lsr} = 20$ km s^{-1} [it is well known that the SiO radial velocity coincides with the stellar velocity (Jewell et al. 1991), while H_2O spectra often exhibit single or double peaks centered at the stellar velocity (Engels, Lewis 1996)]. However, the $J = 1 - 0, v = 2$ spectrum exhibits another component at $V_{lsr} = 52$ km s^{-1}. It is possible that this interloper component comes from a nearby source which is located by chance in the same telescope beam of about 40″ toward this object; such examples are already known for two cases among the densely populated disk IRAS sources (Deguchi et al. 1999). On the other hand, it is possible to interpret this component as part of a doubly peaked profile which is formed in a rotating disk or expanding shell surrounding this object. In this case, the stellar velocity would be $V_{lsr} \simeq 39$ km s^{-1}. If this is correct, it is also possible (but less plausible) to interpret this source as a young stellar object. In past studies, the detection of SiO masers in several star-forming regions has been reported (e.g., Hasegawa et al. 1986; Snyder, Buhl 1974). A doubly peaked profile with a separation of more than 20 km s^{-1} was found in Orion IRc2, and has been explained by a rotating and expanding disk model (Plambeck et al. 1990; Barvainis 1984). On the other hand, SiO masers from proto-planetary nebula show a somewhat broad line profile in past studies; it resembles to a typical profile of SiO masers from a circumstellar envelope of the Mira-type variables (e.g., Nyman et al. 1998). Up to now, no clear doubly peaked profile of SiO masers in the bipolar nebulae has been reported.

The radial velocities of $H^{13}CN$ and SO are shifted by about 12 km s^{-1} from the maser lines. Because of this large separation in radial velocities and the slightly asymmetric profiles of these lines, we consider that these thermal lines come from a background molecular cloud. According to the Columbia CO survey in the galactic disk (Cohen et al. 1986), CO emission at $(l, b) = (55.0°, 0.25°)$ is peaked at $V_{lsr} \simeq 30$ km s^{-1}, which coincides with the radial velocities of $H^{13}CN$ and SO found in this paper. However, we cannot completely neglect the possibility that the two broad lines of $H^{13}CN$ and SO come from the outflowing envelope of this object, unless the component (V_{lsr} =52 km s^{-1}) of SiO is proved to come from a totally different source by chance, and until the CO emission in the background molecular cloud is mapped by telescopes with better spatial resolution.

It is known that very few sources are detected in SiO masers beyond $C_{12} = 0.5$ (Nyman et al. 1998); only two stars, OH 231.8+4.5 and OH 15.7+0.8, are such extreme sources with $C_{12} > 0.5$ accompanying SiO. However, the color C_{23} of these sources are below 0.4. One of the sources with the colors compatible to 19312+1950, is IRAS 18498−0017 (OH 32.8−0.3; $C_{12} = 0.46$ and $C_{25} = 0.74$); H_2O, SiO, and OH masers have been detected in this source (Cesaroni et al. 1988; Engels, Heske 1989; te Lintel Hekkert et al. 1989). Near-infrared images of this source are not available at present in the 2MASS archive. It is quite interesting to see if this source also exhibits a bipolar-type nebulosity or not. The color, $C_{23} \sim 0.7$, of these two objects seems to be meaningfully higher than those of OH 231.8+4.5 and OH 15.7+0.8. However, because the positions of 18498−0017 and 19312+1950 are very near to the galactic plane ($b = -0.04°$ and 0.2°), emission from the interstellar dust grains possibly contaminates the 60 μm flux densities of these objects, as found by the Nobeyama SiO maser survey of the galactic disk IRAS sources (Izumiura et al. 1999). The long-term near-infrared monitoring of 18498−0017 (Engels et al. 1983) found a variability with a time-scale of more than 1700 d, suggesting that 18498−0017 is not a normal Mira variable. It may be at a transient stage to the proto-planetary nebula.

5.4 Summary

In this letter, we have reported the detection of SiO and H_2O masers from a newly found bipolar nebula, IRAS 19312+1950. We also observed thermal lines of SO and $H^{13}CN$ toward this source, though they are shifted in radial velocity and are probably attributed to the molecular cloud in the same direction.

TABLE 5.1
Observational Results

Molecule	Transition	Frequency (GHz)	T_{peak} (K)	V_{lsr} (km s^{-1})	Flux (K km s^{-1})	r.m.s. (K)	obs. date (yyyy.mm.dd)
H_2O	6(1,6)-5(2,3)	22.2351	2.339	17.4	7.455	0.127	2000.05.30
SiO	$1-0$ v=2	42.8206	0.118	26.8	0.357	0.022	2000.05.30
			0.107	52.8	0.345	0.022	2000.05.30
SiO	$1-0$ v=1	43.1221	0.113	25.5	0.607	0.027	2000.05.30
SO	$2(2)-1(1)$	86.0936	0.149	32.0	1.657	0.015	2000.05.25
SiO	$2-1v=1$	86.2434	0.285	17.4	1.962	0.015	2000.05.25
$H^{13}CN$	$1-0$ $(F=2-1)$	86.3402	0.165	32.3	1.110	0.019	2000.05.25

References

[Barvainis(1984)] Barvainis R. 1984, ApJ, 279, 358

[Cesaroni et al.(1988)] Cesaroni R., Palagi F., Felli M., Catarzi M., Comoretto G., Di Franco S., Giovanardi C., Palla F. 1988, A&ApS, 76, 445

[Cohen et al.(1986)] Cohen R.S., Dame T.M., Thaddeus P. 1986, apjs, 60, 695

[Deguchi et al.(1999)] Deguchi S., Fujii T. Izumiura H., Matsumoto S., Nakada Y., Wood P. R., Yamamura I. 1999, PASJ, 51, 355

[Engels and Heske(1989)] Engels D., Heske A. 1989, A&ApS, 81, 323

[Engels et al.(1983)] Engels D., Kreysa E., Schultz G.V., Sherwood W.A. 1983, A&Ap, 124, 123

[Engels and Lewis(1996)] Engels D., Lewis B.M., 1996, A&ApS, 116, 117

[Hasegawa et al.(1986)] Hasegawa T., Morita K.-I., Okumura S., Kaifu N., Suzuki H., Ohishi M., Hayashi M., Ukita N. 1986, in Masers, Molecules and Mass Outflows in Star Forming Regions, ed Haschick A.D. (Haystack Observatory, MA) p275

[Izumiura et al.(1999)] Izumiura H., Deguchi S., Fujii T., Kameya O., Matsumoto S. Nakada Y., Ootsubo T., Ukita N., 1999, ApJS, 125, 257

[Jewell et al.(1991)] Jewell P.R., Snyder L.E., Walmsley C.M., Wilson T.L., Gensheimer P.D. 1991, A&Ap, 242, 211

[Jiang et al.(1996)] Jiang B.W., Deguchi S., Nakada Y. 1996, AJ, 111, 231

[Kwok(1990)] Kwok S. 1990, A.S.P. Conf. Ser. 9, 438

[Kwok(2000)] Kwok S., 2000, The Origin and Evolution of Planetary Nebulae (Cambridge Univ. Press., Cambridge), p.89

[Lewis(1989)] Lewis B.M. 1989, ApJ, 338, 234

[MacLeod et al.(1998a)] MacLeod G.C., Scalise E.Jr., Saedt S., Galt J.A., Gaylard M.J. 1998a, AJ, 116, 1897

[MacLeod et al.(1998b)] MacLeod G.C., van der Walt D.J., North A., Gaylard M.J., Galt J.A., Moriarty-Schieven G.H. 1998b, AJ, 116, 2936

[Morris et al.(1987)] Morris M., Guilloteau S., Lucas R., Omont A. 1987, ApJ, 321, 888

[Nyman et al.(1998)] Nyman L.-Å., Hall P.J., Olofsson H. 1998, A&ApS, 127, 185

[Plambeck et al.(1990)] Plambeck R.L., Wright M.C.H., Carlstrom J.E. 1990, ApJL, 348, L65

[Sahai(1999)] Sahai R. 1999, ApJ, 524, L125

[Skrustkie et al.(2000)] Skrutskie M.F., Stiening R., Cutri R., Beichman C., Capps R., Carpenter J., Chester T., Elias J. et al. 2000 (The 2MASS Team)
http://www.ipac.caltech.edu/2mass/index.html

[Snyder and Buhl(1974)] Snyder L.E., Buhl D. 1974, ApJL, 189, L31

[te Lintel Hekkert et al.(1989)] te Lintel Hekkert P., Versteege-Hensel H.A., Habing H.J., Wiertz M. 1989, A&ApS, 78, 399

[Ueta et al.(2000)] Ueta T., Meixner M., Bobrowsky M. 2000, ApJ, 528, 861

[van der Veen and Habing(1988)] van der Veen W.E.C.J., Habing H.J. 1988, A&Ap, 194, 125

[Volk et al.(1991)] Volk K., Kwok S., Stencel R.E., Brugel E. 1991, ApJS, 77, 607

Chapter 6

Mapping Observations of Proto-Planetary Nebula IRAS 19312+1950

Abstract

Mapping observations of IRAS19312+1950 were made in molecular lines of the CO $J = 1 - 0$, ^{13}CO $J = 1 - 0$, C^{18}O $J = 1 - 0$, CS $J = 2 - 1$, and HCN $J = 1 - 0$ transitions and in the 150GHz continuum band with the Nobeyama 45-m radio telescope. In addition, imaging observations were made in the near-infrared J, H, and K-bands with the ANU 2.3-m telescope. This object exhibits a prominent bipolar nebulosity on near-infrared images. Line profiles of ^{12}CO and HCN consists of a weak broad component of the width of about 50 km s^{-1} and a strong narrow component of the width of about 3 km s^{-1}. Profiles of the ^{13}CO, C^{18}O, and CS lines have only a narrow component. Mapping observations show that both of the components have an intensity peak at the IRAS position of IRAS 19312+1950. The narrow component was clearly resolved with the 15″ telescope beam. A velocity gradient was detected along the direction perpendicular to the bipolar axis, indicating the mass of about 6 $M_\odot$ for the narrow component. The spectral energy distribution of this object shows a flat top feature. The 150 GHz continuum flux density, 0.07 Jy, which was detected in this observation, is consistent with the flux density predicted by the expanding envelope model with mass loss rate of $2 \times 10^{-4} M_\odot$ y^{-1} at the distance of 4 kpc. We consider that the broad component is formed in the expanding envelope of this object. It is argued that the cloud, which is responsible for the narrow component, is also physically associated with this object. We conclude that IRAS 19312+1950 is an object at an early protoplanetary phase of the star, which is evolved from a massive progenitor.

6.1 Introduction

Proto-planetary nebulae are transient objects between the asymptotic-giant-branch (AGB) and planetary nebula phases of stellar evolution. They are key objects for understanding the formation of planetary nebulae. OH and H_2O masers have been searched for late-AGB stars and proto-planetary nebulae (e.g., Likkel 1989; Hu et al. 1994), but a relatively little work has been made in SiO masers. Gomez et al. (1990) observed SiO ($v = 1$, $J = 1 - 0$) and H_2O masers in OH/IR stars and a few proto-planetary nebulae. They found that the detection rate of SiO and H_2O masers drops with the IRAS [25-12] color which is a temperature/evolutionary-stage indicator of dust envelopes. Observations of SiO masers in OH/IR stars were also made by Jewell et al. (1991), and Nyman et al. (1986, 1993).

Though H_2O, and OH masers have often been found in proto-planetary nebulae, SiO masers were rarely found in these objects. The SiO masers are emitted in the circumstellar envelopes very close to the central star ($\sim 10^{14}$ cm), and OH masers further away ($\sim 10^{16}$ cm). Therefore, when the mass loss terminates, SiO masers disappear first, whereas OH masers remain active also during the proto-planetary and early planetary nebula stages (Lewis 1989). Therefore, only a few proto-planetary nebulae with SiO masers have been found in the past; for example, OH231.8+1.4, is an object with SiO masers (e.g. Barvainis et al. 1986; Nyman et al. 1998). Nakashima and Deguchi (2002) found new SiO masers in three of them. In particular, the source, IRAS 19312+1950, have a bipolar nebulosity with large angular size more than $40''$ on the 2MASS near-infrared images (Skrutskie et al. 2000). This is a second example of SiO maser detections in a prominent proto-planetary nebula after OH231.8+4.2.

This object, IRAS 19312+1950, is unusual in several respects. First, it appears oxygen-rich by virtue of detections of SiO, H_2O and OH masers (Nakashima and Deguchi 2000; Lewis 2000; Chapter 5 in this thesis) and thermal lines of SO (Deguchi and Nakashima 2002; Appendix A in this thesis). But, in addition, emission from $H^{13}CN$ was detected toward this object (Nakashima and Deguchi 2000; Deguchi and Nakashima 2002; Chapter 5 and Appendix A in this thesis). This molecule is normally considered an indicator of carbon-rich circumstellar chemistry under equilibrium conditions, though several exceptions have been found at non-equilibrium (Deguchi and Goldsmith 1985; Deguchi et al. 1986).

Secondly, it display a remarkable double peak feature in the SiO maser in the J =1–0, v =2 transition and the SiO maser features exhibit strong time variation (Nakashima and Deguchi 2000; Deguchi and Nakashima 2002; Chapter 5 and Appendix A in this thesis). Spectral features of OH masers are also quite unusual, exhibiting multiple spiky features around the systemic velocity (Lewis 2002).

This object has a cool dust envelope; the IRAS color, $\log(F_{25}/F_{12}) = 0.47$, indicates a presence of cool dust with the temperature of about 200 K around the central star. This IRAS color is at a boundary between late-AGB and PPNe phases (Nyman et al. 1998).

Because IRAS 19312+1950 has prominent and unparalleled characteristics as a protoplanetary nebula, we decide to observe this object more carefully. This object may involve important clues to solve the puzzle of mass ejection mechanisms in one class of cool, mass-losing objects at the very early stage of proto-planetary nebula evolution. In this chapter, we report a result of mapping observations in molecular lines of ^{12}CO, ^{13}CO, $C^{18}O$, HCN, and CS, and in 150GHz continuum band using Nobeyama 45-m telescope. The spatial and kinematical structure of the dust/molecular envelope around the central star have been revealed. In addition, we made photometric and imaging observations in near-infrared J, H, K broad bands and the Br γ and H_2 v=1-0, S(1) bands. We have also made molecular line observations by other lines, which clarify the special circumstellar chemistry of this object. A part of circumstellar chemistry of this object will be, however, presented in Appendix of this thesis.

6.2 Observations and Results

6.2.1 Observations

Mapping observations in the CO $J = 1 - 0$, ^{13}CO $J = 1 - 0$, $C^{18}O$ $J = 1 - 0$, CS $J = 2 - 1$, and HCN $J = 1 - 0$ transitions were made with the 45-m telescope at Nobeyama during 2001 February 4 – 9. A cooled SIS-mixer receiver (S100) with a bandwidth of about 0.5 GHz were used, and the system temperature (including atmospheric noise) was 300 - 500 K (SSB) depending on the frequency and weather. The aperture efficiencies at 86, 100 and 110 GHz were 0.41, 0.36 and 0.31, respectively. The main beam efficiencies at 86, 100 and 110 GHz were 0.49, 0.45 and 0.42, respectively. The half power full widths of the main beam were $19.8''$, $17.1''$, and $15.6''$ at 86, 100 and 110 GHz, respectively. The antenna temperature (T_a) given in the present paper is that corrected for the atmospheric and telescope ohmic loss but not for the beam or aperture efficiency. Acousto-optical spectrometer arrays with wide frequency coverages (AOS-W) were used. The AOS-W 2048-channel spectrometer have 250MHz bandwidth, giving the velocity coverage of about 800 km s^{-1} and the spectral resolution of about 0.85 km s^{-1} at 86 GHz. The rest frequencies of molecular lines were taken from Lovas (1992). For intensity calibration and check of tuning frequencies of molecular lines, we observed the corresponding molecular lines toward W51 (e.g., Bell et al. 1993) every time prior to the observations of IRAS 19312+1950 and confirmed that the strong lines were detected toward this cloud. The telescope pointing was checked using the strong SiO maser source, V1111 Oph, and the point-

ing accuracy was confirmed to be better than 3″ under windless condition. The mapping patterns for lines are summarized in Table 6.1. The bipolar axis of this nebula on the 2MASS images is oriented approximately by 45° from the north (to the east). Therefore, the cross or rectangular mappings were made along the perpendicular and parallel direction to the bipolar axis; it is rotated by 45° to anti-clock wise to the north. The IRAS position of this object (19h 31m 12.800s, 19° 50′ 22.00″, B1950) was taken as a map center. Because contamination by background molecular emission was expected, we have carefully chosen the offset positions for position switching; it is 20′ away from the mapping center (in the galactic latitude). The raw spectral data were processed, flagging out bad scans, integrating with rms-weighted means, and removing slopes in baselines.

The continuum observations at 150GHz were made on 11 and 12 January 2001 with the Nobeyama Bolometer Array (NOBA) mounted on the Nobeyama 45-m telescope. NOBA is a seven-element bolometer array using a differential readout method (Kuno et al. 1993). The band pass of the filter was centered at 147 GHz with a bandwidth of 30 GHz. The half-power full width (HPFW) of the beam was 12″. Maps were made with raster scans along the right ascension and declination. The scanning speed was 15″ s^{-1}, and the scans were separated by 5.3″ by tilting the array pattern 19.1° from scan direction. Since the AC-bridge read-out technique, which effectively eliminates atmospheric emission without a beam switch, was adopted, the original restoration method was applied in order to obtain a two-dimensional map. These maps were combined using a basket-weaving method to correct for any scanning effects. The size of the final map is 1.9′ × 1.9′ with a grid spacing of 5.3″. The final integration time per sampling point was about 40s. The rms noise level of the final map is ∼ 10 mJy $beam^{-1}$. Further details concerning observations and data reduction for NOBA are described in Kuno (1993). Pointing and flux calibrations were performed every hour by observing 3C345 and NGC7027. We assumed that the spectrum of 3C345 is flat in the observational band. Atmospheric extinction was corrected using the opacity of the atmosphere measured between observations. From the errors of these calibrations and the variation in the antenna efficiency due to wind, the uncertainty of the absolute flux density was estimated to be ± 30%.

Near-infrared photometric observations were made with the 2.3-m telescope of Australian National University at Siding Spring Observatory, Australia, on 2000 July 7 using the infrared array camera CASPIR. This camera used a 256×256 InSb detector array with 0.5″ per pixels at the sky, covering a field of view of 128″ × 128″. The seeing size was generally 1–2″. To prevent saturation of the array, a short exposure time was used (0.3 sec × 100 cycle for H and K, 1 sec × 100 cycle for J, and 12 sec × 10 cycle for Br γ and H_2). To determine photometric magnitudes in the standard system, we took images of standard stars near of the IRAS 19312+1950. Data were reduced with the IRAF data reduction package using standard way; dark frames were subtracted from raw data, flat fielding using dome flat frames was done, and magnitudes of stars were measured by aperture photometry technique using DIGIPHOTO package in IRAF.

6.2.2 Results of Molecular Line Mappings

Figures 6.1a–e show spectra of the CO $J = 1 - 0$, ^{13}CO $J = 1 - 0$, C^{18}O $J = 1 - 0$, HCN $J = 1 - 0$, CS $J = 2 - 1$ lines toward IRAS 19312+1950, respectively. Line parameters are given in Table 6.2. We have detected strong CO emission toward IRAS 19312+1950. However, the 60″-grid 9 points cross mappings revealed that emission spikes at V_{lsr} = 27– 33, and 43 km s^{-1}, are extended more than a few arc minutes, indicating that these are from back/foreground clouds. With the 15″ grid mapping, we found that the component at V_{lsr} = 38 km s^{-1} is sharply peaked in intensity at the IRAS position. The raw spectra indicated that the spectral features of the back/foreground clouds are relatively homogeneous over the mapping regions. Therefore, in order to obtain the spectral features of the object, we averaged the spectra at the 22″ to 60″ offset points surrounding the object, and made an average background spectrum (see captions of Figure 6-1).

Then we subtracted it from the original on-source spectrum and obtained the (supposedly) background-free spectra. This process were made for all of the lines, though contamination by background emission was not so severe except in the CO $J = 1-0$, and ^{13}CO $J = 1 - 0$ lines. For the case of the ^{13}CO $J = 1 - 0$ line, the background emission was not perfectly flat, so that the subtracted spectrum (figure 6.1b) still exhibits weak emission at $V_{\rm lsr}$ =28 and 45 km s^{-1}. Figure 6-1 shows the raw spectra at the mapping center (thin line), the averaged background features (broken line), and the background-subtracted spectra (bold line) at the mapping center for each molecular line. For the further analysis, we use the background-subtracted spectra to avoid the background contamination.

All of the spectra exhibit a clear narrow feature with a width about ∼ 2–3 km s^{-1} (here after narrow component) around $V_{\rm lsr}$ =∼ 36 km s^{-1} in each spectrum. The width of the narrow components seems to vary from molecule to molecule. For instance, the lines of ^{12}CO, ^{13}CO and C^{18}O has the full width at half maximum of about 3.0, 2.3, and 2.0 km s^{-1}, respectively.

On the other hand, the background-subtracted spectra of ^{12}CO (solid line in Figure 6.1a) exhibit a weak broad feature with the line width of about 40 km s^{-1} (see Figure 6.1f). This is quite weak and difficult to distinguish from the noise or background emission. However, in figures 6.1a and 6.1f, we can clearly see emission at $V_{\rm lsr}$ = 20–25 km s^{-1} and 48–55 km s^{-1}, which

are significantly above the background emission (broken curve in Figure 6.1a). The presence of this component can be seen more clearly in the HCO^+ spectra which is free from the background contamination (see figure A.2 in Appendix). In the case of HCN, we can also see a possible broad component, though it is not so clear because of the hyperfine splitting of the HCN $J = 1 - 0$ transition: F =0–1, 2–1, and 1–1. These hyper fine lines appear at $\Delta V = -7.44$ and +4.68 km s^{-1} relative to the main $F = 2 - 1$ line (89.08792GHz), and the LTE (optically thin) line intensity ratios are 1:5:3 (e.g. Cao et al. 1993), where the rest frequency of the strongest transition, F = 2–1, was taken as an origin of the radial velocity of HCN. This broad component has also been seen in the spectrum of thermal lines of SO, HCO^+, and SiO (see Appendix A; these are background free spectra).

Figures 6.2a–e show integrated-intensity maps. In these maps, the Y-axis was taken along the direction of the bipolar axis of the nebula; it is inclined by 45° from the north. The background emission was also subtracted in these position-intensity maps. For making these maps, the data taken on the different days in different mapping patterns were combined, because the wind often prevented to continue mappings (of course, wind speed more than 10 m s^{-1} were discarded). In the cases of ^{12}CO and HCN, we made two maps for broad and narrow components. We took emission in radial velocity ranges from 0 to 30 km s^{-1} and from 50 to 60 km s^{-1} for the broad component of ^{12}CO, and from 0 to 32 km s^{-1}, from 26 to 32 km s^{-1}, and from 48 to 70 km s^{-1} for the broad component of HCN. The broad component in the HCN spectrum is somewhat difficult to see because of hyper fine splitting. Radial velocity ranges of the broad component in the HCN spectrum are selected by eye inspection. The other molecular lines, except those of ^{12}CO and HCN, do not exhibit the broad component, therefore maps were made only for narrow components. A remarkable point in these diagrams is that all of the intensity peaks of the narrow and broad components of molecules coincide with the IRAS position of the object. We do not find any difference in position between the narrow and broad components or between different molecular lines. The object seems slightly resolved within about 15″ beam. The directions of elongation seem different in each molecular transition; the narrow component of ^{12}CO and HCN are somewhat elongated along the X-direction; ^{13}CO and $C^{18}O$ are elongated along Y-direction; the broad component of ^{12}CO and the narrow component of CS seem to be unresolved.

In order to evaluate the size of this object more carefully, we computed model intensity variations and compared them with the observations. Figures 6.3a–e show position vs. integrated-intensity plots along the X and Y directions for each observed line. Intensities expected from simple homogeneous disk models with radii of 0″ (point source), 10″, 20″, and 30″ are drawn in the solid and broken curves. In the cases of ^{12}CO and HCN, we make the same plots for broad and narrow components. Horizontal uncertainties correspond with telescope pointing errors. Vertical uncertainties are standard deviations of integrated intensities calculated in velocity regions excluding emission lines. On the basis of comparison of the observed data points with the model curves, we conclude that molecular line emission of this object has an extension at least 15″ in radius. In Figure 6.3a, we can see that an extension of the narrow component of ^{12}CO is clearly larger than that of the broad component. But this phenomenon is not so clear in the case of HCN. It seems that narrow components of all of the lines except that of HCN extend to more than 15″, according to the simple homogeneous disk model. In the case of HCN, it is difficult to discriminate the broad and narrow components in the spectrum because of hyper splitting. We cut off the broad and narrow components from the spectrum to obtain the integrated intensities by eye inspection, but probably intensities of narrow and broad components still contaminate. Error bars of horizontal axis, which is pointing uncertainty of the telescope, are enough small to investigate the extension of the source. Therefore, we can safely believe the patterns of intensities indicated in Figures 6-2.

Figures 6.4a–e show position–velocity (PV) diagrams for each molecular line (background subtracted). No particular spatial velocity gradient was detected except for ^{13}CO, $C^{18}O$ and HCN. For the position–velocity diagrams of the narrow components ($\sim$ 35-36 km s^{-1}) of ^{13}CO, $C^{18}O$ and HCN exhibit a small velocity gradient along the X-axis (3.5×10^{-2} km s^{-1} $arcsec^{-1}$), which is the direction perpendicular to the bipolar axis. Even though the background emission is not homogeneous perfectly, the intensities of the background cloud at around 30 and 45 km s^{-1} remained small compared with the narrow component, especially in ^{12}CO, ^{13}CO, and $C^{18}O$.

6.2.3 Results of 150 GHz Continuum and Near-Infrared Observations

Plate 1 shows the 150 GHz continuum map toward IRAS 19312+1950 overlaid on a JHK false color composite image. The image size is 1.9′ × 1.9′. The 150 GHz continuum emission seems to be extended to the north–east along the bipolar axis. The peak flux density of 150 GHz continuum is 7.7 $\times 10^{-3}$ Jy per beam. The total integrated flux density of the source integrated over inner 25″ is 0.07 Jy ($\pm$0.01Jy). The near-infrared images (Plate 1) show that the number density of bright stars is less at the northeast part of the object than at the southwest part, suggesting that the dusts hide background stars more in northwest part of the object. Magnitudes of the central star (excluding the elongated components toward north-west to south-east) are 10.7, 7.8 and 6.3 mag in the J, H, and K-bands (uncertainty: $\pm$0.1 mag), respectively. Figure 6.5 shows a spectral energy distribution (SED) of the

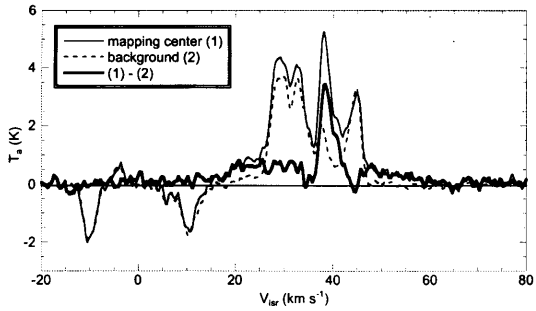

Figure 6.1a: Spectrum of ^{12}CO $J = 1$–0. The bold line indicates a background-subtracted spectrum, and the thin line indicates original spectrum at the mapping center. The broken line indicates the spectrum averaged over the spectra at $(X, Y) = (0'', \pm 60'')$, $(\pm 30'', \pm 30'')$, $(0'', \pm 30'')$, $(\pm 60'', 0'')$, and $(\pm 30'', 0'')$, which is used for the background subtraction.

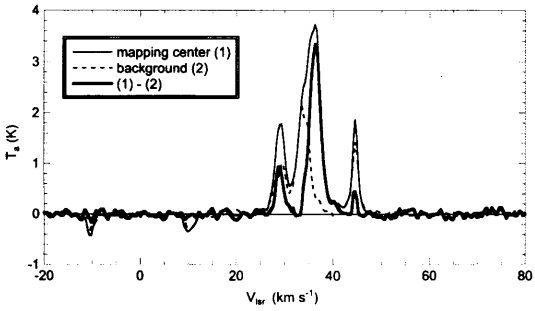

Figure 6.1b: The same as Figure 6.1a but for ^{13}CO $J = 1$–0. The background spectrum is the average of spectra taken at the same positions in the case of ^{12}CO.

IRAS 19312+1950. Black body curves are also drawn. In this figure, mid-infrared fluxes between 12 and 100 μm were taken from IRAS point source catalog. The SED shows a flat spectral (or moderate double peak) shape rather than a clear double peak structure. The double peak feature in the SED is one of the observational characteristics of proto-planetary nebulae (Kwok 2000). Furthermore, a remarkable excess in 60 and 100 μm can be seen; these two points were fit by a blackbody curve at the temperature of 70 K. In the galactic plane, interstellar dusts in the background molecular clouds occasionally emit far infrared radiation at 60 and 100 μm. Therefore, this excess may possibly be due to interstellar contamination. However, the IRAS mid- and far-infrared maps with about 1′ resolution shows a clear intensity peak at the IRAS position of IRAS 19312+1950. They suggest that most of the energy of radiation in the 60 and 100 μm originate from this object. Therefore, we consider that at least half of the far infrared fluxes at 60 and 100 μm come from this object.

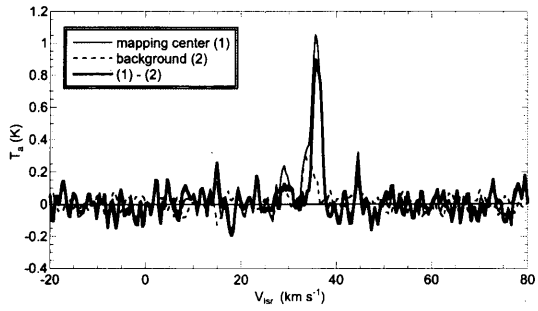

Figure 6.1c: The same as Figure 6.1a but for C^{18}O $J = 1-0$. The broken line indicates the spectrum averaged over the spectra at $(X, Y) = (0'', \pm 60'')$, $(\pm 60'', 0'')$, $(\pm 30'', 0'')$, and $(0'', \pm 30'')$.

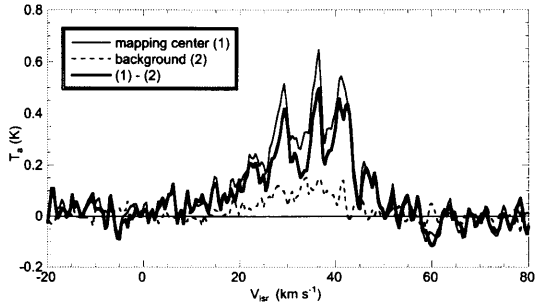

Figure 6.1d: The same as Figure 6.1a but for HCN $J = 1-0$. The broken line indicates the spectrum averaged over the spectra at $(X, Y) = (0'', \pm 60'')$, $(\pm 15'', \pm 15'')$, and $(\pm 60'', 0'')$.

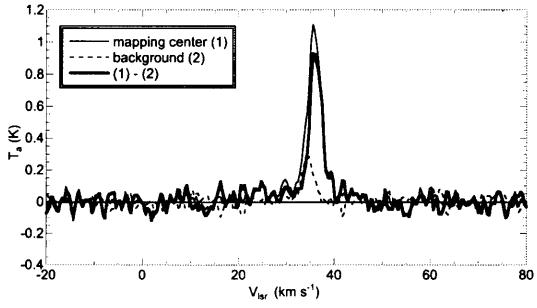

Figure 6.1e: The same as Figure 6.1a but for CS $J = 2-1$. The broken line indicates the spectrum averaged over the spectra at $(X, Y) = (0'', \pm 60'')$, $(\pm 30'', \pm 30'')$, $(0'', \pm 30'')$, $(\pm 60'', 0'')$, and $(\pm 30'', 0'')$.

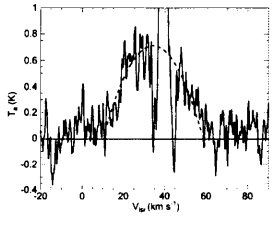

Figure 6.1f: Broad component in the ^{12}CO spectrum. A dotted line is a parabola, the best fit result to the broad componet.

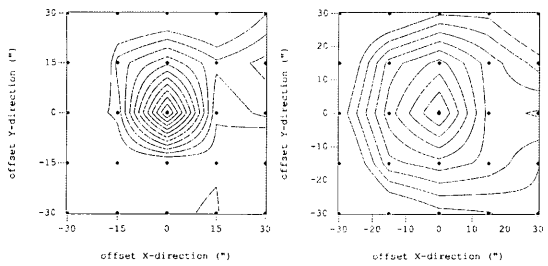

Figure 6.2a: Integrated intensity maps of the broad (left) and narrow (right) components of ^{12}CO. The contours in left and right panels are drawn in every 1.0 K km s^{-1} interval, and the peak intensity of the contour is 14.3 and 18.3 K km s^{-1}, respectively. Observed positions are indicated by small dots in the map. The Y-axis is taken along the bipolar axis of the nebula, i.e., in the direction 45° from the North, and the X-axis perpendicular to it (see text).

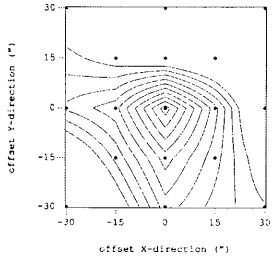

Figure 6.2b: The same as Figure 6.2a but for the narrow component of ^{13}CO. The contour interval is 2.0 K km s^{-1}, and the peak intensity is 29.15 K km s^{-1}.

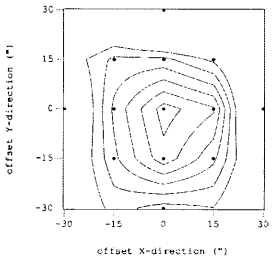

Figure 6.2c: The same as Figure 6.2a but for the narrow component of C^{18}O. The contour interval is 0.5K km s^{-1}, and the peak intensity is 5.73 K km s^{-1}.

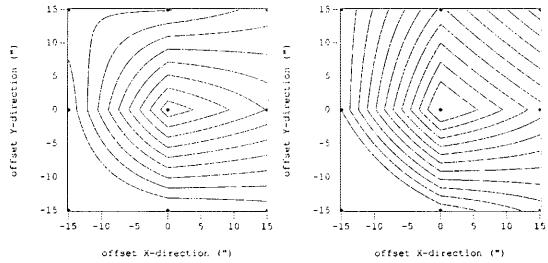

Figure 6.2d: The same as Figure 6.2a but for the broad (left) and narrow (right) component of HCN. The contour intervals are 0.5 and 0.1 K km s^{-1}, and the peak intensities are 5.85 and 3.29 K km s^{-1} for left and right panels, respectively.

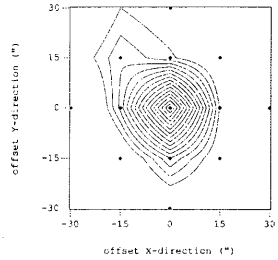

Figure 6.2e: The same as Figure 6.2a but for the narrow component of CS. The contour interval is 0.5 K km s^{-1}, and the peak intensity is 8.59 K km s^{-1}.

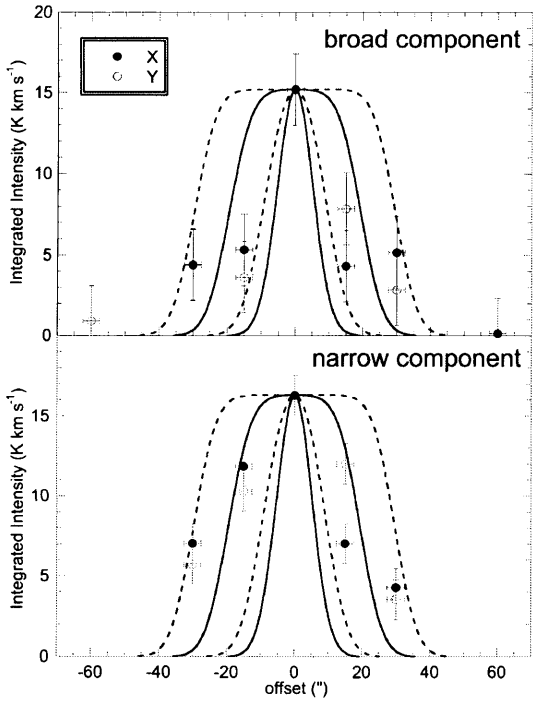

Figure 6.3a: Spatial intensity variation of the broad and narrow components of ^{12}CO. Filled and open circles indicate data at offset positions along X and Y directions, respectively. The Y-axis is taken along the bipolar axis of the nebula, i.e., in the direction 45° from the north, and the X-axis perpendicular to it (see text). Solid and dotted curves show expected intensities of the simple homogeneous disks with radii of 0, 10, 20, and 30″ for the telescope with a Gaussian beam. Peak values of these lines are adjusted to intensities taken at the mapping centers.

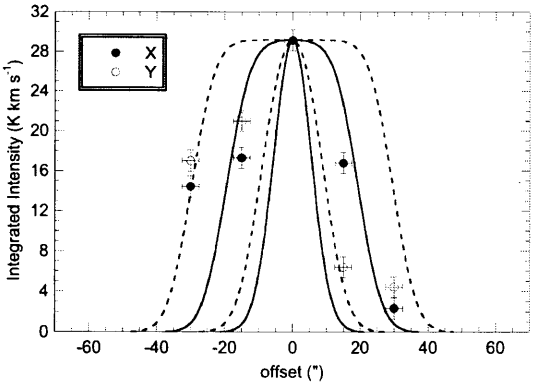

Figure 6.3b: The same as Figure 6-3a, but for the narrow components of ^{13}CO.

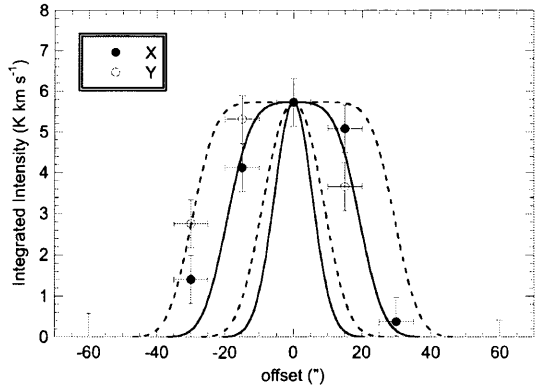

Figure 6.3c: The same as Figure 6-3a, but for the narrow components of C^{18}O.

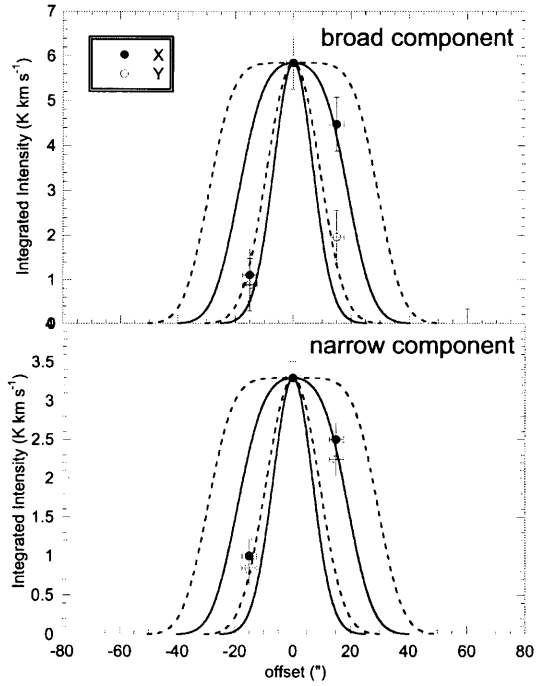

Figure 6.3d: The same as Figure 6-3a, but for the narrow components of HCN.

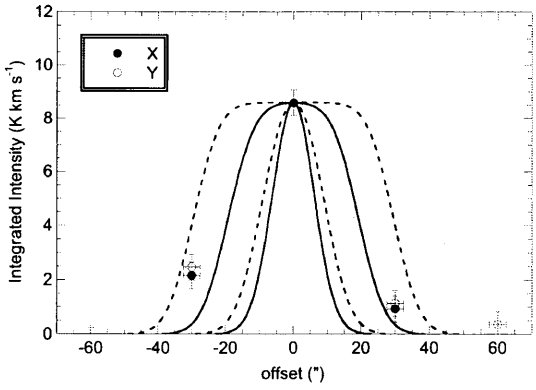

Figure 6.3e: The same as Figure 6-3a, but for the narrow components of CS.

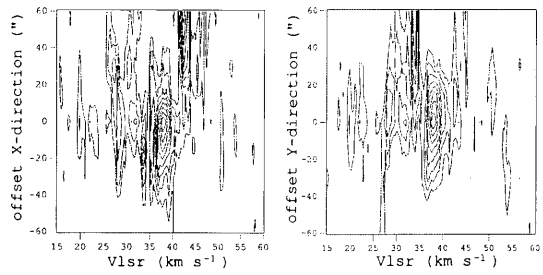

Figure 6.4a: Position–velocity diagram for the ^{12}CO $J = 1$–0 along the X- (left) and Y- (right) axis (X- and Y-axis are perpendicular and parallel to the bipolar axis respectively, see text). The contour interval is drawn in every 0.2 K interval, and the peak intensity is 1.81K.

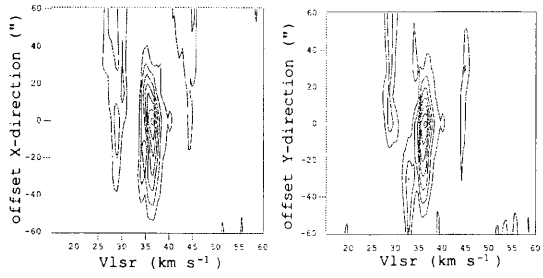

Figure 6.4b: The Same as Figure 6-4a but for ^{13}CO. The contour interval is 0.5K, and the peak intensity is 3.35K.

6.3 Discussion

6.3.1 Distance of the object

We estimate the distance of this object from the observed spectral energy distribution applying a standard interstellar extinction law at the JHK bands; the bolometric correction to the IRAS 12 micron flux density (Deguchi et al. 2001) is computed as $(BC)_{12} = 3.0$, where the half intensities at 60 and 100 micron are assumed to come from this object. The assumed luminosity of the object, 8000 $L_\odot$, gives the distance 3.9 kpc. Some fraction of IRAS 60 and 100 micron flux densities

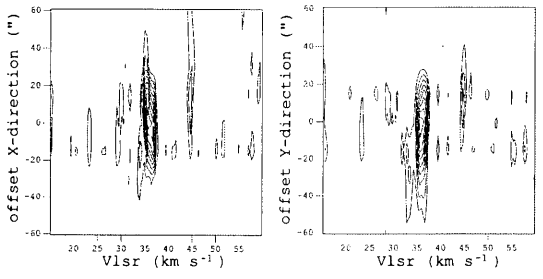

Figure 6.4c: The Same as Figure 6-4a but for C^{18}O. The contour interval is 0.1K, and the peak intensity is 0.90K.

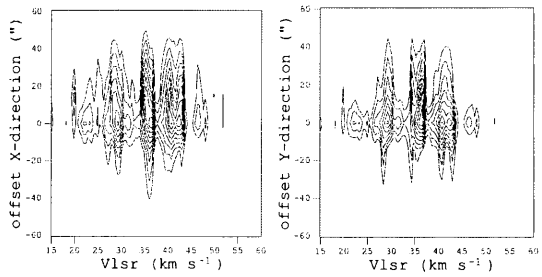

Figure 6.4d: The Same as Figure 6-4a but for HCN. The contour interval is 0.05K, and the peak intensity is 0.50K.

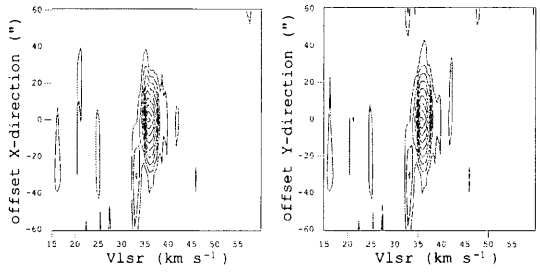

Figure 6.4e: The Same as Figure 6-4a but for CS. The contour interval is 0.1K, and the peak intensity is 0.93K.

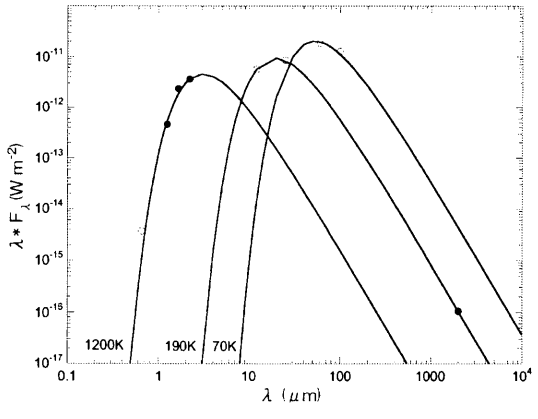

Figure 6.5: Spectral energy distribution of IRAS 19312+1950. The data at 0.65 μm (R-band) was taken from DSS phase II archive. The data between 12 and 100 μm were taken from IRAS point source catalog. Solid lines indicate expected lines from black body radiations at temperatures of 70, 190 and 1200K.

may come from the background cloud toward this object. The distance varies from 3.3 kpc to 5.1 kpc, when all of the IRAS 60 and 100 micron flux come from the source or nothing does, respectively. In addition, the luminosity of the central star at the proto-planetary phase may be larger than the assumed value, 8000 $L_\odot$. In such a case, the distance would increase with the square root of the luminosity. For simplicity, we assume in this paper that the distance to the object is 4 kpc. This value is consistent with the kinematic distance of this source, 4.55 kpc, obtained from V_{lsr} = 38 km s^{-1}.

6.3.2 The broad Component of ^{12}CO

In the background subtracted spectrum of ^{12}CO (bold line in Figure 6-1a), a broad component is seen in the velocity range, V_{lsr} = 15 – 55 km s^{-1}. This component is considered to be formed in an expanding envelope of a mass-losing star. Because the broad component is weak and overlapped with the strong background emission (see dotted line in Figure 6.1a), it is difficult to measure the full width of this weak component. However, it has a width of about 48 km s^{-1}, suggesting a typical expanding velocity of the envelope of 24 km s^{-1}. In addition, the velocity range of SiO maser emission, which is found in $V_{\rm lsr}$ =20–55 km s^{-1} (figure A.3), is well overlapped with the velocity range of the CO broad component. Moreover, the map of the broad component (left panel of Figure 6.2a) shows a clear intensity peak at the center position of this object. These facts strongly suggest that the broad component of CO is associated with this object.

In order to obtain the CO line parameters for the broad component, we fitted the line profile by a parabolic line-shape function (excluding the narrow part of emission), which is expected for the unresolved optically thick line emission in the expanding envelope (Morris and Alcock 1977). A best fit is indicated in Figure 6-1f. The full velocity width at zero maximum and the peak intensity of the fitted parabola are 48.28 km s^{-1}, and 0.71 K, respectively. The center velocity of the peak is 34.31 km s^{-1}, which is close to the peak velocity of the narrow component.

From the CO line intensity, the mass loss rate is calculated with the LVG model and the results are given in the Appendix (Table A.6). The best-fit value of the mass loss rate is $2 \times 10^{-4} M_\odot$ yr^{-1}.

6.3.3 The narrow component

On the other hand, we should be careful in interpreting the narrow component. The width of the narrow component is about 3 km s^{-1}; this is nearly the same for all of the lines of ^{12}CO, ^{13}CO, HCN and CS. While, the widths of the narrow components of weak lines of less abundant species (such as HCO^+, etc.) are dependent on molecule to molecule (Tables A.3 and A.4 in Appendix). These facts suggest that these molecular lines are formed in somewhat turbulent molecular cloud; the line width depends on the optical depths of the lines (e.g. Figure 1 of Lada 1976). The narrow-component emission seems to come from some cool component toward this object, for example, a dark cloud at the fore/background of this source.

We can estimate the column density of H_2 from CO line intensity when we assume the narrow component of CO comes from a dark cloud. Adopting the CO–H_2 conversion ratio of 2.6×10^{20} /(K km/s) (for example, Magnani et al. 1998), we obtain the H_2 column density, 6.1×10^{21} cm^{-2}, from the present observation ($T_{\rm peak}(^{12}CO)$=3.4 K, $HPFW$=2.9 km s^{-1}, and the telescope beam efficiency of 0.48). The total mass of H_2 within 16″ beam (assuming the distance of 4 kpc) is computed to be 7.3 $M_\odot$.

In the Position–Velocity diagrams (figures 6.4c and 6.4e), the narrow component of ^{13}CO and $C^{18}O$ exhibit a small velocity gradients along the direction perpendicular to the bipolar axis. We estimate a mass of this cloud on the basis of the velocity gradient, assuming the Keplerian motion of the narrow component, 0.35 km s^{-1}, at the inner radius of 5.96×10^{17} cm (5″). Then, we got 6 $M_\odot$ as a mass of the cloud when we assume a Keplerian edge-on disk. In fact, an inclination of the ring (which is seen in the SUBARU and UH88 telescopes [Tamura 2001, private communication]) is deduced to be 67°. In this case, the mass would increase by a factor of 1.2.

6.3.4 Dust

We detected continuum emission at a level of 0.07 Jy at 150 GHz. This emission is considered as radiation emitted by dust grains toward this object.

We estimate first the mass of the dust from simple homogeneous cloud model (i.e., Hogerheijde et al. 1997, ApJ 489, 293). When we assume $T_{\rm dust}$ = 10 K and a distance of 4 kpc of the cloud, we get the optical depth of the dust 1.4×10^{-3} at 150 GHz within a telescope beam. Adopting the mass absorption coefficient κ_ν =3×10^{-3} cm^2 g^{-1} (included both of gas and particle), we obtain 350 $M_\odot$ for the total mass of the dust cloud within a telescope beam. This value is inconsistent with the mass of cold cloud estimated from the CO narrow component, suggesting that the 150 GHz continuum emission does not come from the cold thick dark cloud but from the hot dust around the object.

Because dust emissivity increases with the temperature of grains, it is possible that the dust temperature is much higher than 10 K. In fact, the far infrared spectrum in figure 6.5 can be fit by the blackbody with $T_{\rm dust}$=70 K or higher. Dust temperature of an expanding envelope of a mass-losing star is higher near the central star and decrease with radius. Knapp et al. (1993) calculated the continuum flux densities of stars for model envelopes with various mass loss rates, and found that the model flux densities fit well with their observations of the late-type stars. Their model for OH

231.8+1.4 with the mass loss rate $2 \times 10^{-4}\ M_\odot\ \mathrm{yr}^{-1}$ in their paper gave $F_{150\mathrm{GHz}} = 0.39$ Jy at the distance 1.3 kpc. If we take the same model for IRAS 19312+1950, the flux density would be 0.04 Jy at distance of 4 kpc. This value is consistent with the continuum flux density observed in the present paper.

The dust is also responsible for the nebulosity seen on the near-infrared images, which is made by scattering the light from the central star. We can estimate the amount of the dust grains also by assuming the dust optical depth at K band is about unity in the envelope of this star. In this case, a simple estimate on the mass of the ring feature, which is present at the radius of 5″, (found on the SUBARU and UH88 telescope images), gives $2.2 M_\odot$. Here, we assume the 1″-thickness spherical dust shell and the standard gas-dust mass ratio.

From these estimates of the masses and from the fact that the velocities of the narrow components, $\sim$ 35–37 km s^{-1}, coincide well with the center velocities of the broad components (Table A.3), we conclude that the cloud responsible for the narrow component is not indepent from the central star. Rather, we are forced to consider that the narrow-component cloud of the mass of about 5–10 $M_\odot$ is a part of the object.

6.3.5 Is IRAS 19312+1950 a Proto-Planetary Nebula?

In general, PPNe are expected to have the following properties (Kwok 2000); (1) strong infrared excesses due to circumstellar matter; (2) the effective temperature of the central star between F and K type, (3) a detached dust shell due to termination of the AGB-phase mass loss, which has a doubly peaked spectral energy distribution; (4) the nebulosity seen in scattered light and no line emission of highly ionized atoms.

IRAS 19312+1950 shares the first and forth properties. It exhibits a red [12 - 25] IRAS color and shows a clear intensity peak at the IRAS position in the ^{12}CO intensity map. We took a narrow-band image using Br γ filter with ANU 2.3m telescope, but we find no ionized gas feature. Also at mid-infrared wavelengths, no emission feature was recognized in the IRAS low-resolution spectrum (except a probable noise at 17.8 μm; Volk et al. 1991). On the other hand, we should be careful in properties of (2) and (3). Effective temperatures between AGB and PN phases correspond with the surface temperature of F or G-type star, which is about 5000 - 7000 K; in this case, the central star should be seen in optical wavelength. A quite faint counterpart can be seen at the position of the central star in the phase II DSS image in R-band, but the star image is too faint for judging the spectral type. One explanation of this discrepancy of the characteristic is that IRAS 19312+1950 is a very young proto-planetary nebula just after AGB phase. In this case, the object should have almost the same effective temperature with that of AGB stars. The detection of SiO masers in IRAS 19312+1950 supports this explanation (Lewis 1989). The spectral energy distribution in Figure 6.5 does not show clear single nor double peaks. Rather, flux densities at 12, and 25 micron are well fit by the blackbody with a temperature of 190K, which is a temperature reasonable for the dust envelope at medium radii. Then, R, J, H and K band intensities are also well fit by the black body with the temperature of 1200K. These properties suggest that IRAS 19312+1950 is a very young proto-planetary nebula.

Progenitors of O-rich proto-planetary nebulae are inferred to be relatively massive stars ($\geq 4\ M_\odot$). According to the evolutional scenario at the AGB phase, the stars with masses below $\sim 4\ M_\odot$ ends up as a carbon-rich star by the He-burning at the core and succeeding dredge-up. However, in stars above that, the created ^{12}C atoms are further fused by the Hot Bottom Burning at the late-AGB phase (Marigo 2001) and the massive stars remain to be O-rich throughout the AGB phase with experiencing no (or a very short) C-rich era. Therefore, the mass of the progenitor of IRAS 19312+1950 is estimated to be relatively large. In recent days, Ventura et al. (1999) suggested that stars with relatively large initials mass ($\sim 3.8\ M_\odot$) first go through a short ($\Delta t \sim 30000$ yr) J-type (^{13}C-enhanced) carbon star phase before the hot bottom burning (HBB: Iben and Renzini 1983; Wood et al. 1983) convert them back into oxygen-rich stars, and ends back again to C-rich star. Estimated mass of the central star of IRAS 19312+1950 is somewhat large to experience this evolutional scenario.

However, it is possible that all of the OH/IR sources with very red colors ($C_{12} > 0.5$) are not necessarily proto-planetary nebulae, but stars with a detached shell which is a results of short termination of mass loss after He-shell flash (Suh & Jones 1997). In this case, the termination of the mass loss of a certain period (10^2–10^3 yr) can explain the spectral energy distribution as shown in figure 6.5. In this case, a gradual recovery of the mass loss after the He-shell flash can produce SiO masers at the inner envelope. Therefore, the presence of SiO masers in IRAS 19312+1950 can be explained naturally. The defect of this hypothesis is that the mass loss rate have to vary at least more than order of magnitude compared with the rate during the normal period. The calculations made by Blöcker (1995) gave relatively small drop of the mass loss rate after the He-shell flash for high-mass stars ($> 5 M_\odot$). Therefore, it may be difficult to create the developed detached shell as found in IRAS 19312+1950.

The coincidence of the masses, about 10 $M_\odot$, which were calculated for the dust shell and the CO narrow component in the previous sections, even suggests us another idea that IRAS 19312+1950 is the AGB object embedded in a small molecular cloud. The near-infrared radiation emitted by the central star can shine the dusty molecular cloud of the mass of about 10 $M_\odot$. In this case, the cloud cannot be a cradle of the AGB progenitor because the mass of the progenitor is comparable with this cloud. Only a possible case would

be the AGB star colliding with the cloud (for example, a cometary cloud; see Kulkarni et al. 1992). Even in such situation, the relative velocity between the cloud (the narrow component) and the AGB star (the broad component) is so small (< 1 km s^{-1}) that it is unlikely for such event to occur often.

It has been suggested that the origin of bipolar nebulae is a binary system (Morris 1981), which is an attractive hypotheses to explain the complexity of the envelope structure of IRAS 19312+1950. Cohen (1981) observed an excess of blue continuum toward OH231.8+4.2, which is one of the secure precedents of proto-planetary nebula with SiO masers, suggesting the presence of a companion to the Mira star. Sanchez Contreras et al. (2000) noted that the bipolarity of OH231.8+4.2 and shocks are indicators of a star that recently entered the post-AGB phase, while the Mira variable is an AGB object, and they proposed the possibility of a binary system composed of an AGB and a post-AGB star. This kind of second companion might be an origin of the mixture of C- and O-rich chemistries as found in OH 231.8+1.4, and possibly IRAS 19312+1950.

Because the trapped material (supposedly the narrow component) is located considerably far (5-20″) from the central star, the secondary star must be located also at the similar distance. We find no evidence for the other late-type star at such distances. Rather, it is possible that the counter part is evolved quickly to white dwarf and remnant of the ejected material remains still around the binary system. In this case, it is also difficult to keep the ejected material of a few solar masses standing still around the central star. However, the existence of secondary companion enables us to make models explaining the complex chemistry of IRAS 19312+1950.

With these arguments, we think at present that IRAS 19312+1950 is likely to be at an early stage of the proto-planetary nebula. However, the origin of narrow component is still a puzzle. The chemistry of this component is quite similar to that of dark clouds (see Appendix), though the dust temperature seems too high ($\geq$~70 K). They may be a remnant of the material, which is ejected in AGB phase from the central star and is trapped by a distant binary counterpart. Alternatively, a more drastic hypothesis may be a remnant of star forming material. The discussions on these points will be given more in near future.

6.4 Conclusion

We made the mapping observations of IRAS 19312+1950 in molecular lines of CO $J = 1 - 0$, ^{13}CO $J = 1 - 0$, C^{18}O $J = 1 - 0$, CS $J = 2 - 1$, HCN $J = 1 - 0$ transitions and in a 150 GHz continuum. In addition, we also made photometric observations in the J, H, and K bands obtaining a spectral energy distribution of this object between optical and radio frequencies. The main results are:

- The line profile of CO (and possibly HCN) exhibits a weak broad (~ 40 km s^{-1}) and a narrow (~ 3 km s^{-1}) components, whereas the profiles of the other lines (^{13}CO $J = 1 - 0$, C^{18}O $J = 1 - 0$, CS $J = 2 - 1$) exhibit only a narrow component. Both of the components have an intensity peak at the center position of the object.

- The narrow component was resolved by the 45-m telescope beam and it is extended by more than 15″ around the central star.

- The spectral energy distribution of this object exhibit a flat (or moderate double peak) feature at the near-infrared and middle infrared wavelengths with an excesses in the far-infrared band.

From these facts, we conclude that IRAS 19312+1950 is an transient object between AGB and planetary nebula phases, possibly a protoplanetary nebula.

TABLE 6.1
Mapping patterns

molecule	transition	spacing ($''$)	pattern
^{12}CO	$J = 1 - 0$	15	5×5
		60	9 points cross
^{13}CO	$J = 1 - 0$	15	3×3
		30	3×3
		60	5 points cross
$C^{18}O$	$J = 1 - 0$	15	3×3
		30	9 points cross
HCN	$J = 1 - 0$	15	3×3
		60	5 points cross
CS	$J = 2 - 1$	30	3×3
		60	9 points cross

TABLE 6.2
Line parameter.

molecule	transition	V_{peak} (km s^{-1})	T_{a1} (K)	rms (K)	T_{a2} (K)	I.I. (K km s^{-1})
^{12}CO	$J = 1 - 0$	37.85	2.46	0.12	1.81	22.20
^{13}CO	$J = 1 - 0$	36.22	3.73	0.05	3.35	29.26
$C^{18}O$	$J = 1 - 0$	35.60	1.05	0.06	0.90	5.66
HCN	$J = 1 - 0$, $F = 2 - 1$	36.03	0.60	0.04	0.50	3.29
CS	$J = 2 - 1$	35.50	1.11	0.05	0.92	8.79

T_{a1}: peak intensity of original spectrum.
T_{a2}: peak intensity of background-subtracted spectrum.
I.I.: integrated intensity of background-subtracted spectrum.

References

[Bell et al.(1993)] Bell, M. B., Avery, L. W., and Watson, J. K. G. 1993, ApJS, 86, 221

[Blöcker(1995)] Blöcker, T. 1995, A&Ap, 297, 727

[Cao et al.(1993)] Cao, Y. X., Zeng, Q., Deguchi, S., Kameya, O., and Kaifu, N. 1993, AJ, 105, 1027

[Deguchi et al.(1986)] Deguchi, S., Claussen, M. J., and Goldsmith, P. F. 1986, AJ, 303, 810

[Deguchi and Goldsmith(1985)] Deguchi, S., and Goldsmith, P. 1985, Nature, 317, 336

[Deguchi and Nakashima(2002)] Deguchi, S., and Nakashima, J. 2002, PASJ, in preparation

[Gomez et al.(2001)] Gomez et al. 2001, IAU Symposium 209

[Gomez et al.(1990)] Gomez, Y., Moran, J. M., and Rodriguez, L. F. 1990, Rev. Mex. Astron. Astrofis. 20, 55

[Gomez et al.(2001)] Gomez, Y., and Rodriguez, L. F. 2001, ApJ, 557, 109

[Hu et al.(1994)] Hu, J. Y., te Lintel Hekkert, P., Slijkhuis, S. Baas, F., Sahai, R., and Weed, P. 1994, A&ApS, 103, 301

[Iben and Renzini(1983)] Iben, I., and Renzini, A. 1983, ARA&A, 21, 271

[Jewell et al.(1991)] Jewell, P. R., Snyder, L. E., and Walmsley, C. M., Wilson, T. L., and Gensheimer, P. D. 1991, A&Ap, 242, 211

[Knapp et al.(1993)] Knapp, G. R., Sandell, G., and Robson, E. I. 1993, ApJS, 88, 173

[Kulkarni et al.(1992)] Kulkarni, S. R., Vogel, S. N., Wang, Z., and Wood, D. O. S. 1992, Nature, 360, 139

[Kuno et al.(1993)] Kuno, N., Matsuo, H., Mizumoto, Y., Lange, A. E., Beeman, J. W., and Haller, E. E. 1993, Int. J. Infrared Millimeter Waves, 14, 749

[Kwok(2000)] Kwok, S. 2000, The origin and evolution of planetary nebulae (Cambridge Univ. Press, Cambridge)

[Lada(1976)] Lada, C. J. 1976, ApJS, 32, 603

[Lewis(1989)] Lewis, B. M. 1989, ApJ, 338, 234

[Lewis(2000)] Lewis, B. M. 2000 in private communication

[Likkel(1989)] Likkel, L. 1989, ApJ, 344, 350

[Loup et al.(1993)] Loup, C., Forveille, T., Omont, A., and Paul, J. F. 1993, A&ApS, 99, 291

[Lovas(1992)] Lovas, F. J. 1992, J. Phys. Chem. Ref. Data., 21, 181

[Magnani et al.(1998)] Magnani, L., Onello, J. S., Hartmann, D., and Thaddeus, P. 1998, ApJ, 504, 290

[Morris and Alcock(1977)] Morris, M., and Alcock, C. 1977, ApJ, 218, 687

[Nakashima and Deguchi(2000)] Nakashima, J., and Deguchi, S. 2000, PASJ, 52, L43

[Nyman et al.(1993)] Nyman, L. -Å, Hall, P, J., and Le Bertre, T. 1993, A&Ap, 280, 551

[Nyman et al.(1998)] Nyman, L. -Å, Hall, P. J., and Olofsson, H. 1998, A&ApS, 127, 185

[Nyman et al.(1986)] Nyman, L. -Å, Johansson, L. E. B., and Booth, R. S. 1986, A&Ap, 160, 352

[Skrutskie et al.(2000)] Skrutskie, M. F., Stiening, R., Cutri, R., Beichman, C., Capps, R., Carpenter, J., Chester, J., and Elias, J. et al. (The 2MASS Team) 2000, http://www.ipac.caltech.edu/2mass/overview/2massteam.html

[Suh and Jones(1997)] Suh, K. -W., and Jones, T. J. 1997, ApJ, 479, 918

[Tamura(2000)] Tamura, M. 2000 in private communication

[van der Venn and Breukers(1989)] van der Veen, W. E. C. J., and Breukers, R. J. L. H. 1989, A&Ap, 213, 133

[Venture et al.(1999)] Venture, P., D'Antona, F., and Mazzitelli, I. 1999, ApJ, 524, L111

[Volk et al.(1991)] Volk, K., Kwok, S., Stencel, R. E., and Brugel, E. 1991, ApJS, 77, 607

[Wood et al.(1983)] Wood, P. R., Bessell, M. S., and Fox, M. W. 1983, ApJ, 272, 99

Chapter 7

Summary

A study presented in this thesis is a first attempt to study the evolutional of AGB star using SiO masers as a probe of the evolution. A core of this study is a systematic SiO maser survey using Nobeyama 45m telescope toward 548 IRAS sources, which distribute in the Galactic disk. In previous SiO maser surveys, observing samples are limited in IRAS sources with the temperature just around 300K, which are candidates for AGB stars. On the contrary, in this study, temperature range of the observing sample was extended to lower side (about 150 K). It has been known that the temperatures of dust envelopes around late-type stars tend to be lower with its evolutions. According to the temperature range of the present sample, more evolved stars (late-AGB and post-AGB stars) are included in the present sample. We discussed possibilities to study the evolution of late-type stars using SiO masers observations in this thesis.

First of all, we made observations toward IRAS source with relatively high temperature dust (around 300K, candidates for normal AGB stars) in the galactic disk regions ($25° < l < 40°$, $|b| < 5°$, and $40° < l < 70°$, $|b| < 10°$) in SiO maser transitions $J = 1 - 0$, $v = 1$ & 2. Finally, we observed 405 IRAS sources in this regions; 198 SiO maser emitters were detected. Because the observed regions overlapped with the region that has been frequently observed in OH maser at 1612MHz with Arecibo 300m telescope, we can minutely compare the results of SiO maser survey with that of OH maser survey. OH/IR sources have been regarded as relatively evolved late-type stars in comparison with SiO maser sources. A comparison the characteristics of SiO maser sources with that of OH/IR sources in important in terms of the evolution of the late-type stars. As a result of the comparison, a systematic difference in detection rates between SiO and OH maser searches was found. Among the source with higher temperature than 300K, SiO detection rate is higher than OH detection rate. Then, tangential points of the Galactic arms (Sagittarius-Carina and Scutum-Crux arms) exist in the observing regions at relative near points, about 5 kpc from the Sun. These provide us a chance to study a correlation between the galactic arms and the dynamics of AGB stars. Recent results of SiO maser survey suggest that dynamics of AGB stars tend to be influenced from galactic arms. If this were true, models of the evolutions of AGB stars (possibly of the Galaxy) would be restricted in some level. The present results suggest that a weak concentration of SiO sources in the $l - v_{lsr}$ diagram and in the face-on view diagram, were probably attributed to the galactic arms. In addition, data in the present SiO maser surveys give the local inclination of the rotation curve that is consistent with the values obtained previously in observations of the other kinds of disk population stars.

On the other hand, in this study, we made observations toward 143 IRAS sources with cool dust (temperature of the dust is about 150K – 250K) in the galactic disk ($-10 < l < 120, |b| < 10$) in SiO transitions $J = 1-0, v = 1$ & 2. Main components of the observing sample are late-AGB and post-AGB star. Some of the young stars may be contaminated in the sample in terms of the selection criterion. The number ratio of the young star in the sample is about 20 % according to the censuses using source of which kinds has been known. There are two aims in the observation of cool IRAS sources. First one is to cover the wide evolutional range of late-type star. If we combine the data of cool sources with that of normal AGB star, we can caver wide range of the evolution of the late-type stars in SiO maser observations. Second one is to find the proto-planetary nebulae with SiO masers. Finally, we detected 51 SiO maser emitters; 45 were new detections in SiO maser. From the kinematical viewpoint, cool stars did not show any difference with normal AGB stars. Then, we found that the intensity ratio of the SiO $J = 1 - 0, v = 2$ to the $J = 1 - 0, v = 1$ line is correlated with the IRAS color (dust temperature). In has been know that the intensity ration of SiO transitions $J = 1 - 0, v = 2$ to the $v = 1$ is nearly unity in the case of normal AGB stars. However, it is difficult to be understood this phenomena from the theoretical viewpoint, because excitation temperatures of two transitions totally different (v=1, 1600k; v=2, 3200K). In recent days, an overlap of SiO transition, $(J = 0, v = 1)$-$(J = 1, v = 2)$ and H_2O transition, $(\nu 2 = 01273)$-$((\nu 2 = 11166)$ has been suggested as a reason of the unity of SiO maser intensity ratio of normal

AGB stars, but this is not established theory yet. The correlation found in this work suggest that the intensity ratio of $J = 1-0, v = 2$ to the $v = 1$ tends to be strong with decrease of the dust temperature. It sound strange in some sense, because the excitation temperature of the transition of $J = 1-0, v = 2$ is twice of higher than that of $v = 1$. The present discovery of the correlation between SiO maser intensity ratio and IRAS color (dust temperature) would restrict the model of SiO maser pumping.

The observing sample of the SiO maser survey of cool IRAS sources includes many of candidates for proto-planetary nebulae (or post-AGB stars). Second aim of the SiO maser survey of cool IRAS sources is a search of proto-planetary nebulae with SiO masers. Proto-planetary nebulae with SiO masers are key object to clarify the evolution after AGB phase, because these objects exist at extreme early stage in the post-AGB evolution. In the present SiO maser observation of cool sources, finally, we found three SiO maser emission toward strong candidates for proto-planetary nebulae (IRAS18450-0148, IRAS18498-0017, IRAS19312+1950). In particular, a near-infrared counterpart with large extension more than $40''$ were confirmed toward IRAS19312+1950 in 2MASS image archives. Secure precedents of SiO maser emission toward proto-planetary are very rare. IRAS19312+1950 is second example of proto-planetary nebulae with SiO masers and a large near-infrared counterpart. In the near-infrared image of 2MASS archives, we confirm a spur structure in Northeast to Southwest direction, and an elongation of the central star in Northwest to Southeast direction. According to the detection of SiO and H_2O masers detection toward IRAS 19312+1950, this object should exhibit O-rich chemistry. But simultaneous detection of HCN thermal line toward this source confuses us. The detection of HCN suggests that the dust envelope around IRAS19312+1950 have complex chemistry mixed C- and O-rich chemical environment. In fact, 11 species of molecules were found in a multiple molecular line survey toward IRAS 19312+1950 (Appendix A). In this thesis, to reveal the extension and kinematics of the dust envelope of IRAS 19312+1950, mapping observations in the transitions CO 1-0, 13CO 1-0, C18O 1-0, HCN 1-0, CS 2-1 were made with Nobeyama 45-m telescope (Chapter 6). The dust envelope of IRAS 19312+1950 was resolved in all of the observed lines. In the results of the observations of 13CO 1-0, C18O 1-0, velocity gradients were confirmed in the Northwest to Southeast direction (along the elongation of the central star). A mass of the central star estimated by the velocity gradient on the assumption of Keplerian motion suggest that the central star may have relatively large initial mass nearly $8M_{\odot}$. This large mass might be clues to explain the complex chemistry of IRAS 19312+1950, because recent theory suggest that some of O-rich AGB stars with relatively large initial mass come back to the O-rich star after the evolution to C-rich star by a nuclear burning at the bottom of the surface convection layer (Hot Bottom Burning).

In this thesis, a capability of the SiO maser as a probe to investigate the evolution of late-type star was shown. In particular, the intensity ratio of SiO transition $J = 1-0, v = 1$ to the v=1 might be a tool to study the evolution of late-type star. In this thesis, we used SiO masers as a probe to find very young proto-planetary nebula, and succeeded to find a new secure example of proto-planetary nebula with masers. This discovery filled missing link in the early evolution in the post-AGB phase, and opened up the new field of the study of proto-planetary nebulae. In recent days, large-scale infrared data archives gradually open to the public, for example 2MASS, MSX. These archives provide new candidate for proto-planetary nebula. If we observe these new candidates for proto-planetary nebulae in SiO masers, the number of the proto-planetary nebula with maser would increase dramatically in near future. In addition, SiO maser emitters found in this thesis will be important target in the VERA project promoted by NOAJ.

Appendix A

Tentative Summary of Molecular Line Observations toward IRAS 19312+1950, an Unusual Protoplanetary Nebula: Circumstellar Chemistry

Abstract

This is a tentative summary of the molecular-line observations with the 45-m telescope of IRAS 19312+1950,a protoplanetary nebula, exhibiting a bipolar nebulosity on the near-IR images. This is a part of observations in theHCO^+, SO, and SiO (O-bearing) molecules, and CN, CS, HNC, NH_3, N_2H^+, and HC_3N (C- and N-bearing) molecules toward this object. We have also made mapping observations by the CO, ^{13}CO, and HCN (with 16–19″ beams) lines and the result will be published separately. The CO, HCN, HCO^+, SO line profiles are composed of the broad ($\Delta v \sim 30$ km s^{-1}) and narrow ($\Delta v < 5$ km s^{-1})components. The SiO profile has only broad component, and the line profiles of non-O-bearing molecules have only narrow component; Both components are spatially strongly peaked in intensity at the center of this object with a 16–19″ telescope beam. The $^{12}CO/^{13}CO/^{18}CO$ $J = 1$–0 line profiles show several other extended components apparently due toemission from the back/foreground clouds. A numerical model using the LVG code with the mass lossrate of $2 \times 10^{-4} M_\odot$ yr^{-1} gives good fit tothe observed data for the broad component. It is argued thatthe narrow component originates from a cool dust cloud seen toward this object, or alternatively, it comes from a cool material which surrounds outside of the expanding envelope of the AGB/post-AGB object.

A.1 Introduction

The 2MASS images of the infrared source, IRAS 19312+1950, exhibit a bipolar nebulosity of the size of about 30″ in the J, H, and K bands (Skrutskie et al. 2000). The IRAS color of this source, $log(F_{25}/F_{12}) = 0.47$, indicates a presence of cool dust of the temperature of about 200 K in this direction. Detecting SiO and H_2O maser lines toward this object, Nakashima and Deguchi (2000) concluded that this is an O-rich protoplanetary nebula similar to OH231.8+0.4. They also detected weak $H^{13}CN$ $J = 1$–0 and SO 2_2–1_1 lines; the center velocities of these thermal lines were slightly shifted from the maser lines. Based on the near- and mid-IR flux densities, the distance to this object was estimated to be about 4 kpc. It is quite unusual that these weak molecular lines are detectable in the envelope of the AGB or Post-AGB object as distant as 4 kpc way from the sun. For example, the distance to the similar object, OH231.8+0.4, is about 1.3 kpc (Morris et al. 1987). They suspected if these thermal lines are contamination of emission by the dark clouds in this direction.

On the one hand, an unusual nature of this object was eventually revealed by the imaging observations: a near-IR image using the UH 88-inch telescope shows a bright central star and surrounding nebula, extending from NE to SW (Figure 1) by about 30″. It also shows a small ($\sim 5''$) ring-like structure near the central star, which is elongated perpendicularly to the NE-SW bipolar axis. Line emission from H_2 vibrational states was also detected using the ANU 2.3-m telescope [see a note in Nakashima and Deguchi (2000)].

To clarify the details of the circumstellar envelope of this interesting object, we have made mm-wave molecular line observations using the Nobeyama 45-m radio telescope. We detected a number of thermal lines including CO, HCN, HCO^+, etc.; the profiles exhibit broad and/or narrow components depending on molecular species. Certainly, the CO line profile is composed of several peaks in the spectrum, indicating the existence of back/foreground clouds toward this object. Without doubt, the broad component with a full width of about 30 km s^{-1} centered at $V_{lsr} \simeq 34$ km s^{-1} originates from the circumstellar envelope of this object. However, the narrow component at $V_{lsr} \simeq 36$ km s^{-1} also exhibits a strong peak in intensity towards this object. We present a part of these molecular-line observations toward this object in the present paper.

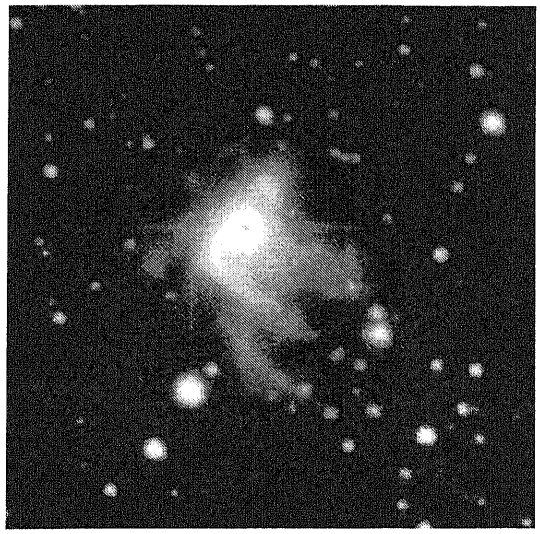

Figure A.1: The JHK composite image of the field of IRAS 19312+1950, using UH 88-inch telescope with the SIRIUS near-IR array camera (by courtesy of M. Tamura and K. Murakawa). The image size is 128″ × 128″. The north is up, the east is left.

A.2 Observations

The observations were made with the 45-m telescope at Nobeyama during 2001 February 4–9, and an additional observation was made on 2001 March 19 for checking time variation of SiO maser line intensities. A cooled SIS-mixer receiver (S100) with a bandwidth of about 0.5 GHz were used, and the system temperature (including atmospheric noise) was 300–500 K (SSB) depending on the frequency and weather. Additional HEMT and SIS-mixer receivers (H20 and S40), were used for observations in the 22 GHz water masers, and in the 43/49 GHz SiO/CS lines, respectively. The aperture and beam efficiencies of the telescope at the observed frequencies were summarized in table 1. The antenna temperature (T_a) given in the present paper is that corrected for the atmospheric and telescope ohmic loss but not for the beam or aperture efficiency. Acousto-optical spectrometer arrays of both low and high resolutions (AOS-W and AOS-H) were used. The AOS-H and AOS-W 2048-channel spectrometers have 40 and 250 MHz bandwidths, giving velocity coverage of about 120 and 800 km s^{-1} and the spectral resolutions of 0.5 and 3.4 km s^{-1} (per two binned channels), respectively at 86 GHz. The time spent for tuning receivers to the observing frequency was, typically, about 20 minutes. The frequencies of molecular lines were taken from Lovas (1992). For the check of tuning frequencies of various molecular lines, we observed the corresponding molecular lines toward W51 (e.g., Bell et al. 1993) every time prior to the observations of IRAS 19312 and confirmed that the strong lines were detected toward the W51 molecular cloud. The telescope pointing was checked using strong SiO maser source, V1111 Oph, and the pointing accuracy was confirmed to be better than 3″ in a windless condition. Observations were made in a position switching mode, and the off-position was chosen 12′ away from the object in right ascension, where a least contamination of background CO emission was confirmed. Total on-source

integration time per molecular line was approximately 30–60 minutes depending on the signal-to-noise ratio. When the detected lines were stronger than $T_a \simeq 1$ K, 5-point cross and 9-point square mappings were made. The IRAS position of this object, (19h 31m 12.800s, 19°50′ 22.00″, B1950), was taken as a map center.

We have detected strong CO emission toward IRAS 19312+1950. However, it turned out from the 30″- and 60″-grid mappings that emission spikes at V_{lsr} = 27–33, and 43 km s^{-1}, are extended more than a few arcmin, indicating that these are from the back/foreground clouds. With the 30″ grid mapping, we found that only the component at V_{lsr} =38 km s^{-1} is sharply peaked in intensity at the object position. The mapping of the other strong lines of high density tracers as HCN, HCO$^+$, and CS, resulted in that the component at V_{lsr} =38 km s^{-1} is sharply peaked at the IRAS position of this source. In this paper, we just show the result of the 5-point 1′-grid mapping in the HCO$^+$ J = 1–0 transition in Figure 1. We can recognize from this figure that the H^{12}CO$^+$ J = 1–0 line consist of the two components: a narrow component at V_{lsr} =38 km s^{-1}, and the weak broad component spreading from V_{lsr} =18 km s^{-1} to 50 km s^{-1}. Because these two components are also found in the other molecular lines as CO, HCN, and SiO, and SO, and they are strongly concentrated on the IRAS position of this object, we conclude that they are not from the back/foreground clouds. Though we have made mapping observations by several strong lines as the CO J=1–0, ^{13}CO J=1–0, CS J=2–1, HCN J=1-0 transitions, these emission lines are somewhat contaminated by emission from the back/foreground molecular clouds. Therefore, we present the result of the mapping by these lines separately. In this paper, we focus our attention only on the observations by the molecular lines which are the high density tracers.

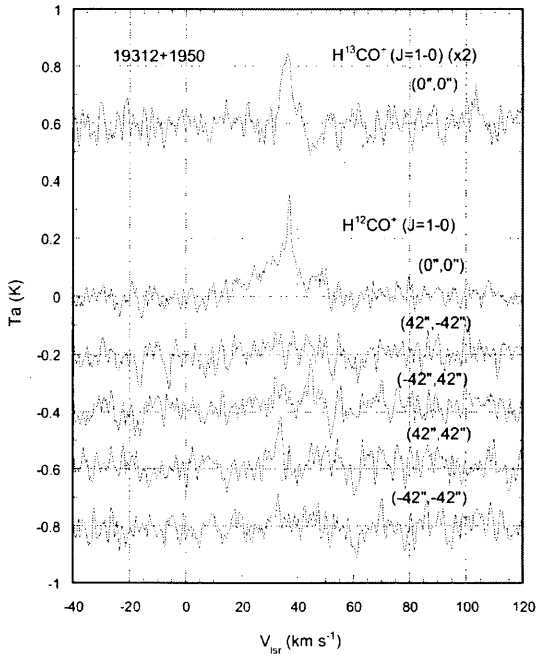

Figure A.2: Line profiles of HCO$^+$ and H^{13}CO$^+$ J = 1–0 transitions. The observed position for each spectrum is indicated in the parentheses (ΔR.A., ΔDec.) on the right. The HCO$^+$ profile at the center clearly shows broad (V_{lsr} = 20–50 km s^{-1}) and narrow (around V_{lsr} = 36 km s^{-1}) components.

A.2.1 Time variation of maser lines

We have also observed the SiO and H_2O maser lines to check the time variation. The results are summarized in Table 2 and the line profiles are shown in Figure 2. It is striking that the SiO J = 1–0 v = 2 spectrum have strong emission at $V_{lsr} \simeq 50$ km s^{-1}, but almost none in the J = 1–0 v = 2 transition. The integrated intensity of the SiO J = 2–1 v = 1 line was increased by a factor of more than 3 in about 40 days. If we compare these line profiles with those taken in May 2000 [Figure 1 in Nakashima and Deguchi (2000)], we can recognize drastic changes in the line profiles during 8 months. In May 2000, the radial velocities of most of maser lines were crowded around $V_{lsr} \simeq 20$ km s^{-1}. However, we observed in 2000 February that they spread between $V_{lsr} \simeq 20$ km s^{-1} and 55 km s^{-1}. This fact suggests that the center velocity of the star is 37 km s^{-1}, when we interpret these maser lines forming in the fore and rear parts of the expanding shell.

Emissions of OH 1612, 1665, 1667 MHz lines have been detected toward this object (Lewis 2000, private communication). Though the profiles of these OH lines are not doubly peaked, emissions spread between V_{lsr} =10 and 55 km s^{-1}. This observation also suggests that the stellar velocity is around $V_{lsr} \simeq 33$ km s^{-1}.

A.2.2 Thermal lines of oxygen-bearing molecules

From the detections of SiO, H_2O and OH maser lines, we can safely suggest that the circumstellar envelope of this object is O-rich. However, the detections of H^{13}CN J = 1–0 line toward this object and the slight velocity shift to the maser lines (Nakashima and Deguchi 2000) puzzled us, and these facts yielded the argument if the thermal lines may be due to contamination by the background cloud.

To clarify the situation, we observed several oxygen-bearing molecules as SiO (J = 1–0, v = 0), SO, and HCO$^+$. The results are summarized in Table 2, and the line profiles are shown in Figure 3. In addition, several lines of O-bearing molecules as SO_2 and OCS, were searched for; frequencies of some transitions of these molecules were fallen in our spectrometer band coverage. We have carefully checked whether or not any emissions are seen in the spectra, but no emission was found from these molecules. The negative results are summarized in table 5.

The line profiles of these O-bearing molecules (except H^{13}CO$^+$) seem to be composed of two compo-

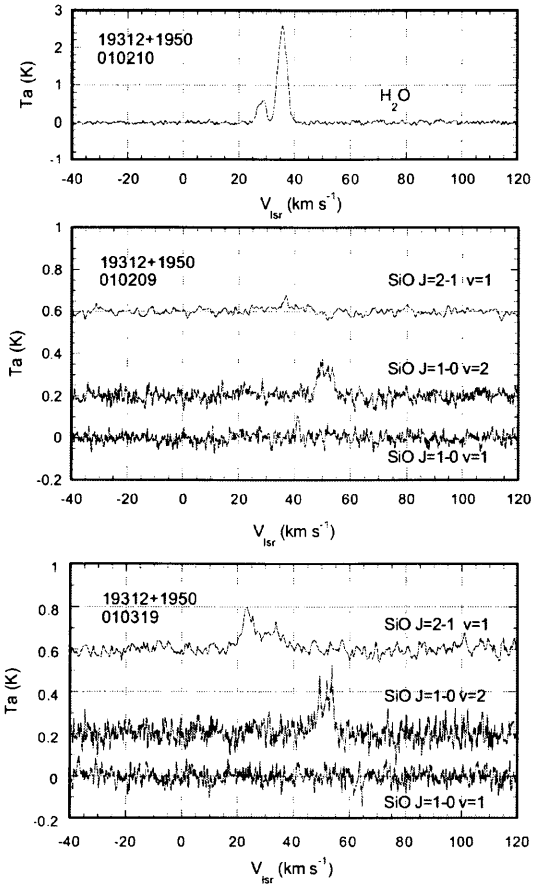

Figure A.3: Line profiles of the maser lines taken in 2001 February 10 and 2001 March 19.

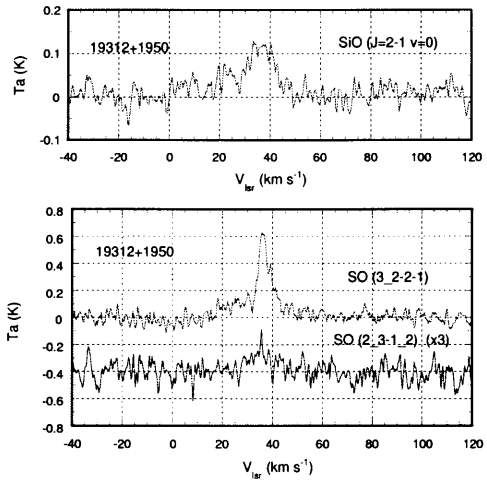

Figure A.4: The line profiles of SiO J=2-1 v=0, and SO 3(2)–2(1) and 2(3)–1(2) transitions. The SiO profile only exhibits a broad component, and SO profiles exhibits both broad and narrow components.

nents: narrow sharp feature peaked at $V_{lsr} \simeq 36$ km s^{-1}, and the broad feature with the full width at zero maximum of about 30 km s^{-1}. It seems that the SiO line profile does not have any narrow component.

It is well known that the profile of the optically thin line in the expanding shell is flat-topped and that of the thick line is parabolic when the telescope beam cannot resolve the envelope (Morris and Alcock 1977). The profiles of the broad components in figures 2 and 3 does not seems to be flat-topped, but rather they looks like parabolic. Therefore, we fitted the profiles of the broad component by a parabolic line-shape function (excluding the narrow part of emission) and the results were given in the 7–9 columns in Table 3. The line parameters for the narrow components, which were computed from the residue by the parabolic fit, are also given in the last two columns in table 4.

The average center velocity of the broad components, 34.3 km s^{-1}, is very slightly shifted from the average peak velocity of the narrow component, 35.6 km s^{-1}. In addition the profile of SiO thermal line ($J = 2$–1 $v = 0$) in figure 3 looks asymmetric with respect to the center velocity. The difference in the radial velocity between the narrow and board components seems meaningful. However, because the broad component is quite weak and overlapped with the narrow component, it is difficult to separate the broad component feature from the narrow component clearly in the present observations.

A.2.3 Thermal lines of non-oxygen-bearing molecules

We have also detected a number of lines of carbon- and nitrogen-bearing molecules. The results are summarized in table 4, and line profiles are shown in Figures 4–5. These lines often have hyperfine splitting except the CS lines. The spectra of these lines does not seems to have the broad component but they exhibits the narrow component, although the hyperfine splitting (shown by arrows in figure 5) tend to conceal the presence of the broad component.

The widths of the lines at the half intensity maxima are approximately 1.5–2.0 km s^{-1}. The average center velocity of these lines in table 4 is 35.9 km s^{-1}, which is consistent with the average velocity of the narrow component of O-bearing molecules. The width of the narrow component seems to vary from molecule to molecule. The CS line has a full width of about 8 km s^{-1}, while, HCO^+ less than 2 km s^{-1}. This fact can be interpreted by a characteristic of the lines formed in a turbulent media where the width depends on the line optical depth.

The molecular species observed as narrow component are somewhat similar to those observed in the C-rich circumstellar envelopes (e.g., Bujarrabal et al. 1994). A number of carbon-chain molecules have been detected in the C-rich protoplanetary nebulae (Fukasaku et al. 1994). However, SiS, which is common in the C-rich envelopes, was not detected in IRAS 19312.

The high HNC/HCN abundance ratio is often considered as a signature of photochemical reactions (Morris et al. 1987; Glassgold 1996). The line intensity of the HNC emission, $T_a \sim 0.6$ K, is comparable with the HCN intensity, $T_a \sim 0.8$ K in this object, suggesting a photochemical origin of this molecule. Even taking into account the line saturation in the HCN lines [$\tau(F = 2-1)$ ~2–4 can be deduced from $T_a(F = 0-1)/T_a(F = 2-1) = 0.56$ and $T_a(F = 1-1)/T_a(F = 2-1) = 0.76$ in this star, where these ratios are 0.2 and 0.6, respectively, in a thermal quilibrium], we can reach the same conclusion that the HNC/HCN abundance ratio is relatively high (> 0.3) in the narrow component.

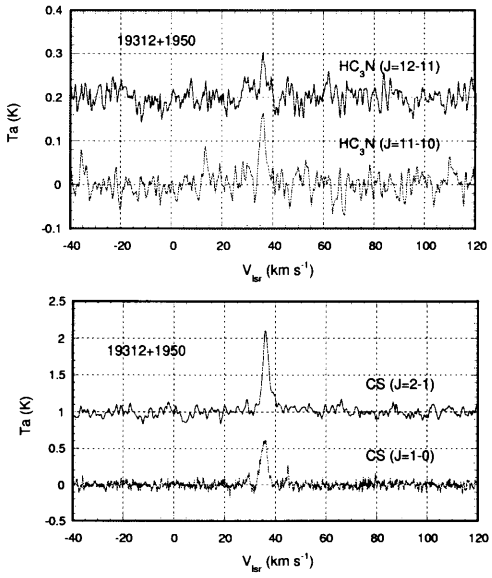

Figure A.5: Line profile of HC_3N and CS. The hyperfine splitting of HC_3N is quite small and not recognizable here. Both of HC_3N and CS lines seem to exhibit a narrow component.

A.3 Discussion

A.3.1 Distance to IRAS 19312+1950

We estimated the distance to this object from the 2MASS J, H, and K, magnitudes and IRAS 12, 25, 60, and 100 micron flux densities; the bolometric correction for the IRAS 12 micron flux density is computed as $(BC)_{12}$ =3.0 (Deguchi et al. 2001), where the half intensities at 60 and 100 micron are assumed to come from this object. The assumed luminosity of the object, 8000 $L_\odot$, gives the distance, 3.9 kpc. A part of the IRAS 60 and 100 micron flux densities may come from the background cloud toward this object. The distance varies from 3.3 kpc to 5.1 kpc, when all of the IRAS 60 and 100 micron flux come from the source or nothing does, respectively. In addition, the luminosity of the central star at the protoplanetary phase may be larger than the assumed value, 8000 $L_\odot$. In such a case, the distance would increase with the square root of the luminosity. For simplicity, we assume in this paper that the distance to the object is 4 kpc.

It is somewhat curious that the distance to this source is quite large compared with the distances to the know objects, for example, as OH231.8 (1.3 kpc; Morris et al. 1987).

A.3.2 The broad component: molecular abundance

In order to obtain the abundance of the detected molecules, the numerical calculations based on the large-velocity-gradient (LVG) model was performed. The numerical code was used to compute the line intensities of linear molecules in the expanding shell (Deguchi et al. 1990). The code was slightly modified to involve the SO molecule which has a slightly complex energy-level structure; line parameters (Einstein A coefficients etc.) of SO were taken from Tiemann (1974) [see the level diagram in Omont et al. 1993].

In this numerical code, the kinetic temperature of the envelope is calculated by taking into account the adiabatic and line (CO, CI, and CII) cooling and the gas–dust drift and CI ionization heating (see the detail in Deguchi et al. 1990). The dissociations of CO, HCN, SiO, SO due to interstellar UV radiation are taken into account; the self absorption of CO UV lines are also

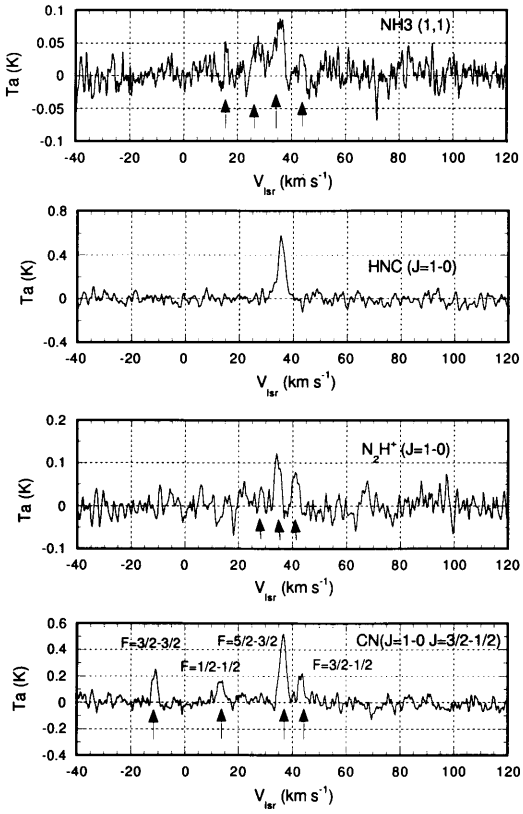

Figure A.6: Line profiles of NH_3, HNC, N_2H^+, and CN. The positions of the hyperfile lines were indicated by arrows. The splitting of HNC are less than 0.7 km s^{-1}, so that they are not shown here. All of these lines exhibits only a narrow components.

taken into account. However, the photodissociation rate of SiO and SO are not well known. Therefore, we assume that photodissociation rate of these molecules are the same as the CO dissociation rate (without self-absorption).

We assume that the envelope is expanding wih a constant velocity of 15 km s^{-1}. The calculation starts from the inner radius of 5×10^{16} cm and stops at the outer radius of 1.07×10^{18} cm (corresponding to 18″ from the star). The mass loss rate (which is assumed to be constant), the kinetic temperature at the inner radius, and molecular abundance are free parameters and a best-fit model to the observational data were sought. The results were shown in table 6, where molecular species, abundance of the observed molecule with the broad component, frequencies, transitions, and the observed main-beam brightness temperature, and the calculated main-beam brightness temperature were given for the model with the mass loss rate of $2.1 \times 10^{-4} M_\odot$ yr^{-1}. In this model, the main-beam brightness temperature was determined mostly from the brightness temperature of the lines around 10^{17} cm with $N_{H_2} = 10^4$ cm^{-3} (except the CO $J = 1$–0 transition). Because the photodissociation of molecules occur slightly outside of this radius, a slight uncertainty of the photodissociation rate in various molecules except CO does not influence much to the results.

The obtained SO abundance, 5×10^{-7}, is similar to those found in normal O-rich envelopes (Guilloteau et al. 1986; Omont et al. 1993).

For the case of HCO^+, the abundance of this molecule is assumed to be constant in the present calculation. Because the molecular abundances of HCN and HCO^+ in the O-rich circumstellar envelopes have been somewhat controversial (Morris et al. 1987; Deguchi et al. 1990), we computed the expected HCO^+ abundance in the same code used in Deguchi et al. (1990). The maximum HCO^+ abundance obtained is about 1.5×10^{-5} per H_2 at the radius of 2.3×10^{17} cm (corresponding to 4″ from the star). Because there are still some arguments in the H_3^+ dissociative recombination rate (Amano 1988), this value is probably available maximum. Therefore, The obtained HCO^+ abundance, 1.8×10^{-7}, is consistent with the chemical model to produce HCO^+ (see Glassgold 1996).

A.3.3 The narrow component: what is it ?

The molecular species detected in the present paper are quite similar to those detected in the envelope of OH231.8+4.2 (Morris et al. 1987), indicating a resemblance of IRAS 19312+1950 to OH231.8+4.2. However, if we compare carefully the object with OH231.8, we notice several differences.

Firstly, SO_2 molecules were not found in IRAS 19312 (see table 4), but were detected in OH231.8 (Morris et al. 1987; SO are detected in both); the line intensity ratio of the SO_2 3_{13}–02_2 (104.029 GHz) to SO 2_2–1_1

line is 6.2 in OH231.8 (Morris et al. 1987), while it is < 0.2 in IRAS 19312+1950 (Nakashima and Deguchi 2000). This fact reminds us that the rich molecular lines detected toward IRAS 19312 (as a narrow component) resemble to the lines usually found in the dark clouds; for example, in L134N, the SO molecules have been found but not SO_2 (Swade 1989).

The NH_3 (1,1) inversion line was detected, but not the (2,2) line in this object, suggesting the rotational temperature of the concerning levels (both para-NH_3) lower than 16 K in the narrow component of this object. In OH 231.8, both lines were detected, suggesting the rotation temperature of (27 ± 4) K (Morris et al. 1987).

A somewhat similar "broad and narrow" components ($\Delta V \sim 66 \pm 20$ and 20 km s^{-1}, respectively) were mentioned by Fong et al. (2001) in the ISO observation of the OI line in the C-rich protoplanetary nebula, CRL 618. These are, however, different from those seen in IRAS 19312; the narrow component in CRL 618 is the usual expansion motions of the envelope (corresponding to the broad component of IRAS 19312), and the broad component in CRL 618 is a high-velocity flow located near the center in the CO lines (Gammie et al. 1989; Cernicharo et al. 1985). On the other hand, the narrow component seen in IRAS19312 is from a very cool, low density gas with very low expansion velocity ($\Delta V < 4$ km s^{-1}; probably the width is made by turbulence). It is difficult to create such a low velocity by dust-driven mass loss.

The preliminary analysis of the CO 15″- and 30″-grid map of this object indicates that the narrow component is apparently extended more than 40″ but the broad component is detected only at the center. The 15″ grid mapping indicates that the intensity peak of the narrow component is slightly ($\sim 5''$) shifted to the east. No elongation along or perpendicular to the bipolar axis was detected in the mapping observations.

From these facts, we are forced to conclude that the narrow component is a small dark cloudlet, which is seen by chance on the same line of sight toward IRAS 19312. However, we cannot completely deny a hypothesis that this narrow component is a part of the gas cloud which is physically related with IRAS 19312, even though they may not be the gas ejecta from the central star itself.

The molecular species detected as narrow component are not common molecules in the O-rich circumstellar envelope. However, this seems to be quite similar to the phenomena found in the envelope of some O-rich stars where molecules as HCN, NH_3, and HCO^+ have been detected in the O-rich envelope (Deguchi et al. 1985; Morris et al. 1987; Nguyen-Quang-Rieu et al. 1988); These molecules can be produced as a result of photodissociation of CO and ion-molecular reactions in the outer envelope.

There is evidence for O-rich material surrounding the carbon stars (Willems and Jong 1986; Nakada et al. 1987; Le Bertre et al. 1990; Jiang 2000). These materials are considered to be the gas and dust which were ejected at the phase of O-rich AGB stars but were trapped by a hypothetical binary companion (Lloyd-Evans 1990). When the central star changes atmosphere from O-rich to C-rich, the presence of the O-rich material would observationally become evident. It is possible that we are looking these trapped materials as narrow component.

It is probably the best to perform mm-wave interferometric observations with high spatial resolution in order to clarify the physical relation between the narrow and broad components.

A.4 Conclusion

We have detected a variety of molecular lines of O-, C- and N-bearing molecules toward IRAS 19312+1950, a protoplanetary nebula. The line profiles consist of narrow and broad components of the widths of 4 and 30 km s^{-1}, respectively. From the parabolic line shape, the broad component is inferred to originate from the circumstellar envelope of this object. The LVG calculation suggest the mass loss rate of about $2 \times 10^{-4} M_\odot$ yr^{-1} for this object. However, the origin of the narrow component is still a puzzle; from the low temperature and variety of molecules detected, it is suggested to be a back/foreground cloud. However, from the present observational evidence, it is difficult to deny the possibility that the narrow component is a material trapped by a hypothetical binary companion.

TABLE A.1
Telescope parameters (2001 March)

Receiver	Frequency (GHz)	HPBW (″)	Beam efficiency	Aperture efficiency
H20	22	72	0.81	0.62
S40	43	40	0.77	0.57
S100	86	18.6	0.49	0.42
S100	100	16.3	0.51	0.41
S100	110	15.4	0.48	0.35

Table A.2
Line parameters for Maser lines

Mol.	Frequency (GHz)	Transition	V_{lsr}(Peak) (km s^{-1})	T_a(Peak) (K)	*Integ.Inten.* K (km s^{-1})	rms (K)	Obs.date (yymmdd)
H_2O	22.235077	6(16)–5(23)	35.6	2.588	12.105	0.031	010210
SiO	43.122080	1–0 v=1	41.1	0.108	0.122	0.021	010209
	42.820587	1–0 v=2	49.9	0.184	3.999	0.021	010209
	86.243442	2–1 v=1	36.9	0.184	0.513	0.020	010209
SiO	43.122080	1–0 v=1	—	—	—	0.033	010319
	42.820587	1–0 v=2	53.8	0.328	1.347	0.042	010319
	86.243442	2–1 v=1	23.2	0.199	1.731	0.020	010319

Table A.3
Line parameters for line with broad and narrow features

Mol.	Ref. Freq. (GHz)	Transition	peak feature V(p) (km s^{-1})	Ta(p) (K)	rms (K)	broad compo. V(par) (km s^{-1})	T(par) (K)	FWZM (km s^{-1})	narrow compo. Ta(nar) (K)	I.I.(nar) (K km s^{-1})
SiO	86.846998	1–0 v=0	33.3	0.128	0.027	35.1	0.086	34.9	—	—
$H^{13}CO^+$	86.754294	1–0	36.2	0.123	0.021	—	—	—	0.123	0.556
HCO^+	89.188518	1–0	36.9	0.326	0.025	32.3	0.060	41.8	0.269	0.849
SO	99.299870	3(2)–2(1)	35.8	0.624	0.019	33.5	0.112	44.5	0.513	2.459
SO	109.252184	2(3)–1(2)	35.6	0.104	0.043	36.2	0.028	35.2	0.076	0.093
SO	100.029569	4(5)–4(4)	—	—	0.023	—	—	—	—	—

Table A.4
Line parameters for lines with narrow features only

Mol.	Ref. Freq. (GHz)	Transition	V(peak) (km s^{-1})	Tpeak (K)	I.I. (K km s^{-1})	rms (K)
NH_3	23.694506	(1,1)	35.7	0.08800	0.655	0.016
	23.722633	(2,2)	—	—	—	0.020
	23.870131	(3,3)	—	—	—	0.017
	24.139417	(4,4)	—	—	—	0.022
CS	48.990964	1–0	36.2	0.62130	1.977	0.042
	97.980968	2–1	36.3	1.1008	3.852	0.059
HNC	90.599998	1–0	35.4	0.58170	1.930	0.039
N_2H^+	93.173505	1–0	34.1	0.122	0.65715	0.020
HC_3N	100.076389	J=11–10	36.3	0.163	0.48126	0.018
HC_3N	109.173634	J=12–11	36.2	0.104	0.40343	0.020
CN	113.490982	1-0 (all)	36.755	0.521	3.4388	0.033

Table A.5
Negative results for S-bearing molecules

Mol.	Freq (GHz)	Transition	rms (K)
SO_2	86.153709	39(9,31)–40(8,32)	0.016
	86.639108	8(3,5)–9(2,8)	0.025
	90.548251	25(3,23)–24(4,20)	0.049
	104.029416	3(1,3)–2(0,2)	0.020
	104.239293	10(1,9)–10(0,10)	0.020
$^{34}SO_2$	88.720604	7(3,5)–8(2,9)	0.042
	104.391850	10(1,9)–10(0,10)	0.025
^{34}SO	97.715388	3(2)–2(1)	0.063
OCS	109.463063	9–8	0.023
SiS	90.771546	5–4	0.058

Table A.6
Model fit for the broad component for mass loss rate of $2.1 \times 10^{-4} M\odot$

Mol.	Abundance per H_2	Ref. Freq. (GHz)	Transition	T_{MB}^{obs} (K)	T_{MB}^{model} (K)
SiO	7.9×10^{-7}	86.847	2–1 $v = 0$	0.18	0.18
HCN	7.6×10^{-7}	88.632	1–0	0.41	0.41
HCO^+	1.8×10^{-7}	89.188	1–0	0.12	0.11
^{13}CO	3.3×10^{-6}	110.201	1–0	< 0.1	0.27
CO	4.6×10^{-4}	115.271	1–0	1.79	1.81
SO	5.3×10^{-7}	86.094	2(2)-1(1)	0.05	0.07
		99.299	3(2)-2(1)	0.22	0.21
		109.252	2(3)-1(2)	0.05	0.17

References

[Amano(1988)] Amano, T. 1988, ApJ, 329, L121

[Bell et al.(1993)] Bell, M. B., Avery, L. W., Watson, J.K.G. 1993, ApJS, 86, 221

[Bujarrabal et al.(1994)] Bujarrabal, V., Fuente, A., Omont, A. 1994, ApJ, 421, L47

[Cernicharo et al.(1985)] Cernicharo, J., Guelin, M., Penalver, J., Martin-Pintado, J., Mauersberger, R. 1989, A&A 221, L1

[Deguchi et al.(1985)] Deguchi, S., Goldsmith, P.F. 1985, Nature 317, 336

[Deguchi et al.(1990)] Deguchi, S., Izumiura, H., Kaifu, N., Mao, X., Nguyen-Q-Rieu, and Ukita, N. 1990, ApJ. 351, 522

[Deguchi et al.(1992)] Deguchi, S., Izumiura, H., Nguyen-Q-Rieu, Shibata, K., Ukita, N., and Yamamura, I., 1992, ApJ. 392, 597

[Deguchi et al.(2001)] Deguchi, S. Fujii, T., Matsumoto, S., Nakashima, J., Wood, P.R. 2000, PASJ 53, 293

[Fong et al.(2001)] Fong, D., Meixner, M., Castro-Carrizo, A., Bujarrabal, V., Latter, W. B., Tielens, A. G. G. M., Kelly, D. M., Sutton, E. C. 2001, A&A, 367, 652

[Fukasaku et al.(1994)] Fukasaku, S., Hirahara, Y., Masuda, A., Kawaguchi, K., Ishikawa, S., Kaifu, N., Irvine, W. M. 1994, ApJ, 437, 410

[Gammie et al.(1989)] Gammie, C. F., Knapp, G. R., Young, K., Phillips, T. G., Falgarone, E. 1989, ApJ, 345, 87

[Guilloteau et al.(1986)] Guilloteau, S., Lucas, R., Omont, A., Nguyen-Q-Rieu 1986, A&A, 165, L1

[Glassgold(1996)] Glassgold, A. E. 1996, ARA&A, 34, 241

[Hasegawa and Kwok(2001)] Hasegawa, T.I., Kwok, S. 2001 (preprint)

[Jiang(2000)] Jiang, B. W., Szczerba, R., Deguchi, S. 2000, A&A, 362, 273

[Le Bertre et al.(1990)] Le Bertre, T., Deguchi, S., Nakada, Y. 1990 A&A 235, L5

[Lloyd-Evans(1990)] Lloyd-Evans, J. 1990, MN, 243, 336

[Lovas(1992)] Lovas, F. J. 1992, J. Phys. Chem. Ref. Data, 21, 181

[Meixner et al.(1998)] Meixner, M., Campbell, M.T., Welch, W.J., Likkel, L. 1998, ApJ, 509, 392

[Morris and Alcock(1977)] Morris, M., Alcock, C. 1977, ApJ, 218, 687

[Morris et al.(1987)] Morris, M., Guilloteau, S., Lucas, R., Omont, A. 1987, ApJ, 321, 888

[Nakada et al.(1987)] Nakada, Y., Izumiura, H., Onaka, T., Hashimoto, O., Ukita, N., Deguchi, S.; Tanabe, T. 1987, ApJ, 323, L77

[Nakashima and Deguchi(2000)] Nakashima, J. Deguchi, S. 2000, PASJ 52, L43

[Nguyen-Quang-Rieu et al.(1988)] Nguyen-Quang-Rieu, Deguchi, S., Izumiura, H., Kaifu, N., Ohishi, M., Suzuki, H., Ukita, N. 1988, ApJ, 325, 795

[Omont et al.(1993)] Omont, A., Lucas, R., Morris, M., Guilloteau, S. 1993, A&A, 267, 490

[Skrutskie et al.(2000)] Skrutskie, M. F., Stiening, R., Cutri, R., Beichman, C., Capps, R., Carpenter, J., Chester, J., Elias, J. et al. 2000 (The 2MASS Team) http://www.ipac.caltech.edu/2mass/overview/2massteam.html

[Swade(1989)] Swade, D.A. 1989, ApJ, 345, 828

[Tiemann(1974)] Tiemann, E. 1974, J. Phys. Chem. Ref. Data, 3, 259

[Willems and de Jong(1986)] Willems, F.J., de Jong, T. 1986, ApJ 309, L39

[Yamamura et al.(1994)] Yamamura, I. Shibata, K. M., Kasuga, T., and Deguchi, S., 1994, ApJ . 427, 406

[Yamamura et al.(1995)] Yamamura, I., Onaka, T., Kamijo, F., Deguchi, S., and Ukita, N., 1996, ApJ. 465, 926

Acknowledgement

My first, and most earnest, acknowledgment must go to my supervisor, Dr. Shuji Deguchi. Nearly five years ago, when I was a master course student of Osaka Kyoiku University, I have been to Nobeyama for the purpose of a study trip to see observations of the SiO maser survey project promoted by Dr. Deguchi; it made me start working at Nobeyama. Dr. Deguchi has been instrumental in ensuring my academic, professional, financial, and moral well being ever since. In every sense, none of this work would have been possible without him.

Far too many people to mention individually have assisted in so many ways during my work at Nobeyama. They all have my sincere gratitude. In particular, I would like to thank, Prof. Yoshikazu Nakada, Dr. Hideyuki Izumiura, Dr. Osamu Kameya, Dr. Hiroshi Imai, Dr. Takahiro Fujii, Dr. Atsushi Miyazaki, Dr. Yoshifusa Ita, and Dr. I. S. Glass, all the corroborators of the SiO maser survey.

I would also like to thank Dr. Shin-ichiro Okumura, Dr. Nario Kuno, and Dr. P. R. Wood, all of the collaborators of my observation. Prof. Kozo Sadakane, who was my supervisor when I am a master course student, have kept encouraging me even after the graduation from Osaka Kyoiku University. I also owe huge debt of gratitude to staffs of Nobeyama Radio Observatory. I had lived in the guesthouse of the observatory through the period of my Ph.D. study, and I am under the heartfelt care of the staff of Nobeyama. I would like to thank them.

My final thank-you goes to my wonderful parents. For always being there when I needed them most, and never once complaining about how infrequently I visit, they deserve far more credit than I can ever give them.